

Afbraak van vluchtige organische stoffen door gecombineerd gebruik
van niet-thermisch plasma en heterogene katalyse

Abatement of Volatile Organic Compounds by Combined Use
of Non-Thermal Plasma and Heterogeneous Catalysis

Arne Vandenbroucke

Promotoren: prof. dr. ir. C. Leys, prof. dr. R. Morent
Proefschrift ingediend tot het behalen van de graad van
Doctor in de Ingenieurswetenschappen: Chemische Technologie

Vakgroep Toegepaste Fysica
Voorzitter: prof. dr. ir. C. Leys
Faculteit Ingenieurswetenschappen en Architectuur
Academiejaar 2014 - 2015



ISBN 978-90-8578-826-3
NUR 926
Wettelijk depot: D/2015/10.500/70

PROMOTOREN

Prof. dr. ir. C. Leys

Vakgroep Toegepaste Fysica EA17
Faculteit Ingenieurswetenschappen en Architectuur
Universiteit Gent

Prof. dr. R. Morent

Vakgroep Toegepaste Fysica EA17
Faculteit Ingenieurswetenschappen en Architectuur
Universiteit Gent

LEDEN VAN DE EXAMENCOMMISSIE

Prof. dr. ir. R. Van de Walle

Decaan FEA
Faculteit Ingenieurswetenschappen en Architectuur
Universiteit Gent

Prof. dr. ir. C. Leys

Vakgroep Toegepaste Fysica EA17
Faculteit Ingenieurswetenschappen en Architectuur
Universiteit Gent

Prof. dr. R. Morent

Vakgroep Toegepaste Fysica EA17
Faculteit Ingenieurswetenschappen en Architectuur
Universiteit Gent

Prof. dr. ir. N. De Geyter

Vakgroep Toegepaste Fysica EA17
Faculteit Ingenieurswetenschappen en Architectuur
Universiteit Gent

Prof. dr. ir. J. Thybaut

Vakgroep Chemische Proceskunde en Technische Chemie EA12
Faculteit Ingenieurswetenschappen en Architectuur
Universiteit Gent

Dr. J.-M. Giraudon

Unite de Catalyse et Chimie du Solide UMR 8181
Universite' des Sciences et Technologies de Lille (Lille 1)

Prof. dr. F.J. Romero-Salguero

Department of Organic Chemistry
Faculty of Sciences
University of Córdoba

Universiteit Gent

Faculteit Ingenieurswetenschappen en Architectuur
Vakgroep Toegepaste Fysica EA17
Onderzoeksgroep Plasmatechnologie
Sint-Pietersnieuwstraat 41, B-9000 Gent



Acknowledgments

If the successful completion of this thesis has learned me one thing, it has to be that hard work pays off in the end. During the course of these exciting six years, I have had the chance to work together with many interesting people to which I want to express my gratitude.

First of all, I would like to express my sincere appreciation to Prof. dr. ir. C. Leys for giving me the opportunity to work at the Department of Applied Physics back in 2009.

My promotors Prof. dr. ir. C. Leys and Prof. dr. R. Morent were indispensable with their guidance during the course of this PhD. Especially, the help and support of Prof. dr. R. Morent cannot be stressed enough as he learned me so many things. I wish to thank him for the many stimulating discussions. Also, I want to thank him for his patience, encouragement and understanding which helped me through some tough times.

I want to express my appreciation to Prof. dr. ir. N. De Geyter for all her kind support and warm help, especially with the FT-IR measurements.

To my present and former colleagues at the Department of Applied Physics I want to say thanks for the enjoyable atmosphere during these past six years. I want to express my gratitude to the technical staff of the department – D. Lauwers, P. Guns, D. Vincke and J. Peelman. Without the technical knowledge and expertise of this team, my research would never have been possible. They were always prepared to adapt and improve the experimental set-up. Special thanks goes out to D. Vincke and J. Peelman who developed the optimized plasma reactor. The successful realization of this piece of craftsmanship was their most challenging task up to then and filled both them and me personally with a feeling of pride. I wish to thank I. Waterloos, W. Meulemans and F. Janssens for the several administrative tasks they fulfilled.

I wish to thank both Prof. dr. J.-F. Lamonier and Dr. J.-M. Giraudon of the Unité de Catalyse et de Chimie du Solide – Lille (France) for the fruitful collaboration. I also want to show my gratitude to Dr. M.T. Nguyen Dinh for all the moments we worked together to obtain meaningful experimental results. Sometimes we really struggled with the set-up but it only helped us to become patient researchers.

I would like to thank Prof. dr. A. Bogaerts and Dr. R. Aerts for the collaboration to develop and validate the plasma-chemical model. Without their enormous expertise in plasma modeling we would never be able to succeed to grasp the complexity of the plasma-chemical processes. I want to especially thank Robby for all the fine moments

we had during international conferences. You became not only a respectable colleague but also a true friend.

I want to express my appreciation to Prof. dr. F.J. Romero–Salguero and Dr. M. Mora of the Department of Organic Chemistry – Cordoba (Spain) for the fruitful collaboration. Special thanks goes out to Manuel for his enthusiasm and for learning me so many things during his three months stay at our lab. You also became more than just a colleague, thank you for all the nice moments we shared.

I wish to thank my thesis students – Ir. A. Van der Stricht, Ir. T. Vandenbrande and Ir. J. Reyniers. By supervising you, I learned a lot of skills that will help me in my future career.

I want to say thank you to Ir. S. Sultana who will carry on this interesting research. I am sure you will succeed in your goal and wish you all the best for the years to come.

I also want to express my appreciation to L. Joye for proofreading the draft version of this thesis.

To my girlfriend Linsy, my lovely daughter Oona and our dog Bruno I want to say thank you from the bottom of my heart for always being there for me. Your love and care gave me courage and motivation when I needed it.

Finally, I want to thank my parents who have always believed in me and supported me. Without you I would never have walked around on this lovely planet let alone have been possible to experience this incredible journey.

Table of contents

Summary	i
Dutch Summary – Nederlandstalige Samenvatting	v
List of Acronyms	xi
List of Publications	xiii
1. Air pollution	1
1.1 Introduction	3
1.2 Volatile organic compounds	4
1.2.1 Definition and classification	4
1.2.2 Sources	6
1.2.2.1 Anthropogenic sources.....	7
1.2.2.2 Biogenic sources	10
1.2.3 Reactions in the atmosphere.....	12
1.2.4 Trichloroethylene.....	15
1.3 Effects	17
1.3.1 Environmental effects	18
1.3.1.1 Global warming.....	18
1.3.1.2 Depletion of the ozone layer	19
1.3.1.3 Formation of photochemical smog	21
1.3.2 Health effects	23
1.3.3 Other effects.....	24
1.4 Legislation	25
2. Conventional VOC abatement technologies	27
2.1 Classification	29
2.2 Selection criteria	31
2.2.1 Economical considerations	31
2.2.2 Technical criteria	32
2.2.3 Gas stream conditions	32
2.3 Non-destructive methods	33
2.3.1 Adsorption	33
2.3.2 Absorption	35
2.3.3 Condensation	36
2.3.4 Membrane separation	38
2.4 Destructive methods	40
2.4.1 Biochemical methods	40
2.4.2 Thermal oxidation	44
2.4.3 Catalytic oxidation	46
2.4.4 Photocatalysis	47

3. Literature overview	51
3.1 Introduction	53
3.2 Non-thermal plasmas for VOC abatement	54
3.2.1 Without catalyst	54
3.2.1.1 What is a non-thermal plasma?	54
3.2.1.2 Reactor concepts	55
3.2.1.3 VOC abatement.....	59
3.2.2 Combined with catalyst.....	85
3.2.2.1 What is plasma-catalysis?	85
3.2.2.2 Different types of catalysts	89
3.2.2.3 VOC abatement.....	90
3.3 Critical process parameters.....	120
3.3.1 Temperature	120
3.3.2 Initial VOC concentration.....	121
3.3.3 Humidity level	121
3.3.4 Oxygen content	124
3.3.5 Gas flow rate	125
4. Plasma reactor concept and techniques for gas and catalyst analysis	127
4.1 Negative DC corona/glow multi-pin-to-plate discharge	129
4.2 Chemical analytical techniques	131
4.2.1 Fourier transform infrared spectroscopy	132
4.2.1.1 The electromagnetic spectrum and spectroscopy ..	132
4.2.1.2 Discovery of infrared light.....	133
4.2.1.3 History of IR spectroscopy.....	134
4.2.1.4 Vibration theory.....	134
4.2.1.5 Instrumentation.....	138
4.2.1.6 Fourier transformation.....	142
4.2.1.7 Measurement and evaluation of IR spectra	143
4.2.2 Mass spectrometry.....	144
4.2.3 Detection of ozone.....	146
4.2.4 X-ray photoelectron spectroscopy	147
4.2.5 Time-of-flight secondary ion mass spectroscopy	149
4.2.6 Raman spectroscopy	150
4.2.7 X-ray powder diffraction	151
4.2.8 Determination of specific surface area of catalysts	152
4.2.9 Determination of metal dispersion on catalyst surface	153
5. Material and methods	155
5.1 General.....	157
5.2 Gas supply system.....	157
5.3 Reactor system	159
5.3.1 Plasma reactor	159
5.3.1.1 Plasma reactor A.....	159

5.3.1.2	Plasma reactor B.....	159
5.3.1.3	Measurement of discharge current and voltage	160
5.3.2	Catalytic reactor	161
5.4	Gas analysis system	162
5.4.1	FT–IR spectrometer	162
5.4.2	Mass spectrometer.....	164
5.4.3	Ozone monitor.....	164
5.5	Preparation of catalysts	165
5.5.1	MnO ₂	165
5.5.2	LaMnO _{3+δ}	165
5.5.3	Pd/LaMnO ₃	165
5.5.4	Ce–Mn binary oxides.....	166
5.5.4.1	CeMn _x O _y	166
5.5.4.2	MnO _y	166
5.6	Catalyst characterization	166
5.6.1	XPS	166
5.6.2	ToF–SIMS	167
5.6.3	Raman spectroscopy	168
5.6.4	X–ray powder diffraction	168
5.6.5	Determination of specific surface area of catalysts	169
5.6.6	Determination of metal dispersion on catalyst surface	169
5.7	Calibration of FT–IR spectrometer	170
5.8	Experimental parameters for the evaluation of the VOC abatement process.....	170
6.	Strategic methodology	173
6.1	Introduction	175
6.2	Identification of by–products of TCE abatement with NTP	175
6.3	Development of a plasma–chemical model for TCE abatement with NTP.....	176
6.4	Improving TCE abatement by combining NTP with heterogeneous catalysis	176
6.4.1	Commercial MnO ₂ catalyst	177
6.4.2	Perovskite–type catalyst LaMnO _{3+δ}	178
6.4.3	Incorporation of Pd into LaMnO _{3+δ}	179
6.4.4	Mn–Ce binary oxide catalysts.....	179
7.	Qualitative by–product identification of plasma–assisted TCE abatement by mass spectrometry and Fourier–transform infrared spectroscopy.....	181
7.1	Introduction.....	183
7.2	Experimental conditions.....	183
7.3	Results and discussion.....	183
7.3.1	Mass spectrometry.....	183
7.3.2	Fourier–transform infrared spectroscopy	187

7.3.3	Overview and discussion of by-product identification..	192
7.4	Conclusions	194
8.	Modeling and experimental study of TCE abatement with a negative direct current corona discharge.....	195
8.1	Introduction	197
8.2	Description of the model and chemistry	197
8.3	Experimental conditions	200
8.4	Results and discussion	201
8.4.1	Effect of the energy density on the removal efficiency of TCE.....	201
8.4.2	Effect of the humidity on the removal efficiency of TCE	202
8.4.3	Destruction pathway of TCE	205
8.4.4	By-products of TCE destruction.....	208
8.4.5	Energy yield	211
8.5	Conclusions	213
9.	TCE abatement with a plasma-catalytic system using a commercial catalyst: Investigation of the synergy effect	215
9.1	Introduction	217
9.2	Experimental conditions	217
9.3	Results and discussion	217
9.3.1	TCE abatement using non-thermal plasma.....	217
9.3.2	TCE abatement using MnO ₂ as catalyst.....	218
9.3.3	TCE abatement using the plasma-catalytic combined system... ..	219
9.3.4	Calculation of the activation energy for TCE abatement with plasma-catalysis	221
9.3.5	Synergy factor in the TCE abatement by plasma-catalysis	222
9.3.6	The role of the ozone in TCE abatement by plasma-catalysis.....	224
9.3.7	Transformations in TCE abatement by plasma-catalysis.. ..	225
9.4	Conclusions	226
10.	Plasma-catalysis of low TCE concentration in air using LaMnO_{3+s} as catalyst: Influence of the air humidity and catalyst temperature	229
10.1	Introduction	231
10.2	Experimental conditions	231
10.3	Results and discussion	231
10.3.1	Destruction of TCE with NTP.....	231
10.3.2	Destruction of TCE with PPC.....	232
10.3.3	Reaction by-products of TCE decomposition.....	234

10.3.4	Effect of the temperature	238
10.3.5	XPS characterization of the used catalysts	240
10.4	Conclusion.....	242
11.	Combination of non-thermal plasma and Pd/LaMnO₃ catalyst for dilute TCE abatement.....	243
11.1	Introduction	245
11.2	Experimental conditions.....	245
11.3	Results and discussion	245
11.3.1	TCE abatement with NTP	245
11.3.2	TCE abatement with PPC.....	246
11.3.3	By-product distribution for NTP/PPC	248
11.3.4	Characterization of the catalyst	251
11.3.4.1	XPS	251
11.3.4.2	ToF-SIMS of the used catalysts	252
11.4	Conclusions	255
12.	Post plasma-catalysis for total oxidation of TCE over Ce-Mn based oxides synthesized by a modified “redox-precipitation route”	257
12.1	Introduction	259
12.2	Experimental conditions	259
12.3	Results and discussion	259
12.3.1	Catalyst properties	259
12.3.2	TCE decomposition efficiency	262
12.3.3	Detection of the gaseous by-products by FT-IR	266
12.3.4	XPS studies of the used catalysts	268
12.3.5	Scheme of TCE degradation.....	271
12.4	Conclusion.....	272
13.	General conclusions and future work	273
13.1	General conclusions	275
13.2	Future work	277
	Appendix.....	281
	References.....	291

Summary

Air pollution is an environmental issue of widespread concern as it deteriorates our climate and is harmful for both human and ecological life. Since the start of the industrial revolution in the 19th century air pollution has grown into a global transboundary problem that adversely affects air, water, soil and ecosystems. The industrialization of many economies has led to the emission of various kinds of harmful substances such as NO_x, SO_x, O₃ and H₂S. Another large and important group of air pollutants consists of volatile organic compounds (VOCs). This group comprises of many different chemicals that easily evaporate due to their high volatility. When they enter the atmosphere they deteriorate its natural balance and cause various effects including the creation of photochemical smog, secondary aerosols and tropospheric ozone. Moreover, they are known to be responsible for global warming and the ozone hole in the stratosphere. Many VOCs are also dangerous to human health because they are potentially toxic, carcinogenic or mutagenic. Therefore, their emission should be reduced in order to improve air quality and restore our environment for future generations.

Conventional end-of-pipe methods to control VOC emissions are well established technologies such as adsorption, thermal and catalytic oxidation, membrane separation, bioreaction and photocatalysis. The disadvantage of these methods is that they become cost-inefficient and difficult to operate when low VOC concentrations need to be treated. With the increased severity of emission limits in mind, this creates the need for alternative and sustainable technologies that overcome these weaknesses. In this regard, the application of non-thermal plasma (NTP) technology for the abatement of VOCs is a promising approach. Plasma, also known as the fourth state of matter, is generated by electrical discharges in which energetic electrons collide with background molecules (N₂, O₂, H₂O). This transforms a neutral gas into an ionized state containing a reactive mixture of electrons, ions, radicals, metastables and photons. When VOCs are subjected to these energetic, active plasma species they collide causing VOC molecules to be decomposed through cleavage of chemical bonds. The energy that is delivered to the plasma source is almost completely consumed to accelerate electrons while the background gas remains near room temperature. This non-equilibrium state makes it unnecessary to heat the entire treated gas flow in contrast to thermal and catalytic oxidation. Another interesting feature is related to the operation at atmospheric pressure which excludes the use of expensive vacuum equipment. Furthermore, NTP is characterized by its quick start-up, compact size and rapid

response to changes in the composition of the waste gas due to fluctuations in the process.

Although NTP technology for end-of-pipe air cleaning has frequently been proposed in literature formation of undesired by-products, poor energy efficiency and mineralization remain serious roadblocks towards industrial implementation. To overcome these technological issues, researchers are exploring the combination of NTP and heterogeneous catalysis in a technique called plasma-catalysis. This innovative method has become a hot research topic over approximately the last ten years. In a plasma-catalytic system, the catalyst can either be located inside the discharge region or downstream of the plasma reactor. For the former case, the catalyst and plasma affect each other, resulting in complex interactions which can alter the properties of the catalyst and/or the plasma. When the catalyst is placed after the plasma reactor, long-lived species produced by the plasma (e.g. ozone, NO_x) can reach the catalyst surface and can improve the performance of the process. For both reactor configurations, the reactions in the gas-phase and on the catalyst surface often add up to induce a synergetic effect on the overall removal efficiency.

The discussion above serves as the main rationale for the work presented in this thesis, which is devoted to investigate the opportunities of combining NTP with heterogeneous catalysts for the abatement of trichloroethylene (TCE), a typical chlorinated VOC. In a first part, the research context is highlighted and an extensive literature overview is presented in order to provide a clear framework for the reader. In a second part, the experimental results are discussed in detail. For the first time, it is shown that the plasma-assisted abatement of TCE with a negative DC corona discharge partially leads to the formation of undesired, toxic polychlorinated by-products such as dichloroacetylchloride (DCAC), trichloroacetaldehyde (TCAA) and phosgene (PG). This is attributed to incomplete oxidation of TCE. Other detected by-products include carbon monoxide, carbon dioxide, hydrogen chloride, chlorine and ozone. Further on, a numerical model is developed in order to theoretically investigate the underlying plasma chemistry for the abatement of TCE. Up to now, only one other study in literature numerically investigated the removal of TCE from $\text{Ar}/\text{O}_2/\text{H}_2\text{O}$ mixtures. Due to the fact that these mixtures have little relevance for industrial applications, the abatement of TCE from dry and humid air is investigated in this work. It is shown that the Cl atom, mainly produced by dissociation of COCl , is one of the controlling species in the TCE destruction chemistry and contributes to the production of chlorine containing by-products. A good agreement is found between experiments and the

model for both dry and humid air. An increase of the relative humidity has a negative effect on the removal efficiency. The main reactions that contribute to the removal of TCE are with $\text{ClO}\cdot$, $\text{O}\cdot$ and CHCl_2 . A reaction pathway for the abatement of TCE in humid air is also proposed. Based on the results gathered in these two studies, appropriate catalysts were chosen to combine with the plasma source by locating them downstream of the discharge. It is shown that manganese based catalysts are efficient candidates for total oxidation of TCE in terms of activity and selectivity. This is mainly attributed to the fact that these catalysts have high ozone decomposition efficiency. This leads to the production of active oxygen species which are able to oxidize remaining TCE and its by-products. It should be stressed that, except for the first catalyst, all others were for the first time investigated in combination with NTP for VOC abatement. Initially, a commercial MnO_2 catalyst is studied. By combining both systems, the activation energy is significantly decreased compared to pure catalytic conditions. This suggests that the polychlorinated intermediates produced by the plasma are more susceptible for catalytic oxidation than TCE. Although no clear synergetic effect is found for TCE abatement, the synergy factor for the yield to CO and CO_2 is high, indicating that the plasma-catalytic system greatly enhances the selectivity of the process towards total oxidation compared to the plasma alone case. Next, lanthanum manganite (LaMnO_3) which is a perovskite type catalyst was tested. This is an environment-friendly and inexpensive material and known to be among the most active catalysts for the oxidation of chlorinated VOCs. For plasma-catalysis in dry air, an optimum catalyst temperature is found to be 100°C resulting from a compromise between catalyst deactivation and enhancement of the catalytic reactions. The influence of humidity is remarkable. Despite the fact that water is able to block the active sites, the performance for TCE abatement is enhanced in humid air due to the role of water to act as a chlorine scavenger at the surface of the catalyst, therefore retarding the perovskite degradation. The incorporation of noble metals in low quantity into a perovskite structure is known to increase the catalytic activity as well as to enhance the stability of the metal against sintering, metal-support interaction and volatilization. Therefore, LaMnO_3 is doped with palladium (Pd) and tested for TCE abatement. When the temperature of Pd/LaMnO_3 is increased to 200°C the formation of DCAC is suppressed while the formation of phosgene is decreased in the order of 50% compared to the plasma alone system. No ozone is detected in the outlet stream which proves that Pd/LaMnO_3 is effective for ozone decomposition and substantially enhances the mineralization of TCE compared to the plasma alone system. As surface area can play an

important role in O_3 decomposition, dispersion of MnO_x is thought to be greatly improved by forming Ce–Mn binary oxides. Furthermore, their strong ability to eliminate chlorine from the catalyst surface and to provide significant amounts of active oxygen have been recognised as important catalytic properties for total oxidation of chlorinated VOCs. Therefore, in a final stage, Ce–Mn binary oxide catalysts were synthesized by a modified “redox–precipitation” route and tested for total oxidation of TCE in combination with the plasma reactor. Complete TCE abatement as well as high CO_x selectivity are achieved thanks to the high efficiency of the catalysts to completely decompose O_3 leading to the production of active oxygen species which are able to oxidize the by-products. The best plasma–assisted catalyst performance observed for $CeMn_4$ may be linked to the presence of residual potassium allowing to avoid the poisoning of catalytic sites with chlorinated organic species as well as slowing down the formation of chlorinated mineral phases.

This work proves that the combination of NTP with manganese based catalysts is an effective method for the abatement of VOCs. As a concluding remark, it should be mentioned that these catalysts were tested in the form of powders. Therefore, it is clear that in order to further explore the opportunities of plasma–catalysis for VOC abatement, appropriate catalyst supports such as honeycomb structures should be studied. This should enable to increase the dimensions of the system to pilot–scale which could pave the way to industrial implementation in the future.

Dutch Summary – Nederlandstalige Samenvatting

Luchtverontreiniging is een milieu probleem dat algemene bezorgdheid veroorzaakt omdat het ons klimaat verstoort en zowel voor de mens als ecosystemen schadelijk is. Sinds het begin van de industriële revolutie in de 19e eeuw is luchtvervuiling uitgegroeid tot een wereldwijd grensoverschrijdend probleem omdat het de kwaliteit van lucht, water en bodem negatief beïnvloedt. De industrialisering van veel economieën heeft geleid tot de emissie van verschillende soorten schadelijke stoffen zoals NO_x , SO_x , O_3 en H_2S .

Een andere grote en belangrijke groep van pollutanten zijn vluchtige organische stoffen (VOS). Deze groep bestaat uit een groot aantal chemicaliën die gemakkelijk verdampen vanwege hun hoge vluchtigheid. Wanneer ze in de atmosfeer terecht komen verstoren ze het natuurlijk evenwicht en veroorzaken ze verschillende effecten waaronder de vorming van fotochemisch smog, secundaire aërosolen en troposferisch ozon. Bovendien zijn VOS verantwoordelijk voor de opwarming van de aarde en het gat in de stratosferische ozonlaag. Veel VOS zijn ook gevaarlijk voor de volksgezondheid omdat ze potentieel giftige, kankerverwekkende of mutagene effecten kunnen veroorzaken. Hun uitstoot moet daarom verminderd worden teneinde de luchtkwaliteit te verbeteren en de toestand van het milieu te verbeteren voor toekomstige generaties.

Conventionele methoden om de uitstoot van VOS te reduceren zijn gevestigde technologieën zoals adsorptie, thermische en katalytische oxidatie, membraanscheiding, biologische methoden en fotokatalyse. Het nadeel van deze technieken is dat ze kapitaal intensief en moeilijk te bedienen zijn wanneer lage VOS concentraties moeten worden behandeld. Met het verstrengen van de emissiegrenswaarden in het achterhoofd, scheidt dit de noodzaak voor de ontwikkeling van alternatieve en duurzame technologieën die deze nadelen kunnen overwinnen. In dit verband is de toepassing van niet-thermische plasma (NTP) technologie voor de bestrijding van VOS een veelbelovende methode. Plasma, ook bekend als de vierde aggregatietoestand, wordt opgewekt door elektrische ontladingen waarbij energetische elektronen met achtergrond moleculen (N_2 , O_2 , H_2O ,...) botsen. Dit transformeert een neutraal gas in een geïoniseerde toestand bestaande uit een reactief mengsel van elektronen, ionen, radicalen, metastabielen en fotonen. Wanneer VOS aan deze energetische actieve plasma deeltjes blootgesteld worden, botsen ze waardoor VOS moleculen afgebroken worden door het splitsen van chemische bindingen. De geleverde energie aan de

plasmabron wordt vrijwel volledig gebruikt om elektronen te versnellen terwijl het achtergrondgas op kamertemperatuur blijft. Door deze niet-evenwichtstoestand is het onnodig om de gehele behandelde gasstroom te verwarmen in tegenstelling tot thermische en katalytische oxidatie. Een ander interessant kenmerk is gerelateerd aan de werking bij atmosferische druk wat het gebruik van dure vacuümapparatuur vermijdt. Bovendien worden NTP systemen gekenmerkt door een snelle opstart, compacte afmetingen en een snelle respons op veranderingen in de samenstelling van het te behandelen gas als gevolg van fluctuaties in het proces.

Hoewel NTP technologie voor de nabehandeling van VOS vaak in de literatuur wordt bestudeerd, blijven de vorming van ongewenste bijproducten, een slechte energie-efficiëntie en lage mineralisatie ernstige werkpunten vooraleer industriële implementatie mogelijk wordt. Om deze technologische problemen op te lossen onderzoeken wetenschappers de mogelijkheden van de combinatie van NTP met heterogene katalyse, beter bekend als plasmakatalyse. Deze innovatieve methode is in de laatste tien jaar uitgegroeid tot een belangrijk onderwerp van onderzoek. In een plasmakatalytisch systeem kan de katalysator zowel in de ontlading als na de plasmareactor geplaatst worden. In het eerste geval, beïnvloeden de katalysator en het plasma elkaar waardoor complexe interacties ontstaan die de eigenschappen van de katalysator en/of het plasma kunnen veranderen. Wanneer de katalysator na de plasmareactor wordt geplaatst, kunnen langlevende deeltjes die door het plasma gevormd worden (bvb. ozon, NO_x) het katalysatoroppervlak bereiken om zo de prestatie van het verwijderingsproces te verbeteren. Voor beide reactorconfiguraties kunnen de reacties in de gasfase en op het katalysatoroppervlak tot een synergie leiden waardoor de afbraakefficiëntie gevoelig verbetert.

De bovenstaande discussie dient als de belangrijkste motivering voor het verrichte onderzoek in dit proefschrift, dat de combinatie van NTP met heterogene katalysatoren bestudeert voor de afbraak van trichloorethyleen (TCE), een typisch gechloreerde VOS. In een eerste deel wordt de context van het onderzoek beschreven en wordt een uitgebreid literatuuroverzicht gepresenteerd om een duidelijk kader voor de lezer te scheppen. In een tweede deel worden de experimentele resultaten in detail besproken. Voor het eerst werd aangetoond dat de plasma-geassisteerde afbraak van TCE met een negatieve gelijkstroom corona ontlading gedeeltelijk tot de vorming van ongewenste, toxische gechloreerde bijproducten leidt zoals dichlooracetylchloride (DCAC), trichlooracetaldehyde (TCAA) en fosgeen (PG). Dit wordt toegeschreven aan de onvolledige oxidatie van TCE. Andere gedetecteerde bijproducten omvatten koolstofmonoxide,

koolstofdioxide, waterstofchloride, dichloor en ozon. Om de onderliggende plasmachemie in het afbraakproces van TCE te doorgronden, wordt een numeriek model ontwikkeld. Tot op heden, modelleerde slechts één andere studie in de literatuur de afbraak van TCE in Ar/O₂/H₂O mengsels. Omdat deze mengsels slechts weinig belang hebben voor industriële toepassingen, wordt de afbraak van TCE in droge en vochtige lucht in dit werk onderzocht. Er wordt aangetoond dat het Cl atoom, voornamelijk geproduceerd door dissociatie van COCl, één van de controlerende species is in de afbraakchemie en bijdraagt tot de productie van gechlореerde bijproducten. Voor zowel droge als vochtige lucht wordt een goede overeenkomst gevonden tussen experimenten en het model. Een verhoging van de relatieve luchtvochtigheid heeft een negatief effect op de verwijderingsefficiëntie. De belangrijkste reacties die bijdragen tot de verwijdering van TCE zijn die met ClO•, O• en CHCl₂. Er wordt tevens een reactieschema voorgesteld die de afbraak van TCE in vochtige lucht beschrijft. Op basis van deze resultaten werden geschikte katalysatoren gekozen om te combineren met de plasmabron. Hiervoor werden de katalysatoren na de ontlading in serie geplaatst. Het blijkt dat mangaan gebaseerde katalysatoren efficiënte kandidaten zijn voor de totale oxidatie van TCE in termen van activiteit en selectiviteit. Dit wordt hoofdzakelijk toegeschreven aan het feit dat deze katalysatoren over een hoog ozonafbrekend vermogen beschikken. Dit leidt tot de productie van actieve zuurstofdeeltjes die in staat zijn resterend TCE en de bijproducten te oxideren. Er dient benadrukt te worden dat, uitgezonderd van de eerste katalysator, alle andere voor het eerst onderzocht geweest zijn in combinatie met NTP voor VOS afbraak. Initieel, wordt een commerciële MnO₂ katalysator onderzocht. Door de beide systemen te combineren wordt de activeringsenergie voor katalytische TCE afbraak aanzienlijk verminderd ten opzichte van zuivere katalytische condities. Dit suggereert dat de polygechlореerde bijproducten, geproduceerd door het plasma, vatbaarder zijn voor katalytische oxidatie dan TCE. Hoewel er geen duidelijk synergetisch effect wordt waargenomen voor de TCE afbraak, is de synergie factor voor de opbrengst van CO en CO₂ hoog. Dit geeft aan dat het plasmakatalytisch systeem de selectiviteit van het proces gevoelig verbetert in vergelijking met de plasmabron. Vervolgens wordt lanthaanmanganiet (LaMnO₃) getest. Dit is een perovskiet soort katalysator. LaMnO₃ is een milieuvriendelijk en goedkoop materiaal en staat bekend als één van de meest actieve katalysatoren voor de oxidatie van gechlореerde VOS. Voor plasmakatalyse in droge lucht wordt een optimale katalysator temperatuur van 100°C vastgesteld. Dit is het gevolg van een compromis tussen katalysatordeactivering

en verbetering van de katalytische reacties. De invloed van de luchtvochtigheid is opmerkelijk. Hoewel water de actieve plaatsen op het katalysator oppervlak kan blokkeren, wordt de TCE afbraak in vochtige lucht verbeterd door het feit dat water chloor residues op het oppervlak kan verwijderen waardoor de afbraak van LaMnO_3 wordt vertraagd. Het is algemeen geweten dat de opname van edelmetalen in lage hoeveelheden in een perovskiet structuur de katalytische activiteit verhoogt en de stabiliteit van het metaal tegen sinteren, metaal–drager interacties en vervluchtiging verbetert. Daarom wordt geopteerd om LaMnO_3 met palladium (Pd) te doperen. Wanneer de temperatuur van Pd/ LaMnO_3 verhoogd wordt tot 200°C , wordt de vorming van DCAC onderdrukt terwijl de vorming van fosgeen met 50% vermindert. Verder wordt er in het effluent geen ozon gedetecteerd wat aantoont dat Pd/ LaMnO_3 effectief is voor ozon afbraak waardoor de mineralisatie van TCE aanzienlijk verbetert in vergelijking met de plasmabron. Omdat het specifiek oppervlak van de katalysator een belangrijke rol speelt in de ozon afbraak, wordt aangenomen dat de dispersie van MnO_x verbeterd wordt door de vorming van binaire Ce–Mn oxides. Deze katalysatoren beschikken over een sterk vermogen om chloor residues op het katalysator oppervlak te elimineren en om aanzienlijke hoeveelheden actieve zuurstofdeeltjes te leveren. Deze eigenschappen zijn van vitaal belang voor de totale oxidatie van gechloreerde VOS. Daarom worden als laatste binaire Ce–Mn katalysatoren gesynthetiseerd volgens een aangepaste "redox–precipitatie" route. Deze katalysatoren worden in combinatie met de plasma reactor getest voor de volledige oxidatie van TCE. Dit resulteert in de volledige afbraak van TCE gekoppeld aan een hoge CO_x selectiviteit. Dit is te wijten aan het hoge rendement van de katalysatoren om ozon af te breken wat leidt tot de productie van actieve zuurstofdeeltjes die de bijproducten verder oxideren. De beste prestaties worden waargenomen voor CeMn_4 . Dit kan worden toegeschreven aan de aanwezigheid van residueel kalium dat tegelijkertijd de vergiftiging van actieve katalytische plaatsen door gechloreerde organische species vermijdt en de vorming van gechloreerde minerale fasen vertraagt.

Dit werk toont aan dat de combinatie van NTP met mangaan gebaseerde katalysatoren een effectieve methode is voor de afbraak van VOS. Er moet echter als laatste op gewezen worden dat deze katalysatoren in de vorm van poeders werden getest. Het is echter duidelijk dat, om de mogelijkheden van plasmakatalyse voor de afbraak van VOS verder te onderzoeken, geschikte katalysatordragers zoals honingraatstructuren moeten worden onderzocht. Op deze manier kunnen de afmetingen van het systeem vergroot worden tot

piloot-schaal wat de uiteindelijke industriële implementatie in de toekomst mogelijk kan maken.

List of Acronyms

AC	alternating current
BE	binding energy
BVOC	biogenic volatile organic compound
CB	conduction band
CFC	chlorofluorocarbons
CLRTAP	Convention on Long-Range Transboundary Air Pollution
CPC	combined plasma catalysis
CVOC	chlorinated volatile organic compound
DBD	dielectric barrier discharge
DC	direct current
DCAC	dichloroacetylchloride
EU	European Union
FID	flame Ionization Detector
FT-IR	Fourier transform – infrared spectroscopy
GC-MS	gas chromatography–mass spectrometry
GHG	greenhouse gas
GWP	global warming potential
IARC	International Agency for Research on Cancer
IPC	in-plasma catalysis
IPCR	in-plasma catalysis reactor
JCPDS	Joint Committee on Powder Diffraction Standards
log P_{ow}	n-octanol–water partition coefficient
MFC	mass flow controller
MS	mass spectrometry
m/z	mass to charge ratio
NIST	National Institute of Standards
NMVOC	non-methane volatile organic compound
NTP	non-thermal plasma
OEL	occupational exposure limit
OES	optical emission spectroscopy
ODP	ozone depleting potential
ODS	ozone depleting substance
PACT	plasma and catalyst integrated technologies
PAN	peroxy–acetyl–nitrates
PDC	plasma–driven catalysis
PEC	plasma–enhanced catalysis
PM	particulate matter
PPC	post-plasma catalysis
PPCR	post–plasma catalysis reactor
ppm	parts per million

PSA	pressure swing adsorption
RF	radio frequency
RH	relative humidity
SBS	sick building syndrome
SEM	secondary electron multiplier
SMF	sintered metal fibres
SPC	single-stage plasma-catalysis
TCAA	trichloroacetylchloride
TCE	trichloroethylene
ToF-SIMS	time-of-flight secondary ion mass spectrometry
TPC	two-stage plasma catalysis
UCCS	Unité de Catalyse et Chimie du Solide
UHV	ultra high vacuum
UNECE	United Nations Economic Commission for Europe
UV	ultraviolet
VB	valence band
VOC	volatile organic compound
XPS	X-ray photoelectron spectroscopy

List of Publications

A1 articles

- A.M. Vandembroucke, R. Morent, N. De Geyter, C. Leys
Decomposition of trichloroethylene with plasma-catalysis: A review
Journal of Advanced Oxidation Technologies 14(1) pp. 165–173, 2011
- A.M. Vandembroucke, R. Morent, N. De Geyter, C. Leys
Non-thermal plasmas for non-catalytic and catalytic VOC abatement
Journal of Hazardous Materials 195 pp. 30–54, 2011
- A.M. Vandembroucke, M.T. Nguyen Dinh, J.-M. Giraudon, R. Morent, N. De Geyter, J.-F. Lamonier, C. Leys
Qualitative by-product identification of plasma-assisted TCE abatement by mass-spectrometry and Fourier-transform infrared spectroscopy
Plasma Chemistry and Plasma Processing 31 pp. 707–718, 2011
- A.M. Vandembroucke, R. Morent, N. De Geyter, C. Leys
Decomposition of toluene with plasma-catalysis: A review
Journal of Advanced Oxidation Technologies 15(2) pp. 232–241, 2012
- A.M. Vandembroucke, M. Mora, C. Jiménez-Sanchidrián, F.J. Romero-Salguero, N. De Geyter, C. Leys, R. Morent
TCE abatement with a plasma-catalytic combined system using MnO₂ as catalyst
Applied Catalysis B: Environmental 156–157 pp. 94–100, 2014
- M.T. Nguyen Dinh, J.-M. Giraudon, J.-F. Lamonier, A.M. Vandembroucke, N. De Geyter, C. Leys, R. Morent
Plasma-catalysis of low TCE concentration in air using LaMnO_{3+δ} as catalyst
Applied Catalysis B: Environmental 147 pp. 904–911, 2014
- N. Nuns, A. Beaurain, M.T. Nguyen Dinh, A.M. Vandembroucke, N. De Geyter, R. Morent, C. Leys, J.-M. Giraudon, J.-F. Lamonier
A combined ToF-SIMS and XPS study for the elucidation of the role of water in the performance of a post-plasma process using LaMnO_{3+δ} as catalyst in the total oxidation of trichloroethylene
Applied Surface Science 320 pp. 154–160, 2014
- A.M. Vandembroucke, R. Aerts, W. Van Gaens, N. De Geyter, C. Leys, R. Morent, A. Bogaerts
Modeling and experimental study of trichloroethylene abatement with a negative direct current corona discharge
Plasma Chemistry and Plasma Processing 35 pp. 217–230, 2014

M.T. Nguyen Dinh, J.-M. Giraudon, A.M. Vandenbroucke, R. Morent, N. De Geyter, J.-F. Lamonier

Post plasma-catalysis for total oxidation of trichloroethylene over Ce-Mn based oxides synthesized by a modified redox precipitation route

Applied Catalysis B: Environmental 172–173 pp. 65–72, 2015

S. Sharmin, A.M. Vandenbroucke, C. Leys, N. De Geyter, R. Morent

Abatement of VOCs with alternate adsorption and plasma-assisted regeneration: A review

Catalysts 5(2) pp. 718–746, 2015

A. M. Vandenbroucke, M.T. Nguyen Dinh, N. Nuns, J.-M. Giraudon,

N. De Geyter, C. Leys, J.-F. Lamonier, R. Morent

Combination of non-thermal plasma and Pd/LaMnO₃ catalyst for dilute trichloroethylene abatement

Chemical Engineering Journal, 283 pp. 668–675, 2016

A2 articles

A.M. Vandenbroucke, R. Morent, N. De Geyter, M.T. Nguyen Dinh, J.-M. Giraudon, J.-F. Lamonier, C. Leys

Plasma-catalytic decomposition of TCE

International Journal of Plasma Environmental Science and Technology 4(2) pp. 135–138, 2010

C1 articles

A.M. Vandenbroucke, R. Morent, N. De Geyter, C. Leys

Atmospheric pressure DC multi-pin-to-plate glow discharge for TCE abatement: Qualitative by-product identification

Cold Atmospheric Pressure Plasmas: Sources and Applications, 4th International Congress, Proceedings pp. 158–161, 2009

A.M. Vandenbroucke, R. Morent, N. De Geyter, M.T. Nguyen Dinh, J.-M. Giraudon, J.-F. Lamonier, C. Leys

Plasma-catalytic decomposition of TCE

International Symposium on Non-thermal/Thermal Plasma Pollution Control Technology & Sustainable Energy, Proceedings. pp. VII-12-1–VII-12-3, 2010

A.M. Vandenbroucke, A. Vanderstricht, M.T. Nguyen Dinh, J.-M. Giraudon, R. Morent, N. De Geyter, J.-F. Lamonier, C. Leys

Non-thermal plasma abatement of trichloroethylene with DC corona discharges

WIT Transactions on Ecology and the Environment 147 pp. 353–361, 2011

A.M. Vandenbroucke, R. Aerts, R. Morent, N. de Geyter, A. Bogaerts, C. Leys
Modeling and experimental validation of TCE abatement and ozone formation with non-thermal plasma

8th International Symposium on Non-Thermal/Thermal Plasma Pollution Control Technology and Sustainable Energy, Proceedings, 2012

A.M. Vandenbroucke, M. Mora, C. Jimenéz-Sanchidrián, F.J. Romero-Salguero, N. De Geyter, C. Leys, R. Morent

Using cerium oxides as catalysts for the abatement of trichloroethylene by plasma-catalysis route

14th International Symposium on High Pressure Low Temperature Plasma Chemistry, Proceedings, 2014

Chapter 1

Air pollution

1.1 Introduction

On September 8th 2014, the European Commission published the following press release [1]:



EUROPEAN COMMISSION

PRESS RELEASE

“Almost all Europeans say protecting the environment is important to them”

Three years on from the most recent similar Eurobarometer survey, it is clear that, despite the economic crisis, Europeans’ concern about the environment has not diminished. In an overwhelming consensus, 95% of the 28.000 interviewed citizens said that protecting the environment is important to them personally and many think more can be done.

Environment Commissioner Janez Potočnik said: “It is good to see such solid and widespread support for the protection of the environment, even in difficult times. People are particularly concerned about air and water pollution, chemicals and waste, and they feel that more must be done by everyone to protect the environment...”

The citation of this press release clearly demonstrates the growing concern of European citizens regarding the condition and protection of our environment. This perception is also largely shared by the population of many other countries around the world. The deterioration of our environment is related to groundwater, soil and air contamination by chemical compounds that have various detrimental effects due to their persistency. Among these phenomena, air pollution is one of the major problems of the 21st century that endanger both human and ecological life due to environmental changes such as global warming, formation of tropospheric ozone and photochemical smog. Since World War II, governments have gradually

become aware that the severity of emission legislation needs to increase in order to ensure the protection of our environment for future generations. International treaties like the Kyoto protocol (1997) and the protocol of Gothenburg (1999) are important examples that have helped to reduce emissions from industrial activities and to increase the awareness of citizens.

Exhausts from mobile (e.g. cars) and stationary sources (e.g. plants) pollute the air with a variety of harmful substances [2]. Next to NO_x , SO_x , H_2S and particulate matter, volatile organic compounds (VOCs) are a large and important group of air pollutants. Therefore, in the following sections a comprehensive survey will be presented focusing on the sources, effects and legislation of air pollution with an emphasis on VOCs. In this work, the technological possibilities for the abatement of VOCs are under particular concern. Therefore, some general facts on VOCs are also provided.

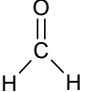
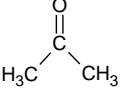
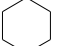
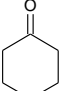
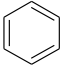
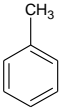
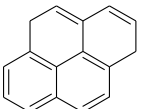
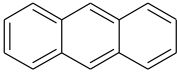
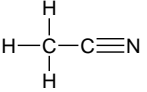
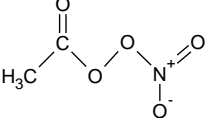
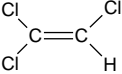
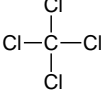
1.2 Volatile organic compounds

1.2.1 Definition and classification

Organic compounds are chemicals containing at least the element carbon and one or more of the following elements: hydrogen, oxygen, sulphur, phosphorus, silicon, nitrogen or a halogen. Exceptions are carbon oxides, inorganic carbonates and bicarbonates. Although there is no general quantitative definition of what VOCs are, the Solvents Emissions Directive of the European Union (1999/13/EC) defines VOCs as any organic compound having a vapour pressure of 0.01 kPa or more at 20°C, or having a corresponding volatility under the particular conditions of use [3]. For hydrocarbon solvents, a vapor pressure of 0.01 kPa at 20°C roughly corresponds to a boiling point in the range 215–220°C. VOCs comprise thus of a very large and heterogeneous group of organic chemicals. Their high volatility causes them to rapidly evaporate and enter the earth's atmosphere. Depending on their chemical structure, concentration and reactivity with other compounds, they can cause various adverse effects on humans and ecosystems.

The emission of VOCs consists of about 2/3 of methane (CH_4), which is primarily released by cattle and decay processes [4, 5]. The reactivity of methane, expressed as ozone forming potential, is 20 to 100 times lower compared to other VOCs. Because methane is also non-toxic, a distinction is made between methane and non-methane VOC (NMVOC). According to their chemical composition VOCs can be further classified as presented in Table 1.1

Table 1.1 Classification of VOCs according to their chemical composition.

VOC class	Example	
	Name	Structure
Aliphatic	Formaldehyde	
	Acetone	
Cyclic	Cyclohexane	
	Cyclohexanone	
Aromatic	Benzene	
	Toluene	
Polycyclic aromatic	Pyrene	
	Anthracene	
Nitrogen containing	Acetonitrile	
	Peroxy-acetyl-nitrate	
Halogens containing	Trichloroethylene	
	Tetrachloromethane	

For this PhD study, the experimental work has focused on the abatement of trichloroethylene (TCE) as model VOC. More information about the properties and health effects of this compound can be found in Section 1.2.4.

Figure 1.1 gives a clear overview of how air pollution in general enters the atmosphere and impacts our environment, public health and topography. The concentration levels of air pollutants are determined by various factors including weather, chemical transformations in the air and transport of pollutants from other areas.

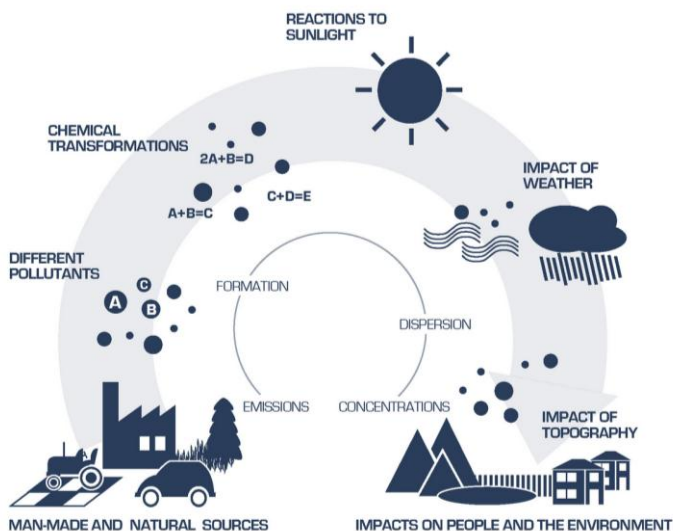


Figure 1.1 Schematic representation of the factors that contribute to air pollution concentration levels [6].

1.2.2 Sources

Many sources contribute to the release and emission of VOCs to the environment. They can be divided into anthropogenic or biogenic sources depending on whether they are released by humans or biological life, respectively. Figure 1.2 summarizes the different sources that will be discussed in this section.

Although biogenic sources represent about 90% of global VOC emission, they produce VOCs in low concentrations while mechanisms exist for their natural degradation. Therefore, they do not unbalance the natural equilibrium of atmospheric compounds developed over millions of years. On the other hand, biogenic sources become less important in industrialised regions where anthropogenic sources

produce large amounts of VOCs which strongly unbalance this delicate equilibrium.

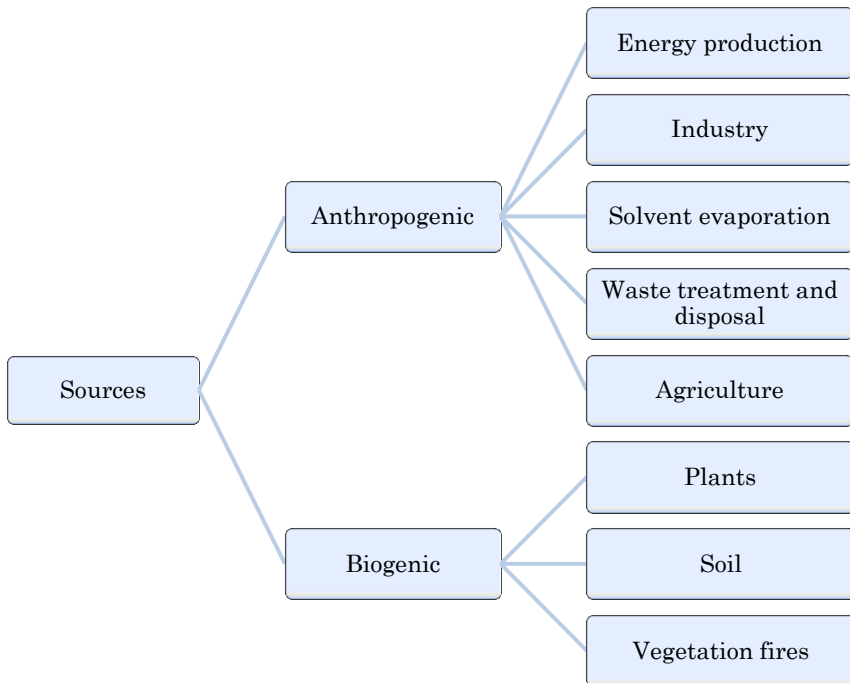


Figure 1.2 Different sources of VOC release to the environment.

1.2.2.1 Anthropogenic sources

Many VOCs are human-made chemicals that are used in different industrial and agricultural activities. VOCs are also released during the production of energy, evaporation of solvents and waste treatment and disposal.

The energy industry covers all activities involved in electricity production, district heating, petroleum refining, the extraction and distribution of solid, liquid and gaseous fuels and the transformation of solid fuels. The production and distribution of energy is the main contributor to anthropogenic VOC emissions and air pollution in general [7]. The release of VOCs to the atmosphere is mainly related to a number of activities that employ fuel combustion to produce energy products and electricity. The expected increase in energy production combined with an increasing demand for electricity and declining use of nuclear energy will likely lead to increased energy related VOC emissions in the future [8].

Solvent evaporation is the main contributor to man-made VOC emissions in the EU. Solvents have a large diversity in chemical structure and may belong to the following chemical classes:

- Aliphatic hydrocarbons (e.g. hexane)
- Aromatic hydrocarbons (e.g. white spirit)
- Halogenated hydrocarbons (e.g. dichloromethane)
- Alcohols, glycols and ethers
- Ketones (e.g. acetone)
- Esters (e.g. ethylacetate)
- Amides (e.g. dimethylformamide)

The industrial use of solvents includes metal surface coating, degreasing, flatwood paneling, printing and fabric coating. On the other hand, non-industrial use of solvents is related to dry cleaning, domestic and commercial painting and other domestic solvent use including nail polish removers, glue solvents, spot removers, detergents and perfumes.

In order to estimate the use of solvents, emission inventories by different sectoral activities are made on an annual basis. For solvents, it is acceptable to assume that 100% of a solvent entering a given sector will eventually evaporate. Hence, if the annual consumption of the solvent in a particular sector is known, the contribution of the sector to VOC emissions is known as well. Another approach to establish a solvent inventory is the application of emission factors which are constant rates of emission expressed in terms of an activity level appropriate for a given type of solvent use. Examples of emission factors include product throughput (e.g. kg VOC/vehicule coated) and isolated industrial processes (e.g. kg VOC/surface coating line).

Next to industrial combustion, industrial processes can be important VOC emission sources. Industrial activities that emit large amounts of VOCs include the polymer industry, the rendering industry and the paper pulp industry [9]. Polyethylene producing factories emit for instance large amounts of ethene which affect plant growth and physiology. In the vicinity of rendering factories, VOCs such as carbonyl compounds, organic acids, furans and sulphur compounds can be responsible for severe odour nuisance [7]. During the production of paper pulp, VOCs such as terpenes, which are usually considered as originating from natural sources, are emitted due to conversion of wood into pulp.

Waste treatment and disposal are responsible for VOC release due to waste incineration, waste storage and landfill, and wastewater treatment. Depending on the origin of the solid waste or wastewater, very different VOCs can be emitted.

Agriculture generates VOC emissions that are released by different activities that fall into two main categories: livestock farming and crop farming. In particular, these emissions are caused by enteric fermentation in livestock, management of animal manure, spreading of nitrogenous fertilisers, rice production under anaerobic conditions, tillage and harvesting and burning of crop residues [9].

Although it may seem strange, even human beings are sources of VOCs. A recent review has reported 1765 VOCs present in exhaled breath, skin emanations, urine, saliva, human breast milk, blood and feces [10]. Fortunately, the concentrations of emitted VOCs by the human volatilome is rather low and has only a negligible contribution to the issue of air pollution.

Figure 1.3 shows the sectoral contribution to anthropogenic NMVOC emissions in Europe for the year 2011. This diagram reveals that solvent and product use account for the largest part with contribution of 43.1%. Between 1990 and 2011, NMVOC emissions in the EU dropped by 59% while a decrease of 3.6% was reported between 2010 and 2011.

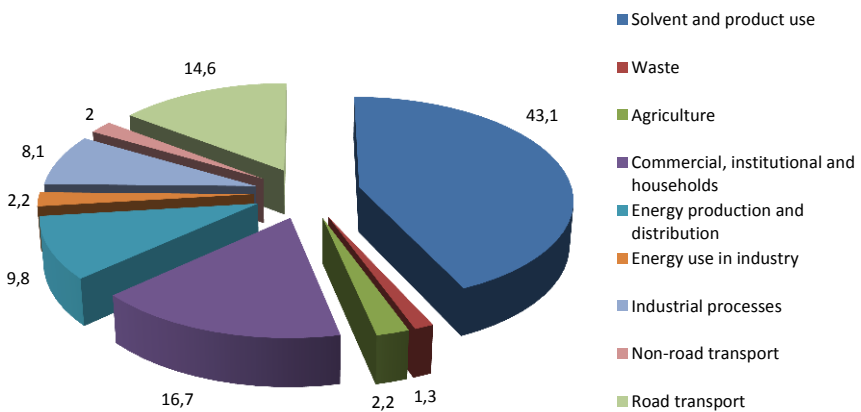


Figure 1.3 Sectoral contribution to anthropogenic NMVOC emissions in Europe (2011) [11].

Figure 1.4 compares the sectoral contribution in Flanders for the years 2000–2012. In 2012 the total NMVOC emission in Flanders was 78 kton which is a decrease of 40% compared to 2000. The absolute NMVOC emission of industry and traffic has known a spectacular decrease with 50% and 70%, respectively. The relative contribution of these sectors has also substantially declined during this period. This is mainly related to the important emission reduction efforts made by the industrial and transport sectors as well as the changeover to less

polluting fuels. However, the NMVOC emission of household products and nature has known an increase. The share of other sectors is more or less constant over this period.

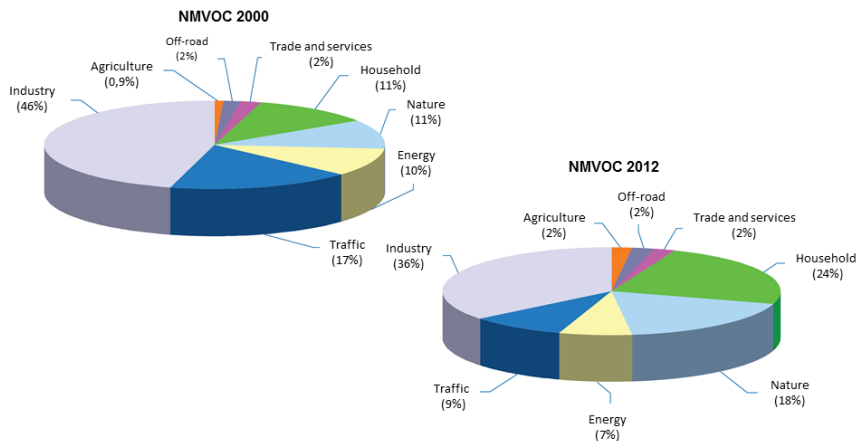


Figure 1.4 Sectoral contribution to NMVOC emissions in Flandres (2000–2012) [12].

1.2.2.2 Biogenic sources

Biogenic emission sources are emissions originating from biological processes. They include VOC emissions from plants, soil and vegetation fires. Although there is no real solution to prevent this kind of emission, it has significant effects on the chemical composition and physical characteristics of the atmosphere and exceeds emissions of anthropogenic sources significantly [13].

The major biogenic VOC (BVOC) is methane, of which half of the annual emission is from biological origin. Natural sources include microbial anaerobic degradation of organic matter, natural gas losses, burning of biomass and production of methane in swamps, landfills and natural wetlands.

The majority of other BVOCs are emitted by plants and mainly include isoprene (~51%), terpenes (~31%), oxygenated organics (~16.2%), alkenes (~2%) and methanol (~0.22%) [14]. Nearly all organs from vegetative parts as well as flowers and roots emit BVOCs. The emission rate is biosynthetically controlled by many abiotic factors such as ambient temperature, sunlight, CO₂ concentration, nutrition, genetics, leaf development, and phenological events [15, 16].

BVOCs have numerous roles in the biosphere. These include compounds to defend against biotic and abiotic stress, for signalling

within and between plants and for plant reproduction (Figure 1.5). Some BVOCs are highly reactive and important for their effects on atmospheric composition and air quality. The decomposition of isoprene is known to produce ozone when reacting with anthropogenic NO_x while monoterpenes and sesquiterpenes can contribute to the formation of cloud condensation nuclei, thus providing ground for the growth of secondary organic aerosols and particles [14, 17].

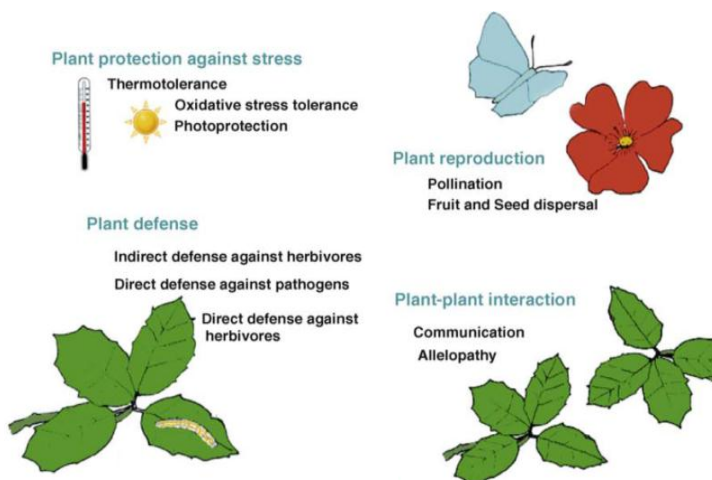


Figure 1.5 Roles of BVOCs in the biosphere [18].

The soil is another huge source and reservoir of BVOCs, which are produced by the decomposition of litter and dead organic material. Another source is the synthesis of BVOCs by tissues of plants and underground living organisms [19]. Soil VOC emissions to the atmosphere are generally 1–2 orders of magnitude lower than those from plants above ground. They are of concern primarily as potential source of groundwater contamination. Figure 1.6 schematically shows the different organisms that are involved in volatile interactions above and below ground. The knowledge on the exchange of VOCs between soil and atmosphere and the features of the soil and particle structure allowing diffusion of VOCs in the soil is scarce. Therefore, relatively little is known regarding the types and quantities of VOCs exchanged in the soil, their sources and sinks, the factors controlling their diffusion and emission and their ecological and environmental effects [19].

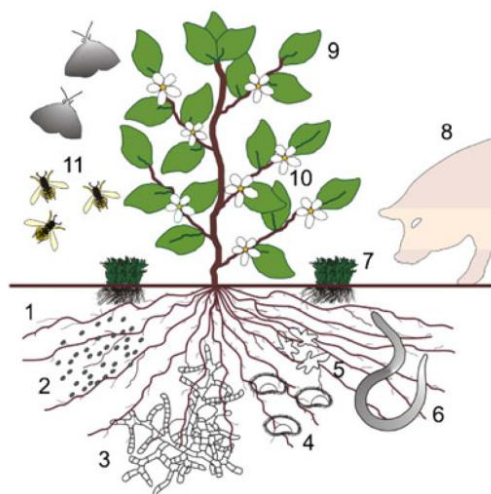


Figure 1.6 Schematic presentation of organisms involved in volatile interactions above and below ground (1 plant root, 2 bacteria, 3 fungi, 4 ciliates, 5 amoeba, 6 nematodes, 7 moos, 8 wild boar, 9 plant leaves, 10 plant flowers, 11 insects) [20].

Finally, BVOCs are emitted by vegetation fires which have a strong impact on atmosphere condition and climate. These fires can be prescribed fires or naturally occurring bushfires and wildfires. Next to CO_2 , CO , CH_4 , NO_x and particulate matter they produce a significant amount of BVOCs, the majority belonging to the isoprenoid family, yielding pollutants such as secondary organic aerosols and ozone [21].

1.2.3 Reactions in the atmosphere

The atmosphere is a thin and fragile layer of air, which surrounds the earth and is retained by gravitational forces [22]. It consists of a large mixture of different chemicals of which N_2 (78.09%), O_2 (20.95%) and Ar (0.93%) are the main constituents. It is divided into different layers which are characterized by temperature, pressure and distance from the earth, as shown in Figure 1.7. The lowest layer of the atmosphere is the troposphere, which extends from the surface to 11 km on average depending on the latitude. It contains 85–90% of the mass of the atmosphere and is the layer where most of the weather systems occur on both a global and local scale.

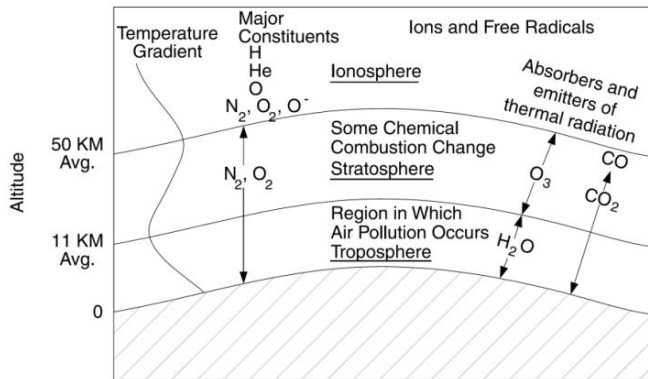


Figure 1.7 Different layers of the atmosphere [23].

Because the troposphere is in contact with the earth's surface it interacts directly with other climate subsystems such as the biosphere (land and vegetation), the hydrosphere (oceans), the cryosphere (ice caps), the lithosphere (topography) and most important of all with the human world. Therefore, air pollution emitted by biogenic or anthropogenic sources is released to the troposphere. Tropospheric chemistry is key for the chemical transformations, transport and deposition of air pollution. Figure 1.8 schematically shows the different processes that VOCs undergo in the troposphere. In general these processes include emission, transport, exchange, distribution, immission and deposition.

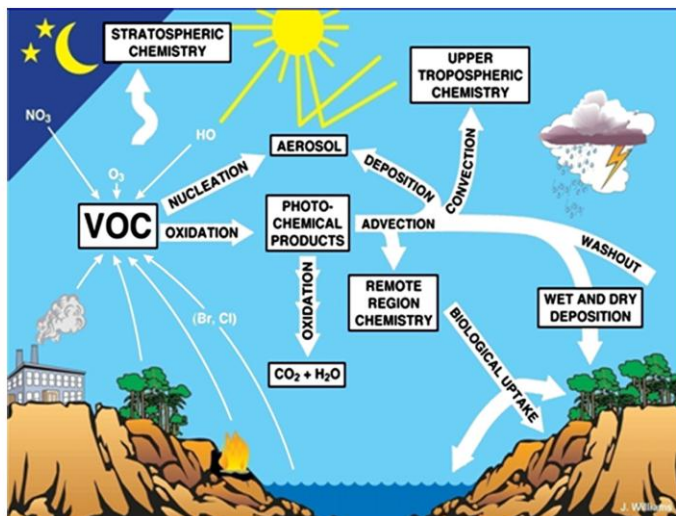


Figure 1.8 Schematic overview of tropospheric chemistry [24].

There are three main removal processes. The primary route is chemical conversion via oxidation in the gas phase to non-polluting constituents such as H_2O or CO_2 . The second is dry deposition whereby VOCs are absorbed by plants, water or soil. It is of limited significance because it often only applies to VOCs in the boundary layer on a local scale. The third is wet deposition or removal by precipitation and is only effective for VOCs that have sufficient solubility in water, which is generally not the case. There are however a number of oxidizing species present in the troposphere that convert pollutants so that they become soluble. Although these species are only present in small amounts, they constitute the pivot of tropospheric chemistry. They are in descending order of importance [2, 25]:

- *The hydroxyl radical OH.* Hydroxyl is a short-lived free radical and by far the most effective scavenger in the troposphere. It is the main oxidant for CO , CH_4 and higher hydrocarbons, H_2S (hydrogen sulfide) and SO_2 (sulfur dioxide).
- *The nitrate radical NO_3 .* At night, this radical takes over from hydroxyl as the dominant oxidant in the atmosphere: hydroxyl is formed by photolysis and its concentration peaks during daytime while NO_3 does not survive sunlight.
- *The oxygen atom $\text{O}(^3p)$.* This excited state of the oxygen atom has the ability to oxidize unsaturated hydrocarbons and other gases containing a double bond such as CS_2 and COS in the upper troposphere.
- *Peroxy and hydroperoxy radicals HO_2 and RO_2 (where R is an alkyl).* HO_2 and RO_2 are very much intertwined with hydroxyl in the oxidation cycle. They are not as efficient as hydroxyl, but react with themselves to form H_2O_2 , an important oxidant in cloud droplets.
- *Hydrogen peroxide H_2O_2 .* This strong acid reacts very efficiently in cloud droplets and oxidizes a number of trace gases, in particular sulfur dioxide. Highly soluble, it also accounts for a large part of the excess acidity in rain.

Together, these oxidants determine the lifetime and the abundance of trace species, acting as atmospheric regulators. The opposite is also true: the abundance of trace species regulates the oxidizing capacity of the atmosphere, since an increase in the emission of a given pollutant reduces the abundance of its principal oxidant. The resulting positive feedback may even eventually lead to an increase of other pollutants.

This underlines the importance of a stable oxidizing capacity in the troposphere, of prime importance to our environment.

Figure 1.9 presents the gas-phase reactions that VOCs undergo in the atmosphere. Initially, they undergo photolysis or react with atmospheric oxidants such as OH radicals, NO₃ radicals, and O₃ molecules. With the involvement of O₂ and nitrogen oxides, subsequent reactions can lead to the generation of new oxidants, i.e., HO₂, RO₂, RO radicals, peroxides, and new VOCs [26].

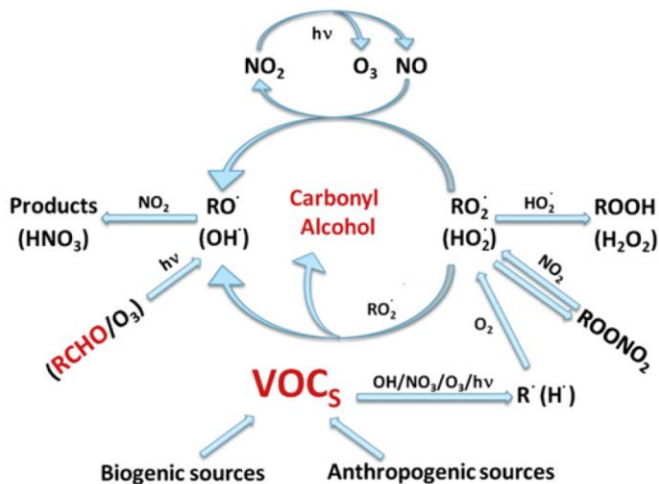


Figure 1.9 Gas-phase reactions of VOCs in the atmosphere [26].

1.2.4 Trichloroethylene

For this PhD study, trichloroethylene (TCE) was chosen as model VOC. TCE is a clear, colorless liquid with moderate volatility and a sweet, chloroform-like odour. Table 1.2 summarizes the physical and chemical properties of TCE.

It is an excellent solvent for a wide range of applications due to favorable properties such as high solvency, low flammability, non corrosiveness, high stability, low specific heat, low boiling point, low heat of vaporisation and low production cost. Therefore, it is widely used as an industrial solvent to clean and degrease metal and semiconductor parts. Figure 1.10 shows a typical degreasing unit which is used to remove grease and adherent material from metal surfaces prior to further treatments such as electroplating, galvanising, tin plating, painting and other surface protection processes.

Table 1.2 Physical and chemical properties of TCE [27].

Property	Value
Chemical formula	C ₂ HCl ₃
CAS number	79-01-6
Molecular weight	131.39 g/mol
Density	1.46 g/cm ³ (20°C)
Boiling point	87.2°C
Melting point	-73.0°C
Vapor pressure	7.8 kPa (20°C)
Vapor density	4.5 (air=1)
n-Octanol-water partition coefficient (log P _{ow})	2.42
Solubility in water	1.28 g/L
Odour treshold	30 ppm
Occupational exposure limit (OEL)	50 ppm
Conversion factor	1 ppm = 5.37 mg/m ³ (25°C)

TCE has however numerous other uses including as a heat transfer medium, an extraction agent for greases, oils and fats, as a chemical intermediate in the production of chlorofluorocarbons and other organic chemicals and as an ingredient in many products for industrial and consumer use [28, 29]. It is e.g. used in dyes, printing inks, paint removers, adhesives, type writer correction fluids as well as spot removers.

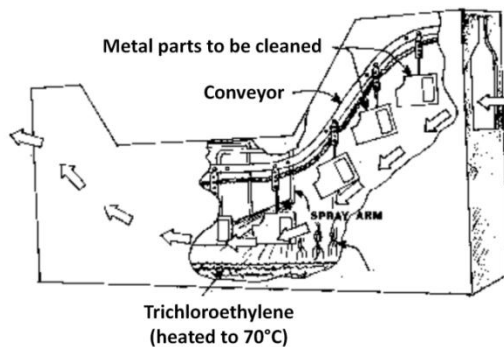


Figure 1.10 TCE degreasing unit.

TCE has been detected in all media but mostly in air due to its volatility. Release of TCE to ambient and indoor air can occur during degreasing operations and consumption of related products [28].

Contamination of groundwater and water supplies is possible during production and disposal processes, and through leaching from landfills or underground storage tanks due to its moderate solubility in water, widespread use and persistency in the environment.

Human exposure to TCE may therefore occur through inhalation, ingestion and dermal contact. Inhalation can affect the central nervous system and is known to cause acute symptoms including sleepiness, fatigue, dizziness, headache, confusion, facial numbness and feelings of euphoria [27]. Toxicologic studies have also reported human health impacts such as speech and hearing impairments, disturbed vision, liver problems, skin rashes, kidney diseases, urinary tract, cardiac arrhythmias and blood disorders [30, 31]. Furthermore, TCE has been extensively studied for its potential carcinogenicity. Although the International Agency for Research on Cancer (IARC) listed TCE as potentially carcinogenic (Group 2A), recent evaluation based on new data has however proven that there is sufficient evidence to conclude that TCE is carcinogenic to humans (Group 1) [32, 33]. It causes cancer of the kidney, liver, cervix and lymphatic system.

1.3 Effects

As the group of VOCs comprises of many chemicals with different structures, their effect on the environment and public health is also very diverse. Figure 1.11 summarizes the impact of air pollution on ecosystems, climate and human health.

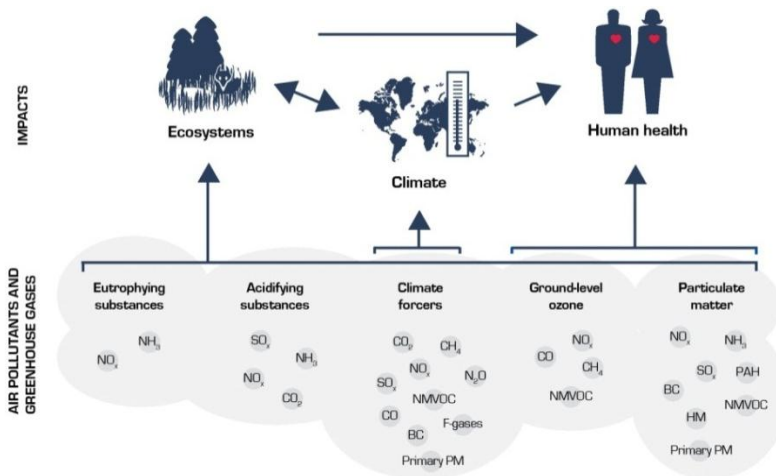


Figure 1.11 Impact of air pollution [6].

1.3.1 Environmental effects

1.3.1.1 Global warming

The earth's atmosphere naturally acts as an insulating blanket which is able to trap enough solar energy to maintain the global average temperature in a comfortable range to support life. This blanket comprises of a collection of several atmospheric gases such as water vapour (H_2O), carbon dioxide (CO_2), methane (CH_4), ozone (O_3), chlorofluorocarbons (CFCs) and nitrous oxide (N_2O), which are collectively known as greenhouse gases (GHGs). Without this natural greenhouse effect the heat of the sun would escape and the earth's average temperature would drop from 14°C to -18°C making life as it exists on earth today virtually impossible [34]. This observed increase in the average temperature is known as 'Global Warming'. The amount of global warming caused by a substance is quantified by its Global Warming Potential (GWP). This is the ratio of the warming caused by the substance to the warming caused by a similar mass of CO_2 .

Since the Industrial Revolution in the 18th century, human activity has steadily caused an increase of the natural greenhouse effect by direct emission of GHGs into the atmosphere and by indirectly inducing changes in the atmospheric chemistry. The concentration of CO_2 in the atmosphere has been changed to such an extent by human activity that the natural greenhouse effect is out of balance. The atmospheric CO_2 concentration has significantly increased from about 280 ppm before the Industrial Revolution to 389 ppm in 2010 [35]. Although CO_2 is the most important anthropogenic GHG, other gases such as CH_4 , N_2O and halogenated hydrocarbons have also a large contribution though their atmospheric concentration is much lower.

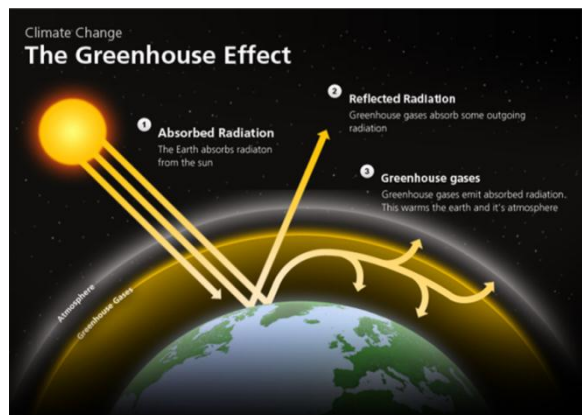


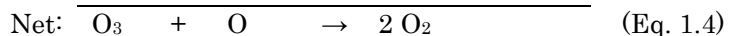
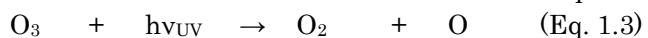
Figure 1.12 The greenhouse effect [36].

The trapping of the solar radiation warms the earth and its atmosphere (Figure 1.12). The mean global surface temperature has risen by about 0.6°C during the 20th century. It is estimated that the temperature would further increase with 2.5–4°C and eventually 3.5–7°C by 2100 compared to 1990 if no action is undertaken [34]. The enhanced greenhouse effect has repercussions on our climate and leads to sea level rise due to polar melting. Other adverse effects are related to an increase of unusual weather events, an altering in the ocean circulation and climate change which will affect both ecosystems and human life in general. In order to reduce the rate of climate change and preserve our planet for future generations it is important to limit the emission of GHGs.

1.3.1.2 Depletion of the ozone layer

The ozone layer is a belt of naturally occurring ozone gas that is found in both the troposphere and the stratosphere. It serves as a shield that protects us from the harmful ultraviolet B (UVB) radiation emitted by the sun. Ozone is a highly reactive molecule which is constantly being formed and broken down in the stratosphere through a natural cycle. Ozone depletion is, however, taking place due to chemical destruction beyond these natural occurring reactions. The ozone balance is regulated by the destruction, formation and accumulation of ozone through catalytic cycles involving nitrogen, hydrogen, chlorine, bromine and iodine oxides [37].

The primary culprits responsible for ozone layer breakdown are chlorofluorocarbons (CFCs). These chemicals are mainly found in spray aerosols heavily used in industrialized nations for much of the past 50 years [38]. They are extremely stable and are therefore able to reach the stratospheric ozone layer. Along with other ozone depleting substances (ODS) such as halocarbons, they accelerate the destruction of ozone thereby deteriorating the ozone layer. When CFCs are exposed to UVB radiation in the stratosphere, they are photolytically destroyed into substances that include halogen atoms. In this process, nitrogen oxides are essential for the formation of ozone while hydrocarbons are necessary for its build-up. The destruction of ozone takes place by the following global reaction [22, 39]:



where X/XO = H/OH, OH/HO₂, NO/NO₂, Cl/ClO, Br/BrO.

The amount of ozone depletion caused by a substance is quantified by its ozone depleting potential (ODP) which is the ratio of the impact on ozone of a chemical compared to the impact of a similar mass of trichlorofluoromethane (CFC-11, CCl_3F) [40]. As the ODP of CFC-11 is fixed at 1.0, ODS can be classified into two groups: those with an ODP above 0.2 (Class I substance) and those with an ODP less than 0.2 (Class 2 substance), with Class 1 substances posing the greatest threat to the environment.

Since the mid 1980s, the ozone layer above the Antarctic has been particularly impacted by this kind of pollution. Figure 1.13 shows the evolution of the ozone layer above the Antarctic from 1970 until 2009. This region's low temperatures cause the formation of polar stratospheric clouds which contain particles that speed up the conversion of CFCs to chlorine and deactivate nitrogen oxides by scavenging nitric acid [37]. In the absence of nitrogen oxides, chlorine radicals take over and effectively destroy ozone. Since ozone filters harmful UVB radiation, less ozone increases UVB levels at the earth's surface. UVB has been linked to skin cancer, cataracts, damage of materials such as plastics, and harm to certain crops and marine organisms [41].

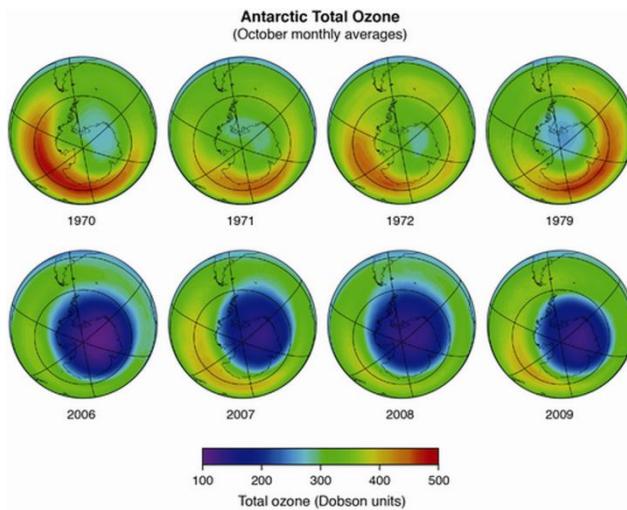


Figure 1.13 The Antarctic ozone hole over the years [42].

Fortunately, multiple governments around the world ratified and adopted the ‘Montreal Protocol on Substances that Deplete the Ozone Layer’ in 1987 [43]. This international treaty was designed to protect the ozone layer by phasing out or substantially reducing nearly 100

chemicals that damage the ozone layer in the upper atmosphere. In 2009 a milestone was reached when the production and use of CFCs was totally phased out. As a result of the protocol, the ozone hole in Antarctica has been slowly recovering and estimations indicate that the ozone layer will return to 1980 levels between 2050 and 2070 [39].

1.3.1.3 Formation of photochemical smog

Air pollution observed in densely populated, urbanized areas is commonly referred to as smog. The term smog is derived from a combination of the words 'smoke' and 'fog' originally identified with smoke from coal fires mixing with low-lying fog.

Historically, there are two types of smog named after the cities where they were first observed, London and Los Angeles. The London smog from 1952 is called sulfurous smog and is characterized by high concentrations of sulfur dioxide (SO₂) and particulate matter (PM) directly emitted by combustion processes [44]. Today, this kind of smog still occurs in many cities burning coal such as Beijing, Shanghai, Cairo and Calcutta.

The Los Angeles smog, first observed in 1943, is an oxidizing smog formed during photochemical reactions of nitrogen oxides and VOCs which are released into the atmosphere from the combustion of fossil fuels in automobiles, power plants, etc [44]. It is therefore also known as photochemical smog. It forms in low atmospheric layers during sunny days with a low air relative humidity. It reduces visibility and is aggressive for plants and human beings due to its oxidizing potential. The principal pollutant of this kind of smog is ozone formed during the reactions between NO_x and VOCs in the presence of solar UVB radiation. It is known as a secondary pollutant because it is not emitted directly but instead formed when precursor gases react in the presence of sunlight. Next to ground-level ozone, other products such as peroxy-acetyl-nitrates (PAN) are harmful and participate in the smog aerosol formation. Most major cities in the world today suffer from photochemical smog with some important examples being Mexico City, Rio de Janeiro, Sao Paulo, Houston and Santiago.

The mechanism of tropospheric photochemistry, which involves the formation of photochemical smog, is a complex series of reactions. A detailed discussion of these reactions does however not belong to the scope of this thesis. Figure 1.14 therefore presents a simplified scheme of the formation of tropospheric ozone in a polluted atmosphere.

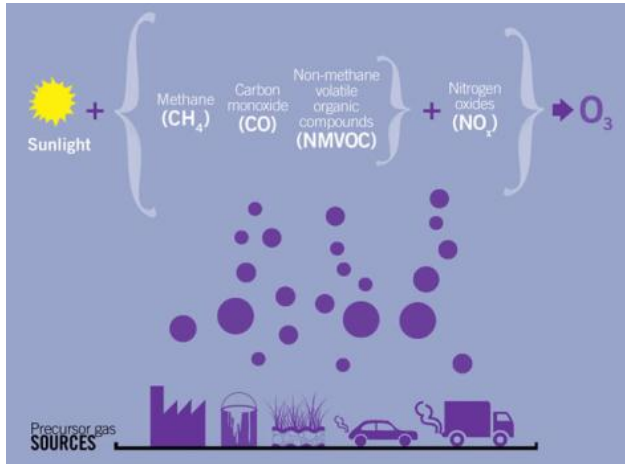
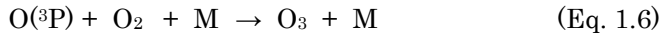
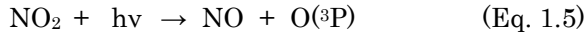
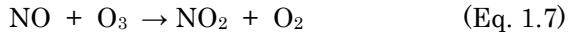


Figure 1.14 Simplified scheme of tropospheric ozone formation [45].

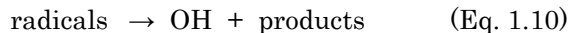
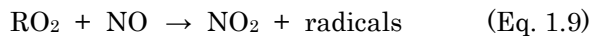
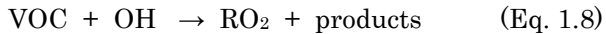
The important reactions involved in the tropospheric ozone formation are initiated by the photolysis of NO_2 and are summarized as follows [46]:



The ozone formation reaction above is normally balanced by the following reaction in which ozone oxidizes NO to NO_2 :



The balance of these reactions normally results in low, acceptable levels of ozone. However, in the presence of reactive VOCs, radicals are formed which consume NO or convert NO to NO_2 . This leads to an increase of ground-level ozone concentrations. The most important processes can be summarized by the following non-elementary reactions [46]:



Although stratospheric ozone plays a crucial role to maintain a mild global average temperature, tropospheric ozone is known to be harmful to humans and ecological life. Breathing ozone can trigger a variety of health problems especially to those who are more vulnerable such as children, people with lung disease, elderly and

outdoor workers. Symptoms including chest pain, coughing, throat irritation and congestion are related to inhalation of ozone [47]. It is also known to worsen bronchitis and asthma. Ozone also affects sensitive vegetation and ecosystems including trees and plants during growing season [48].

1.3.2 Health effects

VOCs are known to impact human health due to their potential toxicity, mutagenicity and carcinogenicity. The degree to which exposure to VOCs can affect human health depends on the VOC concentration, the duration of exposure, the toxicity of the VOC and the sensitivity of the person to the VOC. Figure 1.15 summarizes the health impacts of air pollution in general [6]. VOC vapours penetrate the body especially by inhalation and skin penetration. The VOC toxicity may be acute (short doses) or chronic (long lasting doses).

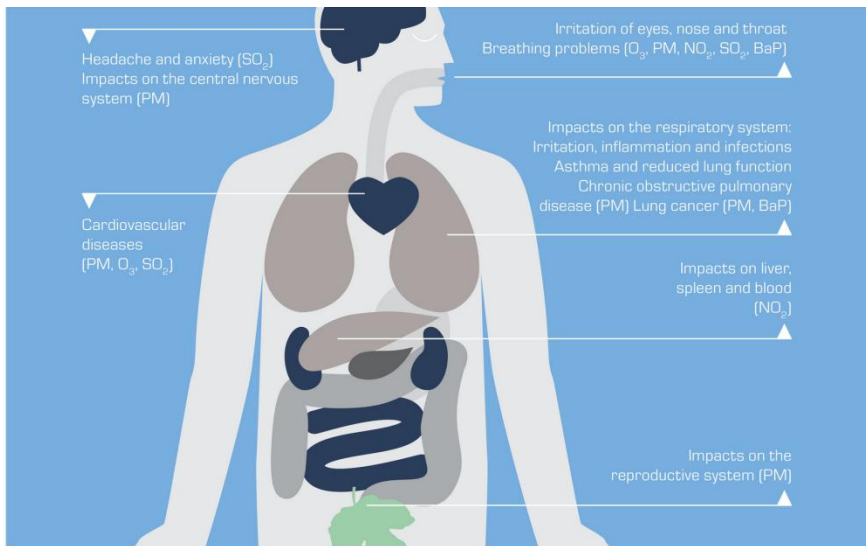


Figure 1.15 Health impacts of air pollution [6].

Humans are exposed to VOCs in both outdoor and indoor environments. Today, buildings are designed to be airtight and built with the use of high thermal insulation in order to minimize energy use for heating. As a consequence, indoor VOC concentrations are higher than outdoor levels due to a combination of insufficient ventilation and the presence of many indoor pollutant emission

sources [49]. Therefore, indoor air quality is mostly much worse and often exceeds outdoor levels by up to 5 times [50]. Sources of common VOCs found indoors include consumer and commercial products, paints and associated supplies, adhesives, furnishings and clothing, building materials, combustion appliances, potable water and tobacco smoke [51]. A term often used to address health issues associated to indoor environments is Sick Building Syndrome (SBS). It refers to non-specific complaints experienced by building occupants and includes symptoms such as headaches, dizziness, nausea, fatigue, rash, throat irritation and difficulty in concentrating [52]. The health effects of some common VOCs encountered in indoor environments are shown in Table 1.3.

Table 1.3 Health effects of some common VOCs [53].

VOC	Health effect
Benzene	Carcinogenic
Toluene	Headache, dizziness
Xylene	Eye and respiratory tract irritation, narcotic effect, nervous system depression and death
Chloroform	Affects central nervous system causing depression, dizziness, liver and kidney damages, skin infection
Ethylene, styrene	Depletion of ozone layer
Acetaldehyde, acetone	Respiratory and eye irritation
Phenol	Offensive odour and toxicity
Epoxides	Toxic, carcinogenic and explosive
Ethers	Producing peroxides, affecting the reproductive system
Vinyl chlorides, freon	Carcinogenic, toxic
Amines	Odour nuisance, carcinogenic

1.3.3 Other effects

Next to the impact on our environment and human health, VOCs are also known to affect our surrounding in other ways. They can physically damage buildings and monuments due to corrosion and soiling of their surfaces. VOCs containing sulfur are also known to cause odour nuisance in the vicinity of agricultural, municipal and industrial activities.

1.4 Legislation

In this section an overview on the history and evolution of legislation to prevent air pollution and improve air quality will be given. As a consequence of the numerous and different legislations imposed by individual countries and continents, this chapter will focus on the legal measures taken by the European Union (EU).

In November 1979, the Convention on Long-Range Transboundary Air Pollution (CLRTAP) in Geneva was the first international agreement to protect our atmosphere [54]. The objective was to protect the human environment against air pollution and to gradually reduce and prevent the spread of cross-border air pollutants. The convention was signed by 34 countries which were members of the United Nations Economic Commission for Europe (UNECE) and entered into force in 1983. It formed the backbone for international cooperation to combat air pollution and built up an institutional framework to bring science and policy closer together. From the agreement arose numerous international environmental laws that still form a control device for the protection against health and environmental damage caused by transboundary air pollution. Since 1983, the Geneva Convention has been supplemented by eight protocols that identify specific obligations to be taken by the ratifying parties, which to date include 47 European countries, Canada, USA and Armenia.

- Protocol on Long-term Financing of the Cooperative Programme for Monitoring and Evaluation of the Long-range Transmission of Air Pollutants in Europe (Geneva, 1984)
- Protocol on the Reduction of Sulphur Emissions or their Transboundary Fluxes by at least 30% (Helsinki, 1985)
- Protocol concerning the Control of Nitrogen Oxides or their Transboundary Fluxes (Sofia, 1988)
- Protocol concerning the Control of Emissions of Volatile Organic Compounds or their Transboundary Fluxes (Geneva, 1991)
- Protocol on Further Reduction of Sulphur Emissions (Oslo, 1994)
- Protocol on Heavy Metals (Aarhus, 1998)
- Protocol on Persistent Organic Pollutants (Aarhus, 1998)
- Protocol to Abate Acidification, Eutrophication and Ground-level Ozone (Gothenburg, 1999)

In order to fulfill the obligations of the protocols under the convention, annual reporting of emission data to the Executive Body

of the CLRTAP is required. The Gothenburg Protocol in 1999 set emission ceilings committed for the year 2010 for four pollutants: sulphur, NO_x, NH₃ and VOCs [55]. Parties where these emissions have a more severe impact on the environment and health and whose emissions are relatively cheap to reduce had to make the biggest efforts. This meant that the VOC emissions from Europe had to be reduced by 40% compared to the base year 1990. For Belgium the emission was recorded at 144 kt VOCs or a reduction of 59% relative to 1990. The Protocol also imposes tight limits on emissions of certain sources (e.g. waste incineration, electricity production, dry cleaning, production of cars) and requires the best available techniques to be implemented to keep emissions down.

Parallel to the development of the Gothenburg Protocol, the EU member states agreed to the National Emission Ceilings Directive (NEC Directive 2001/81/EC) which sets upper limits for the same pollutants for each member state for the total emissions in 2010 [56]. In 2012, the parties of the Gothenburg Protocol agreed on a substantial number of revisions and amended the protocol to include national emission reduction commitments to be achieved in 2020 and beyond.

Like in other EU member states, environmental law in Belgium originates mainly from EU law, whether through directly applicable regulations or directives that are implemented into Belgian national law. In the Belgian federal context, major responsibilities related to environment lie with the regions. Compiling atmospheric emissions inventories is one of these responsibilities. Each region implements the necessary means to establish their own emission inventory in accordance with the EMEP/EEA Emission Inventory Guidebook. The emission inventories of the three regions are subsequently combined to compile the national atmospheric emission inventory.

The United Nations are currently under way to develop a new international climate change agreement that will cover all countries. This agreement will be adopted in December 2015 at the United Nations Climate Change Conference (COP-21) held in Paris and will be implemented in 2020. The objective of the conference is to achieve an agreed and universal outcome with legal force on climate from all the nations worldwide.

Chapter 2

Conventional VOC abatement technologies

2.1 Classification

In this section, an overview will be given of the conventional or classical technologies used in industry for the abatement of gaseous VOC emissions. As these end-of-pipe techniques are relatively old, they are well known and widely used in many sectors of industrial activity. Through the years, they have undergone technical developments to improve their operation and to meet different demands such as lower energy costs and higher flexibility.

Although many technologies exist, they can generally be divided into two basic groups: (1) recuperative techniques that allow recovery of VOCs and (2) destructive methods that convert VOCs into other products. The flowchart shown in Figure 2.1 classifies different technologies for the abatement of VOCs that will further be discussed in more detail. Table 2.1 summarizes various characteristics of these technologies.

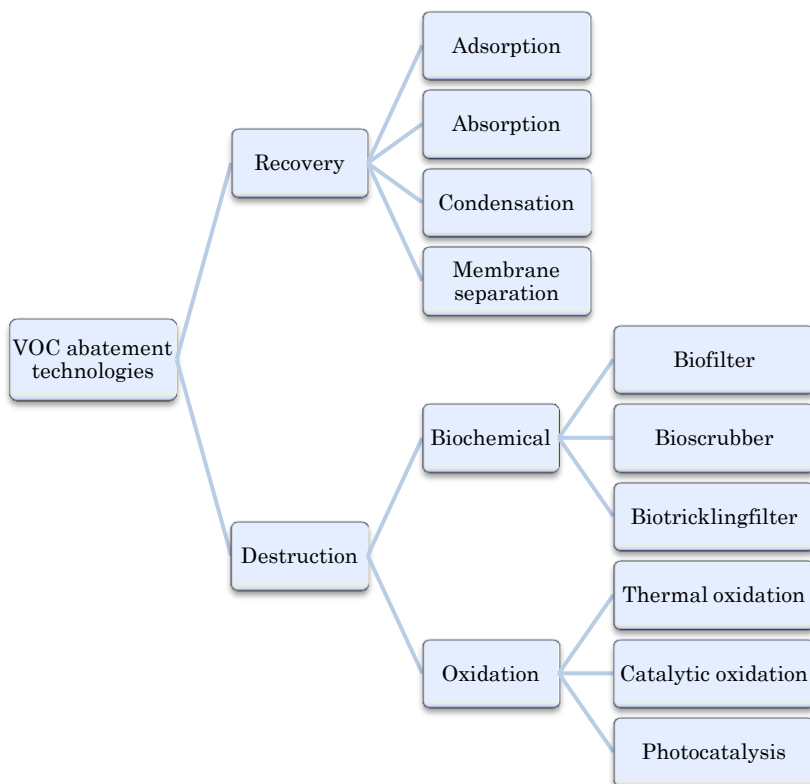


Figure 2.1 Classification of conventional technologies for VOC control.

Table 2.1 Characteristics of various VOC control technologies [27, 57-59].

Technology	Inlet conc. (ppm)	Efficiency (%)	Advantage	Disadvantage
Adsorption	200	50	Low capital investment	Moisture (< 50% RH) and temperature (< 50–60°C) constraints Adsorbent regeneration Pressure drop
	1000	90–95	Product recovery can offset operating costs	
	5000	98	Can accept variations in flow rate	
Absorption	250	90	Especially good for inorganic gases	Limited applicability Rigorous maintenance Possible pretreatment of VOCs
	1000	95	Product recovery can offset annual operating costs	
	5000	98	High flow rates can be processed	
Condensation	500	50	Compact system	Limited applicability Not recommended for compounds with boiling point above 35°C Rigorous maintenance
	10.000	95	Product recovery can offset annual operating costs	
Membrane separation	> 5000	90–99	No further treatment Product recovery can offset annual operating costs	Membranes are rare and costly
Biofiltration	< 1000	60–95	Low initial investment Less non-harmful secondary waste	No recovery of products
Thermal oxidation	20	95	High destruction efficiency	No recovery of products Capital intensive Halogenated and other compounds may require additional control equipment downstream
	100	99	Wide applicability Stable efficiency Heat recovery (max. up to 85%)	
Catalytic oxidation	50	90	High destruction efficiency	No recovery of products Catalyst deactivation
	100	> 95	Can be less expensive than thermal oxidation	

However, before considering to implement a VOC abatement technology, efforts must be addressed concerning modifications in processes and equipment. These include the substitution of raw materials to reduce the input of VOCs to the process, changes in operating conditions to reduce the formation or volatilization of VOCs, modification of technology or equipment and improvements in housekeeping, maintenance, training or inventory control [60].

2.2 Selection criteria

If the implementation of the modifications mentioned above is not practically possible or if they do not offer any solution, a suited VOC abatement technology must be selected. This selection depends on a number of factors that have to be taken into account. The most important criteria are briefly discussed in this section.

2.2.1 Economical considerations

From an economical standpoint, the choice for a certain VOC abatement technology is governed by the total capital investment (TCI) and the total annual costs (TAC).

The capital expenditure covers the cost of equipment, auxiliary equipment, all direct and indirect installation costs and costs of land, buildings, site preparation, offsite facilities and working capital [61]. The TCI consists of depreciable and non-depreciable investments. Depreciable costs can be depreciated during all or part of the time the abatement technology is in operation. These include the equipment mentioned above and any facilities related investments. Costs as land and working capital comprise the non-depreciable elements of the TCI because they can be recovered when the abatement technology ceases operation.

As the name indicates, the TAC, also known as the operational and maintenance costs, are those expenses incurred every year during the life of a system [61]. Due to inflation and other factors, the magnitude of these costs may differ in time. However, the kinds of costs will be the same. The TAC comprises of direct (DAC) and indirect (IAC) annual costs which are offset by recovery credits (RC). These credits deal with energy and materials recovery by the system. The DAC are costs that tend to be (partially) proportional to production while IAC are independent of throughput. The TAC can thus be calculated as follows:

$$\text{TAC} = \text{DAC} + \text{IAC} - \text{RC} \quad (\text{Eq. 2.1})$$

Generally, the TCI for these systems is in direct conflict with the TAC. For example, the installation of an adsorption unit demands high capital investments because these are quite sophisticated systems. On the other hand, recovery of the VOC can provide savings that can greatly decrease the TAC of the system.

2.2.2 Technical criteria

In addition to these economic considerations, there are some technical criteria that affect the choice for a certain VOC control technology. The most important criterium is determined by the demands of regulatory requirements imposed by governmental agencies. This required reduction in emission is VOC-specific and is regulated by European legislation under the “VOC Solvents Emission Directive” [3]. Other technical criteria include for instance the nature of the installation site (available space, utilities such as steam, liquid N₂,...) and possibilities for maintenance (materials, staff, safety aspect,...).

2.2.3 Gas stream conditions

The identification of the gas stream conditions of the waste gas is crucial for a proper choice of a suitable VOC abatement technology. These include the composition of the waste gas (single compounds or mixtures), gas flow rate, VOC concentration, limits of inflammability and explosivity of the treated VOC, gas temperature, oxygen content, VOC solubility, gas pressure and moisture content. Fluctuations of the gas condition as a result of process changes also need to be taken into account. All these data are used to develop a comprehensive emissions inventory which includes information and details of the entire industrial facility source-by-source. In addition, periodical emission averages including worst case emission scenarios must be provided. Figure 2.2 classifies VOC abatement technologies based on their scope of air flow rate and VOC concentration.

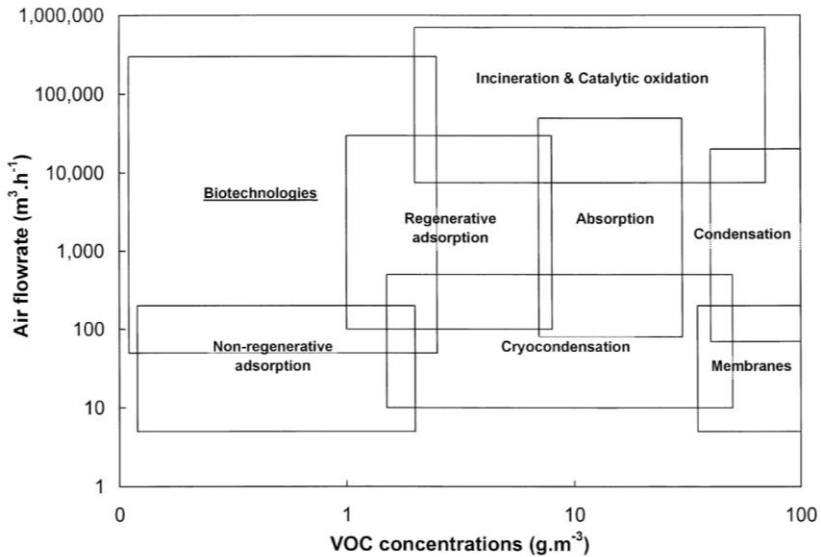


Figure 2.2 Classification of various air pollution control technologies based on air flow rate and initial VOC concentration [59].

2.3 Non-destructive methods

2.3.1 Adsorption

Vapor-phase carbon adsorption is a remediation technology in which pollutants are removed from air by physical adsorption onto activated carbon grains or fibers. Carbon is activated for this purpose by treatment with hot air or steam to create porous particles with a large internal surface area (300–2500 m²/g) that attracts and adsorbs VOC molecules as well as certain metals and inorganic molecules.

The adsorption capacity for a given VOC is represented by an adsorption isotherm of the amount of VOC adsorbed to the equilibrium pressure at constant temperature. Other adsorbents that are often used are zeolites, alumina, silica gel or polymers but they are more expensive than activated carbon. Table 2.2 summarizes different target pollutants and related effective adsorbents.

Table 2.2 Summary of types of pollutants and adsorbent used [23].

Substance to be removed	Adsorbent			
	Activated carbon	Activated alumina	Silica gel	Molecular sieves
Odours	✓			
Oil	✓	✓	✓	✓
Hydrocarbons	✓	✓	✓	
Fluorocarbons	✓		✓	
Chlorinated hydrocarbons	✓		✓	
Organic sulfur compounds	✓	✓		✓
Solvents	✓			
Moisture	✓	✓	✓	

Physical adsorption occurs when VOCs are attracted to the adsorbent by weak Van der Waals forces and is generally characterized by low heat of adsorption and by the fact that the adsorption equilibrium is reversible and rapidly established [58].

This method shows high reliability due to a robust operating configuration. Therefore, it is widely used for the remediation of contaminated sites where reuse of valuable condensable organic compounds is desirable. This can significantly offset the cost of the emission control process. Factors that affect adsorption are temperature, pressure, type and pore size of the adsorbent, the type and concentration of the contaminant, residence time in the bed and humidity [62, 63]. Figure 2.3 shows a typical fixed-bed adsorbing unit for the recovery of solvent vapors.

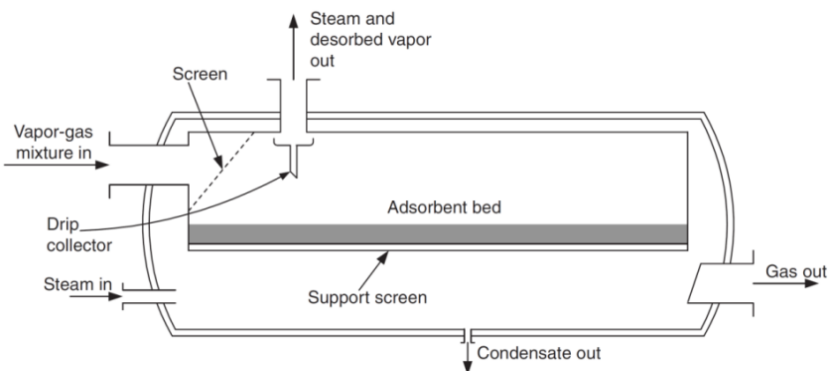


Figure 2.3 Fixed-bed adsorber [23].

When the adsorbent is saturated with VOC, breakthrough occurs and significant quantities of VOC become apparent in the gas stream exiting the adsorption process. At that moment, the bed needs to be regenerated or refilled with virgin carbon to ensure the desired removal efficiency. There are two different implementations for this purpose. Regeneration can be continuously operated by using multiple adsorption beds. While one bed is then regenerated, other beds are still kept working.

Thermal swing adsorption is done by heating the carbon with steam, hot air or hot nitrogen to desorb for example an organic solvent. This occurs at temperatures between 80°C and 200°C. Next, the mixture of steam and solvent can be separated after cooling through gravity decanting or through distillation if the solvent is soluble in water. In this way solvent in the exhaust stream can be recuperated for reuse.

Another method to desorb pollutants from the adsorbent is by reducing the pressure, which is called *pressure swing adsorption* (PSA). By controlling the pressure and cycle time, the pollutant is transferred from the effluent stream to the low-pressure gas regeneration stream. Through adsorption, the nature of pollutants is not changed but they are just transferred to another phase. This requires post treatment of the spent carbon or the additional phase.

Adsorption is suitable for a large range of air flow rates with low or medium VOC concentrations ($< 50 \text{ g/Nm}^3$) and can provide high recovery yields reaching 90–98%.

2.3.2 Absorption

Absorption is used to remove VOCs from gas streams by mixing the polluted air with a liquid solvent (absorbent). In an absorber (or scrubber) all soluble VOCs will transfer to the absorbent. The driving force for this mass transport is the concentration difference of the VOC between the gaseous and liquid phase. This is realised in absorption towers which are specially designed to enhance the gas-liquid contact and facilitate mass transport (Figure 2.4). The scrubbers are filled with random packings while special measures are taken to increase the driving force for mass transfer. Therefore, the absorbent is often atomized with spray nozzles to break the liquid into tiny droplets or thin films.

Absorption is suitable for treating polluted air streams with high humidity (50% RH). Absorption systems are especially attractive for the removal of inorganic and organic odorous compounds from slaughterhouses and food and textile industry. Because pollutants are transferred to the absorbent, the waste liquid must undergo after

treatment by distillation or stripping which may offset annual operating costs. Scrubbers are suitable for air streams with relatively high concentrations ($> 50 \text{ g/Nm}^3$) at temperatures close to ambient. High recovery yields (95–98%) can be attained at low operating costs while recovered solvents can have a high purity.

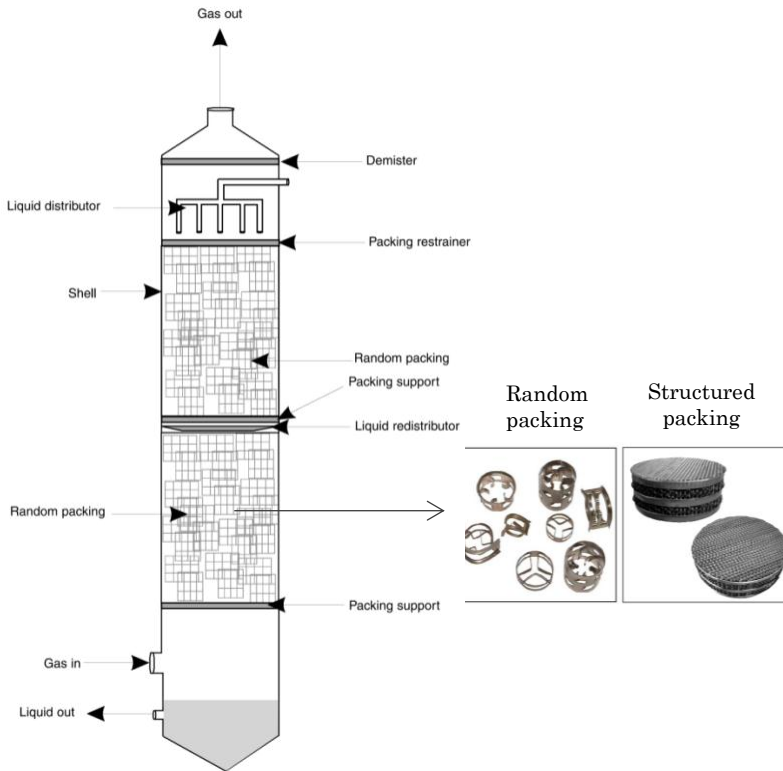


Figure 2.4 Packed column for absorption of VOCs with random and structured packings [23, 64].

2.3.3 Condensation

Condensation of gaseous VOC emissions can be achieved through cooling or pressurization (or both). Cooling occurs in heat transfer equipment which usually use water or refrigerants as coolant. Depressurization of the treated stream can reduce operational costs through recovery of energy. Condensation is efficient for VOCs with a high boiling point ($> 35^\circ\text{C}$) in the concentration range above 5000 ppm [57]. The efficiency of the process improves as VOC inlet concentration and inlet gas pressure increase [65]. Typical removal efficiencies that

can be attained range between 50–90%. Higher efficiencies (95–99%) can be realized with cryogenic condensation using liquid nitrogen as coolant. This method is however rather expensive and sensitive to the presence of moisture [66].

When the VOC concentration is high, condensers are frequently used as preliminary devices prior to incinerators, absorbers or adsorbers. For low concentrated VOC gas streams or for low-boiling VOCs extensive cooling or high pressurization is required to achieve the desired removal rate.

The two most common types of condensers are surface and contact condensers. In surface condensers, no contact occurs between the coolant and the treated gas stream. Figure 2.5 shows a typical shell and tube type surface condenser. The coolant circulates through several tubes while VOCs condense on the outside of the tubes within the shell. Another surface type configuration is the plate and frame condenser where the coolant and the vapor separately flow over thin plates. In contact condensers, cooling is achieved by spraying either a liquid at ambient temperature or a cooled liquid directly into the gas stream. The drawback of this method is that spent coolant is contaminated with VOC and cannot be directly reused and must consequently undergo further treatment before disposal.

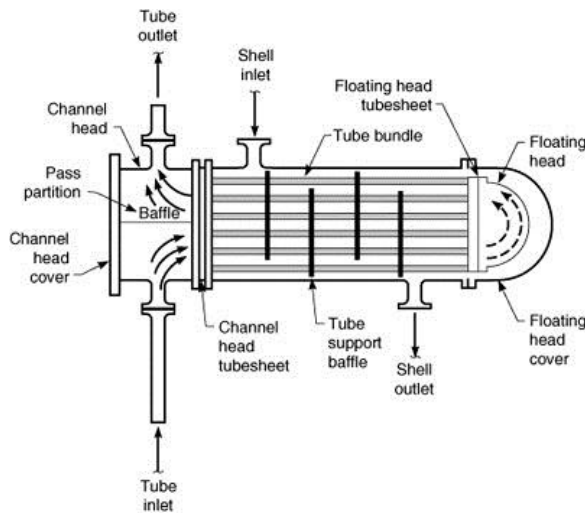


Figure 2.5 Shell and tube type condenser [67].

The condensate may require treatment to remove water or additional separation (typically distillation) if multiple VOCs need to be recovered. Once VOCs are recovered they can be reused in the process or they can alternatively be sold to interested customers.

2.3.4 Membrane separation

Membrane separation uses semi-permeable polymeric membranes to separate VOCs from waste gas streams in an efficient and continuous manner. This technology has emerged as an important technology for the separation of VOCs and other gaseous air pollutants during the past 30 years. The waste stream to be treated is separated into a permeate that contains concentrated VOCs and a treated residue stream that is depleted of VOC. Table 2.3 provides a list of VOCs that can be captured with membrane separation.

Table 2.3 VOCs that can be removed with membrane technology [23].

Acetaldehyde	Hexane
Acetone	Methanol
Acetonitrile	Methyl bromide
Benzene	Methyl chloride
Butane	Methyl chloroform
Carbon tetrachloride	Methyl isobutyl ketone
CFC-11	Methylene chloride
CFC-12	Perfluorocarbons
CFC-113	Propylene oxide
Chlorine	Styrene
Chloroform	Toluene
Ethylene dichloride	Trichloroethylene
Ethylene oxide	Vinyl chloride
HCFC-123	Xylenes

The preferential transport of organic vapor through the membrane is usually achieved by placing a vacuum pump at the permeate side of the system which causes a large pressure difference between the feed and permeate side. Air and VOCs permeate through the membrane at rates determined by their relative permeabilities and the pressure difference across the membrane [68, 69]. Mass transport takes place in three consecutive steps as illustrated in Figure 2.6: (1) sorption of components from the feed onto the membrane at the upstream side; (2) diffusion of the sorbed components through the membrane followed by (3) desorption of the permeate from the membrane at the permeate side.

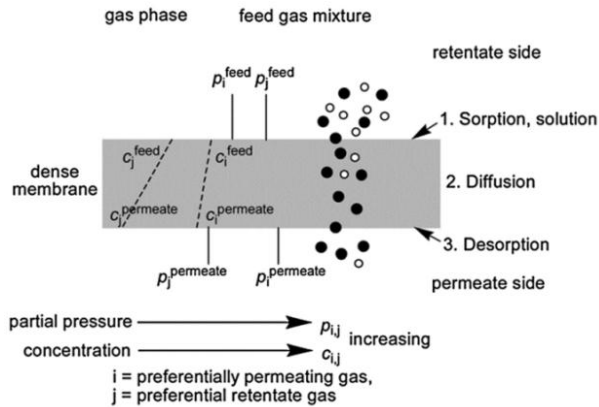


Figure 2.6 Separation mechanism in dense membranes [70].

Membrane modules exist in four different configurations, i.e. flat sheet, tubular, hollow fibre and spiral wound modules [71]. Synthetic membranes have to be chemically, thermally and mechanically stable. Harsh environments are often detrimental for the lifetime of a membrane. They are also sensitive to moisture and their efficiency decreases when fluctuations in VOC concentrations appear. It is best suited for relatively small flows containing moderate VOC concentration (> 1000 ppm) and can reach VOC recovery yields ranging from 90 to 99% [23]. Figure 2.7 shows a typical membrane separation system. The permeate stream containing VOCs can be recycled to the plant or can be sent to a condenser where liquid solvent can be recovered.

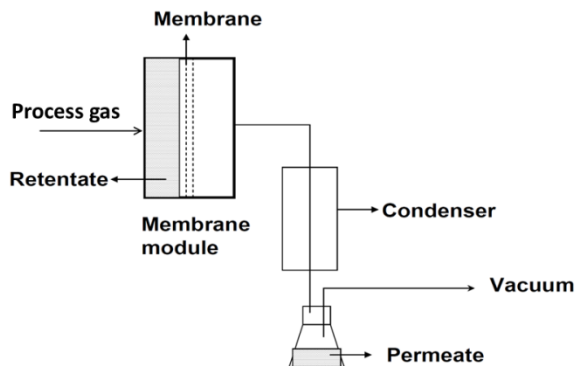


Figure 2.7 Schematic presentation of a membrane separation system [66].

2.4 Destructive methods

2.4.1 Biochemical methods

Biochemical methods utilize a bed of solid natural material (soil, compost, etc.) containing a biolayer with various bacteria or microorganisms. The soil or compost consists of a network of fine pores with large surface area providing an environment in which the bacteria thrive due to the presence of salts and trace elements. The high biological activity of these organisms enables the oxidative degradation of VOCs to CO_2 and H_2O under aerobic and humid conditions [72]. Bioreaction is a green process because emission of pollutants like NO_x , particulate matter, SO_x and CO , which are common hazardous pollutants in combustion processes, does not occur.

Removal and oxidation rates depend on the biodegradability and reactivity of the target VOC (Table 2.4) relies on different processes such as biotransformations, adsorption, absorption and diffusion.

Table 2.4 Biodegradability of VOCs [73].

Rapidly degradable VOCs	Slowly degradable VOCs	Very slowly degradable VOCs
Alcohols	Hydrocarbons	Halogenated
Aldehydes	Phenols	hydrocarbons
Ketones	Methylene	Polyaromatic
Ethers	Chloride	hydrocarbons
Esters		CS_2
Organic acids		
Amines		
Thiols		
Other molecules containing O, N, S functional groups		

Figure 2.8 shows a schematic view of a biofilm and the occurring mass transfer. In this section, three bioreactor configurations that are nowadays used for the treatment of polluted air will be discussed, i.e. biofilters, bioscrubbers and biotricklingfilters. Table 2.5 presents a comparison of the technical characteristics of these technologies.

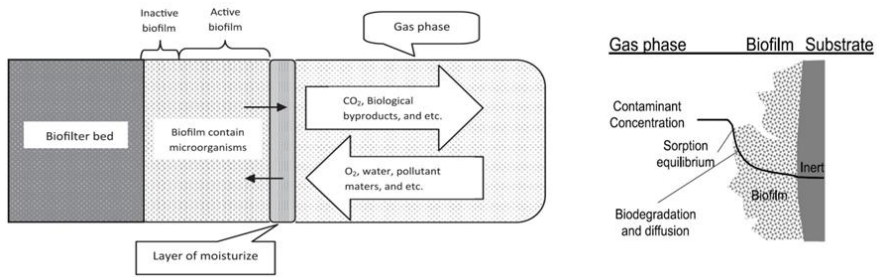


Figure 2.8 Schematic representation and mass transfer in a biofilm [73, 74].

Table 2.5 Technical characteristics of biofilters, bioscrubbers and biotricklingfilters [59].

Bioprocess	Microorganisms	Liquid phase	Depollution step
Biofilter	Immobilized on the filtering material	Occasional bed irrigation with nutrient solution	In the filter bed In the biofilm
Bioscrubber	Suspended in the bioreactor, in the aqueous growth medium	Mobile Continuously dispersed Recycled	VOC/air separation within the absorption column VOC oxidation in the aerated bioreactor
Biotricklingfilter	Immobilized on the filtering material	Mobile Continuous trickling over the filter bed Possible recycling	In the filter bed In the biofilm

2.4.1.1 Biofilters

Biofilters are fixed-film or packed-bed bioreactors in which a natural filter or inert packed-bed is used to immobilize microorganisms. It is the oldest and most frequent bioreactor configuration, originally developed for odour abatement of waste gases [75]. Polluted air is fed in down- or upflow mode through a system of perforated pipes in the reactor in order to achieve biodegradation in the porous packed-bed (Figure 2.9). The biofilm activity is determined

by its microbial density and relies on parameters such as absence of toxic materials, ample inorganic nutrients for the microorganisms, optimum moisture conditions, appropriate temperature, ample oxygen supply and neutral pH range [23, 73]. Proper control of the humidity is essential to maintain high biological activity. Waste air is therefore generally pre-humidified and biofilters have intermittent water spraying.

Biofiltration can attain removal efficiencies up to 60–95% for waste gas concentrations below 5 g/m³ at low or moderate flow rates [76]. The capital cost of a biofilter is influenced by the size of the system but is relatively low because natural materials are used. The oxidation of VOCs is done by microorganisms which do not produce potentially hazardous products.

Disadvantages are related to additional operating costs of various methods for effective moisture control and the fact that some VOCs, especially halogenated compounds such as trichloroethylene and trichloroethane, biodegrade very slowly under aerobic conditions.

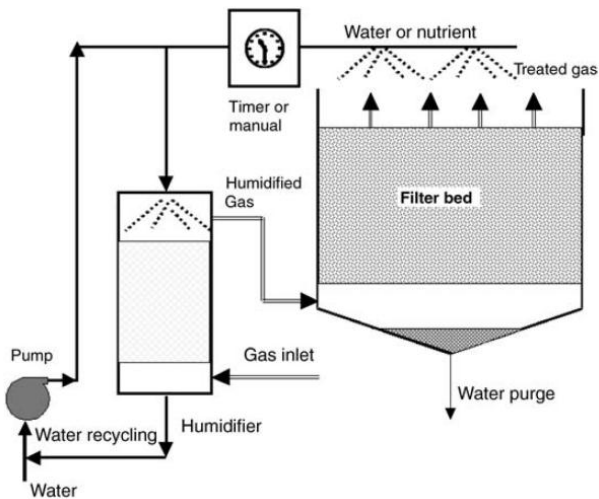


Figure 2.9 Schematic diagram of an open biofilter [73].

2.4.1.2 Bioscrubbers

In a bioscrubber, pollutants in the gas phase are first fed to a scrubbing tower where they are transferred to a dispersed liquid phase (Figure 2.10). The scrubbed gaseous phase is released at the top of the tower. Next, the polluted liquid phase is pumped to a bioreactor where suspended microorganisms feed on the pollutants in order to

regenerate the liquid before returning to the scrubbing tower. Most bioscrubbers are inoculated with activated sludge originating from wastewater treatment plants [76]. Nutrient addition and pH are continuously monitored to maintain microbial growth and high activity [73].

Bioscrubbers are well suited for water soluble VOCs at relatively low flow rates. Concentrations in the gaseous phase may not exceed 5 g/m^3 while Henry coefficients must be smaller than 0.01 [59]. Advantages are related to the small space requirement for installation, small pressure drops and good operational stability and control of the biological parameters (pH and nutrients). Nevertheless, the technology has some drawbacks such as the production of sedimented sludge and waste water and quite low specific surface areas for gas/liquid transfer. Despite technological progress, industrial implementation at full scale is rare.

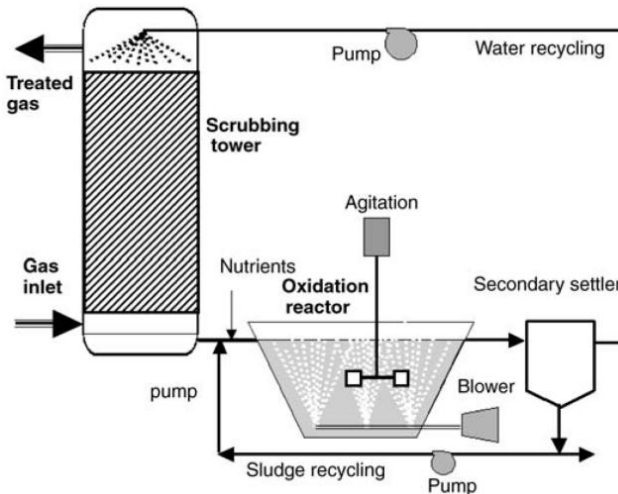


Figure 2.10 Schematic diagram of a bioscrubber [73].

2.4.1.3 Biotrickling filter

In a biotrickling filter, polluted air is passed through an inert packed-bed which is continuously irrigated with an aqueous solution containing the nutrients required by the system (Figure 2.11). Gaseous VOCs are first dissolved in this falling trickling phase and then transferred to the microorganisms that are growing on the surface of the supports in the packed-bed.

Figure 2.11 also illustrates the mechanism that is responsible for the degradation of pollutants in a biotricklingfilter. Pollutants are initially absorbed by the trickling liquid that surrounds the biofilm followed by biodegradation within the biofilm that gradually develops on the bed particles. The flow rate and the recycling rate of the trickling phase through the filter bed are therefore critical parameters because they determine the degree of contact between the VOC and microorganisms. The use of the mobile trickling phase allows a much easier control of pH and temperature and removal of potential inhibiting metabolites compared to biofilters. The major drawback of these systems is related to the accumulation of excess biomass in the filter bed that can lead to clogging problems. Methods to prevent this clogging include bed stirring or bed backwashing with water, chemical treatments with disinfecting reagents or use of biomass predators such as protozoa [59].

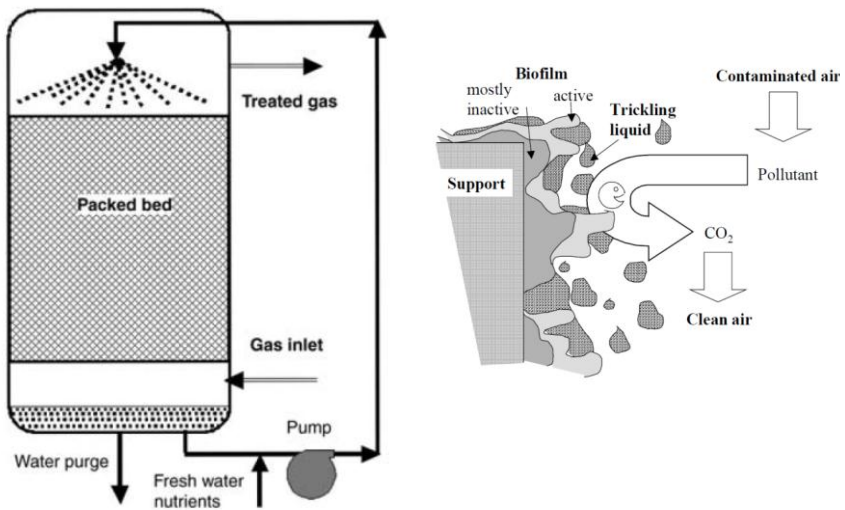


Figure 2.11 Schematic diagram and mechanism of a biotricklingfilter [73].

2.4.2 Thermal oxidation

Thermal oxidation or incineration relies on the combustion of organic compounds by raising the temperature above the auto-ignition point in the presence of oxygen [66]. The organic compounds are oxidized to CO₂ and H₂O while trace elements such as sulfur and chlorine are converted to species such as SO₂ and HCl. The actual

operating temperature of an incinerator is a function of the type and concentration of the VOCs and the desired removal efficiency. High removal efficiencies can be achieved by proper design of the combustion chamber and precise control of the operation.

Thermal oxidation units are typically single chamber, refractory-lined oxidizers equipped with a propane or natural gas burner and a stack. Contaminants are processed by first preheating the gases, then passing them through a burner at a controlled and optimal temperature. Most hazardous waste incinerators are operated between 700–1000°C to ensure nearly complete destruction of the organics in the waste gas stream. Depending on system requirements and characteristics of the contaminated stream, removal efficiencies range from 95 to 99% at residence times typically between 0.5 to 1.0 s.

Thermal oxidation is one of the most proven methods for destroying VOCs. Moreover, the possibility for energy recovery can effectively lower the operational costs. This can be achieved by reusing the thermal energy for preheating the feed in recuperative systems or stored in ceramic beds in regenerative systems (Figure 2.12). In this way, heat recovery efficiencies of 50–70% and 85–95% can be reached, respectively [66].

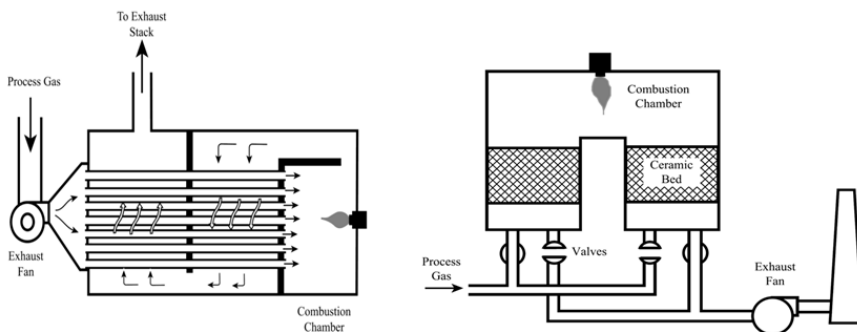


Figure 2.12 Recuperative (left) and regenerative (right) thermal oxidizers [23].

There are however some disadvantages that have to be mentioned: (1) operating costs are relatively high due to supplemental fuel costs; (2) thermal oxidizers are not well suited for gas streams with highly variable flow because of the reduced residence time and poor mixing during increased flow conditions which decrease the completeness of combustion; (3) it is also not recommended for controlling gases containing halogenated or sulfur-containing compounds because of the formation of highly corrosive acid gases which require the installation of an additional post-treatment, (4) thermal incinerators

are also generally not cost-effective for low concentration, high-flow organic vapor streams.

2.4.3 Catalytic oxidation

Catalytic oxidation is a relatively recently applied technology for the treatment of VOCs in air streams. The addition of a catalyst accelerates the rate of oxidation by adsorbing oxygen and contaminants on the catalyst surface where they react to form oxidation products like CO_2 , H_2O and HCl [77]. The catalyst enables the oxidation reaction to occur at much lower temperatures than required by thermal oxidation which substantially reduces fuel requirements and operating costs.

Catalytic surface reactions mainly occur via three reaction mechanisms, i.e. Langmuir-Hinshelwood, Eley-Rideal or Mars Van Krevelen mechanism (Figure 2.13). The first mechanism proposes that both reactants first adsorb onto the surface before a bimolecular reaction takes place. The vast majority of catalytic reactions follow this mechanism. In the second mechanism, only one of the reactants adsorbs onto the surface after which the other reactant interacts with the adsorbed species directly from the gas-phase. In the final mechanism, the surface itself is an active part in the reaction: one reactant forms a chemical bond with the catalytic surface forming a thin surface layer of metal-reactant (1a). The other reactant now directly reacts from the gas-phase with the atoms from the chemically bonded reactant on the surface (1b).

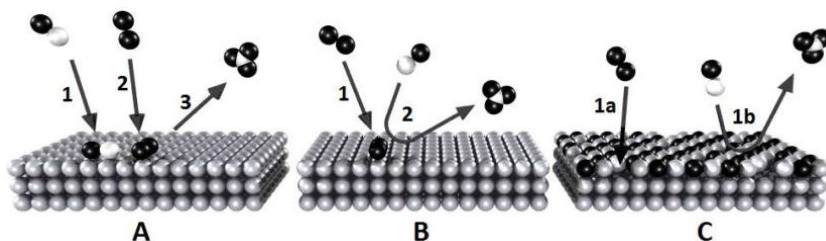


Figure 2.13 Langmuir-Hinshelwood mechanism (A), Eley-Rideal mechanisms (B) and Mars-Van Krevelen mechanism (C) [78].

Figure 2.14 shows a typical catalytic oxidation system. Waste gas is heated by auxiliary burners before entering the catalyst bed. Typical operating temperatures range from 200–350°C for heavy VOCs (C_4 and above), 370–540°C for light VOCs (C_3 and below) and 200–500°C for halogenated VOCs [23]. Next, the preheated feed stream is passed

through the catalyst bed where VOCs are rapidly oxidized. Removal efficiencies typically range from 90 to 98% for low concentrated VOC streams [57, 79]. Catalysts used for VOC oxidation include noble metal (Pd, Pt) and transition metal (Cr, Mn, Ni, Cu, Co) oxides [80].

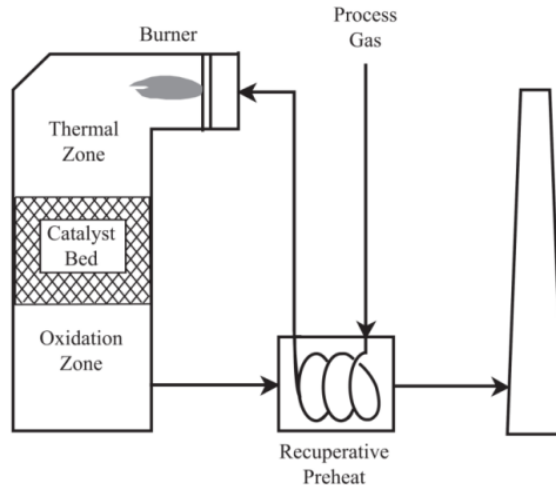


Figure 2.14 Typical catalytic oxidation system [23].

Catalytic oxidation is most suited for systems with lower exhaust volumes when there is little variation in the type and concentration of VOC and where catalyst poisons are not present. However, selection of a catalytic oxidation system should be carefully considered, as their sensitivity to VOC inlet stream flow conditions and catalyst deactivation limits their applicability for many industrial processes. Table 2.6 presents a summary of the different mechanisms of catalyst deactivation that have been reported in literature.

2.4.4 Photocatalysis

Photocatalysis is a process that uses UV light for the activation of catalysts that are usually pure or doped metal oxide semiconductors. In this way, a broad range of pollutants can be completely oxidized to CO_2 , H_2O and mineral acids at low or room temperature without significant energy input [81]. Historically, photocatalysis was applied for waste water purification but rather recently utilization for air treatment has increased.

Table 2.6 Mechanisms of catalyst deactivation [80].

Chemical	Thermal	Fouling	Mechanical
Poisoning: irreversible adsorption or reaction on/with the surface	Metal/metal oxide support interactions	Coking: carbonaceous deposits	Thermal shock
Inhibition: competitive reversible adsorption of poison precursor(s)	Noble metal –base metal interactions	Masking: small particulate deposits	Attrition
Poison induced reconstruction of catalytic surfaces	Oxidation (alloy formation)		Mechanical breakage
Physical/chemical blockage of support pore structure	Noble metal surface orientation		
	Sintering (redispersion)		
	Support changes		
	Alloying		
	Metal volatilization		

The most important and known photocatalyst is TiO_2 due to its superior characteristics: (1) it is inexpensive, safe and very stable showing high photocatalytic efficiency, (2) it promotes ambient temperature oxidation of the major classes of air pollutants, (3) complete degradation of a broad range of pollutants can be achieved under certain operating conditions, and (d) no chemical additives are required [81]. The decomposition rate is influenced by the pollutant concentration, O_2 partial pressure, humidity, temperature and light intensity [80, 82].

The basic mechanism of photocatalysis can be represented by the band gap model (Figure 2.15). The band gap of a semiconductor is the energy interval (E_b) between the valence band (VB) and conduction band (CB). When TiO_2 is illuminated by photons having an energy equal or higher than E_b electron–hole pairs are formed through transfer of VB electrons to the CB (1). After migration to the surface (2), electron–hole pairs can induce redox reactions between adsorbed VOCs with suitable redox potentials and active oxygen species ($\text{OH}\cdot$, $\cdot\text{O}_2^-$) (3). Finally, electron–hole pairs recombine in absence of adsorbed VOCs with release of thermal energy and/or light (4).

Photocatalysis is mainly used to decontaminate, deodorize and disinfect indoor air. Despite intensive research, the implementation of full–scale applications in industry is still scarce.

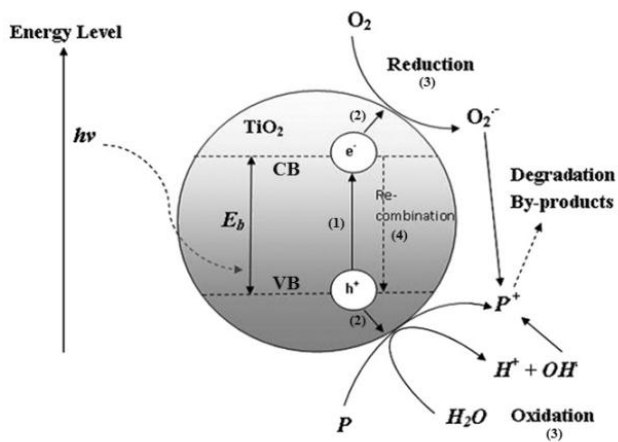


Figure 2.15 Mechanism of electron–hole pair formation in a TiO_2 particle in the presence of pollutant [83].

Chapter 3

Literature overview

This chapter is an updated version of the review article published in the following international journal:

A.M. Vandebroucke, R. Morent, N. De Geyter, C. Leys
Non-thermal plasmas for non-catalytic and catalytic VOC abatement
Journal of Hazardous Materials 195 pp. 30-54, 2011

3.1 Introduction

This chapter gives an overview of the literature on the abatement of VOCs with non-thermal plasma (NTP) generated in electrical discharges. Historically, NTPs were initially investigated during the 1980s for the removal of NO_x and SO_x from flue gas [84-87]. During the last two decades the public's growing concern about environmental pollution has been a driving force for researchers to explore the use of NTP for the abatement of other air pollutants such as VOCs. Especially, the application of NTP technology for the abatement of dilute VOCs from waste gas streams and indoor air has extensively been studied in order to develop a sustainable alternative for conventional technologies.

The use of NTP for air pollution control has several desirable features resulting from its operating conditions such as a quick start-up, rapid response to changes in the composition of the waste gas and operation at ambient conditions which excludes the use of expensive vacuum systems. Furthermore, NTP systems can effectively be combined with other established technologies. In this regard, the combination of NTP with heterogeneous catalysis, referred to as plasma-catalysis, has gained increased interest during the last 15 years. Early studies had already pointed out that catalytic processes can provide a realistic way to enhance the performance of plasma alone systems [88-92]. For instance, Devins and Burton reported in 1954 the formation of hydrazine during the decomposition of ammonia with an electrical discharge and stated the following [92]:

“Catalysis of H atom removal by platinum-coating the wall of the discharge tube increases the overall hydrazine yield.”

In 1983, Gicquel et al. published a review on heterogeneous catalysis in low-pressure plasmas and declared that [89]:

“Perturbation of the plasma medium by the solid is interpreted as a catalytic action to the extent that it leads to an increase of chemical reactivity of the system... These conclusions permit a new approach to non-equilibrium chemical reactivity in the heterogeneous plasma phase.”

These early studies provided the scientific backbone for the research on plasma-catalytic VOC abatement as we know it today.

Figure 3.1 shows the evolution of published research articles on VOC abatement with NTP and plasma-catalysis. This comparison is based on an extensive literature survey carried out by the author of this work and only comprises of articles included in Web of Science. It is clear that since 1992, the number of NTP studies has steadily increased until 2008 whereafter a decline is observed (except for

2013). The number of studies regarding plasma–catalysis has increased since 1996 and has more or less outnumbered NTP studies since 2004.

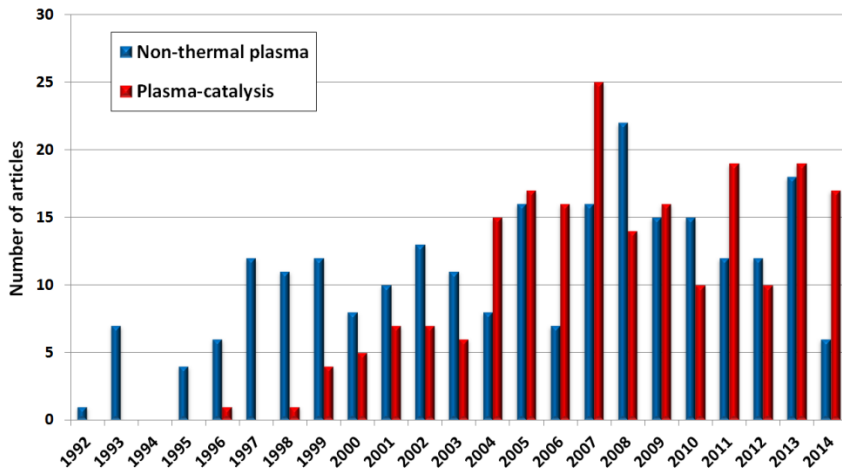


Figure 3.1 Comparison of the number of published research articles on VOC abatement with non–thermal plasma and plasma–catalysis.

In the first section of this chapter, an overview of different NTP reactors is given. In a second section, based on a large number of papers, an extended review is presented dealing with the treatment of VOCs with plasma alone as well as with plasma–catalytic systems. Particular attention is paid to the most studied target compounds, i.e. trichloroethylene, benzene and toluene. Also general mechanisms that govern plasma–catalysis are summarized. In a third section, special attention is given to the influence of critical process parameters on the removal process. In a final section, future trends for this promising hybrid technique are discussed.

3.2 *Non–thermal plasmas for VOC abatement*

3.2.1 Without catalyst

3.2.1.1 What is a non–thermal plasma?

Non–thermal plasmas are generated by applying a sufficiently strong electric field to ensure the discharge of a neutral gas. This creates a quasi neutral environment containing neutrals, ions, radicals, electrons and UV photons. Due to their light mass, electrons

are selectively accelerated by the field and gain high temperatures while the heavier ions remain relatively cold through energy exchange by collisions with the background gas.

The bulk gas molecules (e.g. N_2 , O_2) are bombarded by the electrons, typically having temperatures ranging from 10,000°C to 250,000°C (1–20 eV). This produces excited gas molecules (N_2^* , O_2^*) which lose their excess energy by emitting photons or heat. Next to excitation, other processes like ionization, dissociation and electron attachment occur in the discharge zone. Through these reaction channels, unstable reactive species like ions and free radicals are formed. Free radicals, such as $OH\cdot$ and $O\cdot$, are highly reactive species which are ideal for the conversion of environmental pollutants to CO_2 , H_2O and other degradation products at uncharacteristic low temperatures. The generation of NTP at atmospheric pressure and ambient temperature has been the subject of many research papers during the last two decades. This has led to great advances, mainly on laboratory scale. However, large scale demonstrations of NTP technology for waste gas cleaning are also currently operative [93, 94].

3.2.1.2 Reactor concepts

Researchers have investigated a variety of NTP reactors for environmental purposes. The classification of these different reactors is rather complex and depends on multiple characteristics, such as:

- Type of discharge: (DC or pulsed) corona discharge, surface discharge, dielectric barrier discharge, ferro–electric packed bed discharge,...
- Type of power supply: AC, DC, pulse, microwave, RF,...
- Other characteristics: electrode configuration, voltage level, polarity, gas composition,...

For the conventional NTP reactors that are employed in laboratory experiments, only the main characteristics will be briefly discussed here. A more detailed discussion can be found in literature [95-100].

A *dielectric barrier discharge* (DBD) or silent discharge, typically has at least one dielectric (e.g. glass, quartz or ceramic) between the electrodes. DBDs are generally operated in one of the planar or cylindrical configurations shown in Figure 3.2.

When the local electron density at certain locations in the discharge gap reaches a critical value, a large number of separate and short-lived current filaments are formed, also referred to as microdischarges. These bright, thin filaments are statistically distributed in space and time and are formed by channel streamers with nanosecond duration [101]. When a microdischarge reaches the

dielectric, it spreads into a surface discharge and the accumulation of the transferred charge on the surface of the dielectric barrier reduces the electric field. As the electric field further reduces, electron attachment prevails over ionization and the microdischarges are extinguished. When the polarity of the AC voltage changes, the formation of a microdischarge is repeated at the same location if the electron density again reaches a critical value necessary for electrical breakdown. Therefore, the use of the dielectric in the discharge zone has two functions: (1) limiting the charge transferred by an individual microdischarge, thereby preventing the transition to an arc discharge, and (2) spreading the microdischarge over the electrode surface which increases the probability of electron–molecule collisions with bulk gas molecules [101]. This type of arrangement is often referred to as a volume discharge [102].

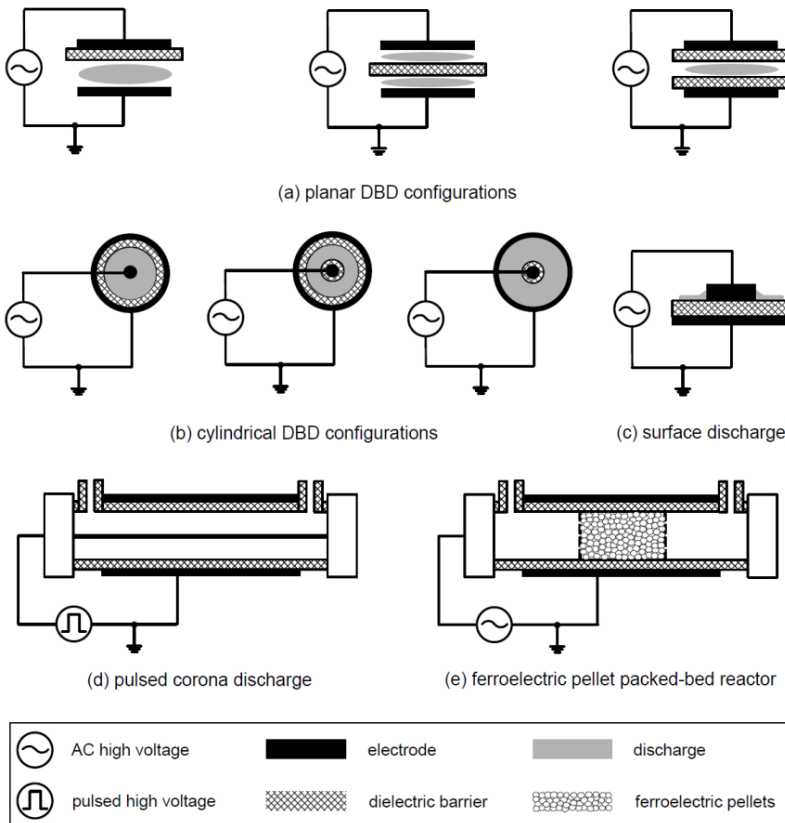


Figure 3.2 Illustrations of various NTP reactor configurations.

Another type of arrangement to generate NTP in a DBD is the surface discharge [102] (Figure 3.2(c)). Here for example, a series of strip electrodes are attached to the surface of a high-purity alumina ceramic base. A film like counter electrode is embedded in the inside of the alumina ceramic base and functions as an induction electrode. The ceramic can be either planar or cylindrical [103, 104]. When an AC voltage is applied between the strip electrodes and the embedded counter electrode, a surface discharge starts from the peripheral edges of each discharge electrode and stretches out along the ceramic surface. The surface discharges actually consist of many nanosecond surface streamers. In another configuration to generate a surface discharge, strip electrodes can be placed on the inner surface of a cylindrical surface discharge reactor [105]. In this set-up, a DBD discharge is also formed between the central rod electrode and the surface electrodes.

A *pulsed corona discharge* (Figure 3.2(d)) applies a pulsed power supply with a fast voltage rise time (tens of nanoseconds) to enable an increase in corona voltage and power without formation of sparks, which can damage the reactor and decrease the process efficiency. The required voltage level to energize the discharge depends on the distance between the electrodes, the pulse duration and the gas composition [106]. The duration of a pulse voltage is typically in the order of 100–200 ns to ensure that spark formation is prevented and that the energy dissipation by ions is minimal. The latter is important to enhance the energy efficiency of the system.

The electrode configuration of a pulsed corona discharge reactor can be either wire-to-cylinder [107-109] or wire-to-plate [110, 111], although the former allows a better spatial distribution of the streamers and a higher energy density deposition in the gas [107]. The pulsed corona discharge usually consists of streamers, for which the ionization zone fills the entire electrode gap (e.g. 10 cm). This is favorable in terms of up-scaling and reducing the pressure drop. However, up-scaling is hampered by the high demands on the electronics of large pulsed power voltage sources.

A *ferroelectric pellet packed-bed reactor* (Figure 3.2(e)) is a packed-bed reactor filled with perovskite oxide pellets. These reactors can have a parallel-plate or a coaxial configuration. Barium titanate (BaTiO_3) is the most widely used ferroelectric material for environmental purposes, owing to its high dielectric constant ($2,000 < \epsilon < 10,000$). Other used ferroelectric materials are NaNO_2 [112], MgTiO_4 , CaTiO_3 , SrTiO_3 , PbTiO_3 [113] and $\text{PbZrO}_3\text{-PbTiO}_3$ [114]. Application of an external electric field leads to polarization of the ferroelectric material and induces strong local electric fields at the contact points between the pellets and between the pellets and

electrodes. This enables the production of partial discharges in the vicinity of each contact point between pellets. The presence of ferroelectric pellets in the discharge zone is beneficial for a uniform gas distribution and electrical discharge but causes an increase in pressure drop over the reactor length.

Ferroelectric packed-bed reactors could serve as an alternative approach to enhance the energy efficiency, because the increase of the electric field will lead to a higher mean electron energy. Hence, the energetic electrons tend to form active species through dissociation and ionization, rather than forming less useful species through rotational and vibrational excitation. This leads to a more favorable consumption of the energy delivered, because electron-impact reactions are mainly responsible for the plasma chemistry that destroys environmental pollutants.

A *DC corona discharge* is generated at atmospheric pressure when sharp points, edges or thin wires are subjected to a sufficiently large electric field. This causes a local increase of the electric field in the vicinity of the sharp curvature of the electrode. This is e.g. the case for a point-to-plate or for a wire-to-cylinder configuration. The corona discharge is initiated by acceleration of free electrons and subsequent electron collision processes. Due to formation of electron/positive-ion pairs and their separating process, an electron avalanche is created which sustains the corona discharge. Visually, this discharge is characterized by a weak glow region around the sharp electrode. Depending on the polarity of this electrode, the formation mechanism of the electron avalanche physically differs [95].

When the electrode with the strongest curvature is connected to the positive output of the power supply, a positive DC corona discharge is generated (Figure 3.3(a)). Propagation of the discharge mainly depends on secondary photo-ionization processes around the sharp tip. The positive corona is characterized by the presence of streamers, i.e. numerous thin current filaments which are chaotically distributed in the gap. At a certain threshold voltage the discharge transitions from the stable corona mode to an unstable spark discharge regime.

In the case that the sharp electrode is connected to the negative output, a negative DC corona discharge is formed (Figure 3.3(b)). Here, impact ionization of gas molecules is generally responsible for the propagation of the discharge. As the applied voltage increases, the negative corona will initially form Trichel pulse corona, followed by pulseless corona and spark discharge [95]. However, certain research groups [115-121] have succeeded in generating a glow discharge at atmospheric pressure before the negative corona shifts to a spark discharge. Akishev et al. [120] applied a special electrode geometry and a fast gas flow to stabilize the discharge, hence delaying it from

creating sparks. Vertriest et al. successfully tested the multi-pin-to-plate reactor concept for VOC abatement [122]. Antao et al. recently reviewed the operating regimes of atmospheric pressure DC corona discharges and their potential applications [123].

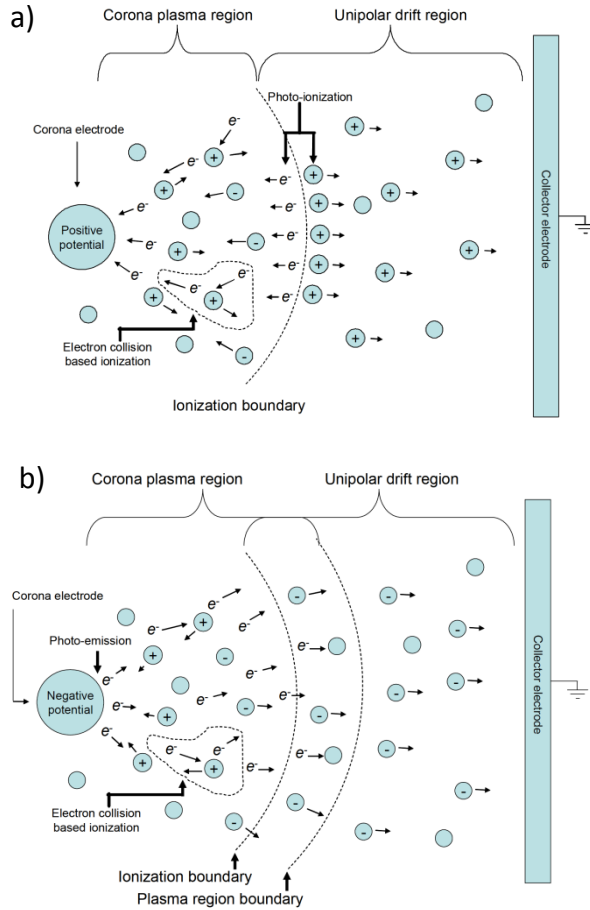


Figure 3.3 Schematic presentation of a positive (a) and negative corona discharge (b).

3.2.1.3 VOC abatement

Table 3.1 to Table 3.3 give an overview of published papers on VOC removal with NTP. For each reference, experimental conditions are

given, along with the maximum removal efficiency and the corresponding energy yield in g/kWh calculated as followed:

$$\text{Energy yield} = \frac{C_{in} \times \eta \times M \times 0.15}{\varepsilon} \quad (\text{Eq. 3.1})$$

where C_{in} is the initial concentration (ppm) of the VOC with molecular weight M (g/mol), η the maximum removal efficiency and ε the corresponding energy density (J/L), i.e. the energy deposited per unit volume of process gas. Each calculation is based on the fact that one mole of a gas occupies 24.04 L volume at standard ambient temperature and pressure (20°C and 101325 Pa).

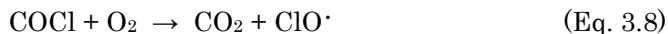
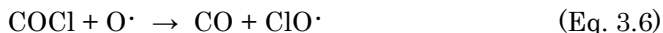
In what follows, particular attention is paid to the most studied target compounds, i.e. trichloroethylene, benzene and toluene. In Table 3.4, a selection has been made of other relevant, but less frequently studied VOCs. For more details about operating conditions and results, the reader can consult the corresponding references.

Trichloroethylene

As can be seen from Table 3.1, TCE is a chlorinated olefin which has attracted a lot of attention because it can be relatively easy removed by NTP without the addition of considerable energy. This results from the fact that reactive radicals, produced in the plasma discharge, easily add to the carbon-carbon double bond thereby initiating the oxidation process.

Evans et al. carried out an experimental and computational study of the plasma remediation of TCE in dry and wet Ar/O₂ mixtures using a silent discharge plasma [124]. They found that the ClO radical is an important intermediate which oxidizes TCE. In wet mixtures, ClO is partially consumed by OH radicals, resulting in a lower decomposition rate of TCE. They suggest a diagram of the dominant reaction pathways in plasma remediation of TCE giving CO, CO₂, COCl₂ and HCl as main by-products. According to the authors, the toxic by-product phosgene (COCl₂) can easily be removed from the exhaust stream by placing a water scrubber downstream of the plasma discharge. This is a cost effective post-treatment because removal of phosgene with their DBD reactor requires high energy. The authors propose the following reactions as the dominant degradation pathway for TCE in dry Ar/O₂ mixtures:

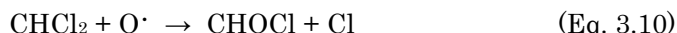




The ClO radical rapidly back-reacts with TCE leading to the formation of phosgene and methylchloride by the following reaction:



Methylchloride then quickly reacts with oxygen in the subsequent reaction:



In wet mixtures, two additional species can be produced by reaction of OH with TCE, $\text{CHCl}_2\text{-COCl}$ (dichloroacetylchloride; DCAC) and CHCl_2 .

DCAC is detected as main by-product of TCE decomposition with a pulsed corona discharge by Kirkpatrick et al.. They suggest the reaction of TCE with ClO radicals leading to the formation of DCAC under dry conditions, as follows [125]:



Under humid conditions the formation of DCAC is suppressed, suggesting that ClO radicals are quenched by OH radicals by the reaction:



Cl radicals can further attack DCAC, leading to the formation of CO, HCl, CCl_4 , CHCl_3 and COCl_2 as final products.

The effect of temperature on the removal chemistry and by-product formation of TCE is studied by Hsiao et al. [126]. Experiments, carried out with a pulsed corona and a DBD reactor, have shown that the removal of TCE and the formation of CO_x depends on temperature but not on reactor type. Moreover, higher temperatures cause a decrease in energy yield for TCE. The formation of by-products (CO, CO_2 , COCl_2 , HCl and DCAC) is almost the same as found by Evans et al. [124].

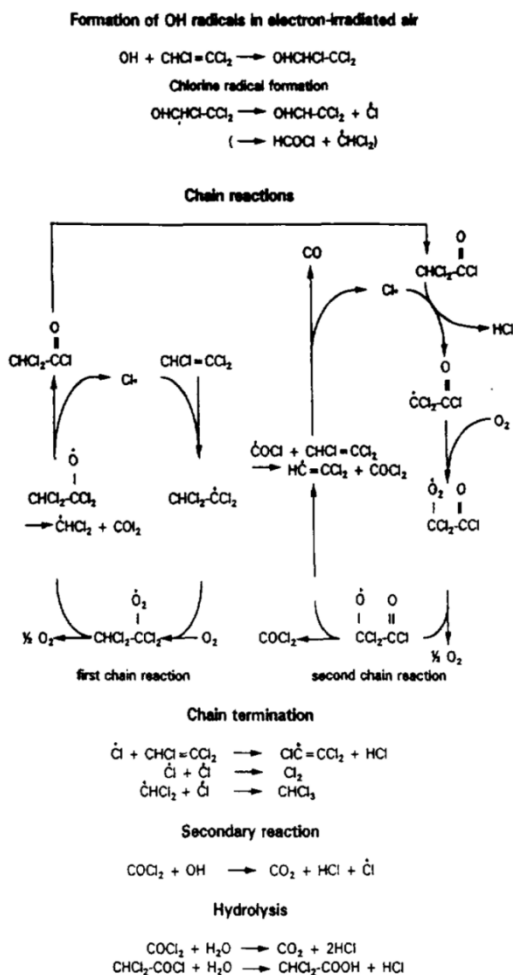
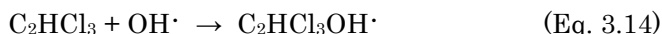


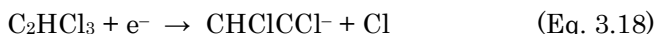
Figure 3.4 TCE decomposition mechanism [54].

Prager et al. [127] report the degradation of TCE with electron beam treatment. They found CO, HCl, COCl₂, DCAC and CHCl₃ as main by-products next to traces of CCl₄ and CCl₃-COCl (trichloroacetylchloride; TCAA). In the proposed degradation mechanism (Figure 3.4), OH radicals add to the double bond of TCE forming OH adducts. These adducts decompose and produce chlorine radicals or to a minor extent dichloromethyl radicals. Next, chlorine radicals add to the double bond and in a subsequent reaction with oxygen, the corresponding peroxy radical is formed. In a bimolecular reaction step, molecular oxygen and alkoxy radicals are formed, which fragmentate to DCAC and chlorine which in turn reenters the first

chain reaction. In a second chain reaction, DCAC is further decomposed to HCl, COCl₂ and CO. To minimize the formation of chloroacetic acids and phosgene, a wet scrubbing system is installed downstream of the electron beam system. Hakoda et al. also conclude that TCE decomposition with electron beam proceeds via a Cl radical addition chain reaction induced by OH radicals via the following reactions [128, 129]:



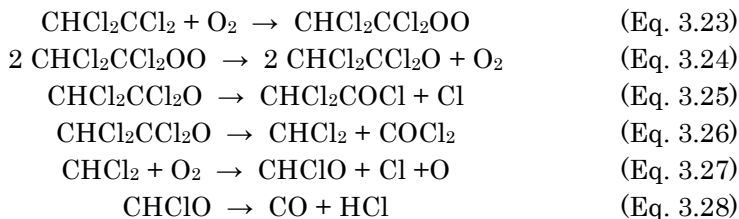
Vitale et al. examined the effect of a carbon-carbon double bond on electron beam treatment of TCE [130]. The primary decomposition products found in their study are CO, CO₂, COCl₂, DCAC and HCl. Chloroform and TCAA were found as minor decomposition products. These researchers propose a reaction pathway in which dissociative electron attachment is believed to be the primary initiation step. This reaction produces chlorine radicals and a doubly chlorinated ethylene anion:



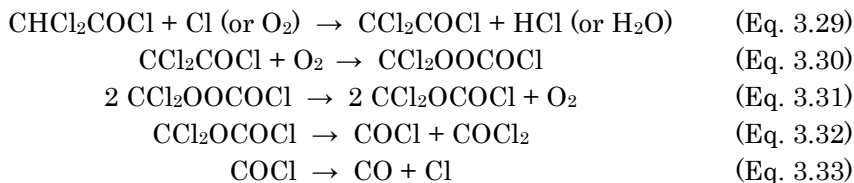
In a study by Yamamoto et al., the pronounced decomposition of TCE in dry nitrogen also strongly argues for dissociative electron attachment as the first stage in the decomposition of TCE [100]. Vitale et al. propose that the chlorinated ethylene anion will likely decompose by direct oxidation:



Then, in a secondary autocatalytic radical reaction, chlorine radicals add to the least substituted carbon atom of the double bond of TCE resulting in the start of a chlorine radical chain reaction [131, 132]. Bertrand et al. [133] suggest that addition to the least chlorinated site is favored over addition at the more chlorinated site by at least a factor 8. A possible chlorine addition reaction mechanism for the favored reaction is as follows:



DCAC decomposes to form HCl, COCl₂ and chlorinated radicals through the following reaction:



Phosgene may further decompose through Cl abstraction by chlorine, oxygen or other radicals forming CO and Cl₂ or Cl radicals. The TCE removal rate is reduced by the presence of reaction products such as phosgene, HCl and DCAC through scavenging of electrons in the plasma which could otherwise initiate more dissociative electron attachment reactions of TCE.

The study of Penetrante et al. shows that for small initial concentrations of TCE in dry air, the reaction with O radicals and electrons seems to be the likely primary decomposition mechanism [134]. These reactions initiate the detachment of Cl radicals, which in turn decompose more TCE molecules by Cl radical addition to the carbon-carbon double bond causing a chain reaction as proposed by Vitale et al. [130].

Futamara and Yamamoto [135] have applied a pulsed corona and a ferroelectric (BaTiO₃) packed-bed reactor for TCE removal. In wet nitrogen, dichloromethane, chloroform, pentachloroethane, carbon tetrachloride, 1,1,2,2- and 1,1,1,2-tetrachloroethanes and tetrachloroethylene are detected as major by-products for the packed-bed reactor by using GC-MS (Gas Chromatography-Mass Spectrometry). Chloro- and dichloroacetylenes, (Z)- and (E)-1,2-dichloroethylenes, and 1,1,2-trichloroethane are obtained as minor by-products. With a pulsed corona reactor, 1,1,2-trichloroethane is the main by-product along with tetrachloroethylene, (Z)-1,2-dichloroethylene and negligible amounts of polychloromethanes. When air is used as carrier gas for the decomposition with the packed-bed reactor, only phosgene could be detected. For both reactors and for both carrier gases CO, CO₂, NO_x and N₂O are also

formed as by-products. Formation of DCAC is however not observed in aerated conditions, which is in contrast with previous mentioned studies. The authors propose a plausible reaction mechanism under deaerated conditions. In the presence of O₂, they suggest that triplet oxygen molecules scavenge intermediate carbon radicals derived from TCE decomposition in an autoxidation process. Unstable alkylperoxy radicals are generated and further oxidatively decompose to render CO and CO₂, as shown in the following general reaction:



Urashima and Chang suggest that electron impact processes produce C, H, N radicals and negative ions. According to the authors the oxidation processes will take place directly by radicals or via oxidation of negative ions [136]. They propose a mechanism of TCE destruction based on 162 reactions [137].

In a study performed by Han et al., the effect of oxygen concentration on by-product distribution is examined [138]. TCE decomposition efficiency improves with decreasing oxygen content except for 0% oxygen. The formation of DCAC is maximal for 2% oxygen, while TCAA formation decreases with decreasing oxygen concentration. They suggest that oxygen species, like O(¹D) or other states in the discharge, react more strongly with the precursor of DCAC (CHCl₂-CCl₂•) than that of TCAA (CCl₃-CH•). When nitrogen is used as carrier gas, the GC-MS could detect HCl, Cl₂, C₂H₂Cl₂, CHCl₃, CCl₄ and C₂HCl₅ as by-products. The authors suggest that collisions between TCE and electrons and (or) N₂ excited species (N₂^{*}) generate chlorine radicals. The main decomposition mechanism is considered to be the chlorine radical chain reaction as mentioned before by other authors.

Table 3.1 Overview of published papers on TCE removal with NTP.

Plasma type	Carrier gas	Flow rate (mL/min)	Concentration range (ppm)	Maximum removal efficiency (%)	Energy density (J/L)	Energy yield (g/kWh)	Ref.
DBD	Ar/O ₂	10 ⁴	500	> 99	50	193.5*	[124]
	Ar/O ₂ /H ₂ O			90	150	58*	
DBD ^a	air	700	250	> 99	140	34.6*	[139]
DBD ^b	humid air	500	150 – 200	> 99	480	8.1*	[140]
DBD	dry air	400	1000	95	150	122.5*	[141]
			100	> 99	135	14.3*	
DBD	dry air	400	100	99	200	9.6*	[142]
DBD	dry air	2000	250	98	120	39.5*	[143]
DBD	dry air	510	430	> 99	350	23.8*	[144]

* Calculated from data retrieved from reference

Table 3.1 Overview of published papers on TCE removal with NTP (continued).

Plasma type	Carrier gas	Flow rate (mL/min)	Concentration range (ppm)	Maximum removal efficiency (%)	Energy density (J/L)	Energy yield (g/kWh)	Ref.
DBD	humid air	200 – 510	750	98 – 99	2400	6*	[145]
DBD Surface discharge	dry air	400	1000	99 95 – 99	1400 1150	13.7* 16.3*	[146]
DBD Pulsed corona	dry air	2 x 10 ⁴	160	85 90	100 50	26.3* 55.7*	[126]
Pulsed corona ^a	humid air	–	1000	90	100	174.1*	[125]
Pulsed corona	dry air	–	100	80	50	30.9	[72]

^a Copper rod inner electrode

^b Inner electrode made of sintered metal fibres

* Calculated from data retrieved from reference

Table 3.1 Overview of published papers on TCE removal with NTP (continued).

Plasma type	Carrier gas	Flow rate (mL/min)	Concentration range (ppm)	Maximum removal efficiency (%)	Energy density (J/L)	Energy yield (g/kWh)	Ref.
Positive corona	dry air	1500	100	67	580	2.2*	[147]
DC negative glow discharge	humid air	10 ⁶	120	47	37	29.5*	[122]
Capillary tube discharge reactor	dry air	1000	452	80	–	–	[148]
DC negative glow	dry air	500	500	85	240	36.4*	[149]
DC negative glow	humid air	500	580	90	520	20.6*	[150]

^a Pulsed corona discharge with reticulated vitreous carbon electrodes

* Calculated from data retrieved from reference

Benzene

Benzene has attracted attention for NTP removal because it is a carcinogenic compound that has detrimental effects on human health. Table 3.2 summarizes published papers on benzene removal with NTP.

In order to minimize operation costs for NTP removal it is important to optimize the operation conditions. Ogata et al. investigated the effects of properties of ferroelectric materials, AC frequency, initial concentration of benzene and the concentration of O₂ in the background gas for the removal of benzene in air using a ferroelectric packed-bed reactor [113]. Under dry conditions benzene removal results in a low CO₂-selectivity and in the formation of various by-products, such as CO, C₂H₂, N₂O, NO and NO₂.

To improve this technique for practical applications, Ogata et al. have studied the effect of water vapor on the removal of benzene with a ferroelectric packed-bed reactor [151]. They suggest that a portion of the lattice oxygen species in BaTiO₃ pellets are deactivated by adsorption of H₂O on the surface of the pellets. This results in a suppressed formation of CO and N₂O, a higher CO₂-selectivity and a lower decomposition of benzene. These observations are confirmed by Kim et al. [152]. The negative effect of humidity on benzene removal is ascribed to the interaction of water vapor with the surface of BaTiO₃ pellets which may alter the surface state. As a consequence, plasma properties may be negatively affected [153], resulting in slower chemical destruction pathways.

Cal et al. [154] investigated the decomposition of benzene in a DBD reactor as a function of the relative humidity (RH) without the presence of ferroelectric pellets. In both dry and wet gas streams, near complete destruction (> 99.9%) of benzene is achieved and no intermediate hydrocarbons are observed with GC-MS. However, in wet gas streams the mineralization degree is greatly improved compared to dry air. Unfortunately, at high RH, a polymeric film is produced on the dielectric plates which slowly decreases the removal efficiency of benzene through time.

Lee et al. also used a DBD discharge to decompose 100 ppm of benzene in air [155]. The authors suggest a plausible reaction mechanism that includes the formation of all by-products detected by GC-MS and FT-IR (Fourier Transform - Infrared) spectroscopy. According to the authors, the plasma can produce O radicals from O₂, which can react with benzene to form CO₂, H₂O and benzene cation by a series of reactions. Benzene could directly be decomposed by the plasma to form phenol and benzenediol. The plasma is also capable of decomposing stable CO₂ to form CO radicals that would add to phenol. This leads to the formation of secondary products such as benzaldehyde and benzoic acid. Finally, decomposition of H₂O by the

discharge forms H and OH radicals which lead to the formation of benzene, phenol and benzenediol.

Also, Ye et al. have investigated the feasibility of benzene destruction with a DBD discharge [156]. Experiments are carried out with a laboratory scale and a scale-up DBD reactor. With the former reactor, high removal efficiencies are obtained with lower flow rates, lower initial concentrations and higher input power (Figure 3.5). In contrast, higher initial concentration and input power provide a high energy efficiency for benzene removal. For the scale-up reactor, adding DBD systems in series can enhance the decomposition efficiency to a large extent. However, after a certain treatment time brown polymeric deposits are formed on the inside wall of the reactor which can finally lead to mechanical failure of the dielectric due to thermal energy built up. The deposit can be removed by passing air through the reactor at 6 kV for several minutes. GC-MS analysis revealed that phenol, hydroquinone and nitrophenol are the main products contained in the deposition. The feasibility study shows that multiple DBD systems in series can enhance the removal efficiency of benzene to a large extent and proves that DBD treatment is competitive with other technologies although formation of solid residues and aerosol particles are issues that must be solved to secure an effective operation.

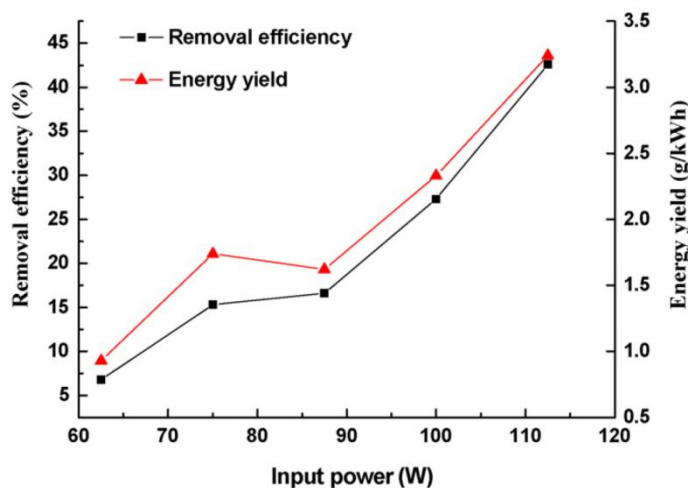
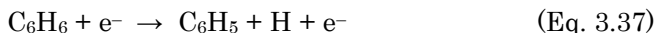
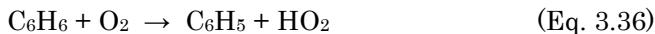


Figure 3.5 Effect of input power on benzene removal efficiency and energy yield [83].

In a study by Jiang et al. [157], a DC microhollow cathode glow discharge is applied to remove 300 ppm benzene from dry air. The authors use a zero-dimensional plasma chemistry code (KINEMA)

[158] to model the benzene dissociation mechanism in a benzene/dry air mixture plasma. Important dissociation reactions predicted by the model are:



Modeling results reveal that the dominant dissociation reactions for benzene destruction in the DC glow discharge are atomic oxygen impact reactions. They suggest that the benzene destruction rate and efficiency are limited due to atomic oxygen losses in the boundary layer of the dielectric walls, which confines the discharge in the direction perpendicular to the gas flow direction.

Satoh et al. have applied a positive DC corona discharge between a multi-needle and a plane electrode for the removal of 300 ppm benzene in different N_2/O_2 mixtures [158]. Analysis of the exhaust stream is performed with FT-IR and shows C_2H_2 , HCN, NO and HCOOH as intermediate products and CO_2 as an end product. At low oxygen concentrations (0.2%) benzene is primarily converted into CO_2 via CO, whereas at high oxygen concentrations (20%) benzene is converted into CO_2 via CO and HCOOH. After treatment, benzene fragments are deposited on the plane electrode and discharge chamber at low oxygen concentrations. It is found that an increase in the oxygen concentration inhibits the decomposition of benzene, which is also the case with a DBD discharge [159]. However, with a packed-bed reactor, a higher N_2/O_2 ratio improves the decomposition of benzene [113] which indicates that the effect of the amount of oxygen in the background gas depends on the type of discharge.

Kim et al. [160] also investigated the influence of oxygen and found an optimum O_2 concentration of 3–5% for benzene removal with a DBD discharge. Further increase of the oxygen concentration drastically decreases the decomposition efficiency. They suggest that higher benzene destruction at lower O_2 partial pressure is due to the contribution of N radicals and excited N_2 molecules. Comparison of the reaction rate constants indicate that the reaction with $\text{N}_2(\text{A}^3\Sigma^+_u)$ is more plausible and is even faster than the reaction with O radicals ($k = 1.6 \times 10^{-14} \text{ cm}^3 \text{ molecule}^{-1} \text{ s}^{-1}$). However, as O_2 partial pressure increases, quenching of $\text{N}_2(\text{A}^3\Sigma^+_u)$ becomes significant [161] and the rate of reaction slows down. In addition, more O atoms are produced due to direct electron-impact dissociation and collision dissociation by $\text{N}_2(\text{A}^3\Sigma^+_u)$, but at the same time O atoms are also consumed in the formation of O_3 . Because the gas-phase reaction between ozone and benzene is very slow ($k = 1.72 \times 10^{-22} \text{ cm}^3 \text{ molecule}^{-1} \text{ s}^{-1}$), it does not contribute to the decomposition of benzene.

$C_6H_6 + N_2(A^3\Sigma^+_u) \rightarrow \text{products}$	1.6×10^{-10}	(Eq. 3.38)
$C_6H_6 + N \rightarrow \text{products}$	$< 10^{-15}$	(Eq. 3.39)
$N_2(A^3\Sigma^+_u) + O_2 \rightarrow N_2 + O_2$	2.4×10^{-12}	(Eq. 3.40)
$N_2(A^3\Sigma^+_u) + O_2 \rightarrow N_2 + 2 O$	2.5×10^{-12}	(Eq. 3.41)

In a recent study by Dey et al. [162] the formation of by-products of benzene oxidation in a Ar/O₂ flow with a DBD reactor is carefully analyzed with GC-FID (Flame Ionization Detector) and GC-MS. A plausible sequential reaction mechanism is given to rationalize the observation of the various by-products. In the gas phase, only phenol and biphenyl are detected at a maximum total benzene conversion of 3%. GC analysis of an ethanolic solution of the polymeric deposit on the dielectric surface reveals the presence of substituted phenols besides phenol and biphenyl (Figure 3.6). It is suggested that the intermediate phenyl radical plays the role of the primary precursor.

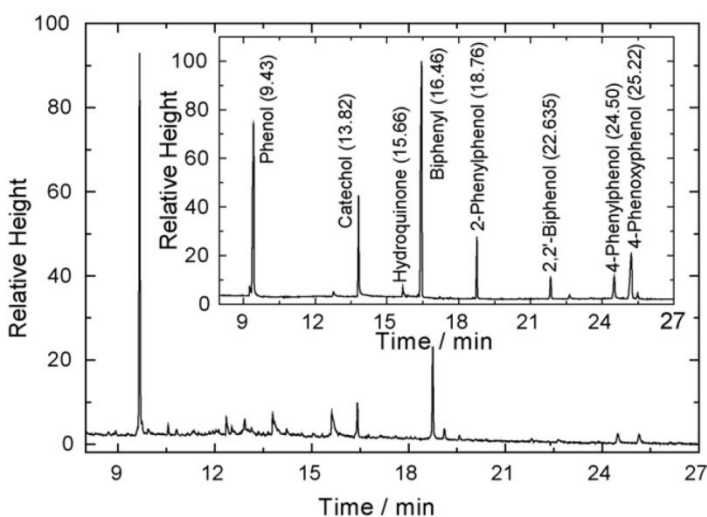


Figure 3.6 Gas chromatogram of surface washed ethanolic solution from 10 min DBD discharge. Inset: Gas chromatogram of ethanolic solution of various standards employed [89].

Table 3.2 Overview of published papers on benzene removal with NTP.

Plasma type	Carrier gas	Flow rate (mL/min)	Concentration range (ppm)	Maximum removal efficiency (%)	Energy density (J/L)	Energy yield (g/kWh)	Ref.
DBD	air (0–90% RH)	500 – 2000	500 – 2700	> 99.9	2000 – 3000	–	[154]
DBD	dry air	200	100	90	680	1.5*	[155]
DBD	humid air	10 ⁴	276	> 99	810	3.9*	[156]
DBD	dry air (5% O ₂)	4000 – 5000	200	75	305	5.7*	[160]
DBD	Ar/2–40% O ₂	275	500 – 10 ⁴	30	–	–	[162]
DBD	dry air	250	300 – 380	11	170	2.5	[163]
DBD	dry air	500	105	35	360	1.2*	[164]
DBD	dry air	400	200	70	3150	0.5*	[165]

* Calculated from data retrieved from reference

Table 3.2 Overview of published papers on benzene removal with NTP (continued).

Plasma type	Carrier gas	Flow rate (mL/min)	Concentration range (ppm)	Maximum removal efficiency (%)	Energy density (J/L)	Energy yield (g/kWh)	Ref.
DBD	dry air	4000	203 – 210	40	370	2.6*	[166]
DBD	dry air	1667	407	50	–	–	[167]
DBD	dry air	35 x 10 ³	250	50	230	6.3*	[168]
Pulsed corona	dry air	100	300	75	30	86.1*	[169]
Positive DC corona ^a	dry air	–	300	> 99	–	–	[158]
DC glow ^b	dry air	100	296	90	4000	0.9*	[157]

^a Corona reactor is sealed after addition of benzene/air mixture

^b Microhollow cathode

* Calculated from data retrieved from reference

Table 3.2 Overview of published papers on benzene removal with NTP (continued).

Plasma type	Carrier gas	Flow rate (mL/min)	Concentration range (ppm)	Maximum removal efficiency (%)	Energy density (J/L)	Energy yield (g/kWh)	Ref.
BaTiO ₃ -packed bed	dry air	200	200	> 99	3000	0.8*	[113]
BaTiO ₃ -packed bed	humid air (0.5% H ₂ O)	200	200	75	1800	1*	[165]
BaTiO ₃ -packed bed	dry air	203 – 210	200	65	400	3.7*	[170]
BaTiO ₃ -packed bed	dry air	–	110	98	130	9.4*	[171]
BaTiO ₃ -packed bed	dry air	200	200	60	600	2.3*	[172]

* Calculated from data retrieved from reference

Table 3.2 Overview of published papers on benzene removal with NTP (continued).

Plasma type	Carrier gas	Flow rate (mL/min)	Concentration range (ppm)	Maximum removal efficiency (%)	Energy density (J/L)	Energy yield (g/kWh)	Ref.
BaTiO ₃ -packed bed ^a	humid air (0.5% H ₂ O)	200	200	95	1600	1.4*	[173]
Pulsed corona	humid air (50% RH)	16.7 x 10 ³	200	24	173	3.2*	[174]
DBD	dry air	400	100	39.1	9.9	45.4*	[175]
Surface/packed bed discharge	dry air	500	400	67	400	8.4	[176]
DBD packed with glass beads (coil electrode)	dry air	500	400	67	–	–	[177]

^a Glass layer between two concentric electrodes

* Calculated from data retrieved from reference

Table 3.2 Overview of published papers on benzene removal with NTP (continued).

Plasma type	Carrier gas	Flow rate (mL/min)	Concentration range (ppm)	Maximum removal efficiency (%)	Energy density (J/L)	Energy yield (g/kWh)	Ref.
DBD ^a	dry air	250	100	82	650	1.5*	[178]
DBD packed with glass beads	dry air	200	240	60	255	6.5*	[179]

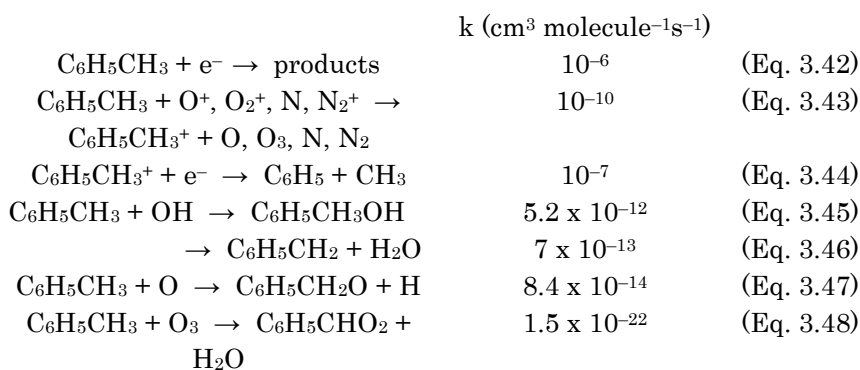
^a Inner electrode made of sintered metal fibres

* Calculated from data retrieved from reference

Toluene

Table 3.3 tends to give an overview of published work on toluene removal with the aid of NTP. Toluene can be regarded as the most studied VOC for abatement on laboratory scale. Therefore only a selection of papers will be discussed here. Other references can be found in Table 3.4.

Kohno et al. [148] have applied a DC capillary tube discharge reactor and investigated the effect of gas flow rate, initial toluene concentration and reactor operating conditions. According to the authors, the following destruction process can be expected in a NTP environment:



FT-IR spectroscopy detects CO_2 , CO , NO_2 and H_2O as gaseous by-products and a significant amount of brown particles are deposited at the exit of the reactor. It is suggested that CO_2 and CO mainly form carbon and nitrogen hydride bonded aerosol particles and tars.

CO_2 and H_2O are observed as main reaction products by Mista et al. [180]. They also detect a thin polymeric film (brown residues) covering the discharge electrode and dielectric layer. Operation at higher energy densities can successively be applied to oxidize the condensed polymeric species to CO_2 . Machala et al. [181] suggest that formation of aerosols including peroxy-acetyl-nitrates species (PANs) may be possible during toluene removal through a mechanism that is similar to formation of photochemical smog in the atmosphere. In pure nitrogen [182], GC-MS analysis showed that N_2 plays a major role in the polymerisation process through the formation of C-N=C and C-(NH)-bonds. A proposal of the polymerisation process is given to explain the formation of micrometric sized particles in the plasma reactor.

In [183] a wire plate DBD has been used to examine the humidity effect on toluene decomposition. A maximum removal efficiency of

73% was achieved in a gas stream containing 0.2% H₂O in N₂ with 5% O₂. This controlled humidity is governed by two opposite effects: as humidity increases, more H₂O molecules collide with high-energy electrons and form OH radicals, resulting in a higher removal efficiency. On the other hand, the electronegative characteristic of H₂O limits the electron density in the plasma and quenches activated chemical species, as concluded by Van Durme and coworkers [184]. Kim et al. have confirmed that 5% O₂ is the optimum oxygen partial pressure in a dry nitrogen stream, as is the case for benzene [160].

Recently, Schiorlin et al. [185] have tested three different corona discharges (positive DC, negative DC, positive pulsed) for toluene removal and have observed that process efficiency increases in the order positive DC < negative DC < positive pulsed. By investigating the effect of humidity on the removal efficiency, it is concluded that for both negative DC and positive pulsed corona, OH radicals are involved in the initial stage of toluene oxidation. When the RH was greater than 60%, removal efficiency slightly drops due to saturation and inhibition of the OH radical forming reactions, i.e. dissociation of H₂O molecules induced by interaction with electrons or by reaction with O(¹D).

A positive DC corona discharge has been applied by Van Durme et al. in order to abate toluene from indoor air and to unravel the degradation pathway [184]. The removal of toluene is achieved with a characteristic energy density of 50 J/L. Figure 3.7 shows that partially oxidized intermediates are formed under the applied conditions. By determining the effect of humidity, the authors find out that OH radicals play a major role in the oxidation kinetics due to initiation by H-abstraction or OH-addition. The by-products detected by GC-MS consist of benzaldehyde, benzylalcohol, formic acid, nitrophenols and furans.

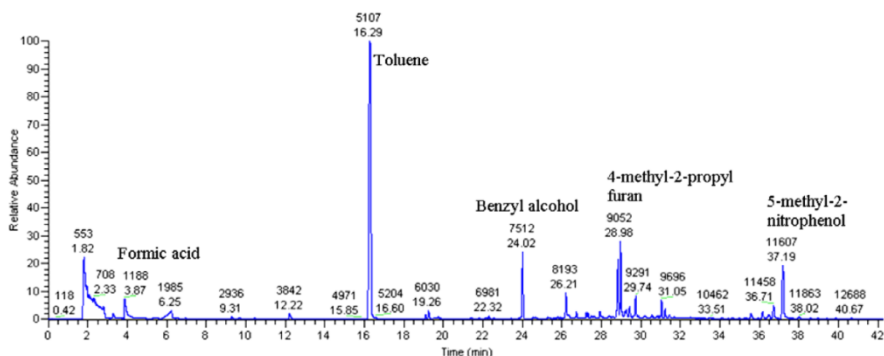


Figure 3.7 Chromatogram of GC-MS analysis for the identification of toluene degradation products [111].

Table 3.3 Overview of published papers on toluene removal with NTP.

Plasma type	Carrier gas	Flow rate (mL/min)	Concentration range (ppm)	Maximum removal efficiency (%)	Energy density (J/L)	Energy yield (g/kWh)	Ref.
DBD	dry air (5% O ₂)	4000 – 5000	200	75	310	6.6*	[160]
DBD	N ₂ dry air	2000	400	21 23	240	4.7* 5.2*	[182]
DBD	N ₂ /5% O ₂ (0.2% RH)	100	50	73	600	0.8*	[183]
DBD	humid air (55% RH)	1000	100	46	2100	0.3*	[186]
DBD packed with glass pellets	dry air	600	1100	75 – 80	1000	11.5*	[187]

Table 3.3 Overview of published papers on toluene removal with NTP (continued).

Plasma type	Carrier gas	Flow rate (mL/min)	Concentration range (ppm)	Maximum removal efficiency (%)	Energy density (J/L)	Energy yield (g/kWh)	Ref.
DBD packed with glass pellets	humid air (95% RH)	500	500	91	18.5	11.5	[188]
DBD packed with glass beads	dry air	315	240	36	172	6.8*	[189]
Multicell DBD packed with glass beads ^a	dry air	1000	110	72	2502	0.4*	[190]
DC back corona	dry air	100 – 750	5 – 200	93	2400	0.4*	[180]

^a Three cells

* Calculated from data retrieved from reference

Table 3.3 Overview of published papers on toluene removal with NTP (continued).

Plasma type	Carrier gas	Flow rate (mL/min)	Concentration range (ppm)	Maximum removal efficiency (%)	Energy density (J/L)	Energy yield (g/kWh)	Ref.
Pulsed corona	dry air	450	500	> 99	1000	6.7*	[185]
Positive corona	humid air (26% RH)	10 ⁴	0.5	80	65	0.1*	[184]
BaTiO ₃ -packed bed	dry air	–	101	95	125	–	[171]
Dielectric capillary plasma electrode discharge	air	–	266.5	> 99	3500	1*	[191]
Capillary tube discharge reactor	dry air	350	1246	86	–	–	[148]

* Calculated from data retrieved from reference

Table 3.3 Overview of published papers on toluene removal with NTP (continued).

Plasma type	Carrier gas	Flow rate (mL/min)	Concentration range (ppm)	Maximum removal efficiency (%)	Energy density (J/L)	Energy yield (g/kWh)	Ref.
DBD	dry air	100	160	48	9	115.8*	[192]
Glow discharge	air (18% RH)	–	15	85	15	–	[193]
DBD	dry air	8666	270	35	570	2.2*	[194]
DBD	dry air	333	320	70	650	5	[195]
DBD	dry air	500	107	82	80	14.9*	[196]
DBD	dry air	300	100	28	192	2*	[197]
DBD ^a	humid air	250	100	100	650	2*	[178]

^a Inner electrode made of sintered metal fibres

* Calculated from data retrieved from reference

Table 3.3 Overview of published papers on toluene removal with NTP (continued).

Plasma type	Carrier gas	Flow rate (mL/min)	Concentration range (ppm)	Maximum removal efficiency (%)	Energy density (J/L)	Energy yield (g/kWh)	Ref.
Pulsed corona	humid air (57% RH)	2.5×10^6	70	74	92	7.7	[198]
DBD	dry air	1	160	58	760	1.6*	[199]
DBD	humid air (50% RH)	200	50	74	1527	0.3*	[200]
DBD	dry air	510	50	56	360	1*	[201]

Table 3.4 Published papers on removal of other VOCs with NTP.

Target compound	Reference
Acetaldehyde	[175, 202-209]
Acetone	[104, 207, 210-217]
Acetylene	[218, 219]
Dichloromethane	[210, 220-224]
Formaldehyde	[225-229]
Methane	[157, 205, 230-236]
Methanol	[126, 134, 224, 237-239]
Propane	[107, 207, 240-244]
Propene	[107, 207, 218, 242, 245, 246]
Styrene	[247-254]
Tetrachloromethane	[134, 210, 222, 255-258]
Xylene	[108, 191, 213, 259-261]

3.2.2 Combined with catalyst

3.2.2.1 What is plasma-catalysis?

Many studies have shown that NTP is attractive for the removal of NO_x, SO_x, odours and VOCs. There is however a consensus among researchers that application of NTP for VOC abatement suffers from 3 main weaknesses, i.e. incomplete oxidation with emission of harmful compounds (CO, NO_x, other VOCs), a poor energy efficiency and a low mineralization degree.

The combination of NTP with heterogeneous catalysts can be divided in two categories depending on the location of the catalyst: in-plasma catalysis (IPC) and post-plasma catalysis (PPC). The latter is a two stage process where the catalyst is located downstream of the plasma reactor while the former is a single stage process with the catalyst being exposed to the active plasma. In literature, several different terms and corresponding abbreviations have already been proposed to represent IPC and PPC. For in-plasma catalysis, one can find among others: plasma-driven catalysis (PDC) [93], in-plasma catalysis reactor (IPCR) [262], single-stage plasma-catalysis (SPC) [263], plasma and catalyst integrated technologies (PACT) [264] or combined plasma catalysis (CPC) [265, 266]. For PPC, the following terms have been proposed: plasma-enhanced catalysis (PEC) [93], post-plasma catalysis reactor (PPCR) [262], two-stage plasma catalysis (TPC) [263].

In plasma–catalysis, synergetic effects are related to the activation of the catalyst by the plasma. Activation mechanisms include ozone, UV, local heating, changes in work function, activation of lattice oxygen, adsorption/desorption, creation of electron–hole pairs and direct interaction of gas–phase radicals with adsorbed pollutants [160].

The plasma–catalyst interactions described in the following paragraphs contribute to one or more of these catalyst activation mechanisms. The presented experimental findings, applying to specific working conditions, may appear as scattered pieces of information. Indeed further research is needed to connect the loose ends and unravel the detailed mechanisms. However, it is meaningful to try and extract some general pathways at this stage.

Influence of the catalyst on the plasma processes

Discharge mode

The physical properties of a discharge will be affected if a catalyst is introduced into the discharge zone. When for example a dielectric surface is introduced in the gap of a streamer–type discharge, the discharge mode at least partially changes from bulk streamers to more intense streamers running along the surface (surface flashover) [169]. Similar field effects can lead to higher average electron energies when the discharge zone is filled with ferroelectric pellets, leading to a more oxidative discharge [267]. Parameters that influence the effect of the packed bed on the discharge are the dielectric constant of the pellet material and the size and shape of the pellets. The dielectric constant affects the electric field in the void between the pellets and thereby the mean electron energy. With increasing pellet size the number of microdischarges decreases, but the amount of charge that is transferred per micro–discharge increases [268].

Reactive species production

Obviously, introducing a heterogeneous catalyst changes the physical characteristics of the discharge, so the chemical activity will be affected as well. Roland et al. [269] studied the oxidation of various organic substances immobilized on porous and non–porous alumina and silica catalysts and concluded that short–living active species are formed in the pore volume of porous materials when exposed to NTP. On the other hand, introducing a catalyst can reduce the concentration of ionic species [270]. However, this effect did not impair the catalyst’s role in reducing the emissions of ozone and carbon monoxide for this particular application (indoor air control).

Influence of the plasma on the catalytic processes

Catalyst properties

Non-thermal plasmas are used for catalyst preparation [271-276]. Plasma treatment of the catalyst enhances the dispersion of active catalytic components [277, 278] and influences the stability and catalytic activity of the exposed catalyst material [279]. The oxidation state of the catalyst can also be altered by NTP. For instance, when a Mn_2O_3 catalyst is exposed for a long time to a DBD plasma, X-ray diffraction spectra reveal the presence of Mn_3O_4 , a lower-valent manganese oxide with a larger oxidation capability. Due to plasma-catalyst interactions, less parent Ti-O bonds are found on TiO_2 surfaces after several hours of discharge operation [280]. Even new types of active sites with unusual properties may be formed [281], such as stable Al-O-O* with a lifetime exceeding more than two weeks, as observed in the pores of Al_2O_3 in IPC experiments [281]. Plasma exposure can result in an increase or decrease of the specific surface area or in a change of catalyst structure [277, 279, 282].

Adsorption

Adsorption processes play an important role in plasma-catalytic reaction mechanisms. If the catalyst has a significant adsorption capacity for pollutant molecules, it prolongs the pollutant retention time in the reactor. In the case of IPC, the pollutant concentration in the discharge zone is increased. The resulting higher collision probability between pollutant molecules and active species enhances the removal efficiency. Adsorption of VOC and active species increases with the porosity of the catalyst [283]. Under conditions where plasma-generated ozone is not effective in itself to destroy pollutants, high decomposition rates are obtained due to the adsorption of ozone on the catalyst surface and the subsequent dissociation into atomic oxygen species [284]. Humidity is a critical parameter in plasma-catalytic processes. The adsorption of water on the catalyst surface results in a decrease of the reaction probability of the VOC with the surface and therefore reduces the catalyst activity [285].

Thermal activation

Although gas heating will result in higher catalyst surface temperatures [163], the heating effect is in general too small to account for thermal activation of the catalyst. However, hot spots can be formed in packed-bed reactors as a result of localized heating by intense microdischarges that run between sharp edges and corners of

adjacent pellets. Increased catalyst temperatures can promote catalytic VOC removal [286].

Plasma-mediated activation of photocatalysts

In photocatalysis, VOCs are adsorbed on the surface of a porous semiconductor material that is exposed to UV radiation. The UV photons generate electron-hole pairs, inducing the subsequent oxidation of the adsorbed VOC by valence band holes. In a final step the oxidation products are desorbed. Among other photocatalysts (e.g. ZnO, ZnS, CdS, Fe₂O₃, WO₃), TiO₂ is one of the most efficient for the decomposition of a wide range of VOCs. Moreover, the combination of TiO₂ with NTP results in higher oxidation efficiencies and better selectivity to CO₂. For the anatase phase of TiO₂, having a bandgap of 3.2 eV, it takes a photon with a wavelength shorter than 388 nm to create an electron-hole pair. Although there are excited nitrogen states that emit light in this wavelength range, there is experimental evidence that photocatalysis induced by UV light from the plasma cannot explain the observed synergy in several hybrid plasma/TiO₂ systems reported in literature. For instance, Sano et al. [287] has detected no enhancement in acetylene conversion when the reactor walls are coated with TiO₂. Emission spectra of the surface discharge plasma with and without catalyst coating reveal that UV light from the plasma is absorbed by TiO₂, but the intensity is too weak for photoactivation. This observation has been confirmed by Huang et al. [288], who employed a wire-cylinder DBD reactor with a photocatalyst sheet stuck along the inner wall of the tube. Kim et al. have tested a DBD reactor packed with Ag/TiO₂ for benzene removal [289]. When O₂-benzene mixtures are diluted with argon, significantly higher decomposition efficiencies are observed compared to N₂ dilution. This result suggests that the role of UV light for photoactivation is negligible because light emission from excited argon ranges in the visible range (400 – 850 nm). However, other groups report that UV light emitted from the plasma can act as a source for activation of TiO₂ [155, 290, 291]. Subrahmanyam et al. suggest that the increased activity with sintered metal fibres modified with TiO₂ might be related to activation as well as to photocatalytic action in the presence of UV light emitted by the plasma discharge [139]. In some cases, TiO₂ shows plasma-induced catalytic activity under conditions where there is no or very little UV emitted by the plasma [289, 292]. Direct plasma activation has been observed when TiO₂ is exposed to an atmospheric pressure argon discharge at room temperature [293]. The question then arises how the plasma-exposed TiO₂ is activated, if not by UV photons. Different mechanisms to

bridge the TiO₂ band-gap by plasma-driven processes can be envisaged, but to date there is insufficient information to elaborate on the relative importance of electrons, ions, metastables, charging effects, surface recombination, etc.

3.2.2.2 Different types of catalysts

As in classical heterogeneous catalysis, the catalyst material can be introduced in the hybrid system in different ways for both IPC (Figure 3.8) and PPC: in the form of pellets (a so-called packed-bed configuration) [147, 267, 294-296], foam [183, 277, 297-299] or honeycomb monolith [270, 300-303], as a layer of catalyst material [304] or as a coating on the reactor wall [164, 287] or electrodes [139, 140, 305-309].

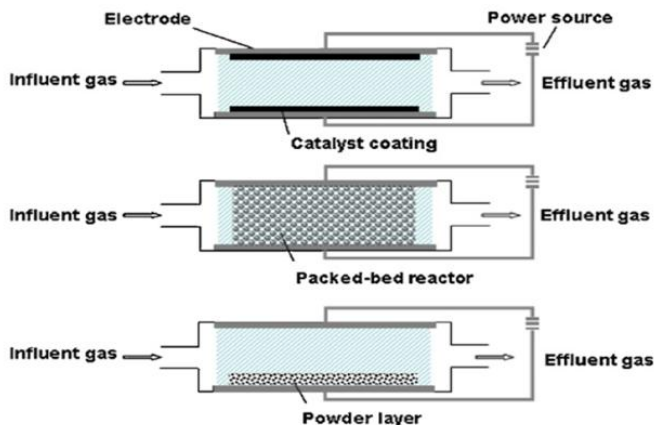


Figure 3.8 Most common catalyst insertion methods for IPC configuration [237].

Many catalysts have been tested for VOC abatement with IPC and PPC. Historically, the first materials tested were porous adsorbents placed inside the discharge region as in references [114, 310]. The idea is that, by introducing these materials, the retention time of VOC molecules would increase along with the probability of surface reactions with active chemical plasma species (electrons, radicals, ions, photons). Adsorbents that were used to achieve a more complete oxidation are γ -Al₂O₃ [269, 310-312] and zeolites or molecular sieves [141, 312-316]. Furthermore, these materials are coated or impregnated with (noble) metals such as silver, palladium, platinum, rhodium, nickel, molybdenum, copper, cobalt or manganese to provide

catalytic activity [146, 160, 282, 284, 286, 316-324]. Adsorbents also function as support for metal oxides [322, 325-332].

Extensive attention has been given during recent years to the use of photocatalysts, in particular to TiO₂. In most studies, TiO₂ is inserted in the discharge region in order to achieve activation through different mechanisms. This catalyst has also been coated with (noble) metals [152, 160, 284, 289, 292, 333, 334] and metal oxides [141, 142, 165, 335]. Additionally, it has been used as a coating on activated carbon filter [288] or fiber [336], on glass fibres [337, 338] or beads [155, 187, 290], nickel foam [339], silica gel pellets [164] and on UV lamp [340].

3.2.2.3 VOC abatement

Table 3.5 to Table 3.7 give a summary of literature on VOC removal with plasma-catalysis. For each paper catalyst information and operating conditions are presented along with the maximum removal efficiency and energy density. In this section, particular attention is again paid to the most studied target compounds, i.e. trichloroethylene, benzene and toluene. Table 3.8 presents a list of other relevant, but less frequently studied VOCs that have been examined in plasma-catalytic studies. For more details about operating conditions and results, the reader can consult the corresponding references.

Trichloroethylene

Table 3.5 presents published papers regarding TCE abatement. Oda et al. have investigated the effect of TCE initial concentration, pellet size and sintering temperature for TiO₂ catalysts on the TCE decomposition performance [335]. When the barrier type reactor was filled with TiO₂ sintered at 400°C, the breakdown voltage to generate NTP greatly reduces in comparison to the empty reactor and the reactor filled with TiO₂ sintered at 1100°C. They suggest that the nonuniform geometrical distribution of the disk-like dielectric pellets sintered at 400°C disturbed the electric field and generated an electric field concentration at the contacting area of the pellets. This results in the formation of contacting point discharges or surface discharges on the pellet surfaces, lowering the breakdown voltage and improving the decomposition energy efficiency. Moreover, they indicate that too fine TiO₂ particles disturb the gas flow and cause insufficient filling of the discharge area with plasma.

In another study by Oda et al. [341], MnO_2 is used as a post-plasma catalyst in a direct (contaminated air is directly processed by the plasma) and an indirect process (plasma-processed clean air is mixed with the contaminated air). Manganese oxide is very efficient in enhancing the decomposition efficiency for both processes. The catalysts effectiveness to dissociate ozone generates oxygen radicals which are excellent oxidizers for TCE removal.

Han et al. have further examined the effect of the manganese dioxide post-plasma catalyst for the direct and indirect process [143]. For the direct process oxygen species, generated from collisions between excited species (or electrons) with O_2 , mainly oxidize TCE into DCAC. The increased decomposition efficiency for the direct process is ascribed to the oxidation of the remaining TCE into trichloroacetaldehyde ($\text{CCl}_3\text{-CHO}$, TCAA) by oxygen species produced during ozone decomposition at the surface of MnO_2 . The CO_x yield increases from 15% to 35% at an energy density of 120 J/L when MnO_2 is present. When the energy density is raised to 400 J/L, a CO_x yield of 98% is established. For the indirect process, similar conclusions are made although the CO_x yield is not as good as for the direct process.

Magureanu et al. have tested a plasma-catalytic DBD reactor with an inner electrode made of sintered metal fibres (SMF) coated by transition metal oxides [140]. Figure 3.9 shows the CO and CO_2 selectivity over the range of energy densities used. The selectivity to CO_2 reaches 25% with the SMF and showed a significant improvement with MnO_x/SMF , up to 60%. The use of MnO_x/SMF does however not substantially lower the selectivity to CO . Thus, as compared to the reactor with SMF electrode, TCE conversion and CO_2 selectivity were significantly enhanced using MnO_x/SMF . The ability of MnO_2 to decompose ozone *in situ*, produces strong oxidizing atomic oxygen species on the catalyst surface. These species may lead to an enhanced oxidation of TCE resulting in a high CO_2 selectivity [139, 140, 306]. After reaction, XPS (X-ray Photoelectron Spectroscopy) analysis of the catalyst has revealed that both manganese and iron have preserved their initial oxidation state. The used catalyst however, shows an enrichment of iron on the catalyst surface suggesting a redispersion of manganese on the surface during reaction. Finally, XPS also reveals some chlorine deposition on the catalyst surface after reaction.

In another study conducted by Magureanu et al. [144], gold nanoparticles embedded in SBA-15 have been tested for PPC. The catalyst with the least amount of Au (0.5 wt%) seems to enhance the CO_x selectivity the most and has the best catalytic performance. As for MnO_2 , the Au/SBA-15 can dissociate ozone, produced in the plasma,

to oxygen radicals that decompose TCE. They suggest that in the presence of ozone generated in the plasma, isolated gold cations are the active sites that elucidate the catalytic behaviour.

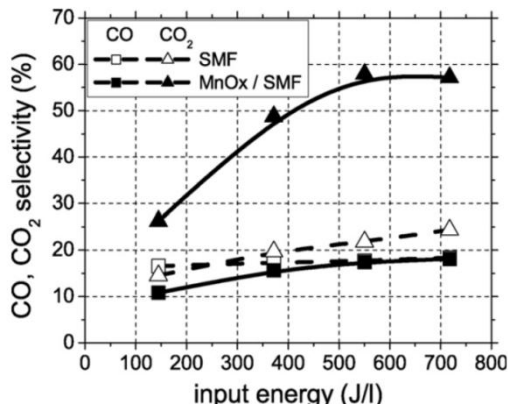


Figure 3.9 Selectivity to CO and CO₂ as a function of input energy for inner electrodes made of SMF and MnOx/SMF [67].

To achieve a more complete oxidation of TCE at a reduced energy cost, Morent et al. have used a hybrid plasma–catalyst system with cylindrical TiO₂ pellets for IPC [147]. They suggest that the increased removal fraction for the plasma–catalytic system can be explained through adsorption on and/or photoactivation of TiO₂. Adsorption of TCE molecules on the surface of TiO₂ increases the residence time of TCE in the discharge.

To confirm the presence of excited species of nitrogen, Subrahmanyam et al. give an UV–VIS emission spectrum of the DBD plasma discharge in the wavelength range 250–500 nm. It is proven that emission of excited nitrogen molecules (N₂^{*}) is in the range of the band gap of the TiO₂/SMF catalyst [139]. They suggest that the increased activity of TiO₂/SMF might be due to photocatalytic action in the presence of UV light as well as activation of TiO₂ by the plasma discharge.

Vandenbroucke et al. [320] have investigated the use of a DC glow discharge combined with Pd/γ–Al₂O₃ located in an oven downstream. When the catalyst temperature was set at 100°C, the combined system showed synergetic effects on the removal of TCE. By comparing the experimental removal efficiency of the hybrid system with the removal calculated by multiplying the individual effects (plasma and catalyst alone), 12 to 22% additional TCE was decomposed. A more elaborated review on plasma–catalytic abatement of TCE can be found in [342].

Table 3.5 Overview of published papers on TCE removal with plasma-catalysis.

Plasma type	Catalyst	Position	T _{cat} (°C)	Carrier gas	Flow rate (mL/min)	Conc. range (ppm)	Maximum removal efficiency (%)	Energy density (J/L)	Ref.
DBD	MnO ₂	PPC	20	air	500	250	95 – 99	240	[138]
DBD	TiO ₂ /SMF CoO _x (3 wt%)/SMF MnO _x (3 wt%)/SMF TiO ₂ /MnO _x /SMF	IPC	–	air	700	250	> 99	–	[306]
DBD	MnO _x (3 wt%)/SMF	IPC	20	air	500	150 – 200	95 – 99	550	[140]
DBD	MnO	IPC	20	dry air	1000	250 2000	> 99 > 99	120 40	[146]
DBD	TiO ₂ V ₂ O ₅ (0.7 wt%)/TiO ₂ V ₂ O ₅ (4.6 wt%)/TiO ₂ WO ₃ (4.2 wt%)/ TiO ₂	IPC	20	dry air	400	100	> 99 95 – 99 90 – 95 > 99	180 140 140 180	[142]

Table 3.5 Overview of published papers on TCE removal with plasma–catalysis (continued).

Plasma type	Catalyst	Position	T _{cat} (°C)	Carrier gas	Flow rate (mL/min)	Conc. range (ppm)	Maximum removal efficiency (%)	Energy density (J/L)	Ref.	
DBD	TiO ₂ sintered at 1100°C – 0.5–1 mm – 1–2 mm – 2–3 mm	IPC	20	dry air	400	1000			[335]	
								> 99		200
								> 99		120
								> 99		120
	TiO ₂ sintered at 400°C					> 99	120			
DBD	MnO ₂	IPC	20	dry air	400	1000	> 99	120	[341]	
DBD	Au/SBA–15	PPC	–	dry air	510	430	> 99	670	[144]	
DC positive corona	TiO ₂	IPC	–	dry air	1500	100	85	600	[147]	

Table 3.5 Overview of published papers on TCE removal with plasma-catalysis (continued).

Plasma type	Catalyst	Position	T _{cat} (°C)	Carrier gas	Flow rate (mL/min)	Conc. range (ppm)	Maximum removal efficiency (%)	Energy density (J/L)	Ref.
DC negative glow	Pd(0.05 wt%)/Al ₂ O ₃	PPC	100	humid air	2000	600 – 700	80	300	[320]
Surface discharge	V ₂ O ₅ /TiO ₂ Cu-ZSM-5	IPC	20	dry air	400	1000	> 95 > 95	50 50	[146]
DC negative glow	MnO ₂	PPC	300	dry air	500	500	90	240	[149]
DC negative glow	LaMnO _{3+δ}	PPC	150	humid air	500	510	93	460	[150]

Benzene

Table 3.6 presents published papers regarding benzene abatement. Ogata et al. have performed much research on the removal of benzene with plasma-catalysis. In a first study [310], they test an adsorbent hybrid reactor packed with a mixture of BaTiO₃ and Al₂O₃ pellets and compare the results with a BaTiO₃ packed reactor and a two stage reactor (BaTiO₃ packed reactor with Al₂O₃ downstream). The hybrid reactor shows the best performance, owing to its better energy efficiency, CO₂-selectivity and suppressed N₂O formation. The combined effect of benzene concentration on Al₂O₃ followed by surface decomposition and gas-phase reaction is thought to be responsible for the enhanced decomposition. Cyclic operation of adsorption and plasma discharge is suggested to further improve the energy efficiency. In [311] they continue examining a catalyst hybrid reactor with metal supported Al₂O₃ and have found that Ag-, Co-, Cu and Ni-supported Al₂O₃ shows a slightly better CO/CO₂ ratio and a lower N₂O formation than the adsorbent hybrid reactor. Next, a zeolite hybrid plasma reactor (mixture of zeolite and BaTiO₃) has been applied for dilute benzene decomposition [313]. The higher adsorption capacity of zeolite structures compared to alumina allow a higher decomposition efficiency and CO/CO₂ ratio if the micropore surface area is large enough for accommodation of benzene molecules. The authors have also found that benzene adsorbed outside of a zeolite crystalline pore decomposed more easily than that inside a zeolite pore. In [318] they expand the study and examine the effect of BaTiO₃ pellet size and mixing ratio of BaTiO₃ and adsorbent, catalyst or zeolite. Plasma energy is found to be almost independent of the pellet size. However, with pellets larger than 2 mm in diameter sparking occurs earlier. For the catalyst hybrid reactor (with metal supported Al₂O₃), larger BaTiO₃ pellets in comparison to catalyst pellets, are beneficial because high energy plasma is formed around the contact points of the BaTiO₃ pellets (Figure 3.10). This shows the importance of the combination method to effectively induce catalytic properties.

Kim et al. have also tested various catalyst formulations and reactor types to enhance the decomposition of benzene with NTP. A BaTiO₃ packed-bed reactor has been modified by replacing the ferroelectric material with TiO₂, Pt/TiO₂ or Ag/TiO₂ pellets [170]. The reactor is placed in an oven that controls the temperature at 100°C. Experiments reveal that the catalytic activity for benzene decomposition is in the order Ag/TiO₂ > TiO₂ > Pt/TiO₂. The silver catalyst also improves the CO₂-selectivity with 15% compared to the BaTiO₃ packed-bed reactor. Beside CO₂ and CO, no other by-products are formed, which is confirmed by good carbon balances. Results

indicate that the energy density is the governing factor for benzene decomposition rather than the amount of Ag/TiO₂ (grams of catalyst) in the reactor [166] or the gas residence time [171]. However, larger amounts of Ag/TiO₂ slightly reduce the formation of N₂O. In this study, formic acid is found as minor by-product at lower energy density. While a pulsed corona and surface discharge reactor form aerosols during benzene removal, negligible amounts are detected in the reactor packed with Ag/TiO₂ [166]. In a subsequent study [343], Ag-loading amount on TiO₂ (percentage of Ag on catalyst) confirms to have no effect on the benzene removal. This parameter however plays an important role for the oxidative decomposition of intermediates on the TiO₂ surface, indicated by the carbon balance. Larger Ag-loading seems to benefit the carbon balance and CO₂-selectivity. Further work has examined the activation mechanism of the Ag/TiO₂ catalyst in the hybrid reactor [289]. Thermal catalytic experiments and comparison of the effects of dilution gases (Ar, N₂) on benzene removal respectively reveal that temperature is not an important parameter and contribution of plasma generated UV light to the photoactivation of the catalyst is negligible. The authors therefore suggest that *in situ* decomposition of ozone over Ag/TiO₂ and plasma-induced catalysis at higher energy density play a dominant role. The observed zero-order kinetics to benzene concentration supports the latter assumption. The catalyst shows good durability against catalyst deactivation for over 150 h of continuous operation tests [171].

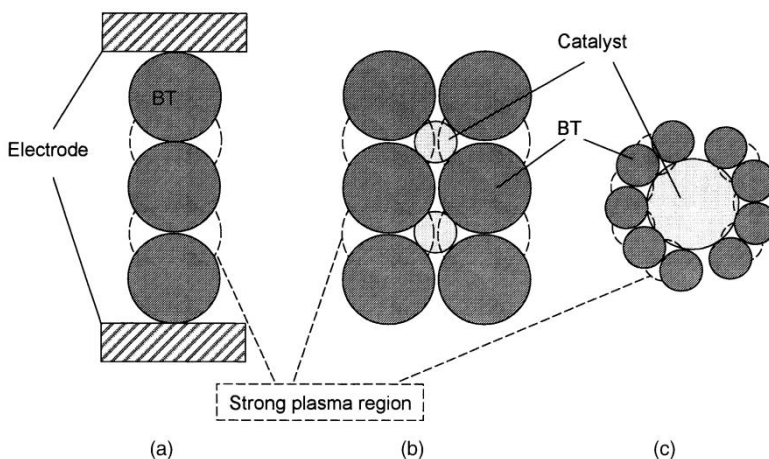


Figure 3.10 Image of plasma discharge in a (a) BaTiO₃ packed-bed DBD and in hybrid reactors with mixtures of (b) BaTiO₃ > catalyst and (c) BaTiO₃ < catalyst [245].

Finally, Kim et al. [160] have tested a cycled system of adsorption and oxygen plasma as earlier proposed by Ogata et al. [310] and Song et al. [312]. Benzene oxidation is examined as function of oxygen partial pressure (0 – 80% O₂) and different catalyst types (TiO₂, γ-Al₂O₃, zeolites) inside the reactor. An increase of O₂ partial pressure improves both the decomposition and CO₂-selectivity of benzene regardless of the catalyst used. Tests with the cycled system demonstrate that the regeneration mode must be done with pure oxygen to fully suppress harmful N_xO_y formation. The authors suggest a plausible reaction mechanism where removal of benzene mainly proceeds on the surface of the main catalysts (Figure 3.11).

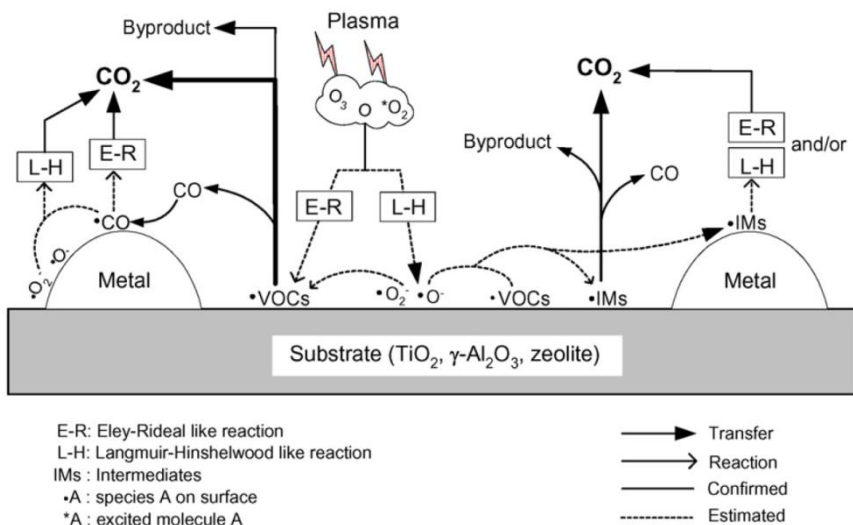


Figure 3.11 Plausible mechanism for IPC for VOCs on various catalysts [87].

Recently, Fan et al. have also investigated a cycled system with a storage and a discharge stage packed with a metal supported zeolite (Ag/HZSM-5) [344]. High oxidation rate of adsorbed benzene as well as low energy cost (3.7×10^{-3} kWh/m³) are achieved at a moderate discharge power. Additionally, Ag/HZSM-5 exhibited good stability during cycled operation.

In a study by Futamura et al. [164], a DBD discharge is applied to investigate the synergetic effect of filling the plasma reactor with different catalysts (TiO₂, MnO₂ and TiO₂-silica gel). They suggest a mechanism for MnO₂-catalyzed oxidation of benzene (Figure 3.12). Apparently, adsorption of ozone forms oxygen atoms on the MnO₂ surface which partially desorb as O(³P) in the gas phase, acting as possible oxidants for benzene decomposition.

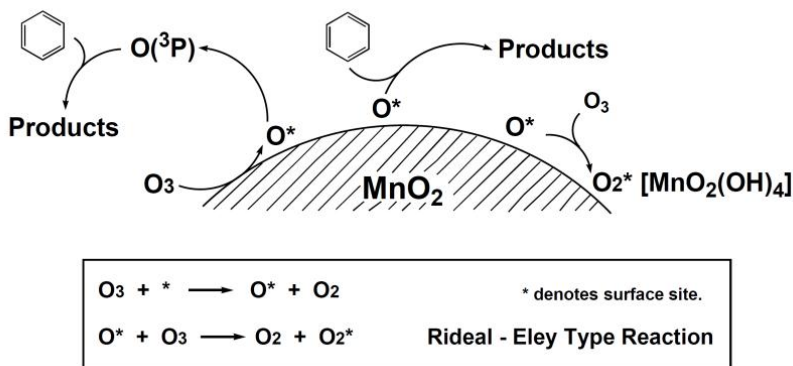


Figure 3.12 Mechanism for MnO₂-catalyzed oxidation of benzene [91].

Park et al. [165] have attached sheet type catalysts (TiO₂, Pt/TiO₂ and V₂O₅/TiO₂) on the dielectric barrier of a DBD discharge. Benzene decomposition efficiency decreases in the order V₂O₅/TiO₂ > Pt/TiO₂ > TiO₂. Suppression of N₂O formation and improved mineralization degrees are obtained with all catalysts. Results indicate that high energy electrons along with UV light generated from DBD plasma excite the TiO₂ catalysts.

A hybrid plasma-photocatalyst system has also been tested by Lee and coworkers [155]. Comparison of OES (Optical Emission Spectroscopy) spectra of the DBD glow discharge and an UV lamp confirms that the discharge emits UV light with an energy corresponding to 3 – 4 eV. The authors assume that photocatalysis could be possible using plasma as a photoactivation source, as proposed by Park et al. [165]. Titanium dioxide is coated on glass beads and on three types of γ -Al₂O₃ with different surface area, pore volume and pore diameter. High porous alumina dramatically enhances the benzene conversion and mineralization degree.

In [167] the influence of humidity on benzene removal is investigated with a DBD packed with Raschig rings coated with nano TiO₂ films. Humidity negatively affects decomposition of benzene for three reasons: deactivation of high energy electrons, inhibition of ozone formation and suppression of the catalyst activity of TiO₂ for benzene oxidation with ozone.

Harling et al. [345] have examined the effect of temperature (20 – 600°C) and catalyst position (IPC/PPC). Figure 3.13 shows IR spectra of the plasma-catalytic destruction of benzene as a function of temperature with Ag/ γ -Al₂O₃ in a two stage configuration. When compared to thermal catalysis, NO_x formation is detected and increasing amounts are produced at elevated temperatures.

Additionally, higher levels of destruction are observed at lower temperatures for plasma-catalysis.

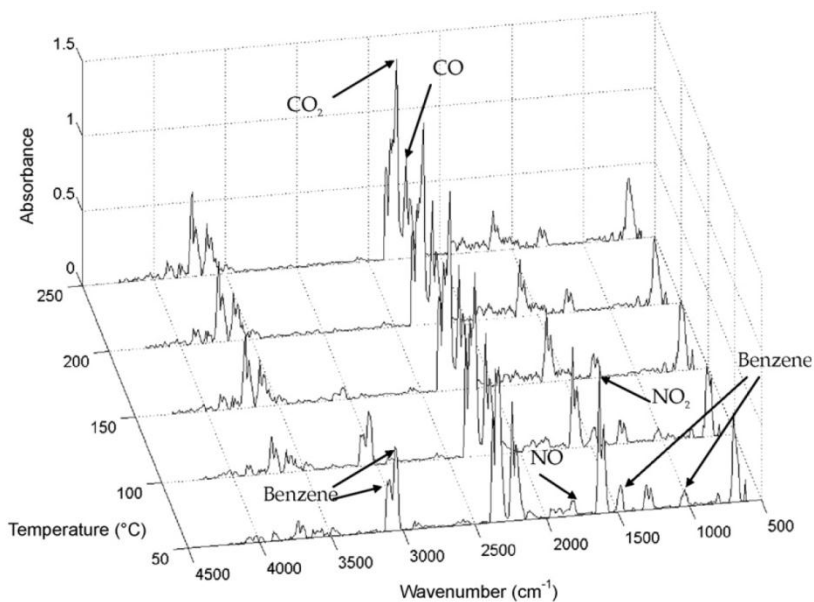


Figure 3.13 FT-IR spectra showing the plasma-catalytic destruction of benzene with Ag/ γ -Al₂O₃, as a function of temperature in a two-stage configuration [272].

Table 3.6 Overview of published papers on benzene removal with plasma-catalysis.

Plasma type	Catalyst	Position	T _{cat} (°C)	Carrier gas	Flow rate (mL/min)	Conc. range (ppm)	Maximum removal efficiency (%)	Energy density (J/L)	Ref.
DBD	TiO ₂	IPC	–	dry air	100	100	60	900	[93]
	MnO ₂				500	105	54	360	
	TiO ₂ -silica				500	105	50	320	
DBD	TiO ₂	IPC	20	dry air	250	300 – 380	12	170	[163]
	MnO ₂						16	170	
DBD	TiO ₂ Pt(1 wt%)/TiO ₂ V ₂ O ₅ (1 wt%)/TiO ₂	IPC	–	dry air	400	200	90 > 99 > 99	3150	[165]
DBD	Ag(2 wt%)/TiO ₂	IPC	100	dry air	4000	110	> 99	125	[171]
DBD	Kr/I ₂ (KrI* excimer UV radiation)	IPC	20	dry air	13 x 10 ³ – 130 x 10 ³	30 – 940	66.5	–	[168]

Table 3.6 Overview of published papers on benzene removal with plasma–catalysis (continued).

Plasma type	Catalyst	Position	T _{cat} (°C)	Carrier gas	Flow rate (mL/min)	Conc. range (ppm)	Maximum removal efficiency (%)	Energy density (J/L)	Ref.
DBD	TiO ₂	IPC	20	dry air	–	188	98	–	[346]
DBD glow discharge	TiO ₂ /Al ₂ O ₃	IPC	–	dry air	200	100	50	140	[155]
Pulsed Corona	silica gel	IPC	–	dry air	100	300	85	–	[169]
Multistage corona ^a	TiO ₂ Sol–gel TiO ₂ Pt/Sol–gel TiO ₂	IPC	20	dry air	60	1500	92.7 91.7 > 99	–	[347]
Surface discharge	Ag(1 wt%)/TiO ₂	IPC	100	dry air humid air	200 – 3000	200 – 210	89 86	383 391	[152]

Table 3.6 Overview of published papers on benzene removal with plasma-catalysis (continued).

Plasma type	Catalyst	Position	T _{cat} (°C)	Carrier gas	Flow rate (mL/min)	Conc. range (ppm)	Maximum removal efficiency (%)	Energy density (J/L)	Ref.
Surface discharge	Ag(4 wt%)/TiO ₂	IPC	100	dry air	4000 – 10 ⁴	200	> 99	89 – 194	[160]
	Ni(2 wt%)/TiO ₂						> 99		
	Ag(0.5/5 wt%)/Al ₂ O ₃						> 99		
	Pt(0.5 wt%)/Al ₂ O ₃						> 99		
	Pd(0.5 wt%)/Al ₂ O ₃						> 99		
	Ferrierite						> 99		
	Ag(2 wt%)/H–Y						> 99		
Packed bed DBD	TiO ₂	IPC	100	dry air	2000	203 – 210	82	388	[170]
	Pt(1 wt%)/TiO ₂						80		
	V ₂ O ₅ (1 wt%)/TiO ₂						90		
Pulsed corona	CuO(5 wt%)/AC	IPC	20	humid air (50%)	16.7 x 10 ³	248	96.5	173	[174]

^a Four stages in serie

Table 3.6 Overview of published papers on benzene removal with plasma-catalysis (continued).

Plasma type	Catalyst	Position	T _{cat} (°C)	Carrier gas	Flow rate (mL/min)	Conc. range (ppm)	Maximum removal efficiency (%)	Energy density (J/L)	Ref.
BaTiO ₃ packed bed	TiO ₂	IPC	20	dry air	1000	500	66	60	[345]
	Ag(0.5 wt%)/TiO ₂						60		
	Al ₂ O ₃						52		
	Ag(0.5 wt%)/Al ₂ O ₃	PPC	20				49		
	TiO ₂						34		
	Ag(0.5 wt%)/TiO ₂						46		
	Al ₂ O ₃						28		
Ag(0.5 wt%)/Al ₂ O ₃	39								
DBD	MnO _x /SMF	IPC	20	humid air	250	100	90	650	[178]
AgO _x -MnO _x /SMF	95								
DBD	γ-Al ₂ O ₃	IPC	20	dry air	3000	320	80	800	[348]
Pt/γ-Al ₂ O ₃	88								
Pt/γ-Al ₂ O ₃ (preheated)	97								

Toluene

Table 3.7 gives an extensive overview of papers that have been published on the plasma-catalytic abatement of toluene. A concise discussion is given on selected papers. Other references can be found in Table 3.8.

Song et al. have applied a DBD packed with macro-porous γ - Al_2O_3 and investigated the effect of adsorption and elevated temperature [312]. Higher operating temperatures (100°C) cause a reduction in adsorption capability. However, toluene removal is more favorable under these conditions in comparison with the use of non-adsorbing glass beads. The use of γ - Al_2O_3 beads proves to reduce some of the gas phase by-products, such as O_3 and HNO_3 , generated by the NTP process. Malik et al. have also indicated that selecting the alumina packing with higher overall surface area can lower ozone generation without affecting the destruction efficiency of toluene [349].

In a study by Li et al. [350], a DC streamer corona discharge is employed in combination with TiO_2 pellets. Positioning the photocatalyst between the needle and mesh electrodes benefits the plasma discharge due to a higher streamer repetition rate. This configuration shows the best performance for decomposition (76%) and energy efficiency (7.2 g/kWh). This is attributed to the simultaneous decomposition of gas phase and adsorbed toluene and to possible TiO_2 activation by plasma inducing catalytic reactions. In absence of the TiO_2 layer, both the decomposition (44%) and efficiency (3.2 g/kWh) significantly drop. The authors claim that intermittent operation can improve the efficiency due to the regeneration of the catalyst surface through desorption during the discharge.

Guo et al. [351] have applied a DBD to study the effect of $\text{MnO}_x/\text{Al}_2\text{O}_3/\text{nickel}$ foam for IPC. Earlier results have confirmed that $\text{MnO}_x/\text{Al}_2\text{O}_3/\text{nickel}$ foam is the most effective for toluene removal among different catalysts tested [299]. Figure 3.14 shows that the MnO_x catalyst greatly improves the energy yield as compared to the plasma alone system. A sampling method has been developed to detect OH radicals in the gas phase and on the catalyst surface [352]. The catalyst can enhance the toluene removal efficiency due to efficient reactions of OH radicals with toluene on the surface or the active sites and other active species on the catalyst. With the plasma-catalytic system toluene removal decreases with increased humidity. It is suggested that water molecules cover the catalyst surface, resulting in a lower reaction probability [353].

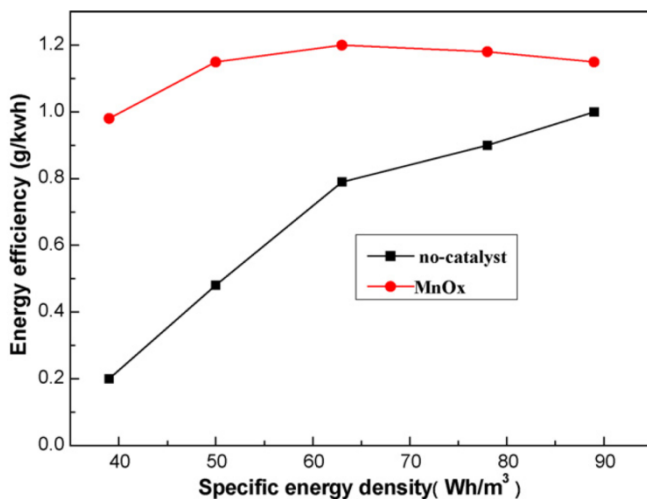


Figure 3.14 Effect of energy density on energy yield of different catalysts (RH: 20%; initial toluene concentration: 105 ppm; gas flow rate: 450 mL/min) [278].

Indeed, Van Durme et al. [354] have concluded that water molecules adsorb on the catalyst surface to form mono- or multilayers that block active sites and create an extra diffusion layer for toluene to reach the catalyst surface. This hypothesis has also been confirmed by Huang et al. [200, 297, 298]. In a recent paper [355], Huang et al. have investigated the effect of water vapor on toluene removal efficiency, carbon balance, CO₂ selectivity and outlet ozone concentration. A wire-plate DBD filled with MnO_x/Al₂O₃/nickel foam or TiO₂/Al₂O₃/nickel foam is used to perform experiments. The results show that increased humidity lowers the formation of ozone through quenching of energetic electrons. Also, catalytic decomposition of ozone is depressed by the presence of water vapor due to competitive adsorption causing deactivation of the catalyst and suppression of catalytic ozonation. The carbon balance and CO₂ selectivity reach maximum values when RH is in the range 25–75%. Furthermore, Wu et al. [192] calculated desorption activation energies of toluene and water on NiO/γ-Al₂O₃ for IPC removal and concluded that the adsorption of water on the catalyst surface is stronger than the adsorption of toluene.

Van Durme et al. [284] have also studied the effect of humidity on PPC removal of toluene. As for IPC, PPC is less efficient when RH increases. With Pd/Al₂O₃ as PPC removal efficiencies are > 90% and 37% at dry air and air with 74% RH (25°C), respectively. The negative humidity effect is mostly attributed to changing Van der Waals interactions.

In a recent study by Huang et al. [339], NTP has been combined with a photocatalyst located downstream. Experimental results indicate that catalytic ozonation plays a vital role in toluene decomposition. The dominant active species in the NTP-driven photocatalyst system are active oxygen species formed from ozone catalytic decomposition. The decomposition pathway of toluene has been elucidated in subsequent work [356]. Detected by-products for IPC removal of toluene with TiO₂/Al₂O₃/nickel foam include benzene, benzaldehyde, formic acid and small amounts of acetic acid and 2-methylamylene.

Subrahmanyam et al. modified a sintered metal fiber filter, which acts as inner electrode, with MnO_x and CoO_x [308]. Figure 3.15 shows the influence of this modification and energy density on the conversion of 100 ppm toluene. At an energy density of 235 J/L, nearly 100% conversion has been achieved with both MnO_x and CoO_x/SMF. Whereas SMF only shows 50% CO₂ selectivity, MnO_x/SMF reaches 80% even at 235 J/L. Interestingly, no polymeric carbon deposits are detected. All the catalytic electrodes maintain the same activity during almost 3 hours of toluene decomposition. This proves that the electrodes maintain their stability during VOC destruction.

Magureanu et al. [316] have tested MnPO₄, Mn-APO-5 and Mn-SAPO-11 as PPC catalysts in an oven for temperatures up to 400°C. Even at low temperature, a remarkable synergetic effect has been observed while the catalysts alone are not active at that temperature level. The authors expect a further increase in the plasma-catalytic synergy by placing the catalyst in the discharge region, where short-lived species produced in the plasma will most likely contribute to oxidation on the catalyst surface.

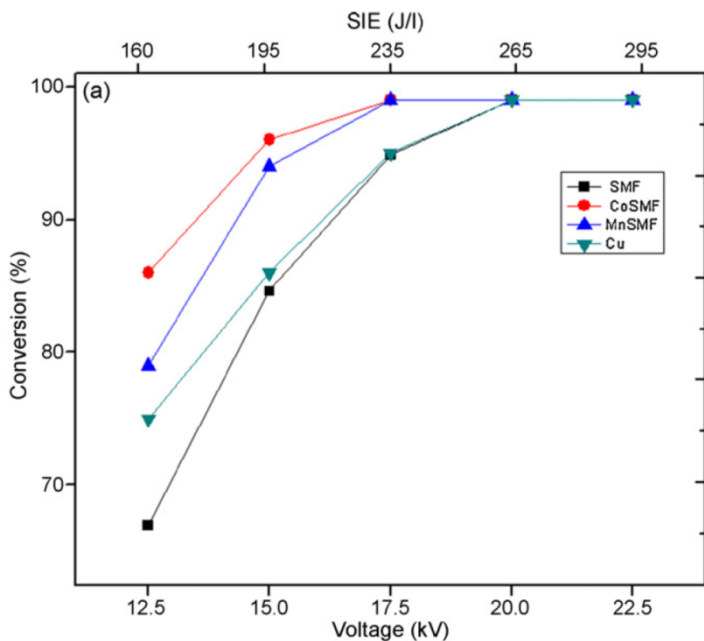


Figure 3.15 Influence of SMF modification and energy density on the conversion of 100 ppm toluene [235].

Table 3.8 Published papers on removal of other VOCs with plasma-catalysis.

Target VOC	Ref.
Acetaldehyde	[175, 209, 287, 357-359]
Acetone	[187, 216, 217, 267, 334, 360]
Acetylene	[218, 283, 337, 338, 361]
Dichloromethane	[282, 317, 362, 363]
Formaldehyde	[227-229, 364-366]
Methane	[169, 233, 234, 321, 367]
Methanol	[238]
Propane	[312, 322, 330]
Propene	[322]
Styrene	[171, 249, 324, 368, 369]
Tetrachloromethane	[323, 370]
Xylene	[171, 261, 333, 371-378]

Table 3.7 Overview of published papers on toluene removal with plasma–catalysis.

Plasma type	Catalyst	Position	T _{cat} (°C)	Carrier gas	Flow rate (mL/min)	Conc. range (ppm)	Maximum removal efficiency (%)	Energy density (J/L)	Ref.
DBD	Al ₂ O ₃	IPC	20 100	air (18% RH)	10 ⁴	220	60 – 65 80	110	[312]
DBD	Fe ₂ O ₃ /MnO honeycomb	PPC	20	dry air	2500	85	65	72	[303]
DBD	SMF CoO _x (3 wt%)/SMF MnO _x (3 wt%)/SMF	IPC	–	air	500	250	60 70 65	160	[306]
DBD	SMF CoO _x (3 wt%)/SMF MnO _x (3 wt%)/SMF Cu	IPC	–	air	500	500	90 92 95 90	298	[308]

Table 3.7 Overview of published papers on toluene removal with plasma-catalysis (continued).

Plasma type	Catalyst	Position	T _{cat} (°C)	Carrier gas	Flow rate (mL/min)	Conc. range (ppm)	Maximum removal efficiency (%)	Energy density (J/L)	Ref.
DBD	MnPO ₄ Mn-APO-5 Mn-SAPO-11	PPC	400	air	50 – 150	560	70 65 70	900 – 2700	[316]
DBD	Ag/TiO ₂	IPC	100	air	4000	101	95	125	[171]
DBD	Ti-MPS Mn(5 wt%)-Ti-MPS Mn(10 wt%)-Ti-MPS	PPC	–	air	200	1000	45 58 75	300	[379]
Wire-cylinder DBD	TiO ₂ /activated carbon filter	IPC	–	air (0.5% H ₂ O)	200	100	55	–	[288]

Table 3.7 Overview of published papers on toluene removal with plasma-catalysis (continued).

Plasma type	Catalyst	Position	T _{cat} (°C)	Carrier gas	Flow rate (mL/min)	Conc. range (ppm)	Maximum removal efficiency (%)	Energy density (J/L)	Ref.
Wire-cylinder DBD	Al ₂ O ₃	IPC	–	dry air	2000	186	75	700	[332]
	TiO ₂ /Al ₂ O ₃						86		
	MnO ₂ (5 wt%)/Al ₂ O ₃						84		
	MnO ₂ (10 wt%)/Al ₂ O ₃						96		
	MnO ₂ (15 wt%)/Al ₂ O ₃						96		
Wire-cylinder DBD	TiO ₂ /glass pellets	IPC	20	dry air	600	1100	80	1000	[187]
Wire-plate DBD	TiO ₂ /Al ₂ O ₃ /Ni foam	PPC	–	dry air	200	50	95	900	[297]
Wire-plate DBD	MnO ₂ /Al/Ni foam	IPC	–	5% O ₂ /N ₂	100	50	> 95	750	[277]

Table 3.7 Overview of published papers on toluene removal with plasma–catalysis (continued).

Plasma type	Catalyst	Position	T _{cat} (°C)	Carrier gas	Flow rate (mL/min)	Conc. range (ppm)	Maximum removal efficiency (%)	Energy density (J/L)	Ref.
DBD (pulsed)	Mn-1 Mn-2 Mn-3	PPC	300	air	300	200	90 – 95	1400	[380]
DBD packed with glass beads	N150 (MnO ₂ –Fe ₂ O ₃) Al ₂ O ₃ MnO ₂ (9 wt%)/Al ₂ O ₃ activated carbon (AC) MnO ₂ (3 wt%)/AC	PPC	–	air	588	240	76 74 88 98.5 99.7	172	[189]
Multistage packed bed DBD	MnO ₂ MnO ₂ –CuO	PPC	–	air	10 ⁴	70	> 99 > 99	340	[381]

Table 3.7 Overview of published papers on toluene removal with plasma-catalysis (continued).

Plasma type	Catalyst	Position	T _{cat} (°C)	Carrier gas	Flow rate (mL/min)	Conc. range (ppm)	Maximum removal efficiency (%)	Energy density (J/L)	Ref.
BaTiO ₃ packed bed DBD	Al ₂ O ₃	IPC	400	dry air	1000	500	95	60	[326]
	Ag ₂ O(7 wt%)/Al ₂ O ₃		300				> 99		
	MnO ₂ (7 wt%)/Al ₂ O ₃		330				> 99		
	Al ₂ O ₃	PPC	425				78		
	Ag ₂ O(7 wt%)/Al ₂ O ₃		300				> 99		
	MnO ₂ (7 wt%)/Al ₂ O ₃		330				> 99		
BaTiO ₃ packed bed DBD	TiO ₂	IPC	480	dry air	1000	500	91	60	[345]
	Al ₂ O ₃						> 99		
	Ag(0.5 wt%)/Al ₂ O ₃						> 99		
	TiO ₂	PPC	600				95		
	Al ₂ O ₃						> 99		
	Ag(0.5 wt%)/TiO ₂						95 – 99		
Ag(0.5 wt%)/Al ₂ O ₃	99								

Table 3.7 Overview of published papers on toluene removal with plasma-catalysis (continued).

Plasma type	Catalyst	Position	T _{cat} (°C)	Carrier gas	Flow rate (mL/min)	Conc. range (ppm)	Maximum removal efficiency (%)	Energy density (J/L)	Ref.
Pulsed corona	Pt-honeycomb	PPC	240	air	2 x 10 ⁴	330	90 – 95	142	[302]
Pulsed corona	Reticulated vitreous carbon Pt/Rh coated electrodes	IPC	160	dry air	1000	200	85	140 – 150	[305]
Pulsed corona	AlO ₂ silica gel	IPC	–	air	100	300	> 95	5.4	[169]
Pulsed corona	Al ₂ O ₃	IPC	–	air	400	1100	> 99	1100	[349]
DC positive corona	TiO ₂	IPC PPC	–	air	1000	80 – 100	75 70	160 330	[350]

Table 3.7 Overview of published papers on toluene removal with plasma-catalysis (continued).

Plasma type	Catalyst	Position	T _{cat} (°C)	Carrier gas	Flow rate (mL/min)	Conc. range (ppm)	Maximum removal efficiency (%)	Energy density (J/L)	Ref.
DC positive corona	TiO ₂	IPC	20	dry air	10 ⁴	0.5	82	17	[354]
	CuOMnO ₂ /TiO ₂	PPC					78	2.5	
DC positive corona	Cu-Mn/TiO ₂ (a)	PPC	20	air (50% RH)	10 ⁴	0.5	40	14	[284]
	N140						47	16	
	N150						34	16	
	Pd(0.5 wt%)/Al ₂ O ₃						47	10	
	Cu-Mn/TiO ₂ (b)						62	20	
Wire-cylinder corona	TiO ₂ (3 wt%)/Al ₂ O ₃ TiO ₂ (3 wt%)/glass beads	IPC	–	10% O ₂ /N ₂	4000	1000	70 – 75 80 – 85	–	[290]
Positive DC streamer	Cu-Mn/Al ₂ O ₃	PPC	300	air	133 x 10 ³	45	96	20	[319]

Table 3.7 Overview of published papers on toluene removal with plasma–catalysis (continued).

Plasma type	Catalyst	Position	T _{cat} (°C)	Carrier gas	Flow rate (mL/min)	Conc. range (ppm)	Maximum removal efficiency (%)	Energy density (J/L)	Ref.
Surface discharge	Ni/cordierit honeycomb Mn–Cu/cordierit honeycomb V/cordierit honeycomb	PPC	–	air	666 x 10 ³	30	40 – 45	–	[270]
Surface discharge	zeolites	IPC	–	air (0.5% H ₂ O)	500	200	–	–	[314]
Pulsed wire–cylinder	Pt/Al ₂ O ₃	IPC	195	air	2 x 10 ⁴	300	92	–	[382]
DBD	Ag–Ce–O Ag–Co–O Ag–Mn–O	PPC	20	air	500	107	75 100 100	60.5	[196]

Table 3.7 Overview of published papers on toluene removal with plasma-catalysis (continued).

Plasma type	Catalyst	Position	T _{cat} (°C)	Carrier gas	Flow rate (mL/min)	Conc. range (ppm)	Maximum removal efficiency (%)	Energy density (J/L)	Ref.
DBD	SBA-15 Mn(1 wt%)/SBA-15 Mn(3 wt%)/SBA-15 Mn(5 wt%)/SBA-15 Mn(8 wt%)/SBA-15 Mn(10 wt%)/SBA-15	IPC	20	air	300	100		192	[197]
DBD	NiO/ γ -Al ₂ O ₃ MnO ₂ / γ -Al ₂ O ₃ CeO ₂ / γ -Al ₂ O ₃ Fe ₂ O ₃ / γ -Al ₂ O ₃ CuO/ γ -Al ₂ O ₃ γ -Al ₂ O ₃	IPC	40	dry air	100	160	88.8 78.8 77.1 70.7 63.5	9 73.2	[192]
DBD	Rashig rings	IPC	20	dry air	333	320	97	445	[195]

Table 3.7 Overview of published papers on toluene removal with plasma–catalysis (continued).

Plasma type	Catalyst	Position	T _{cat} (°C)	Carrier gas	Flow rate (mL/min)	Conc. range (ppm)	Maximum removal efficiency (%)	Energy density (J/L)	Ref.
Back corona discharge	AgMnO _x /Al ₂ O ₃	IPC	20	dry air	500	110	90	123	[383]
DBD	BaTiO ₃ /TiO ₂	IPC	20	dry air	8666	270	69	570	[194]
DBD	MnO _x /SMF AgO _x –MnO _x /SMF	IPC	20	humid air	250	100	100 100	650	[178]
DBD	ceramic rings BaTiO ₃ rings Ba _{0.8} Sr _{0.2} Zr _{0.1} Ti _{0.9} O ₃ rings	IPC	20	dry air	1	160	75 80 97	760	[199]
DBD	TiO ₂ /γ–Al ₂ O ₃ /nickel foam	IPC PPC	20	humid air (50% RH)	200	50	94 95	1527	[200]

Table 3.7 Overview of published papers on toluene removal with plasma–catalysis (continued).

Plasma type	Catalyst	Position	T _{cat} (°C)	Carrier gas	Flow rate (mL/min)	Conc. range (ppm)	Maximum removal efficiency (%)	Energy density (J/L)	Ref.
DBD	Ag–Al catalyst	IPC	100	dry air	510	50	60	360	[201]

3.3 Critical process parameters

Various process parameters determine the initial condition of the feeded gas stream. In the following section these parameters are discussed which are critical for an effective operation of both catalytic and non-catalytic NTP systems. For each parameter, the different influences on the removal performance of the configuration will be discussed and compared if possible.

3.3.1 Temperature

In most cases, the NTP process removes VOCs more effectively as the process temperature increases. This is ascribed to an increased reaction rate of O and OH radicals with VOCs due to the endothermic behaviour of these reactions [126, 225, 226, 241, 243, 260, 303, 384-386]. This is however only the case for VOCs that are primarily decomposed through radical reactions. When electron impact is thought to be the primary decomposition step (e.g. CCl₄), no temperature dependence on the removal is observed because the electron density is not really influenced hereby [387, 388]. However, in [370] CCl₄ destruction is greatly improved at high temperature. This can be explained by the fact that the maximum energy density is also significantly higher than in [387], which might lead to higher decomposition.

The improved removal rate and energy efficiency can also be explained by an increase in the reduced electric field (E/n) with increasing temperatures. The reduced electric field, being the ratio of the electric field (E) and the gas density (n), is an important factor that determines the electron energy in the plasma. Since the gas density decreases as the gas temperature increases at constant pressure, NTP systems tend to operate at a higher reduced electric field [260, 389].

When the catalyst is located downstream, NTP produced ozone can be decomposed by reaction with molecular oxygen in the gas phase:



The rate constant of this reaction is accelerated at elevated temperatures (5 times higher at 300°C compared to 100°C). However, the lifetime of the produced oxygen atoms in the gase phase is too short to react with VOCs adsorbed on the catalyst surface. At the same time, reactions at the catalyst surface between adsorbed oxygen atoms and VOCs are also accelerated. The net-result of these two competing effects is the most likely explanation for the different

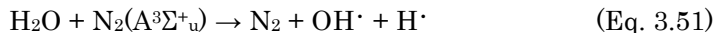
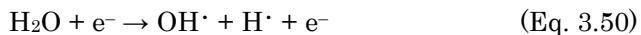
temperature dependencies found in literature: with increasing temperature, VOC decomposition efficiency can remain almost constant [316], can increase [322, 326, 345, 386] or can decrease [303].

3.3.2 Initial VOC concentration

Generally, the VOC concentration of actual industrial exhaust streams strongly varies. Therefore the effect of VOC concentration on the removal process has been abundantly studied. When the initial concentration rises, each VOC molecule shares fewer electrons and reactive plasma species. Consequently, numerous research papers have pointed out that higher initial VOC concentrations are detrimental for the removal efficiency in catalytic and non-catalytic NTP systems. Some papers also indicate that the characteristic energy [186, 189, 390-392] (i.e. the energy density needed to decompose 63% of the initial VOC concentration) and the energy yield [122, 389, 393] are an increasing function of the initial VOC concentration. For some halogenated carbons, the initial concentration barely seems to affect the decomposition efficiency. This is the case for HFC-134a [394], CFC-12 [395], HCFC-22 [396], bromomethane [397], trifluoromethane [398] and TCE [135]. This may be partly attributed to secondary decomposition induced by fragment ions and radicals produced by primary destruction steps [135, 399]. Another plausible explanation may be that for these compounds the primary destruction by reactive plasma species is the rate-determining step, leading to similar decomposition efficiencies regardless of the initial concentration [396].

3.3.3 Humidity level

The effect of humidity is of great interest for practical applications in industry since process gas consists of ambient air that usually contains water vapor at fluctuating concentrations. It appears that the effect of water vapor strongly depends on its concentration as well as on the type of the target VOC and the type of discharge. Water plays an important role in the plasma chemistry since it decomposes into OH and H radicals in a NTP environment as follows:



The oxidation power of OH is generally much stronger than those of other oxidants such as oxygen atoms and peroxy radicals.

The introduction of water vapor can induce changes in the electrical and physical properties of the discharge. The effect of water vapor has been mostly studied with (packed) DBD reactors. For this type of discharge, the presence of water vapor is known to reduce the total charge transferred in a microdischarge which ultimately decreases the volume of the reactive plasma zone [153]. The plasma characteristics of corona discharges are also affected by the presence of water vapor. At higher RH, lower currents are observed for a given voltage [184]. This is attributed to a higher probability of the plasma attachment processes resulting in a reduced OH production [400]. Water has also an adverse effect on VOC removal due to its electronegative characteristic which limits the electron density and quenches activated chemical species [183]. Ge et al. [401] optimized parameters of a negative corona discharge for OH radical production and found an optimum relative humidity of 40–60% at ambient temperature.

The effect of humidity has been tested for several VOCs. It seems that the addition of water negatively influences the properties of the discharge irrespective of the VOC chemical structure. However, the enhanced production of OH caused by higher water vapor content competes with the latter effect, depending on the VOC chemical structure [224]. The influence on the removal process is designated as an enhancement, a suppression or a neutral effect depending on the chemical structure of the target VOC. Table 3.9 gives an overview of research results concerning the effect of humidity on the decomposition efficiency in various plasma reactors. Some studies have shown that an optimal water vapor content exists for achieving a maximum VOC removal efficiency. Interestingly, this optimum is around 20% RH for both TCE [402] and toluene [183, 184]. Furthermore, addition of water counteracts the formation of ozone due to consumption of O(¹D) (reaction (51)) which is the most important origin of ozone formation [167]. It has also been shown that water vapor decreases the formation of CO and enhances the selectivity towards CO₂ [172, 338, 403, 404].

In case of a PPC system, catalytic ozonation will play a minor role due to the inhibition of ozone formation by humidity. Secondly, the catalyst surface can be covered with layers of H₂O preventing the adsorption of ozone and VOCs and consequently minimalizing direct catalyst/VOC intermolecular interactions [284, 297, 354, 405]. In this context, the morphology and chemical composition of the catalyst are important factors that influence the interactions with H₂O. Therefore, it is desirable to choose a catalyst that is less susceptible to H₂O adsorption. Finally, increased humidity can poison catalytic active sites and lower the catalysts activity [297, 405].

Table 3.9 Influence of humidity on VOC removal with NTP.

Target VOC	Plasma type	Influence	Ref.
Acetylene	DBD	Suppression	[338]
Acetone	DBD	Neutral	[217]
Benzene	Packed DBD	Suppression	[151]
Benzene	DBD	Suppression	[154]
Benzene	Packed DBD	Suppression	[406]
Benzene	Pulsed corona	Suppression	[174]
Benzene	Corona	Suppression	[407]
Benzene	DBD	Enhancement	[178]
Bromomethane	Pulsed DBD	Neutral	[397]
Butane	DBD	Suppression	[403]
Chloroform	Gliding arc	Suppression	[408]
Dichloromethane	Packed DBD	Suppression	[393]
Formaldehyde	DBD	Neutral	[225]
Formaldehyde	Corona	Enhancement	[228]
Isovaleraldehyde	DBD	Neutral	[404]
Methane	DBD	Enhancement	[232]
Methane	DBD	Enhancement	[234]
Methanol	Packed DBD	Neutral	[393]
Naphtalene	Surface DBD	Suppression	[409]
Nitrobenzene	DBD	Enhancement	[410]
Propane	DBD	Neutral	[243]
Styrene	Corona	Suppression	[251]
Styrene	Corona	Suppression	[254]
TCE	DBD	Suppression	[403]
TCE	Surface ischarge	Suppression	[411]
TCE	SPCP*	Neutral	[412]
TCE	Corona	Enhancement	[150]
Tetrachloromethane	Packed DBD	Suppression	[256]
Tetrachloromethane	Gliding arc	Suppression	[408]
Toluene	Corona	Enhancement	[340]
Toluene	Packed DBD	Neutral	[393]
Toluene	Pulsed corona	Suppression	[221]
Toluene	Gliding arc	Neutral	[389]
Toluene	Surface discharge	Neutral	[314]
Toluene	Gliding arc	Enhancement	[413]
Toluene	Glow discharge	Enhancement	[193]
Toluene	Corona	Enhancement	[407]
1,1,1-Trichloroethane	DBD	Suppression	[414]
p-Xylene	DBD	Enhancement	[260]
p-Xylene	Corona	Neutral	[407]

* Surface Discharge Induced Plasma Chemical Processing

3.3.4 Oxygen content

Similar to the presence of water vapor, the oxygen content in the gas stream affects the discharge performance and plays a very important role in the occurring chemical reactions. A small increase in oxygen concentration generally leads to an enhanced generation of reactive oxygen radicals, resulting in a higher removal efficiency. However, due to its electronegative character, higher oxygen concentrations tend to trigger electron attachment reactions. Consequently, this limits the electron density and changes the electron energy distribution functions [202, 256]. Also, oxygen and oxygen radicals are able to consume reactive species such as excited nitrogen molecules and nitrogen atoms, which are otherwise used for destroying VOCs [230, 231, 415]. Collectively, the phenomena described above ensure the existence of an optimal oxygen content for VOC removal with NTP (Table 3.10). It appears that the optimal oxygen content ranges between 1 to 5%. For practical application in industrial waste gas treatment, it is however in most cases difficult to control the oxygen content to this level because process gas depends on its industrial environment and in a lot of situations it consists of ambient air.

Similar effects are observed for IPC systems. Additionally, direct reactions between oxygen radicals and VOC molecules adsorbed on the catalyst surface add to the positive effect of a moderate O₂ addition to N₂ [364]. However in [160], several catalysts (TiO₂, γ -Al₂O₃, zeolites) have been tested at varying oxygen content for the removal of toluene and benzene with a cycled system of removal and adsorption. For all catalysts tested, the removal efficiency increased with oxygen content ranging from 0 to 100%. Operation at higher oxygen content is also able to reduce the formation of N₂O and NO₂. Additionally, removal of styrene with a DBD packed with sol-gel prepared TiO₂ coated γ -Al₂O₃ proved to benefit from higher oxygen content in terms of catalytic activity and CO_x-selectivity [249].

As for the influence of the oxygen content on the performance of PPC configurations, no studies were found in literature.

Table 3.10 Optimal oxygen content for VOC removal with NTP.

Target VOC	Optimal O ₂ content (%)	Ref.
Acetaldehyde	3 – 5	[202]
Acetaldehyde	5	[204]
Benzene	0.2	[158]
Benzene	3 – 5	[160]
Benzene	3	[176]
Butane	5	[416]
Carbon tetrafluoride	1	[417]
Dichloromethane	1 – 3	[220]
Formaldehyde	5	[229]
2-Heptanone	2 – 3	[390]
HCFC-22	0.5	[396]
HFC-134a	0.5	[394]
Methylbromide	2	[418]
Naphtalene	0	[419]
Naptalene	100	[420]
TCE	2	[421]
Toluene	3 – 5	[160]
Toluene	2	[299]
Toluene	2	[421]
Toluene	0.1	[422]
Trichloromethane	0.5	[415]
Trifluoromethane	2	[398]
p-Xylene	5	[260]

3.3.5 Gas flow rate

The gas flow rate applied in laboratory experiments generally ranges from 0.1 L/min to 10 L/min. The effect of decreasing the gas flow rate logically implies an increase in residence time of the VOC in the system. Hence, the collision probability for electron-impact reactions and for reactions between VOCs and plasma generated radicals and metastables is enhanced which increases the decomposition efficiency.

When the NTP system is combined with a catalyst, the same argumentation can be made. In that case, the increased probability of surface reactions is beneficial for the removal process.

In the interest of practical operation, some groups have studied multistage NTP reactors with the aim to increase the residence time without decreasing the gas flow rate [190, 292, 347, 423-425].

Chapter 4

Plasma reactor concept and techniques for gas and catalyst analysis

4.1 *Negative DC corona/glow multi-pin-to-plate discharge*

The plasma reactor concept used in this work is based on results obtained by Akishev et al. [116, 119-121]. Their aim was to generate large active volumes of non-thermal plasma at atmospheric pressure in order to avoid expensive vacuum equipment and to expand the potential for applications. In this regard, the glow discharge seemed an attractive candidate as it is characterised by its large active plasma volume. This type of discharge was however a phenomenon that only manifested at reduced pressure. Akishev et al. succeeded to generate a DC glow discharge in a pin-to-plate geometry in air at atmospheric pressure [120]. Normally, a negative corona discharge will quickly develop into a spark discharge when increasing voltage. Akishev et al. experimentally demonstrated that the charge density on the anode surface can be reduced by applying certain stabilisation techniques [426]. This allows the discharge current to increase thereby delaying the spark regime and producing an intermediate, steady-state glow regime. These stabilisation techniques included [426]:

- **Modification of the cathode geometry**
The sharp cathode pins were replaced by hollow crenellated pins which allows the discharge to ignite at different points. This leads to a better spreading of the discharge current.
- **Modification of the anode profile**
The flat anode surface was replaced by a surface with spherical surface segments centered around the tip of each electrode pin. This enlarges the anode surface and increases the current at which sparking occurs. It also ensures a more uniform distribution of the current density across the spherical segments which delays local charge build-up.
- **Application of a gas flow**
Sparks arise at ionisation instabilities in the discharge. The gas flow is able to blow these instabilities away. The gas stream additionally creates turbulence that can disperse these zones.

Figure 4.1 shows the three regimes of the DC glow discharge at atmospheric pressure. As the applied voltage increases, the corona discharge is initiated at an onset voltage V_0 . In 1914, Townsend proposed an empirical formula that dictates the relationship between the discharge current I and the inter electrode voltage V for a coaxial geometry [427]:

$$I = CV(V - V_0) \quad (\text{Eq. 4.1})$$

where C is a constant depending on the geometry. This means that in the corona regime the reduced current I/V increases linearly with increasing voltage as shown in Figure 4.2. In the intermediate glow regime this relationship is no longer linear but exponential. Finally, the discharge transfers to the spark regime. Additional theoretical background regarding these discharges can be found in Section 3.2.1.2.

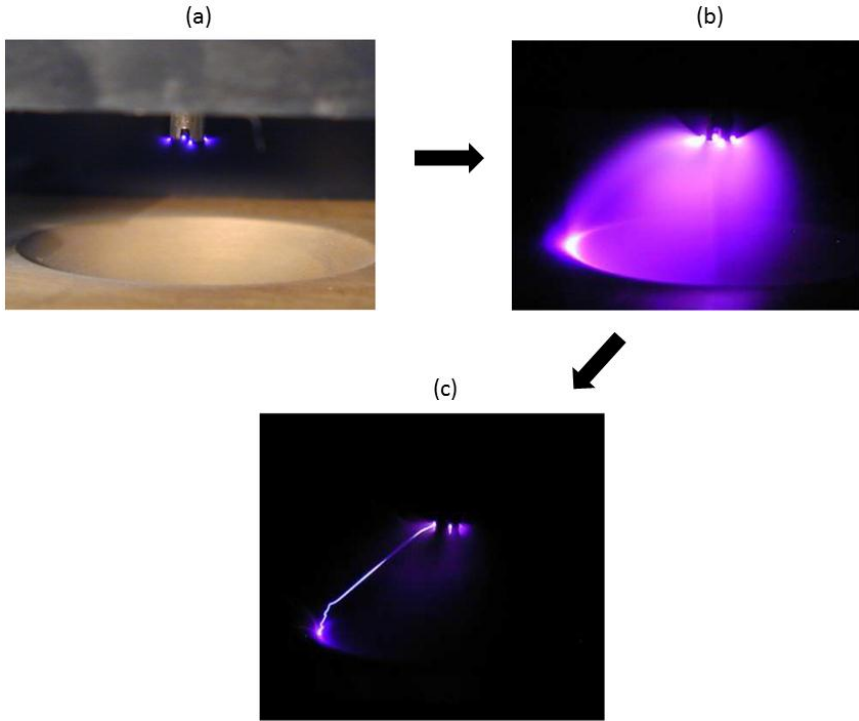


Figure 4.1 Different discharge regimes of a negative DC excited glow discharge at atmospheric pressure in a pin-to-plate geometry: (a) corona regime; (b) glow regime; (c) spark regime [428].

This type of discharge was successfully applied for the abatement of VOCs in waste air by using a multi-pin-to-plate configuration [122]. This reactor concept has several desirable features because it can easily be scaled-up, it is cost-saving due to the low investment for a DC high voltage source and it allows to treat high flow rates at atmospheric pressure and room temperature. In this work, the feasibility of combining this multi-pin-to-plate negative DC glow

discharge with heterogeneous catalysts for VOC abatement is investigated in order to enhance the performance of plasma alone systems.

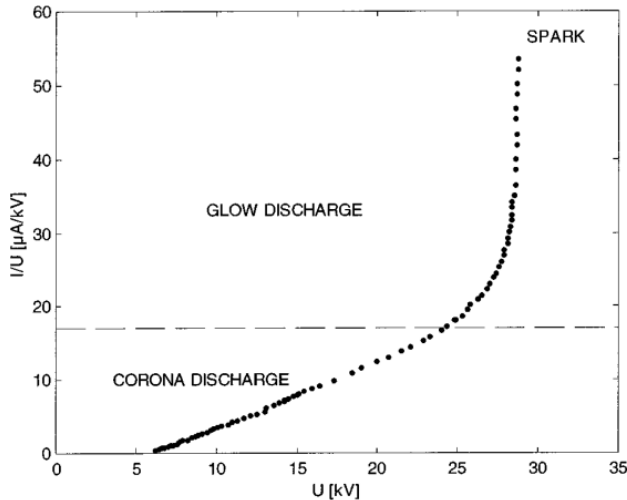


Figure 4.2 Reduced current–voltage characteristic of a negative DC discharge in flowing atmospheric air in a pin–to–plate geometry [428].

4.2 *Chemical analytical techniques*

In order to evaluate the performance of the abatement process of TCE, the influent and effluent of the reactor system were analyzed by Fourier transform infrared spectroscopy (FT–IR) and in some cases with mass spectrometry (MS). Furthermore, fresh and used catalysts were examined by X–ray photoelectron spectroscopy (XPS) and time–of–flight secondary ion mass spectrometry (ToF–SIMS) to analyze the elemental composition of the catalysts and their surface state. Some of the catalysts were characterised by Raman spectroscopy and X–ray powder diffraction while for others the specific surface area and metal dispersion were also determined. This section details the background and working principle of these analytical techniques with a clear emphasis on FT–IR due to the fact that a lot of time and effort was put into the proper implementation of the FT–IR apparatus and into the identification and quantification of the by–products of TCE abatement.

4.2.1 Fourier transform infrared spectroscopy

4.2.1.1 The electromagnetic spectrum and spectroscopy

Electromagnetic radiation is a flux of energy that exists as particles or packets called photons. Each photon has both electric and magnetic field components. The complete range of photon energies is called the electromagnetic spectrum shown in Figure 4.3.

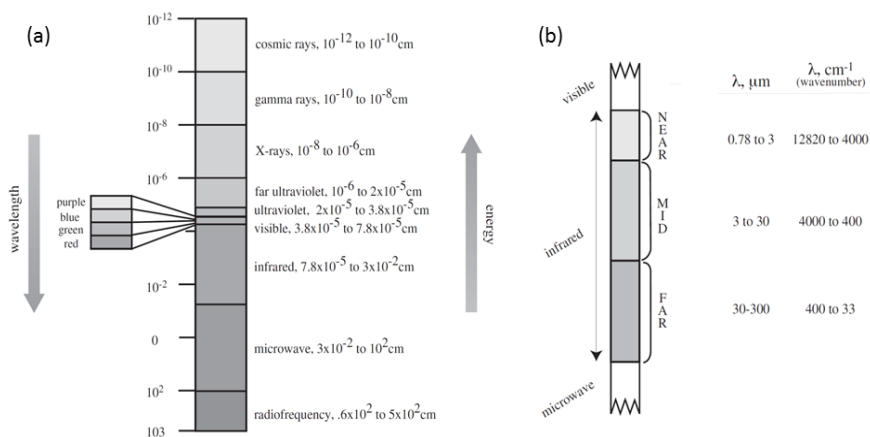


Figure 4.3 (a) The electromagnetic spectrum and (b) the IR regions.

Spectroscopy is the study of interaction between energy and matter. Absorption of energy of different magnitudes causes different changes in matter (Figure 4.4). The magnitude of the absorbed energy is determined by the chemical structure of the matter and forms the basis for spectroscopy [429].

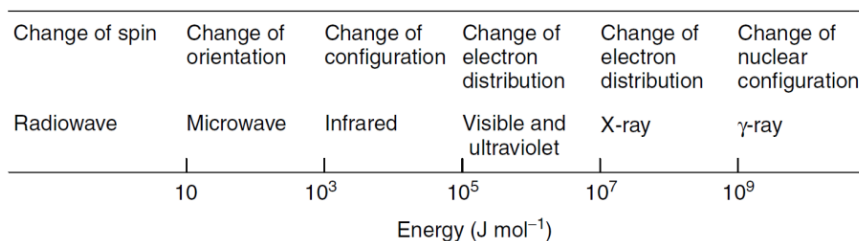


Figure 4.4 Regions of the electromagnetic spectrum and corresponding changes in matter through absorption [430].

In general, electromagnetic radiation is defined by the wavelength λ or the linear frequency ν . The wavelength is the distance between two

maxima of a sinusoidal wave. Infrared light is a type of electromagnetic radiation having wavelengths ranging from 0.78 to 300 μm . It is bound by the red end of the visible region at high frequencies and the microwave region at low frequencies (Figure 4.3).

The frequency is the number of wavelengths per unit of time. Since all electromagnetic waves travel at the speed of light c , the frequency corresponding to a given wavelength can be calculated as:

$$\nu = c/\lambda \quad (\text{Eq. 4.1})$$

According to the Planck's radiation law, the frequency of electromagnetic radiation is proportional to its energy:

$$E = h \cdot \nu \quad (\text{Eq. 4.2})$$

In infrared spectroscopy, wavenumber $\tilde{\nu}$ is used to describe the electromagnetic radiation. Wavenumber is the number of wavelengths per unit distance. For a wavelength in microns, the wavenumber in cm^{-1} is given by:

$$\tilde{\nu} = 10^4/\lambda \quad (\text{Eq. 4.3})$$

The spectral infrared region is further divided into the near, middle and far infrared (Figure 4.3). The middle infrared is the spectral region where the strong fundamental vibration–rotation bands of molecules appear. Nearly every pollutant will have a characteristic absorption band in this region. It is sometimes called the “fingerprint” region of the spectrum because the absorption bands in this region differ widely as to shape, location and intensity distribution [431]. The near and far infrared are of less importance to determine the chemical structure of the sample.

4.2.1.2 Discovery of infrared light

Our knowledge of the absorption of infrared light by molecules dates back to some experiments by Sir William Herschel. In 1800, while analyzing the spectrum of sunlight, he discovered the existence of heating rays beyond the visible limit of the red end of the solar spectrum. He found that these rays had the highest heating ability of all and concluded that there must be a different kind of light beyond the red portion of the spectrum (Figure 4.5). This kind of light, which is invisible to the human eye, became known as infrared light (below red) light.

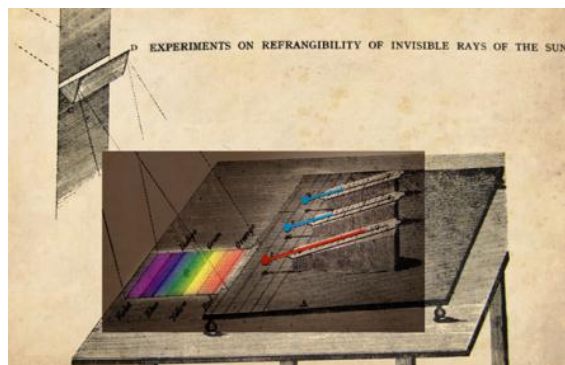


Figure 4.5 The Herschel experiment [432].

Herschel then placed a water-filled container between the prism and thermometer and observed that the temperature measured was lower than the one measured without water. Consequently, the water must partially absorb the radiation. In addition, Herschel could prove that depending on how the prism was rotated the difference in the temperature measured for each color varied. These historical findings opened the way to infrared spectroscopy.

4.2.1.3 History of IR spectroscopy

Since the development of the first spectrophotometers in the beginning of the 20th century, a rapid technological development has taken place. The first-generation spectrometers were all dispersive. Initially, the dispersive elements were prisms which later on changed over to gratings. In the mid 1960s, IR spectroscopy witnessed a revival due to the advantage of spectrometers that utilized the Fourier transform (FT). These second-generation spectrometers, with an integrated Michelson interferometer, provided some significant advantages compared to dispersive spectrometers. Today, almost every spectrometer used in mid-infrared spectroscopy is of the FT type.

4.2.1.4 Vibration theory

IR spectroscopy is based on the absorption of infrared light by the gas to be measured. This absorption excites molecular vibrations and rotations which have frequencies that correspond to those within the IR range of the electromagnetic spectrum. The following simple model of a harmonic oscillator used in classical physics describes IR absorption. If atoms are considered to be particles with a given mass, then the vibration in a diatomic molecule (e.g. HCl) can be described

as follows: the molecule consists of masses m_1 and m_2 connected by a spring. At equilibrium, the distance between the two masses is r_0 . If the molecule is stretched by an amount $\Delta r = x_1 + x_2$, then a restoring force F is produced. If the spring is released, the system will vibrate around the equilibrium position. According to Hooke's law, for small deflections the restoring force F is proportional to the deflection:

$$F = -k \cdot \Delta r \quad (\text{Eq. 4.4})$$

Since the force acts in a direction opposite to the deflection the proportionality constant or force constant k is negative in sign. The force constant is called the spring constant in the mechanical model whereas in a molecule the force constant is a measure of the bond strength between the atoms. For a harmonic oscillator it is possible to calculate the vibrational frequency ν of a diatomic molecule as follows:

$$\nu = \frac{1}{2\pi} \sqrt{\frac{k}{\mu}} \quad (\text{Eq. 4.5})$$

with $\mu = \frac{m_1 \cdot m_2}{m_1 + m_2}$ being the reduced mass.

On the basis of the equation above it is possible to state the following:

- The higher the force constant, i.e. the bond strength, the higher ν (in wavenumbers).
- The larger the vibrating atomic mass, the lower the vibrational frequency ν (in wavenumbers).

For the harmonic oscillator model, the potential energy is symmetric (Figure 4.6). According to quantum mechanical principles molecular vibrations can only occur at discrete, equally spaced vibrational levels, where the energy of the vibration E_v is given by:

$$E_v = (v + 1/2)h \cdot \nu \quad (v = 0, 1, 2, 3, \dots) \quad (\text{Eq. 4.6})$$

where h is Planck's constant and v is the vibrational quantum number. Even in the case $v = 0$, which is defined as the ground vibrational state, a molecule does vibrate:

$$E_v = 1/2 h \cdot \nu \quad (\text{Eq. 4.7})$$

When absorption occurs, the molecule acquires a clearly defined amount of energy ($E = h \cdot \nu$) from the radiation and moves up to the next vibrational level ($\Delta v = +1$). If the molecule moves down to the

next vibrational level ($\Delta v = -1$) a certain amount of energy is emitted in the form of radiation.

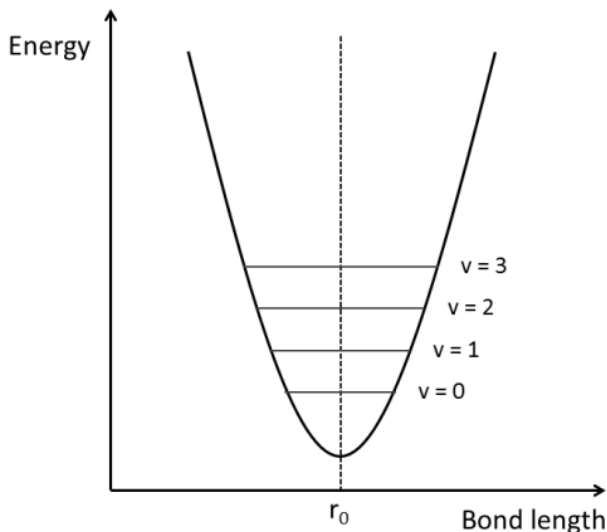


Figure 4.6 The harmonic oscillator model.

A more accurate model of a molecule is given by the anharmonic oscillator. The potential energy is then calculated by the Morse equation and is asymmetric (Figure 4.7). The energy levels are no longer equally spaced and are given by:

$$E_v = (v + 1/2)h \cdot \nu - (v + 1/2)^2 x \cdot h \cdot \nu \quad (\text{Eq. 4.8})$$

with x being the anharmonicity constant.

The anharmonic oscillator model allows for two important effects. As two atoms approach each other, the repulsion increases very rapidly. If a sufficient large vibrational energy is reached the molecule will dissociate. In the case of the anharmonic oscillator, the vibrational transitions no longer only obey the selection rule $\Delta v = \pm 1$. This type of vibrational transition is called a fundamental vibration for $v = 0 \rightarrow 1$ and a hot band for $v = 1 \rightarrow 2$, $2 \rightarrow 3$, etc. Vibrational transitions with $\Delta v = \pm 2, \pm 3, \dots$ are also possible and are termed overtones.

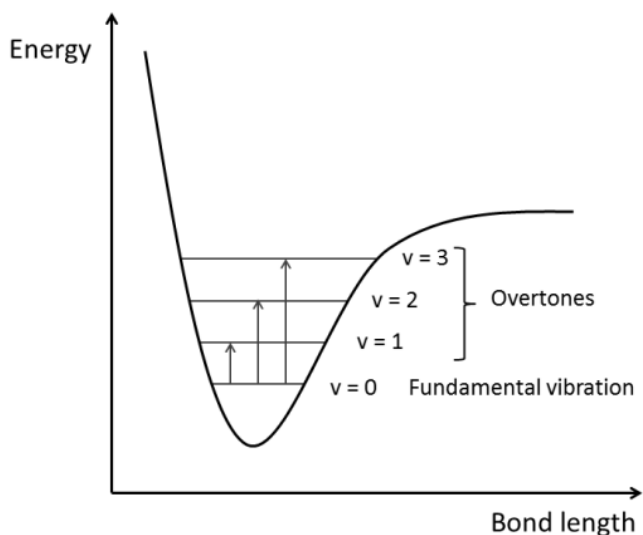


Figure 4.7 The anharmonic oscillator model.

Infrared light can only be absorbed by a molecule if the dipole moment of the specific group of atoms changes during the vibration. The greater the change in dipole moment, the stronger the corresponding IR absorption band will be. Vibrations not accompanied by changes in the dipole moment cannot be excited by IR light and are termed IR inactive or transparent. As a consequence, diatomic molecules such as N_2 or O_2 do not absorb IR light. This is a great advantage since these molecules are the main components of air and thus do not interfere with the IR spectra of molecules of interest such as the target VOC and its by-products.

The absorption of specific wavelengths of IR radiation can trigger different types of excitation, rotations, vibrations and their combinations [431]. Vibrations can involve a change either in bond length (stretching) or bond angle (bending) (Figure 4.8). Some bonds can stretch in-phase (symmetrical) or out-of-phase (asymmetric) as shown in Figure 4.9.

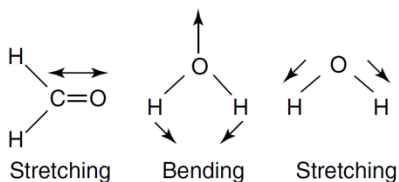


Figure 4.8 Stretching and bending vibrations.

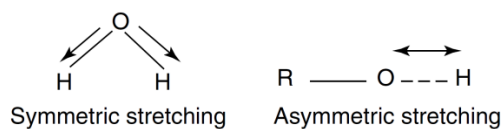


Figure 4.9 Symmetric and asymmetric stretching vibrations

Bending vibrations also contribute to IR spectra as illustrated in Figure 4.10.

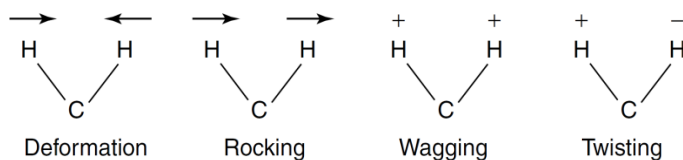


Figure 4.10 Different types of bending vibrations.

4.2.1.5 Instrumentation

Figure 4.11 schematically shows the general lay-out of a typical FT-IR spectrometer. Infrared light emitted from a source is directed into an interferometer which modulates the light. After the interferometer, the light passes through the sample compartment and is then focused onto the detector. The signal measured by the detector is called the interferogram.

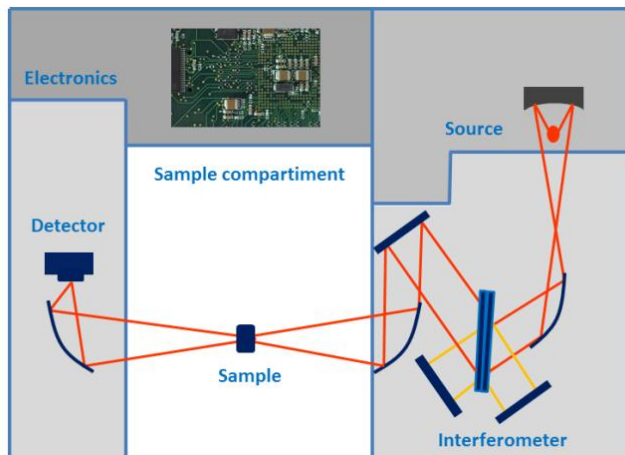


Figure 4.11 General lay-out of a FT-IR spectrometer.

The interferometer is the heart of the spectrometer (Figure 4.12). The collimated light from the IR source impinges on a beamsplitter which ideally transmits 50% of the light and reflects the remaining part. Having travelled the distance L the reflected light hits a fixed mirror M1 where it is reflected and hits the beamsplitter again after a total path length $2L$. The transmitted part of the beam is directed to a movable mirror M2. As this mirror moves back and forth around L by a distance Δx , the total path length is $2(L + \Delta x)$. The light returning from the two mirrors is recombined at the beamsplitter with the two beams having a difference in path length of $2\Delta x$. The beams are spatially coherent and interfere with each other when recombined.

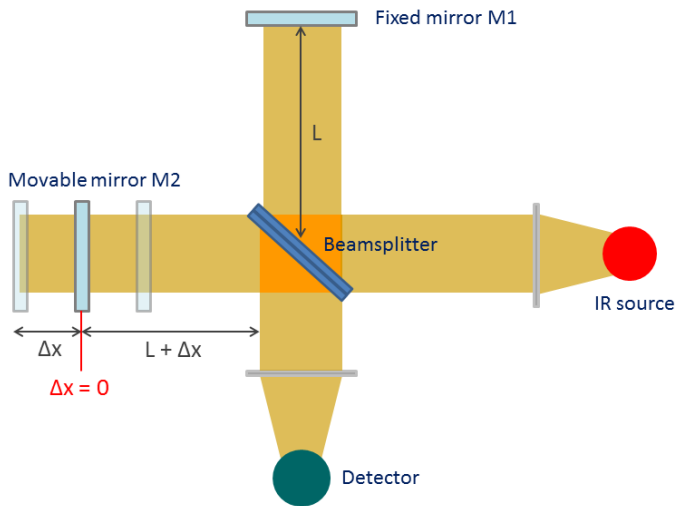


Figure 4.12 The Michelson interferometer.

Figure 4.13 shows the interferogram generated by the detector for a monochromatic source. The interferometer splits and recombines the two beams with a relative phase difference that depends on the mirror displacement or optical retardation [433]. The two beams undergo constructive interference yielding a maximum detector signal if the optical path difference is an integral multiple of the wavelength λ , i.e. if:

$$2 \cdot \Delta x = n \cdot \lambda \quad (n = 0, 1, 2, \dots) \quad (\text{Eq. 4.9})$$

Destructive interference and a minimum detector signal occur if $2\Delta x$ is an odd multiple of $\lambda/2$. The complete functional relationship between $I(\Delta x)$ and Δx is given by:

$$I(\Delta x) = S(\nu) \cdot \cos(2\pi \cdot \nu \cdot \Delta x) \quad (\text{Eq. 4.10})$$

in which we use wavenumber $\tilde{\nu} = 1/\lambda$ which is more common in FT-IR spectroscopy. $S(\tilde{\nu})$ is the intensity of a monochromatic spectral line at wavenumber $\tilde{\nu}$ as shown in Figure 4.13. The intensity plotted as a function of frequency is called a spectrum and can be obtained by Fourier transformation of the signal which is a function of optical retardation. The cosinusoidal interference pattern from a monochromatic source is very useful because it enables a very precise tracking of the movable mirror. All state-of-the-art FT-IR spectrometers use the interference pattern of the monochromatic light emitted by a HeNe laser to monitor the mirror position. The IR interferogram is exactly digitized at the zero crossings of the laser interferogram.

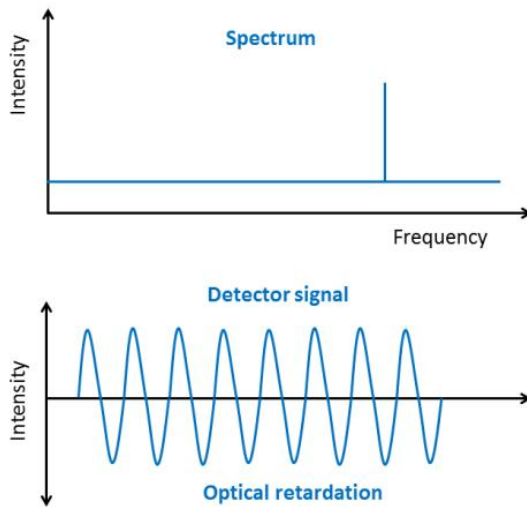


Figure 4.13 Monochromatic source and corresponding detector signal.

Since spectrometers are equipped with a polychromatic light source the interference mentioned above occurs at each wavelength. The interference patterns produced by each wavelength are summed to obtain the resulting interferogram. At the zero path difference of the moving mirror all wavelengths have a phase difference of zero and therefore undergo constructive interference. The intensity is thus a maximum value. As the optical retardation increases, each wavelength undergoes constructive and destructive interference at different mirror positions [433]. Figure 4.14 shows a spectrum consisting of 9 single frequencies, the corresponding wavelengths and

the resulting detector signal to illustrate the discussion mentioned above.

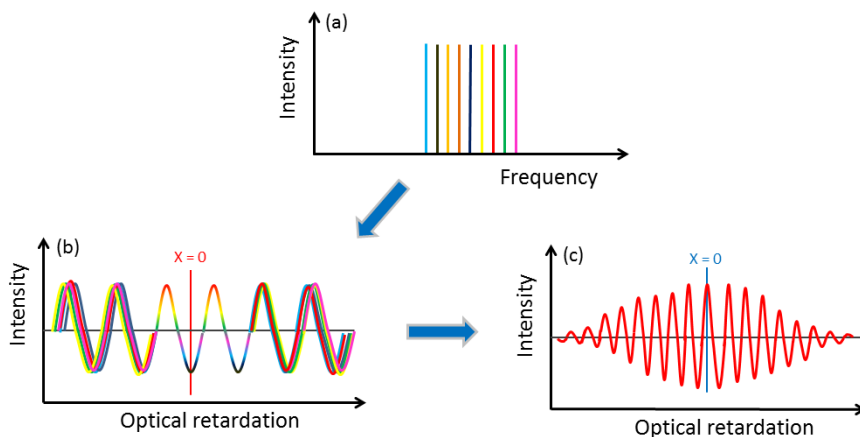


Figure 4.14 (a) Spectrum consisting of 9 single frequencies; (b) the corresponding 9 wavelengths and (c) the resulting detector signal.

Spectrometers are equipped with a broadband light source, which yields a continuous, infinite number of wavelengths. The interferogram is the continuous sum, i.e. the integral of all the interference patterns produced by each wavelength. This results in the intensity curve as a function of the optical retardation shown in Figure 4.15.

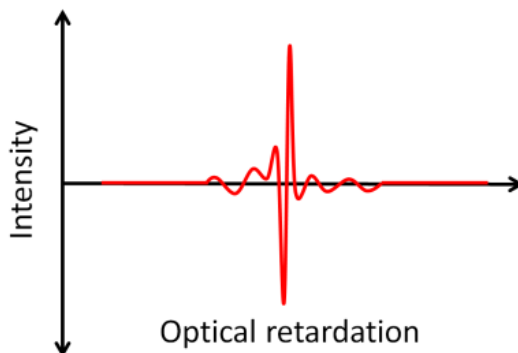


Figure 4.15 Typical interferogram.

The widespread use of FT-IR spectrometers for qualitative and quantitative analysis is a result of the speed and improved signal to

noise ratio compared to dispersive systems. Other advantages are related to the following phenomena [433]:

- The sampling interval of the interferogram, δx , is the distance between zero-crossings of the HeNe laser interferogram and is therefore precisely determined by the laser wavelength. Since the point spacing in the resulting spectrum, $\delta\tilde{\nu}$, is inversely proportional to δx , FT-IR spectrometers have an intrinsic highly precise wavenumber scale (typically a few hundreds of a wavenumber). This advantage of FT-IR spectrometers is known as Connes' advantage.
- The Jacquinot advantage arises from the fact that the circular apertures used in FT-IR spectrometers have a larger area than the slits used in grating spectrometers, thus enabling higher throughput of radiation.
- In grating spectrometers the spectrum $S(\tilde{\nu})$ is measured directly by recording the intensity at successive, narrow wavelength ranges. In FT-IR spectrometers all wavelengths from the IR source simultaneously impinge on the detector. This leads to the multiplex or Fellgett's advantage
- The combination of the Jacquinot and Fellgett advantage means that the signal-to-noise ratio of an FT-IR spectrometer can be more than 10 times that of a dispersive spectrometer.

4.2.1.6 Fourier transformation

Data acquisition results in a digitized interferogram, $I(x)$, which is converted into a spectrum by means of the mathematical operation called a Fourier transform (FT). The general equation for the Fourier transform is applicable to a continuous signal. However, if the signal (interferogram) is digitized and consists of N discrete, equidistant points then the discrete version of the FT must be used [434]:

$$S(k, \Delta\tilde{\nu}) = \Sigma I(n, \Delta x) \exp\left(\frac{i2\pi nk}{N}\right) \quad (\text{Eq. 4.11})$$

The continuous variables x and $\tilde{\nu}$ have been replaced by $n.\Delta x$ and $k.\Delta\tilde{\nu}$, representing the n discrete interferogram points and the k discrete spectrum points.

4.2.1.7 Measurement and evaluation of IR spectra

In the classical infrared measurement technique the gas sample is passed through the gas cell which is placed in the beam path of the IR spectrometer. The IR light transmits the sample and is analyzed in relation to the incident radiation. To calculate an absorbance spectrum the following steps need to be performed. An interferogram measured without any sample (e.g. synthetic air) in the gas cell is Fourier transformed. This results in the single-channel reference spectrum $R(\tilde{\nu})$. A second interferogram, measured with the sample (e.g. reactor effluent) in the gas cell, is Fourier transformed. This results in the single-channel sample spectrum $S(\tilde{\nu})$ which looks similar to the reference spectrum, but shows less intensity at those wavenumbers where the sample absorbs radiation. The final absorbance spectrum $T(\tilde{\nu})$ is obtained by subtracting the sample spectrum by the reference spectrum.

To identify the chemical structure of an unknown substance, the position of its characteristic absorption peaks needs to be compared with standard reference spectra included in the NIST databank [435]. This identification is straight forward for single compound samples. For gas mixtures containing multiple compounds, the structural analysis can be more complex due to overlap and interference of absorption peaks. If the IR spectrum under consideration is not included in the databank the absorption peaks need to be assigned to functional groups. Many functional groups of organic molecules show characteristic vibrations corresponding to absorption peaks within defined ranges of the IR spectrum. The position and intensity of the absorption bands are extremely specific in the case of a pure substance. This enables the IR spectrum, similar to the human fingerprint, to be used as a highly characteristic feature for identification.

If the samples are evaluated for quantitative analysis, spectra in the mid-infrared are calculated in absorbance A according to the Lambert-Beer's law:

$$A = \varepsilon \cdot c \cdot d = -\log(I/I_0) \quad (\text{Eq. 4.12})$$

with ε the molar absorption coefficient, d the optical pathlength of the gas cell, c the concentration, I_0 and I the intensity of the incident and transmitted radiation, respectively. The molar absorption coefficient is a value which depends on either the wavelength or the wavenumber, which is typical for the compound analyzed. Because of the Lambert-Beer law, the relationship between absorbance and concentration of the absorbing substance is a linear function. In

practice the relationship between concentration and absorbance is empirically determined by calibration. Calibrating means finding the mathematical connection between concentration and measurement values. For this purpose, gas mixtures with known concentration are measured, which allows to calculate the calibration function.

4.2.2 Mass spectrometry

Mass spectrometry is a technique that is used to detect gas-phase ions and neutral species generated from a gaseous, liquid or solid sample in order to quantitatively determine its composition. It can also reveal the structural information of detected compounds. This powerful diagnostic method is characterized by its unequalled sensitivity, detection limits, speed and diversity of applications [436].

Figure 4.16 illustrates the principle of MS. In a first stage, the ion source converts the sample into gaseous ions through electron impact ionisation. All ions are then transferred through the mass analyzer where they are characterized by their mass to charge ratio (m/z) and relative abundance. Finally, the ions are detected and the collected data is converted into a mass spectrum.

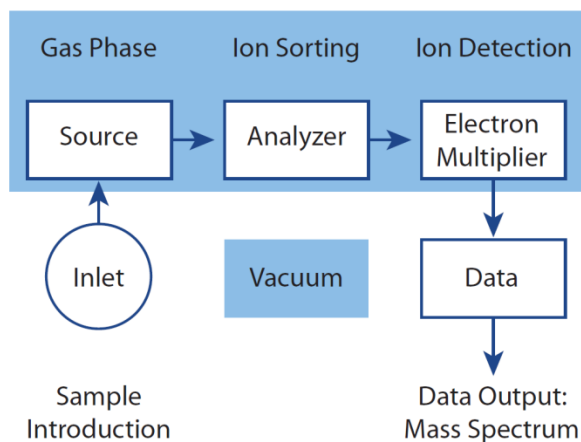


Figure 4.16 Principle of mass spectrometry [436].

The MS used during this PhD study is a quadrupole mass spectrometer. Figure 4.17 shows the principle of this type of MS. The quadrupole MS has many advantages such as the simple manner of scanning the entire mass range, high sensitivity, high measuring and repetition rate.

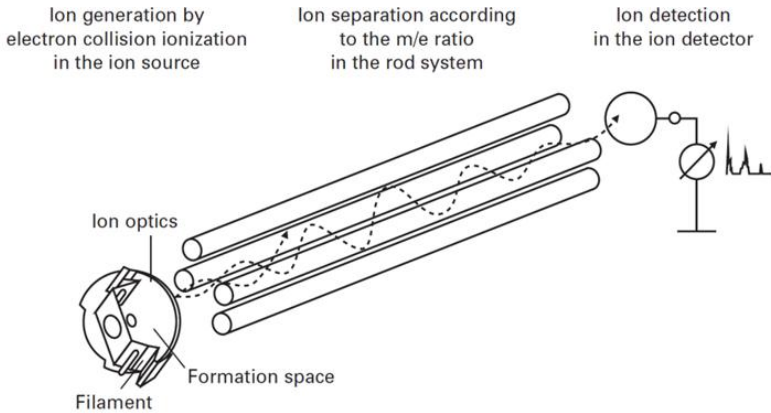


Figure 4.17 Principle of a quadrupole mass spectrometer [437].

The quadrupole MS is in principle an ionization vacuum gauge equipped with a rod system, which first separates the type of ions produced by the ionization process according to their m/z before measuring them with an ion detector. The mass filter consists of 2 pairs of parallel, equidistant metal rods biased at equal but opposite potentials (Figure 4.18). The ions are separated in a high frequency electric quadrupole field between the four rod electrodes with field radius r_0 . The voltage between the electrodes consists of a high frequency alternating voltage $V\cos\omega t$ and a superimposed direct voltage U . When ions are trapped in the direction of the field axis perpendicular to the plane of the diagram, they perform oscillations perpendicular to the field axis under the influence of the high frequency field. For certain values of U, V, ω and r_0 only ions with a particular ratio m/z can pass through the separating field and reach the ion detector. Ions which have a different m/z ratio are rejected by the quadrupole field and can therefore not reach the detector.

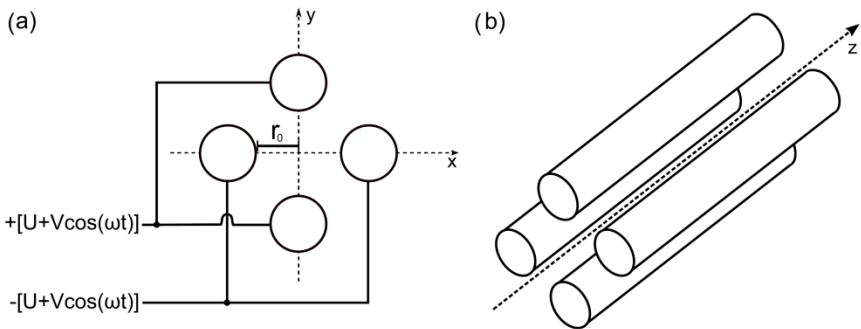


Figure 4.18 Quadrupole mass analyzer [436].

The ions which have been separated according to their m/z ratio in the rod system strike the detector resulting in an ion current which is measured by a sensitive amplifier. There are two main types of detectors. In a Faraday cup, fast moving ions strike the metal cup where they give up their charge while they are neutralized (Figure 4.19(a)). The current flowing away from the cup is transformed into a voltage signal which is proportional to the number of impinging ions. The Faraday collector has a cup-like shape to recapture secondary electrons upon ion impact. Faraday cups have a relatively low but stable sensitivity and a slow response time. In a secondary electron multiplier (SEM), ions strike a surface (dynode) and cause secondary electron emission. There are two types of SEM detectors depending on whether they are built with discrete dynodes (Figure 4.19(b)) or with one continuous dynode (Figure 4.19(c)). In principal, ions generate secondary electrons by impact on the dynode which are accelerated to cause even more secondary electrons on the following dynode. The amplified electron current is again converted into a voltage signal which is proportional to the number of impinging ions. For a SEM with continuous dynode, the principle is similar but the dynode is made of a material with high resistance and hence a large voltage drop along its length. SEMs have a high amplification factor and fast response time but a limited lifetime.

Recently, Benedikt et al. have reviewed the use of quadrupole mass spectrometry for the analysis of reactive plasmas [436].

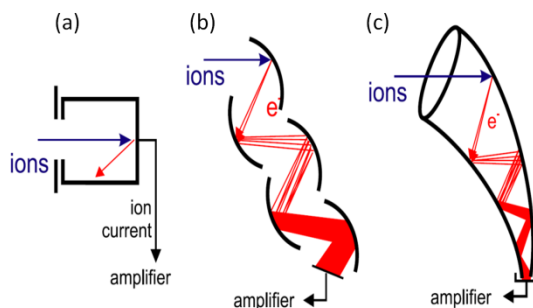


Figure 4.19 Different types of ion detectors: (a) Faraday cup, (b) SEM with discrete dynodes and (c) SEM with continuous dynode [436].

4.2.3 Detection of ozone

The concentration of ozone is determined with an UV absorption ozone monitor. The measurement is based on absorption of 254 nm UV light due to an internal electronic resonance of the O_3 molecule.

The monitor uses a mercury lamp constructed so that a large majority of the light emitted has a wavelength of 254 nm. Light from the lamp shines down a hollow quartz tube which is alternately filled with sample gas and with scrubbed gas to remove ozone. The ratio of the intensity of light passing through the scrubbed gas to that of the sample forms a ratio I/I_0 . This ratio forms the basis for the calculation of the ozone concentration which is based on the Lambert–Beer equation:

$$C_{O_3} = -\frac{10^6}{\varepsilon \cdot L} \times \frac{T}{273^\circ K} \times \frac{29.92 \text{ in Hg}}{P} \times \ln \frac{I}{I_0} \quad (\text{Eq. 4.13})$$

where I is the intensity of light passed through the sample, I_0 the intensity of light through the sample free of ozone, ε the molar absorption coefficient, L the optical path length, C_{O_3} the concentration of ozone in ppm, T the sample temperature in degrees Kelvin and P the pressure in inches of mercury.

4.2.4 X–ray photoelectron spectroscopy

As catalytic reactions take place at the surface of heterogeneous catalysts, understanding the nature of the outer atomic layers of such surfaces is of great interest for the creation and improvement of such materials. In this regard, XPS is a very powerful surface analysis technique which can provide quantitative information on the elemental atomic surface composition. It can also resolve different types of bonds and functionalities at the surface.

The main principle of XPS is based on the photoelectric effect first noted by Hertz in 1887 [438]. X–ray photons are used to ionise surface atoms whereafter the energy of the ejected photoelectrons is detected and measured. A solid sample is therefore irradiated with soft X–rays under ultra high vacuum (UHV) conditions ($< 10^{-6}$ Pa). This is crucial to avoid surface contamination of the sample and to minimize the collision probability of emitted electrons with molecules of the background gas. X–ray absorption by atoms at the surface of the sample leads to the ejection of an electron (photoionisation) from either a tightly bounded, inner core electron shell or from a more weakly bounded valence electron shell (Figure 4.20). Based on the conservation of energy, the kinetic energy E_K of the emitted electron is given by the following equation:

$$E_K = h\nu - E_B + \Phi_{sp} \quad (\text{Eq. 4.14})$$

where E_K is the measured kinetic energy of the emitted electron, $h\nu$ is the energy of the exciting X-ray photon, E_B is the electron binding energy to the atom and Φ_{sp} is the work function of the spectrometer.

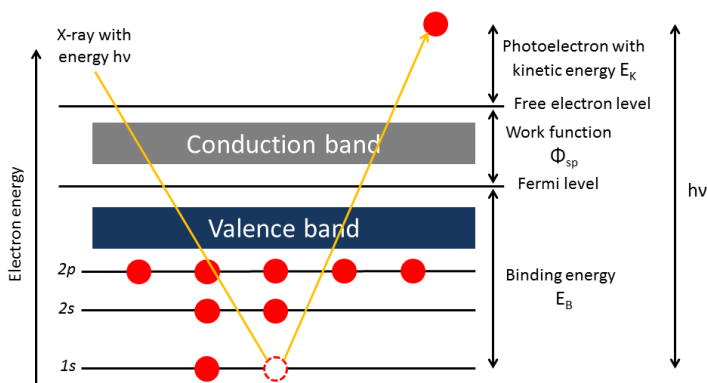


Figure 4.20 Principle of XPS.

The intensity and energy of the photoelectron emission is analyzed, producing an XPS spectrum. Careful analysis of this spectrum reveals the elemental composition of the sample. Moreover, relative amounts of binding/oxidation states of specific elements can be obtained by peak deconvolution followed by peak integration of high resolution elemental spectra (core level spectra).

The most important parts of an XPS spectrometer are a monochromated X-ray source ($MgK\alpha$ or $AlK\alpha$), a UHV system connected to the sample chamber and an electron analyzer (mostly a spherical sector analyzer) with electron detector (Figure 4.21).

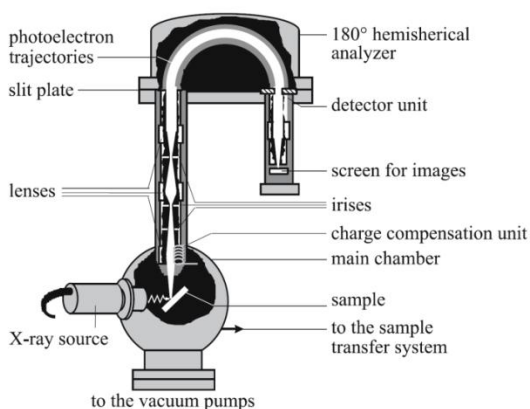


Figure 4.21 Typical build-up of an X-ray photoelectron spectrometer [439].

4.2.5 Time-of-flight secondary ion mass spectroscopy

Time-of-flight secondary ion mass spectroscopy (ToF-SIMS) is an analytical method for the chemical characterisation of solid surfaces. With this method, the atomic and molecular composition of the outermost 1–3 monolayers can be obtained [440]. The sample is therefore bombarded with a pulsed primary ion beam of high energy, typically Bi, Xe, Ga or Cs, and focused on the surface of the sample (Figure 4.22). The energy of the ion beam is transferred to the region near the surface by collisions between the primary ions and the sample atoms as well as by collisions between sample atoms. This collision cascade transports a small fraction of the energy back to the surface and leads there to emission of neutral species, secondary electrons and secondary ions (sputtering) [440].

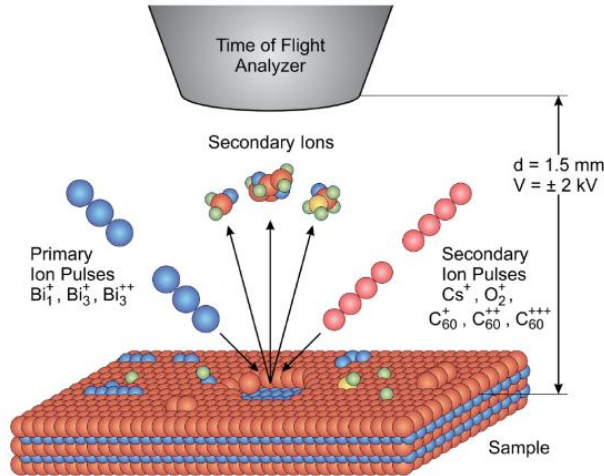


Figure 4.22 Principle of ToF-SIMS [441].

The secondary ions are then electrostatically accelerated into a field-free drift region with a nominal kinetic energy E_k of:

$$E_k = eV_0 = \frac{mv^2}{2} \quad (\text{Eq. 4.15})$$

where V_0 is the accelerating voltage, m the mass of the ion, v the flight velocity of the ion and e its charge. Hence, ions with lower mass have a higher flight velocity than the ones with higher mass. As a result the mass separation is obtained in the flight time t from the sample to the detector which is expressed by:

$$t = \frac{L}{\sqrt{2eV_0/m}} \quad (\text{Eq. 4.16})$$

where L is the effective length of the mass spectrometer. In this way, an accurate determination of the flight time yields the chemical composition of the emitted ions and thus the elemental and molecular composition of the sample surface.

The instrumentation of a ToF-SIMS analyzer primarily consists of an UHV system, a primary ion source (ion gun), an electron source for charge compensation and a ToF mass spectrometer (Figure 4.23).

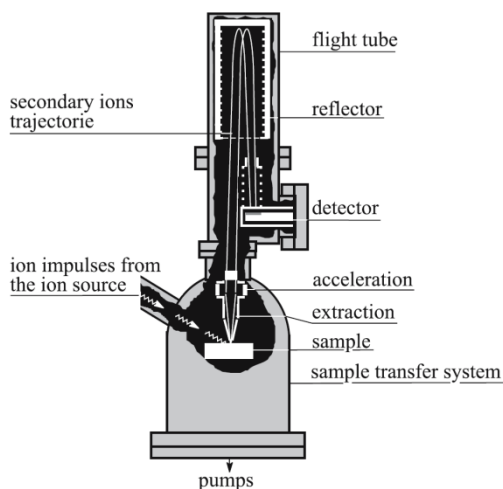


Figure 4.23 Typical build-up of a ToF-SIMS analyzer [439].

4.2.6 Raman spectroscopy

Raman spectroscopy is a spectroscopic technique based on inelastic scattering of monochromatic light, usually emitted by a laser source. Inelastic scattering means that the frequency of photons in monochromatic light changes upon interaction with a sample (Figure 4.24). Photons of the laser light are absorbed by the sample and then reemitted. The frequency of these reemitted photons is shifted up or down in comparison to their original frequency, which is known as the Raman effect. This shift provides information about vibrational, rotational and other low frequency transitions in molecules. Based on this information, a fingerprint can be obtained by which molecules can be identified.

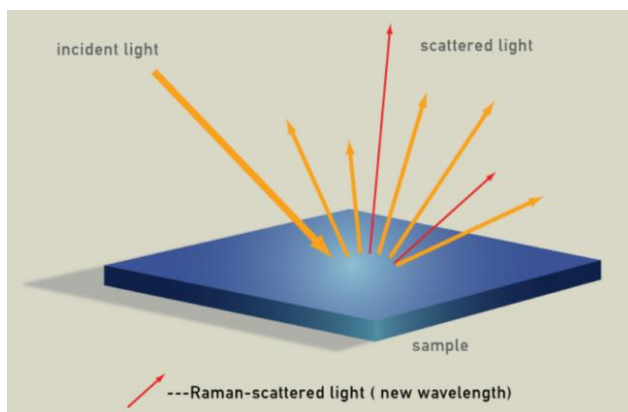


Figure 4.24 Principle of Raman spectroscopy [442].

4.2.7 X-ray powder diffraction

X-ray powder diffraction is a rapid analytical technique primarily used for phase identification of a crystalline material. The scattering of X-rays from atoms in a crystal produces a diffraction pattern which contains information about the atomic arrangement within the crystal. A typical X-ray diffractometer consists of three basic elements: an X-ray tube, a sample holder and an X-ray detector (Figure 4.25). X-rays are generated in cathode ray tube by heating a filament to produce electrons. These electrons are accelerated by applying a voltage thereby bombarding the target material (Cu, Fe, Mo, Cr). When the electrons gain sufficient energy to dislodge inner shell electrons of the atoms, characteristic X-rays are produced. The X-rays are collimated and directed onto the sample. As the sample and detector are rotated, the intensity of the reflected X-rays is recorded. When the geometry of the incident X-rays impinging the sample satisfy the Bragg equation:

$$n\lambda = 2d \sin \theta \quad (\text{Eq. 4.17})$$

constructive interference occurs and a peak in intensity occurs.

A detector records and processes this X-ray signal and converts the signal to a count rate which is then output to a device such as a printer or computer monitor. The geometry of an X-ray diffractometer is such that the sample rotates in the path of the collimated X-ray beam at an angle θ while the X-ray detector is mounted on an arm to collect the diffracted X-rays and rotates at an angle of 2θ .

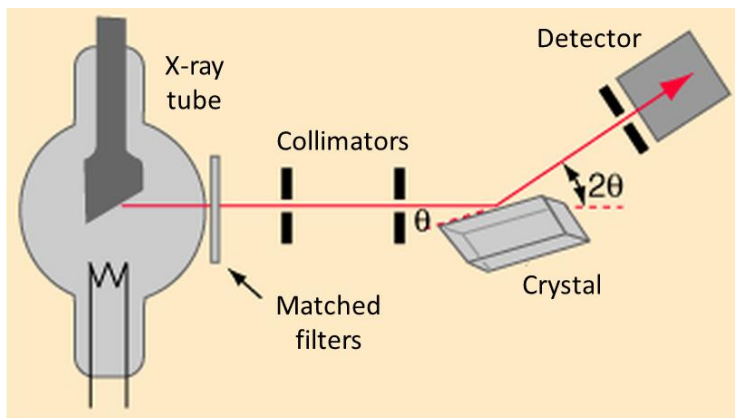


Figure 4.25 Principle of X-ray powder diffraction [443].

4.2.8 Determination of specific surface area of catalysts

In this work, the specific surface area of catalysts has been determined by adsorption using the Brunauer–Emmett–Teller (BET) isotherm. The BET method involves the determination of the amount of the adsorbate or adsorptive gas required to cover the external and the accessible internal pore surfaces of a solid with a complete monolayer of adsorbate. This monolayer capacity can be calculated from the adsorption isotherm by means of the BET equation.

The gases used as adsorptives have to be only physically adsorbed by weak bonds at the surface of the solid (van der Waals forces) and can be desorbed by a decrease of pressure at the same temperature. The most common gas is nitrogen at its boiling temperature (–195.7°C). In order to determine the adsorption isotherm volumetrically, known amounts of adsorptive are admitted stepwise into the sample cell containing the sample previously dried and outgassed by heating under vacuum. The amount of gas adsorbed is the difference of gas admitted and the amount of gas filling the dead volume (free space in the sample cell including connections). The adsorption isotherm is the plot of the amount gas adsorbed (in mmol/g) as a function of the relative pressure p/p_0 . The plot should give a straight line $y_{BET} = i + kx$ within the so called BET relative pressure range. Both the intercept and the slope, which are determined by means of linear regression, must be positive. From these values, the monolayer capacity n_{mono} (in mmol/g) can be calculated according to $n_{mono} = (i + k)^{-1}$. The specific surface area

α_{BET} is calculated from the monolayer capacity by assessing a value σ for the average area occupied by each molecule in the complete monolayer:

$$\alpha_{BET} = n_{mono}\sigma N_A \quad (\text{Eq. 4.18})$$

with N_A the Avogadro constant.

4.2.9 Determination of metal dispersion on catalyst surface

The metal dispersion on the catalyst surface is defined as the percentage of all metal atoms in the sample that are exposed and available to catalyze surface reactions. The dispersion δ is calculated from:

$$\delta = M \frac{L_m}{N_A} \times \frac{100}{\chi m_s} \times 100\% \quad (\text{Eq. 4.19})$$

where M is the molecular weight of the metal, L_m is the number of exposed metal atoms found by adsorption, χ is the loading defined as the total amount of metal in the sample and m_s is the mass of the sample.

The metal dispersion on the catalyst surface was determined by H_2 pulsed chemisorption measurements. Therefore, variable volumes of analysis gas are injected into the inert carrier gas stream which continuously flows over the sample. The detector measures the volume of gas that remains unadsorbed by the sample. Subtraction from the total amount injected gives the total amount adsorbed.

Chapter 5

Material and methods

5.1 General

The experimental set-up shown in Figure 5.1 consists of three main parts, i.e. the gas supply system, the reactor system and the gas analysis system. In the following sections these parts will be discussed in more detail. During the course of this study, modifications and optimizations were implemented to improve the operation and ease of use of the set-up. In this chapter, the preparation of the catalysts is also described. In order to characterize the catalysts, numerous analytical techniques were used for which the experimental conditions are summarized here. Furthermore, the calibration of the FT-IR spectrometer is discussed. Finally, the experimental parameters used to evaluate the VOC removal process are introduced.

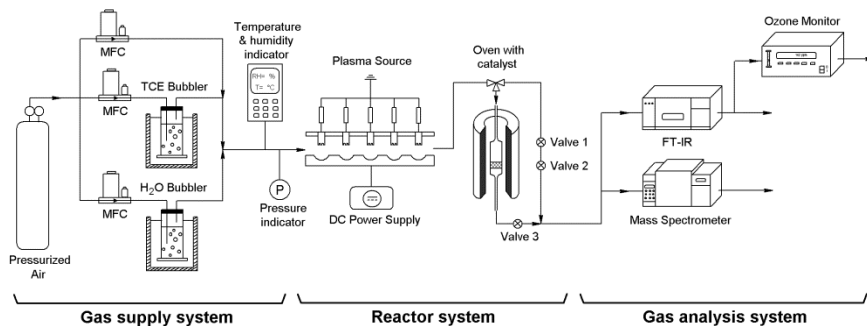


Figure 5.1 The experimental set-up.

5.2 Gas supply system

The function of the gas supply system is to generate a VOC-polluted air stream as feed for the reactor system. It is essential that this system is able to supply a feed stream with stable conditions such as air flow rate, air humidity and initial VOC concentration. To generate a typical feed stream, air was fed to 2 mass flow controllers. During the course of this work the original mass flow controllers (MKS Instruments, 1559AX-020L-SV) were replaced by new ones with a better stability (Bronkhorst, ElFlow). TCE vapor was generated by passing a small air flow through a bubbling bottle containing liquid TCE (99.99% purity, Acros). The bubbling bottle was located in a thermostatic water bath maintained at -8°C by adding antifreeze to the water. This low temperature is needed to decrease the volatility of TCE which facilitates the generation of TCE/air mixtures with stable initial concentrations. The TCE/air mixture is then diluted with a larger air flow to obtain the desired initial TCE concentration and

flow rate. In order to add humidity to the TCE/air mixture, an additional bubbling bottle containing demineralized water was used. This bubbling bottle was also located in a thermostatic water bath. By controlling the flow rate through the bottle and the temperature of the water bath, the air humidity could be fixed at the desired value.

The air humidity and temperature were measured with a Testo 445 device (Figure 5.2). The temperature/humidity probe was therefore located in a closed vessel in which the feed gas circulated. The vessel was placed between the gas supply system and the reactor inlet. The gas pressure of the air flowing through the set-up was measured by means of a Digital Pressure Indicator 705 (Figure 6.2).

In order to stabilize the feed gas mixture, the plasma reactor was turned off and the flow was sent through a bypass of the catalytic reactor. As the vapor-liquid equilibrium in the bubbling bottles is very pressure sensitive, special care needed to be paid to maintain a constant pressure in the entire system during the stabilisation period. Therefore, 2 valves (Figure 5.1, valve 1 & 2) were installed in the bypass to simulate the pressure drop over the catalyst bed. This pressure drop increased along with the catalyst temperature as the powder became more compact at elevated temperatures. By using 2 valves, the pressure drop could be more easily mimicked than with 1 valve. An extra valve was installed (Figure 5.1, valve 3) to prevent backflow through the catalyst bed when the 3-way valve was switched from catalyst to bypass.



Figure 5.2 Testo 445 climate measurement device with temperature/humidity probe (left) and Digital Pressure Indicator 750 (right).

5.3 Reactor system

5.3.1 Plasma reactor

During the course of this work, use was made of two different home made plasma reactors both based on a multi-pin-to-plate negative DC corona/glow discharge. These reactors are nominated “Reactor A” and “Reactor B” depending on whether the number of electrode pins is 5 or 10, respectively.

5.3.1.1 Plasma reactor A

Figure 5.3 shows the plasma reactor A with 5 electrode pins. The feed gas flowed through a rectangular duct with a cross section of 40 mm × 9 mm and a length of 200 mm. The plasma reactor consisted of five aligned, crenellated cathode pins which were positioned 28 mm from each other. The distance between the five cathode pins and the single anode plate was 10 mm. In order to observe the discharge a small window was installed at the front side of the reactor. The discharge was powered with a 30 kV/20 mA DC power supply (Bayerle) and generated at atmospheric pressure and room temperature.

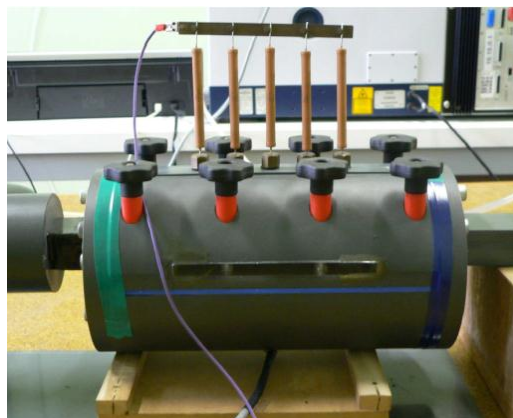


Figure 5.3 Plasma reactor A with 5 electrode pins.

5.3.1.2 Plasma reactor B

Figure 5.4 shows the plasma reactor B which is an optimized version of reactor A. The cylindrical casing of the reactor was made of Teflon and inserted in a glass tube which was closed by airtight fittings in order to prevent any leakages. The feed gas also flowed

through a rectangular duct with a cross section of 40 mm × 9 mm and a length of 400 mm which is twice the length of reactor A. The plasma reactor consists of 10 aligned, crenellated cathode pins which were positioned 28 mm from each other. The distance between the 10 cathode pins and the single anode plate is 10 mm. The discharge is powered with a DC power supply (Technix, SR40-R-1200) and generated at atmospheric pressure and room temperature.

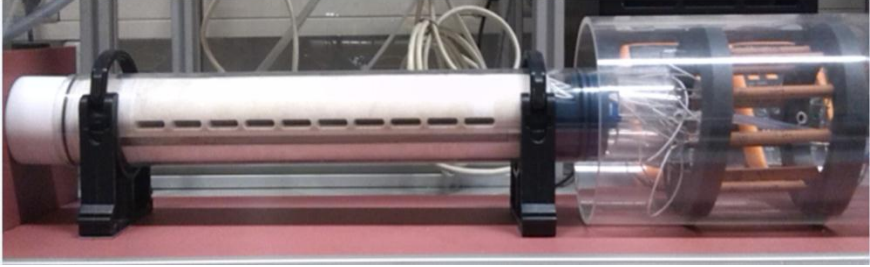


Figure 5.4 Plasma reactor B with 10 electrode pins.

5.3.1.3 Measurement of discharge current and voltage

Figure 5.5 shows the electrical scheme of the discharge. To determine the plasma voltage U_{pl} , a high voltage probe (Fluke 80 K-40, division ratio 1/1000) was used to measure the total voltage U_{tot} applied to the plasma reactor. The discharge current I was determined by recording the voltage signal U_m across a 100 Ω resistor R_m placed in series between the counter electrode and ground. Two multimeters $\text{\textcircled{V}}$ were used to monitor both U_{tot} and U_m .

The threshold current for the glow-to-spark transition was increased by profiling the anode surface with hollow spherical surface segments centered on the tip of each crenellated cathode pin [120]. The spherical surface segment had a radius of curvature of 17.5 mm and a depth of 5 mm. Stable and uniform glow discharge operation was ensured by the gas flow and by ballasting each cathode pin with a 1.5 M Ω resistor R_p . The fraction of the total electrical power that was dissipated in these resistors amounted to 10% at most.

As can be seen from Figure 5.5, the plasma voltage U_{pl} was calculated as follows:

$$U_{pl} = U_{tot} - U_b - U_m \quad (\text{Eq. 5.1})$$

$$U_{pl} = U_{tot} - \frac{R_b I}{N} - RI \quad (\text{Eq. 5.2})$$

where N is the number of electrode pins.

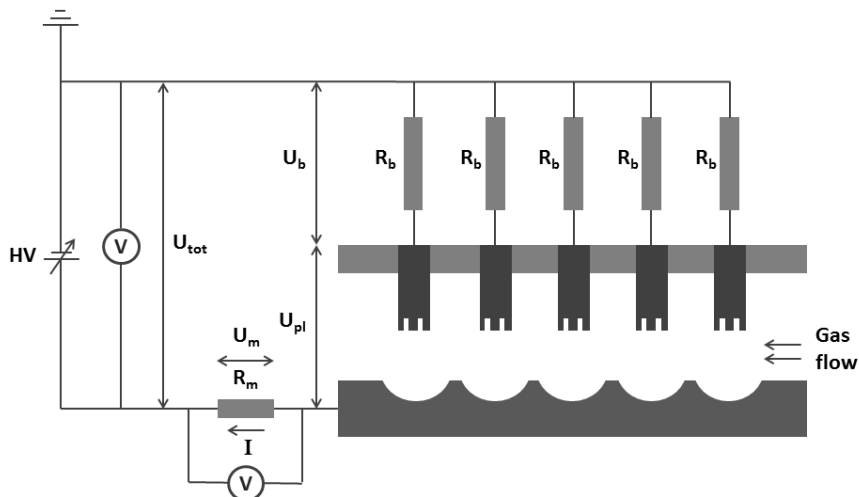


Figure 5.5 Electrical scheme of the multi-pin-to-plate discharge.

5.3.2 Catalytic reactor

The catalytic reactor consisted of a cylindrical glass tube located in a temperature controlled vertical tubular oven (Figure 5.6). This oven was a home made model delivered by UCCS from Lille University. The tube was made in Pyrex glass and had an inner diameter of 20 mm and an effective length of 100 mm. A sintered, porous plate inside the tube held the catalyst powder in place. Measurements were performed after thermal balance was reached.

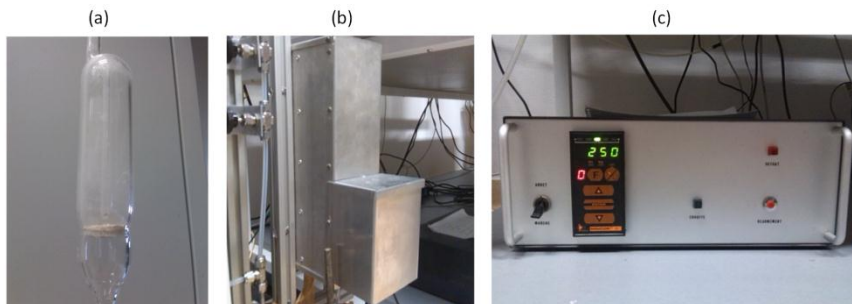


Figure 5.6 Catalytic reactor system with (a) glass tube, (b) oven and (c) temperature controller.

5.4 Gas analysis system

5.4.1 FT-IR spectrometer

Figure 5.7 shows the Bruker Vertex 70 FT-IR spectrometer used during this work. For a description of the working principles, reference is made to Section 4.3.1. The following experimental conditions were used to measure both the background and sample spectrum. The latter measurements were recorded after steady-state condition was reached, typically after approximately 5 minutes.

- Resolution: 4 cm^{-1}
- Number of scans: 20
- Scan velocity: 20 kHz
- Aperture: 1 mm

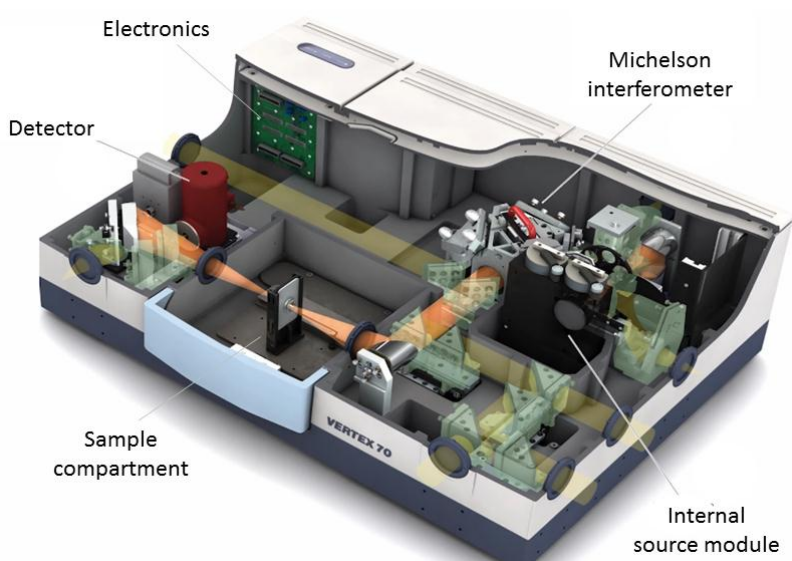


Figure 5.7 Bruker Vertex 70 FT-IR spectrometer [444].

The optical bench of the FT-IR was purged with air delivered from a CO_2 -dryer while the sample compartment was purged with dry synthetic air in order to avoid any interference of these compounds. The mercury-cadmium-telluride (MCT) detector was nitrogen cooled and OPUS (Bruker) software was used to collect and analyze the obtained spectra.

Figure 5.8 shows the three gas cells with different optical path length that were used during this course of this PhD study:

- Gas cell with 10 cm optical path length (Figure 5.8(a))
- Gas cell with adjustable optical path length (0.8 – 8 m) (Figure 5.8(b))
- Gas cell with 20 cm optical path length (Figure 5.8(c))

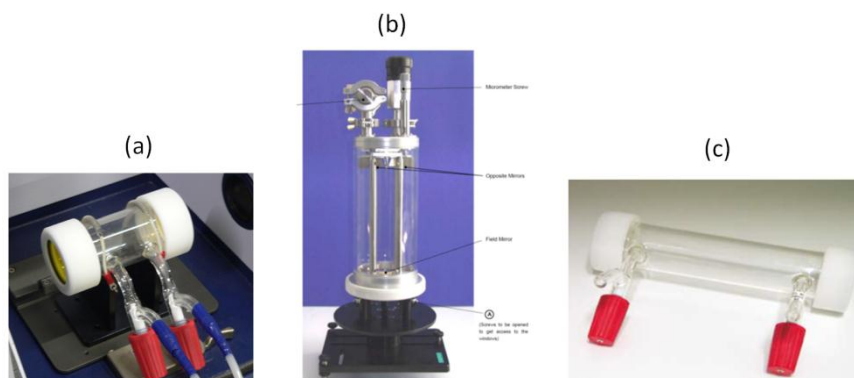


Figure 5.8 The different gas cells used during this PhD study.

All these gas cells enabled online measurements. In order to correctly analyze the gas composition a certain amount of gas needs to pass the cell to achieve an equilibrium state. The 10 cm gas cell, which was initially used, allowed quick analysis as the volume of the cell was the smallest. However, the signal to noise ratio was relatively small which impeded accurate quantitative analyses. The long path gas cell with adjustable length was able to detect gas species in several times lower concentrations than the 10 cm gas cell. Although it seems a better option than the 10 cm gas cell, we experienced some serious issues. Firstly, as a consequence of the large cell volume, the time needed to obtain an equilibrium state was quite long. This was not so practical as the total time needed to perform a certain experiment drastically increased. Secondly, we experienced serious problems due to the formation of deposits on the golden mirrors inside the cell. The cell was mounted in a heating jacket which prevented to check the interior status of the cell. As we were not aware of the formation of deposits, it accumulated and finally destroyed the mirrors. Unfortunately, we were not able to use the long path gas cell any more. As an alternative, we chose to acquire a 20 cm gas cell. This cell had a better signal to noise ratio than the 10 cm gas cell while the time needed to obtain equilibrium was still short.

5.4.2 Mass spectrometer

The mass spectrometer (MS) used in these experiments was a Quadrupole MS (OmniStar GSD 301 O₂ Pfeiffer Vacuum) equipped with a Faraday cup and an SEM (channeltron) detector (Figure 5.9). Balzers Quadstar 200 (QMS 200) software (Pfeiffer Vacuum) was applied for collecting and displaying data. Only the maximum peak intensities and the corresponding m/z numbers were collected. The peaks were represented as bar lines over the corresponding m/z. The qualitative identification of the by-products was achieved using Scan Bargraph mode and a SEM voltage of 1600 V in the mass range 0–200 m/z and an acquisition rate of 1.5 scan/min. A resolution of 50 with electron ionization energy of 60 V was adopted.



Figure 5.9 OmniStar GSD 301 O₂, Pfeiffer Vacuum [445].

5.4.3 Ozone monitor

The ozone measurements were carried out with an Envitec ozone monitor model 450 (Figure 5.10). The specifications of the ozone monitor are listed in Table 5.1.



Figure 5.10 Envitec ozone monitor Model 450 [446].

Table 5.1 Specifications of the ozone monitor.

Measurement range	0 – 1000 ppm
Lower detectable limit	0.003 ppm
Sample flow rate	1 – 2.5 L/min
Accuracy	± 0.1%
Resolution	0.01 ppm

5.5 Preparation of catalysts

5.5.1 MnO₂

Manganese oxide was purchased from Panreac. Before its use, it was calcined for 4 h at 500°C under a stream of dry synthetic air with a flow of 200 mL/min.

5.5.2 LaMnO_{3+δ}

Perovskite (LaMnO_{3+δ}) was synthesized via the amorphous citrate precursor method. Stoichiometric amounts of aqueous solution of the salts of the corresponding metal nitrates (La(NO₃)₃·6H₂O ≥ 99.0% Fluka, Mn(NO₃)₂·6H₂O Aldrich, C₆H₈O₇ Fluka) were mixed with an aqueous solution of citric acid so that the ratio of the number of total metal moles to that of citric acid was equal to one. The resulting solution was stirred at room temperature and evaporated at 60°C for 2 h to obtain syrup. After drying in an oven at 100°C overnight and then at 220°C for 2 h the resulting powder was calcined in air at 700°C (2°C/min) for 10 h.

5.5.3 Pd/LaMnO₃

Pd(0.5wt%)/LaMnO₃ (PdLM) was prepared with the wet impregnating method using Pd(NO₃)₂ (46% wt/wt%, Acros) as palladium precursor. The mixture was stirred at room temperature and the water was removed at 60°C for 2 h by rotary evaporation. After drying in an oven at 100°C overnight, the resulting powder was calcined in dry air flow (200 mL/min) at 350°C for 4 h.

5.5.4 Ce–Mn binary oxides

5.5.4.1 CeMn_xO_y

The KMnO₄ precursor was titrated with an aqueous solution of Ce³⁺(Ce(NO₃)₃·6H₂O (Alfa Aesar 99.5%) and Mn²⁺ ions (Mn(NO₃)₂·4H₂O, 99.98%, Aldrich) at varying pH (from 3.0 to 8.0) considering the redox reactions under concern [447]. The amount of the various precursors was determined in accordance with the quantitative relationships provided by the system of equations previously given in [447] referring to electron and mass balances and the designed catalyst composition, respectively. In a typical experiment a suitable amount of KMnO₄ (Fluka, 99%), in excess of 10% from the stoichiometry, dissolved in 40 mL of deionized water was added to the metal nitrate precursors aqueous solution (30 mL). A KOH solution (0.2 M solution) was then added dropwise, under constant stirring, to a final pH of 8.0 (±0.5). The solid was then digested for 30 min, subsequently filtered, washed with distilled water several times and dried overnight at 100°C. The resulting powders were further calcined in air at 500°C (4 h). The Ce–Mn based samples were labeled CeMn_x (x = 1, 4).

5.5.4.2 MnO_y

Ammonia (Verbièse, 25%) was added dropwise to an aqueous solution of the Mn nitrate precursor (Mn(NO₃)₂·4H₂O, 99.98%, Aldrich) under constant stirring until the pH reached a value of 10.0. The resulting solid was then kept under stirring for 15 min. After filtration and washing, the solid was dried overnight at 100°C and subsequently calcined in a similar procedure for CeMn_x to yield the MnO_y catalyst.

5.6 *Catalyst characterization*

5.6.1 XPS

XPS spectra of the samples were recorded using a Kratos AXIS Ultra DLD spectrometer (Figure 5.11) with a monochromatic Al K α radiation source ($h\nu = 1486.7$ eV) operating at 15 kV and 10 mA. High resolution (0.1 eV) spectra were then recorded for pertinent photoelectron peaks at pass energy of 40 eV to identify the chemical state of each element. All the binding energies (BEs) were referenced

to the C1s neutral carbon peak at 285 eV. The processing and curve fitting of the high resolution spectra were performed using CasaXPS software.



Figure 5.11 Kratos AXIS Ultra DLD spectrometer [448].

5.6.2 ToF–SIMS

Positive and negative ToF–SIMS measurements were performed with a ToF–SIMS spectrometer (ION–TOF GmbH Germany) equipped with a bismuth liquid metal ion gun (LMIG) (Figure 5.12). The compacted samples were bombarded with pulsed Bi^{3+} primary ion beam (25 keV, 0.25 pA) rastered over a $500 \times 500 \mu\text{m}^2$ surface area. With a data acquisition of 100 s, the total fluence does not amount up to 10^{12} ions/cm² ensuring static conditions. Charge effects were compensated by means of a 20 eV pulsed electron flood gun. In these experiments, the mass resolution ($m/\Delta m$) was about 7000 at $m/z = 139$ for La^+ . The containing chlorine fragments were identified by their exact mass, coupled with the appropriate intensities for the expected isotope pattern.



Figure 5.12 Ion ToF–SIMS 5 [449].

5.6.3 Raman spectroscopy

The Laser Raman Spectra (LRS) of the samples were recorded on a LabRam Infinity (Jobin Yvon – Horiba) spectrometer equipped with a liquid nitrogen cooled CCD detector and a frequency doubled Nd:YAG green laser at 532 nm (Figure 5.13). The power applied on the sample was 60 μ W for the Ce–Mn samples as higher applied power led to phase transformation leading to CeO₂ and Mn₃O₄ due to sample heating phenomenon [19].



Figure 5.13 LabRam Infinity.

5.6.4 X–ray powder diffraction

Phase analysis was performed by X–ray powder diffraction using a D8 Advance–Brücker (Figure 5.14) using the $K_{Cu\alpha 1} = 1.5406 \text{ \AA}$. The data of 2θ in the 10–90° range were collected with a step size of 0.02° and an integration time of 5 s. The diffraction patterns were indexed by comparison with the Joint Committee on Powder Diffraction Standards (JCPDS) files.



Figure 5.14 D8 Advance–Brücker.

5.6.5 Determination of specific surface area of catalysts

The specific surface areas of the catalysts were measured with a Tristar II 3020 (Micromeritics) set-up (Figure 5.15). Prior to measurement, the catalysts were preheated at 150°C in flowing N₂ for 1 h.



Figure 5.15 Tristar™ II 3020 (Micromeritics).

5.6.6 Determination of metal dispersion on catalyst surface

The metal dispersion on catalysts was determined by H₂ pulsed chemisorption measurements at 100°C using a Micromeritics AutoChem II 2920 apparatus (Figure 5.16). Before analysis, the sample was treated at 200°C in H₂ for 2 h (3°C/min) and then in Ar at 400°C for 2 h (10°C/min).



Figure 5.16 AutoChem II 2920 Micromeritics.

5.7 Calibration of FT-IR spectrometer

The FT-IR spectrometer was calibrated with calibration mixtures delivered by Air Liquide. Table 5.2 shows the composition of the calibration mixture.

Table 5.2 Composition of the FT-IR calibration mixture.

Name	Formula	Concentration (ppm)	Integration limits (cm ⁻¹)
Carbon monoxide	CO	250	2144–2223
Carbon dioxide	CO ₂	250	2283–2393
Trichloroethylene	C ₂ HCl ₃	500	916–966

The calibration was repeated approximately each 2 months to ensure accurate determination of the concentration of these compounds. Therefore, the mixture was passed through the gas cell with a flow of 2 L/min until steady-state condition was reached. Then, 20 spectra recorded each minute were averaged to obtain the required surface area of the absorption peaks under consideration.

After calibration of the FT-IR for CO and CO₂, a peak area in IR absorbance was adopted to calculate the concentration with a special care in CO peaks due to overlapping with ozone and N₂O peak. For experiments carried out with air from the compressor the atmospheric CO₂ contribution was removed to determine the actual CO₂ concentration.

5.8 Experimental parameters for the evaluation of the VOC abatement process

The VOC abatement process can be evaluated by various parameters. The most frequent and practical ones will be introduced here.

- Discharge power P is the power deposited into the plasma:

$$P = U_{pl}I \quad (\text{Eq. 5.3})$$

where U_{pl} is the plasma voltage and I the discharge current.

- Energy density ED is the energy deposited per unit volume of process gas:

$$ED = \frac{E}{V} = \frac{P}{Q} \quad (\text{Eq. 5.4})$$

where E is the energy deposited in the treated volume V and Q is the gas flow rate. The unit of ED is J/L although other units such as kWh/m^3 are also possible.

- The TCE abatement is the basic parameter which indicates the relative amount of removed TCE:

$$TCE \text{ abatement} = \frac{[TCE]_{in} - [TCE]_{out}}{[TCE]_{in}} \times 100 \quad (\text{Eq. 5.5})$$

where $[TCE]_{in}$ is the initial TCE concentration and $[TCE]_{out}$ the concentration in the effluent. In this work, other terms are also used such as removal efficiency and conversion.

- The selectivities of CO , CO_2 , CO_x and chlorinated byproducts are defined as:

$$S_{CO} = \frac{[CO]}{2 \times [TCE]_{conv}} \times 100 \quad (\text{Eq. 5.6})$$

$$S_{CO_2} = \frac{[CO_2]}{2 \times [TCE]_{conv}} \times 100 \quad (\text{Eq. 5.7})$$

$$S_{CO_x} = S_{CO} + S_{CO_2} \quad (\text{Eq. 5.8})$$

$$S_{Cl\text{-byproducts}} = 100 - S_{CO_x} \quad (\text{Eq. 5.9})$$

where $[CO]$ and $[CO_2]$ are the concentrations of carbon monoxide and carbon dioxide detected in the effluent gas as a result of TCE oxidation and $[TCE]_{conv}$ is the concentration of TCE converted by the plasma.

- The yields to CO and CO_2 are defined as follows:

$$Y_{CO} = \frac{[CO]}{2 \times [TCE]_{in}} \times 100 \quad (\text{Eq. 5.10})$$

$$Y_{CO_2} = \frac{[CO_2]}{2 \times [TCE]_{in}} \times 100 \quad (\text{Eq. 5.11})$$

- The carbon mass balance is defined as follows:

$$CMB = \frac{[CO_x]}{2 \times ([TCE]_{in} - [TCE]_{out})} \quad (\text{Eq. 5.12})$$

where $[CO_x] = [CO] + [CO_2]$.

Chapter 6

Strategic methodology

6.1 Introduction

The aim of the following chapter is to provide the reader a clear overview of the strategic methodology that was applied during the course of this PhD. This discussion acts as a rationale for the different studies that were performed.

6.2 Identification of by-products of TCE abatement with NTP

The literature overview presented in Chapter 3 has clearly shown that NTP is a promising technology for the oxidative abatement of VOCs. In an ideal oxidation process, these pollutants are mineralized to CO_2 , H_2O , HX and X_2 with X being a halogen (if this element is present in the target compound). However, incomplete oxidation of VOCs by NTP has led to the formation of undesired by-products (e.g. NO_x , CO , O_3 , other VOCs, aerosols) and can sometimes even result in an increase of the overall toxicity of the treated gas stream [140, 152, 184, 186, 450]. Different studies have shown that this is also the case for the abatement of TCE [124, 135, 138]. In an early stage of this PhD study it became clear that the abatement of TCE with the negative DC glow discharge also resulted in the formation of undesired and toxic by-products as illustrated in Figure 6.1. Nevertheless, a thorough analysis of the identification of by-products is indispensable to e.g. know the by-product distribution. Therefore, in a first stage of this PhD study, the by-product formation of plasma-assisted TCE abatement was qualitatively analyzed by means of FT-IR spectroscopy and mass spectrometry.

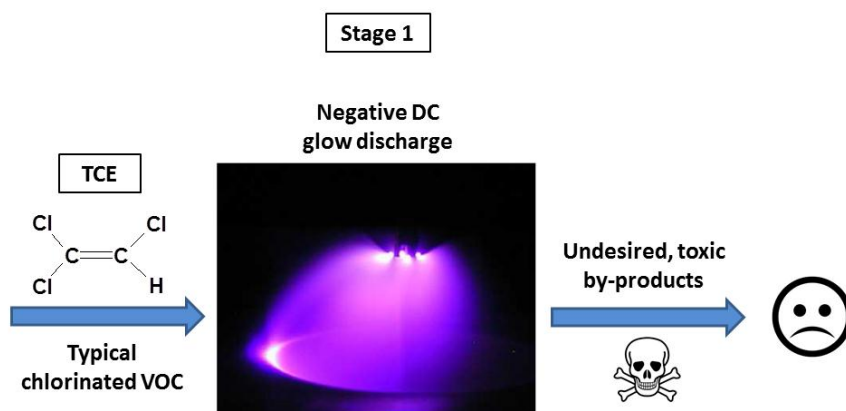


Figure 6.1 Formation of undesired and toxic by-products due to incomplete oxidation of TCE by the negative DC glow discharge.

6.3 Development of a plasma–chemical model for TCE abatement with NTP

In a NTP, highly accelerated electrons gain sufficient energy to trigger multiple chemical processes such as excitation, ionization and dissociation of bulk gas molecules (N_2 , O_2 , H_2O). This produces a chemical environment containing a variety of reactive species such as ions, radicals and metastables that are capable of converting VOCs to less harmful products. Due to the creation of this diverse mixture of reactive species in the active plasma zone, there is however still a lack of insight in the underlying mechanisms and reactions that enable the removal of VOCs. Therefore, in a second stage of this PhD study, a plasma–chemical model was developed and validated with experimental results. In order to successfully accomplish this goal, a collaboration was established with the research group PLASMANT of the University of Antwerp. This group develops and applies numerical models for inter alia gas discharge plasmas with the aim to optimize its applications (e.g. in materials and nanotechnology, analytical chemistry, environmental and medical applications). The development of the plasma–chemical model enabled to obtain a better understanding of the TCE abatement process which yielded measures to improve the efficiency and enabled the synthesis of suitable catalysts for plasma–catalytic applications.

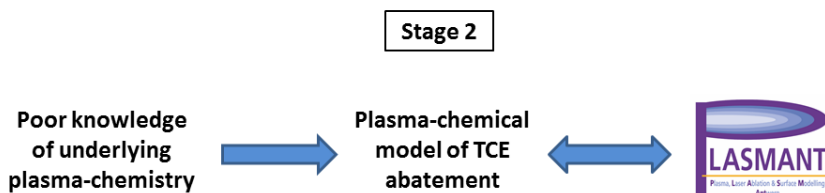


Figure 6.2 Motivation for the establishment of a plasma–chemical model for TCE abatement with NTP.

6.4 Improving TCE abatement by combining NTP with heterogeneous catalysis

Numerous VOC abatement studies have proven that the combination of NTPs with heterogeneous catalysts is able to outperform plasma alone systems in terms of efficiency, selectivity and energy cost. Consequently, suitable catalysts have to be selected based on the target VOC and the by–product distribution in order to

successfully hybridize with NTP systems. This should lead to the development of efficient and low-cost catalysts, which can catalyze the complete oxidation of VOCs into CO_2 at low temperature. Therefore, in a final stage of this PhD study, several catalysts were investigated in order to determine their activity, selectivity and durability for the abatement of TCE in combination with the negative DC glow discharge. To achieve this goal, two collaborations were established with research groups specialised in environmental catalysis (Figure 6.3). The first collaboration was with the Department of Organic Chemistry of the University of Cordoba. During this initial plasma-catalytic study, we investigated TCE abatement by combining the plasma discharge with a commercial MnO_2 catalyst. In a second collaboration with the Unité de Catalyse et Chimie du Solide (UCCS) from the University of Science and Technology in Lille (Lille 1), we further investigated the use of other manganese-based catalysts in order to optimize the catalytic formulation for total oxidation of TCE. The rationale for the choice of these catalysts is presented in the following sections.

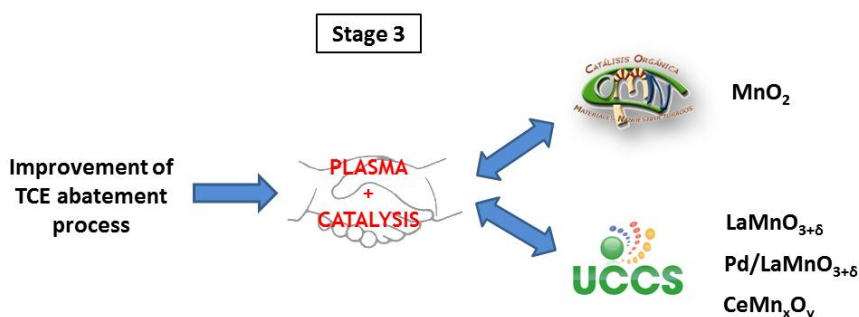


Figure 6.3 Improvement of TCE abatement process by combining NTP with heterogeneous catalysis.

6.4.1 Commercial MnO_2 catalyst

The formation and emission of large amounts of ozone during plasma-assisted VOC abatement is a serious drawback because O_3 is responsible for respiratory diseases and is implied in the formation of photochemical smog. To prevent the emission of O_3 , several catalytic formulations have been tested. It is found that p-type oxide semiconductors are the most active substances for ozone decomposition [451, 452]. Among these, MnO_2 has shown to possess interesting properties for use as catalyst, such as ease of synthesizing crystalline phases [453] and the mobility of oxygen in the crystal

lattice. This can create vacancies, which promote the formation of oxygen groups at the catalyst surface [454], making them appropriate materials for VOC oxidation reactions [455].

Some groups have investigated the performance of MnO_2 combined with NTP for VOC removal. Futamura et al. observed synergetic effects for the decomposition of fluorinated hydrocarbons with DBD reactors filled with MnO_2 [456]. Jarrige et al. coupled a pulsed corona discharge with a fixed catalytic bed of $\text{MnO}_2/\text{Al}_2\text{O}_3$ downstream [330]. At ambient temperature, ozone was almost completely decomposed by the catalyst, producing reactive oxygen species leading to a greatly enhanced conversion and CO_2 -selectivity for the removal of propane. Han et al. also investigated the use of MnO_2 downstream of a DBD reactor and reported a significant improvement of the energy efficiency at low energy input [143].

In order to investigate the opportunities of a plasma-catalytic system with MnO_2 downstream we chose a commercial type MnO_2 catalyst as first attempt to improve the performance of the plasma alone system.

6.4.2 Perovskite-type catalyst $\text{LaMnO}_{3+\delta}$

Further on, we studied lanthanum manganite ($\text{LaMnO}_{3+\delta}$) which is a perovskite type catalyst. These catalysts (ABO_3 , A = La, Y and B = Ni, Co, Fe, Mn) are known to be among the most active catalysts for the oxidation of chlorinated VOCs (CVOCs) [457-460]. Their high catalytic activity is attributed to the presence of stable mixed valence states in the “B” site, the availability of weakly bonded oxygen at the surface and the presence of crystal lattice defects [78, 458, 461, 462]. Moreover, perovskites are cheaper than noble metal catalysts and are more effective due to their superior thermal stability and lower poisoning by sulfur, phosphorus and halogen [463].

$\text{LaMnO}_{3+\delta}$ presents the peculiarity of having cationic gaps as a consequence of the presence of Mn^{4+} cations in the “B” site generated during the calcination in air. The presence of Mn in two oxidation states ($\text{Mn}^{3+}/\text{Mn}^{4+}$) which generates interesting redox properties combined with the availability of loosely bound oxygen to its surface contribute to the catalytic activity of this material [461, 464]. Hence, $\text{LaMnO}_{3+\delta}$, which is an environment-friendly and inexpensive material, has been tested as catalyst. This is the first time that this type of catalyst has been investigated for plasma-catalytic VOC abatement.

6.4.3 Incorporation of Pd into LaMnO_{3+δ}

The incorporation of noble metals (Pt, Pd, Rh) in low quantity into a perovskite structure has shown to increase the catalytic activity as well as to enhance the stability of the metal against sintering, metal–support interaction and volatilization [465]. Therefore, in a further stage, palladium (Pd) was incorporated into LaMnO_{3+δ}. This was also the first time that this type of catalyst has been investigated for plasma–catalytic VOC abatement.

6.4.4 Mn–Ce binary oxide catalysts

As surface area can play an important role in O₃ decomposition, dispersion of MnO_x is thought to be greatly improved by forming Mn–Ce binary oxides. In this regard, new CeMn_xO_y oxides have been synthesized by the “driving redox–precipitation reactions synthesis” developed by Arena et al. [447, 466, 467]. It has been reported that these new nanostructured CeMn_xO_y catalysts possess superior textural and redox properties in comparison to co–precipitated systems. Indeed, the resulting strong MnO_y–CeO₂ interaction along with higher average oxidation number of both Mn and Ce ions have been claimed to be responsible for the strong promotion of the reactive surface oxygen availability and the CO oxidation activity in the range of 50–150°C [467]. Furthermore, their strong ability to eliminate chlorine from the catalyst surface and to provide significant amounts of active oxygen have been recognised as important catalytic properties for total oxidation of chlorinated VOCs [468–470]. Therefore, in a final stage, Mn–Ce binary oxide catalysts were synthesized by the “redox–precipitation” route and tested for total oxidation of TCE in combination with the plasma reactor. As for LaMnO_{3+δ} and Pd/ LaMnO_{3+δ} this was also the first time that this type of catalyst was tested for plasma–catalytic VOC abatement.

Chapter 7

Qualitative by-product identification of plasma-assisted
TCE abatement by mass spectrometry and
Fourier-transform infrared spectroscopy

This chapter is published as a research article in the following international journal:

A.M. Vandebroucke, M.T. Nguyen Dinh, J.-M. Giraudon, R. Morent, N. De Geyter, J.-F. Lamonier, C. Leys

Qualitative by-product identification of plasma-assisted TCE abatement by mass-spectrometry and Fourier-transform infrared spectroscopy

Plasma Chemistry and Plasma Processing 31 pp. 707–718, 2011

7.1 Introduction

This chapter is devoted to the qualitative by-product identification of plasma-assisted TCE abatement. For this purpose, the analytical information of FT-IR spectroscopy and mass spectrometry was combined in order to detect all by-products. A summary is also given on previous studies investigating plasma-assisted TCE abatement in order to make a comparison with own results.

7.2 Experimental conditions

Table 7.1 summarizes the experimental conditions used in this chapter.

Table 7.1 Experimental conditions

Air source	compressor
Flow rate	2 L/min
Relative humidity (20°C)	8%
Initial TCE concentration	1000 ppm
Plasma reactor	A
Optical path length FT-IR	80 cm

7.3 Results and discussion

7.3.1 Mass spectrometry

Figure 7.1 exhibits the 60 eV mass spectrum of the inlet gas stream. With no NTP, the mass spectrum only shows the characteristic TCE fragment ions (Table 7.2) and the one of CO₂ ($m/z = 44$). The mass spectrum of the outlet gas (Figure 7.2) shows a decrease in the abundance of the TCE fragment ions, which suggests partial TCE degradation. Additionally, new ions are detected. The peaks in these spectra are firstly identified by comparison to the National Institute of Standards (NIST) mass spectral library. Identification is simplified in many cases because of the characteristic peak intensity patterns which arise as a result of the natural abundance of the chlorine isotopes.

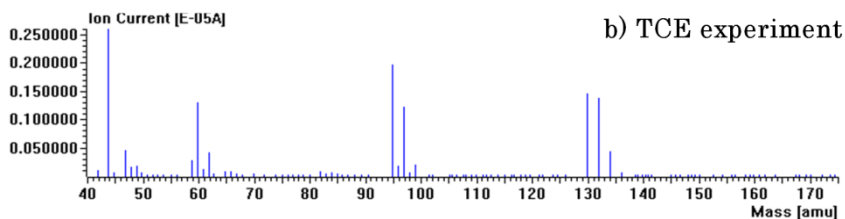
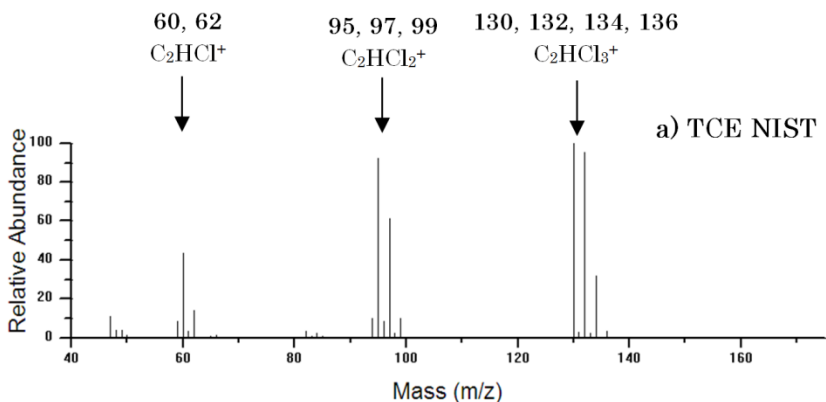


Figure 7.1 TCE mass spectrum: (a) reported by NIST [471],
(b) experimental gas inlet (300 J/L).

Table 7.2 Major ions in the NIST mass spectra of selected compounds [471].

Compound	Name	m/z (relative abundance)
HCl=CCL ₂	Trichloroethylene (TCE)	C₂HCl₃⁺ : 130(100), 132(95), 134(32), 136(3) C₂HCl₂⁺ : 95(92), 97(61), 99(10) C₂HCl⁺ : 60(43), 62(14) CCl⁺ : 47(11), 49(4)
CHCl ₂ -C(O)Cl	Dichloroacetyl chloride (DCAC)	C₂HCl₃O⁺ : 146(2), 148(2) C₂HCl₂O⁺ : 111(10), 113(6), 115(1) CHCl₂⁺ : 83(100), 85(62), 87(10) C₂HClO⁺ : 76(13), 78(4) CHCl⁺ : 48(13), 50(4) CCl⁺ : 47(8), 49(3)

Table 7.2 Major ions in the NIST mass spectra of selected compounds [471] (continued).

Compound	Name	m/z (relative abundance)
CCl ₃ -CHO	Trichloro- acetaldehyde (TCAD)	C₂HCl₃O⁺ : 146(5), 148(4)
		C₂HCl₂O⁺ : 111(41), 113(27)
		CHCl₂⁺ : 83(40), 85(25)
		CCl₂⁺ : 82(100), 84(68)
		CHCl⁺ : 48(27), 50(8)
		CCl⁺ : 47(61), 49(23)
C(O)Cl ₂	Phosgene	CCl₂O⁺ : 98(7), 100(4)
		CClO⁺ : 63(100), 65(34)
		CCl⁺ : 47(3), 49(1)
Cl ₂	Dichlorine	Cl₂⁺ : 70(100), 72(63), 74(10)
		Cl⁺ : 35(83), 37(26)
		HCl⁺ : 36(100), 38(32)
HCl	Hydrogen chloride	Cl⁺ : 35(17), 37(5)
		CO₂⁺ : 44(100)

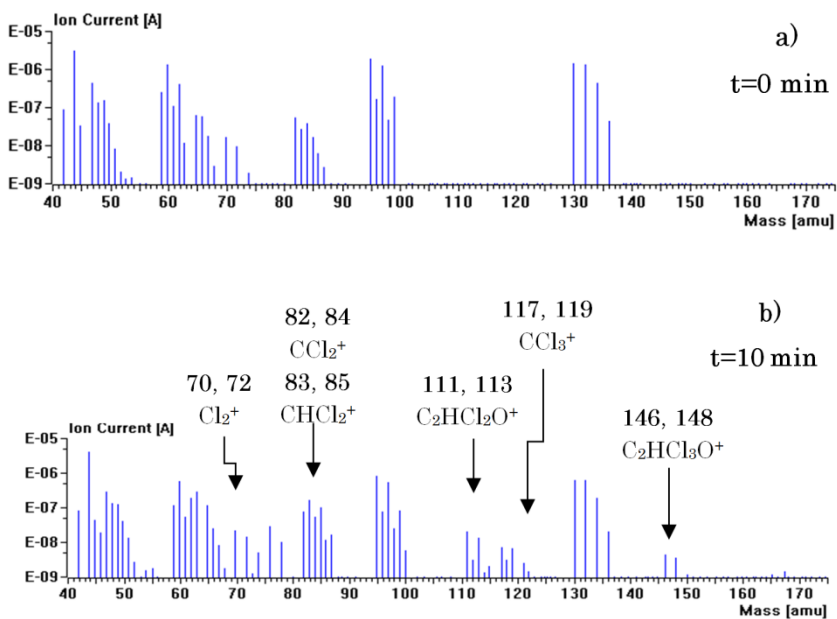
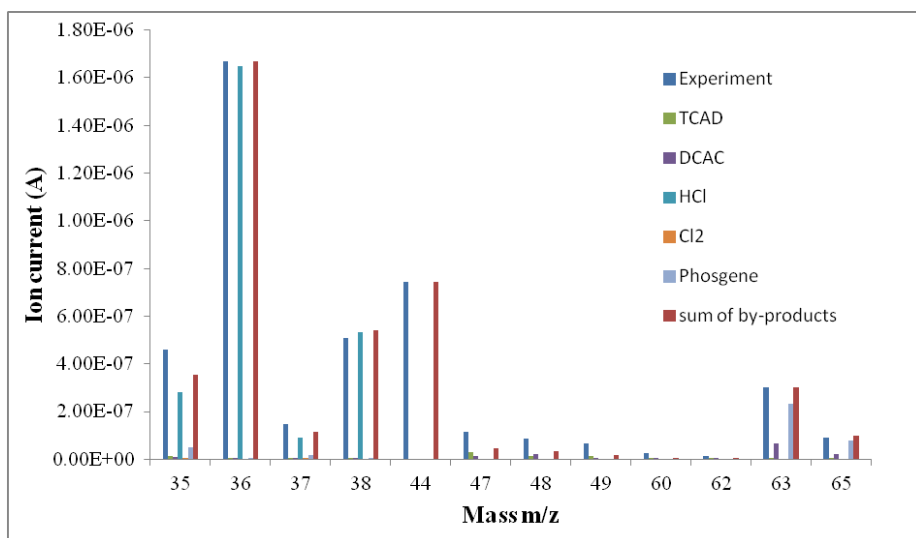


Figure 7.2 Mass spectrum of the gas outlet after (a) 0 min, (b) 10 min of NTP exposure (300 J/L).

The characteristic fragment ions (Table 7.2) of m/z 146, 148, 150 ($C_2HCl_3O^+$), m/z 117, 119 (CCl_3^+), m/z 111, 113 ($C_2HCl_2O^+$) can be ascribed to dichloroacetylchloride (DCAC) or/and to trichloroacetaldehyde (TCAA) with possible contribution of adventitious tetrachloromethane at m/z 117 and 119. However, the simultaneous detection of the fragment ions of m/z 82, 84 (CCl_2^+) and of m/z 83, 85 ($CHCl_2^+$) (with a relative higher intensity) accounts for a mixture of the two chlorinated VOCs. A good agreement is obtained when comparing the mass spectrum peaks intensity in the 80–150 m/z range considering only the contribution of DCAC and TCAA to the experimental one. Hence, production of TCAA and DCAC with a respective contribution of 12% (TCAA) and 88% (DCAC), considering a similar response factor, can account for the mass spectrum in the considered m/z range.

The formation of hydrogen chloride and molecular dichlorine from TCE was established by the peaks in the mass spectrum at m/z of 36 ($H^{35}Cl^+$) and 38 ($H^{37}Cl^+$) and of m/z 70 ($^{35}Cl^{35}Cl^+$), 72 ($^{35}Cl^{37}Cl^+$) and 74 ($^{37}Cl^{37}Cl^+$), respectively. CO_2 and phosgene are also detected in the outlet gas mixture by their characteristic fragment ions m/z of 44 (CO_2^+) and 63/65 m/z ($CO^{35}Cl^+$ and $CO^{37}Cl^+$). The background subtracted mass spectrum is simulated in the m/z range of 30–70 considering the presence of HCl, Cl_2 , phosgene and CO_2 with the presence of DCAC and TCAA determined previously. The simulated spectrum fits in a rather good accordance the experimental one (Figure 7.3).



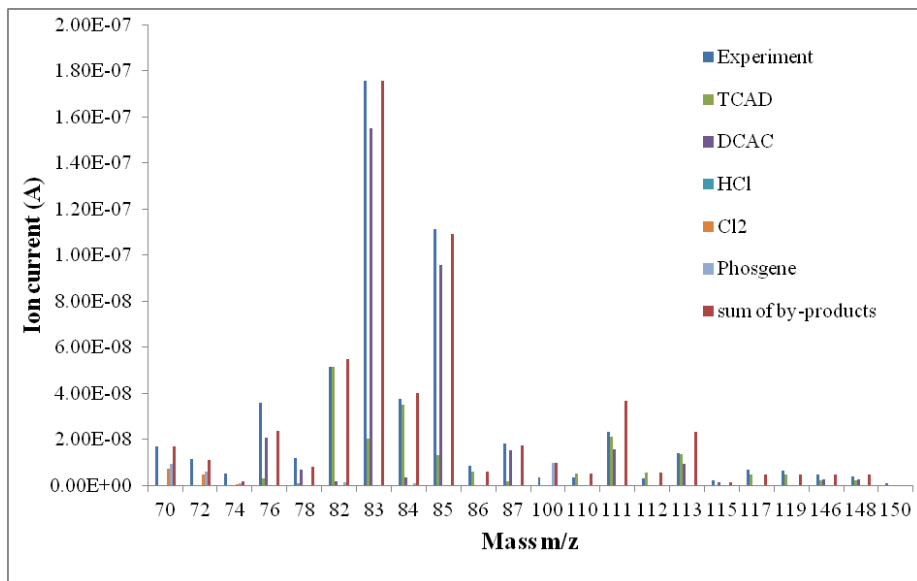


Figure 7.3 Experimental and simulated mass spectra of the outlet gas mixture sampled after 10 min of NTP exposure in the m/z range (a) 30–70 and (b) 70–150.

Therefore, these results suggest that under the presence of NTP degradation conditions, TCE is decomposed to CO₂ with HCl, Cl₂, phosgene, DCAC and TCAA participating as by-products. CO as a by-product must also be present but is not detected here. Indeed, CO formation cannot be monitored owing to the presence of N₂ in the carrier gas, and the unit mass resolution of the quadrupole mass analyzer.

7.3.2 Fourier–transform infrared spectroscopy

Figure 7.4 shows the FT–IR spectra of both the inlet and outlet stream when the plasma reactor is operated at the same conditions as that in Figure 7.2. The characteristic IR bands of TCE are listed in Table 7.3. Figures 7.5 to 7.7 show zoomed spectra to study the plasma treated exhaust stream in more detail. In these spectra, numbers are used to allocate different IR bands to the appropriate (by)–product (Table 7.4).

Table 7.3 Characteristic IR bands of TCE [472-474].

Wavenumber range (cm ⁻¹)	Vibration
655 – 605	C–Cl vibration
785	C–Cl vibration
865 – 815	no unambiguous explanation
970 – 885	C–H out of plane deformation
1305 – 1215	C–H deformation
1615 – 1530	C=C stretch vibration
3115 – 3065	C–H olefinic C–H stretch vibration

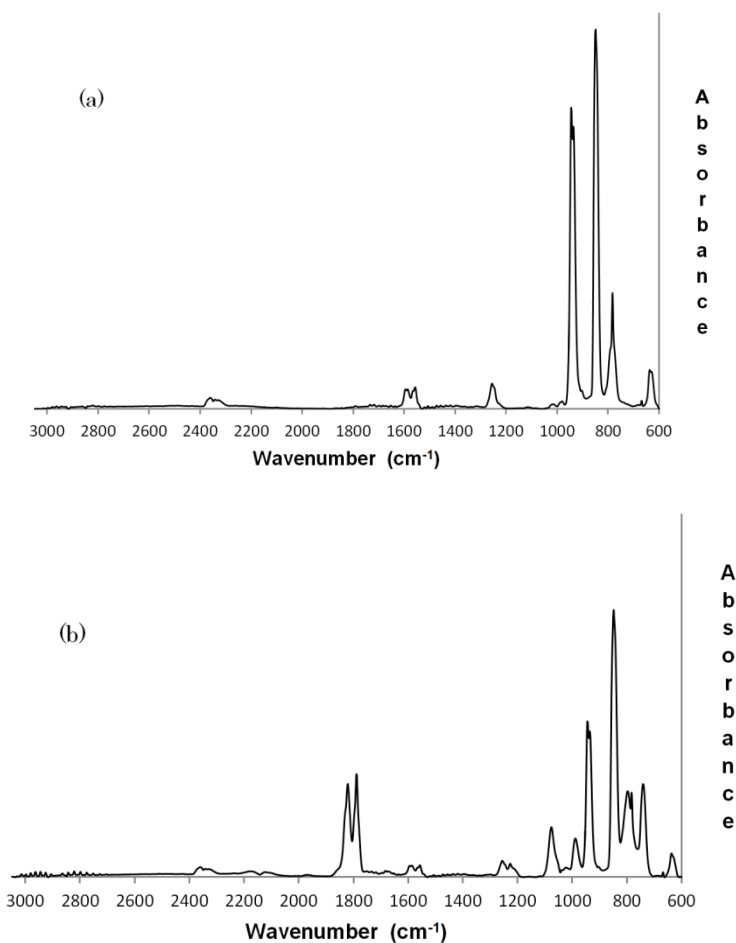


Figure 7.4 FT–IR spectra between 600 and 3050 cm⁻¹ of TCE before (a) and after (b) plasma treatment at an energy density of 300 J/L.

The decomposition efficiency of TCE is calculated by taking the ratio of the integrated surface area of the in- and outlet band of TCE at 945 cm^{-1} . Preliminary experiments showed that this band is not disturbed by interference of bands originating from by-products. Based on the spectra of Figure 7.4, the calculated decomposition efficiency reaches 47%.

By carefully comparing Figure 7.5 and 7.6 with reference spectra of NIST, the formation of DCAC is detected. This is confirmed by the presence of the peaks, allocated with number 2, at 740, 800, 989, 1076, 1225, 1789 and 1820 cm^{-1} . TCE is also further decomposed to other products such as CO, CO_2 and HCl. For HCl, this is verified by the characteristic band in the region $2698 - 3040\text{ cm}^{-1}$ (Figure 7.7). CO and CO_2 can respectively be detected by the bands in the region $2035-2225\text{ cm}^{-1}$ and $2285-2396\text{ cm}^{-1}$ (Figure 7.7). Molecular chlorine cannot be detected by the FT-IR spectrometer because this diatomic molecule is IR-transparent. The formation of toxic phosgene is suggested based on the following observations. In Figure 7.4, the intensity of the C-H out of plane deformation band of TCE at 945 cm^{-1} shows a significant decrease while the band at 850 cm^{-1} of TCE does not decrease to the same extent after plasma treatment. Hence, analysis of the spectra suggests that phosgene interferes with the band of TCE at 850 cm^{-1} . The band of DCAC at 1820 cm^{-1} also shows a small shoulder at 1830 cm^{-1} . Therefore, it is believed that this shoulder originates from the C-O stretch vibration from phosgene which, according to the NIST databank, is located at 1827 cm^{-1} . Moreover, the small band at 1685 cm^{-1} (Figure 7.6) can be ascribed to the C-Cl₂ vibration of phosgene. Finally, ozone is detected in the outlet stream at $1014-1046\text{ cm}^{-1}$ (Figure 7.5) with a concentration of 82 ppm. The exposure of air to the active plasma volume inherently leads to the formation of ozone from oxygen [101, 475].

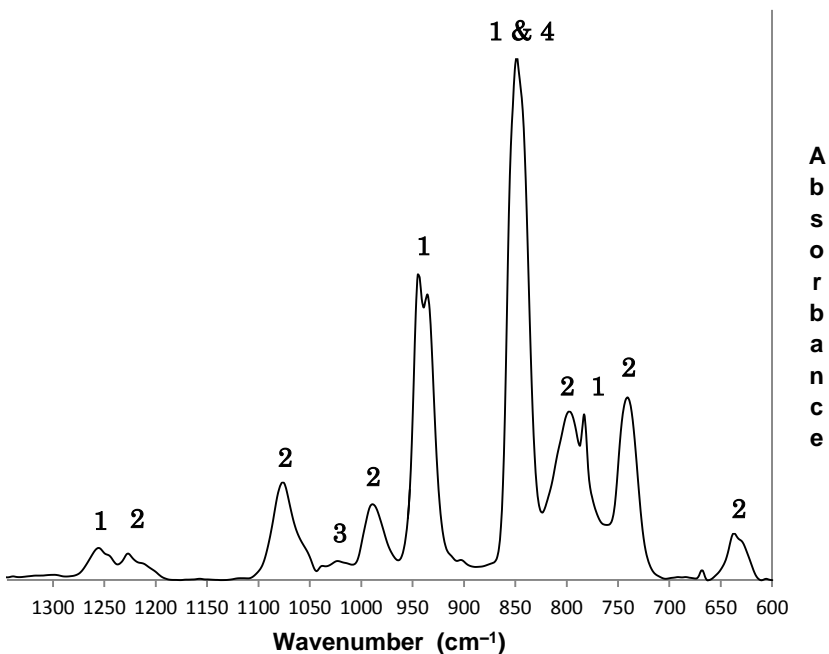


Figure 7.5 Detailed FT-IR spectrum between 600 and 1350 cm^{-1} of the plasma treated TCE stream.

Table 7.4 (By)products of TCE abatement detected with FT-IR spectroscopy.

Number	Compound	Structure
1	Trichloroethylene	$\text{CHCl}=\text{CCl}_2$
2	Dichloroacetylchloride	$\text{CHCl}_2-\text{C}(\text{O})\text{Cl}$
3	Ozone	O_3
4	Phosgene	$\text{C}(\text{O})\text{Cl}_2$
5	Carbonmonoxide	CO
6	Carbon dioxide	CO_2
7	Hydrogen chloride	HCl

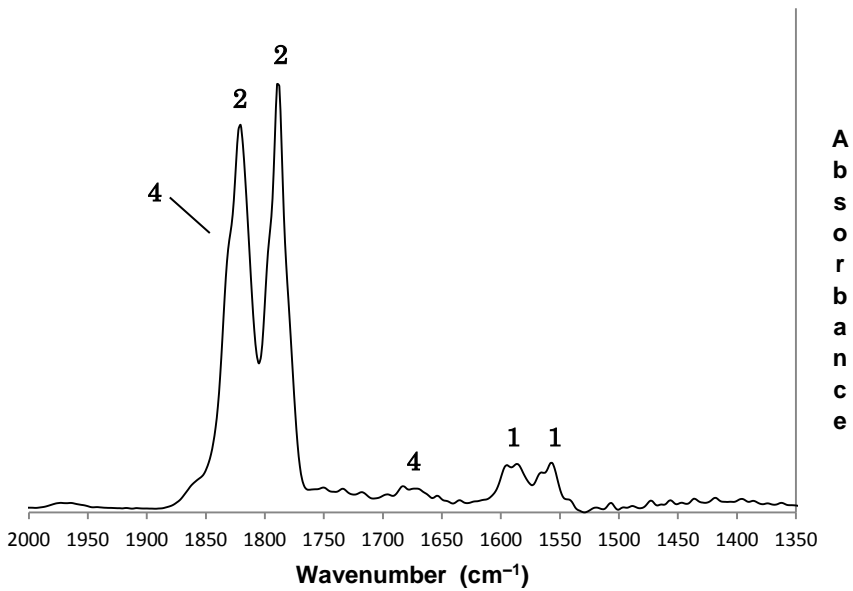


Figure 7.6 Detailed FT-IR spectrum between 1350 and 2000 cm⁻¹ of the plasma treated TCE stream.

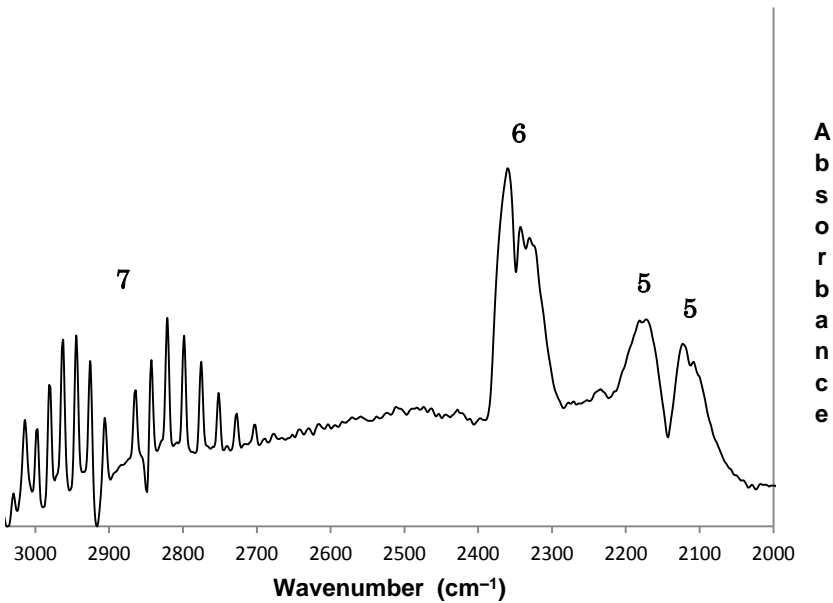
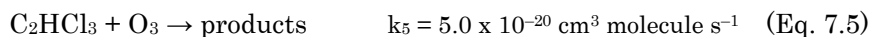
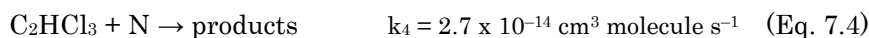
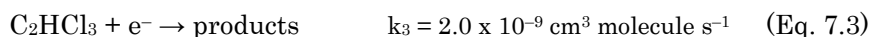
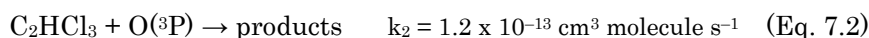
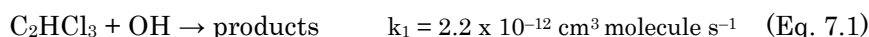


Figure 7.7 Detailed FT-IR spectrum between 2000–3050 cm⁻¹ of the plasma treated TCE stream.

7.3.3 Overview and discussion of by-product identification

In a NTP environment, electron collisions with VOC and background molecules induce electron and radical impact dissociation reactions that allow the destruction of VOCs [148]. In the case of TCE decomposition in humid air, the following reactions have to be taken into account:



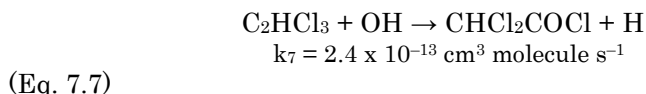
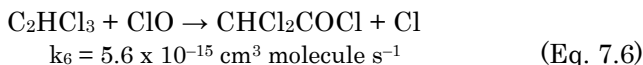
A comparison of these rate coefficients [476], shows that the reaction with nitrogen radicals (Eq. 7.4) and ozone (Eq. 7.5) have a less pronounced role in the oxidation kinetics of TCE. In humid air, electron-impact dissociation of H_2O and O_2 produces hydroxyl radicals and atomic oxygen species, respectively. The large k -values of the reactions of these species with TCE indicate that they likely are the primary decomposition routes. The experimental results in this paper were obtained with an initial TCE concentration of 1000 ppm. According to Penetrante et al. [134], dissociative electron attachment (Eq. 7.3) can also play a significant role at this initial concentration. In this case, Eq. 7.3 becomes competitive with electron scavenging by attachment to O_2 and H_2O .

The distribution of by-products of VOC abatement depends on various parameters such as the type of discharge, carrier gas, humidity,... Different groups have studied the decomposition of TCE with NTP technology and discussed the formation of by-products. It is however useful to summarize previous work in order to make a comparison with own results.

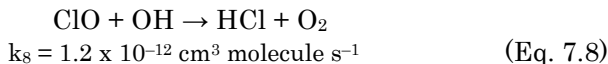
Evans et al. [124] have reported that the ClO radical is an important intermediate which oxidizes TCE in dry and wet Ar/ O_2 mixtures. The authors suggest a diagram of the dominant reaction pathways of TCE remediation in dry Ar/ O_2 mixtures giving CO, CO_2 , COCl_2 and HCl as main by-products. Additionally, $\text{CHCl}_2\text{-C(O)Cl}$ (dichloroacetylchloride, DCAC) and CHCl_2 can be produced by reaction of the OH radical with TCE in wet Ar/ O_2 mixtures. Hsiao et al. [126] have studied the plasma-assisted decomposition of TCE in air and confirmed the formation of the same by-products as detected

in the latter study. Under our conditions, these products are also found after plasma treatment. However, MS spectrometry additionally confirms the formation of TCAA and Cl₂.

Under dry air conditions, Kirkpatrick et al. [125] have also suggested the reaction of TCE with ClO radicals leading to the formation of DCAC as main by-product as follows:



In saturated humid conditions, DCAC formation is suppressed, suggesting that ClO radicals are quenched by OH radicals by the reaction:



DCAC can further decompose by attack of Cl radicals, leading to the formation of CO, HCl, CCl₄, CHCl₃ and COCl₂ as final products. In the present study, DCAC is found to be a by-product although humid air (8% RH) is used as carrier gas. This suggests that at low relative humidity quenching of ClO by OH radicals (Eq. 7.8) does not play a significant role.

For small initial TCE concentrations in dry air (100 ppm), Penetrante et al. [134] have presumed that the primary decomposition mechanism is initiated by reactions with O radicals and electrons. Next, these reactions initiate the detachment of Cl radicals which causes a Cl radical addition chain reaction as proposed by Vitale and co-workers [130].

By combining the data gathered with mass and FT-IR spectroscopy in the present study, the formation of CO₂, HCl, DCAC and phosgene (COCl₂) can be confirmed by both techniques (Table 7.5). FT-IR measurements additionally detects small production of CO. Molecular chlorine, which is transparent for IR light, is detected with mass spectrometry. For TCAA, no reference IR spectrum is found in the NIST databank. However, analysis of the mass spectrum can reveal the formation of this chlorinated VOC as a by-product. Hence, the decomposition of TCE with non thermal plasma operated at an energy density of 300 J/L led to the formation of phosgene, DCAC and TCAA as incomplete oxidation products. Under these conditions, TCE is to a lesser extent decomposed to CO_x, HCl and Cl₂. The production of ozone is also confirmed in the outlet stream.

Table 7.5 By-products of TCE abatement detected with mass spectroscopy and/or FT-IR spectroscopy.

	MS	FT-IR
DCAC	✓	✓
TCAD	✓	
Phosgene	✓	✓
O ₃		✓
CO		✓
CO ₂	✓	✓
HCl	✓	✓
Cl ₂	✓	

7.4 *Conclusions*

In this paper the decomposition of TCE in humid air is studied with a negative DC glow discharge operating at 300 J/L. The abatement of TCE has qualitatively been analyzed with mass spectrometry and FT-IR spectroscopy in order to detect all by-products. By combining data from both techniques, the formation of DCAC, TCAA and phosgene as intermediate oxidation products can be confirmed. TCE is decomposed to a lesser extent to CO₂, CO, HCl and Cl₂. Formation of ozone is also detected in the outlet stream. This information on the by-product distribution will enable to select appropriate catalysts to achieve a high mineralization degree at low energy cost in a plasma-catalytic system, which will be the subject of the following chapters.

Chapter 8

Modeling and experimental study of TCE abatement with a negative direct current corona discharge

This chapter is published as a research article in the following international journal:

A.M. Vandenbroucke, R. Aerts, W. Van Gaens, N. De Geyter, C. Leys, R. Morent, A. Bogaerts

Modeling and experimental study of trichloroethylene abatement with a negative direct current corona discharge

Plasma Chemistry and Plasma Processing 35 pp. 217–230, 2015

8.1 Introduction

In this chapter, a kinetic model for the abatement of TCE is presented. The plasma–chemical model and experimental validation allow to obtain a better understanding of the chemical processes occurring in the discharge. Moreover, it is possible to derive the degradation pathway of TCE, based on the distribution of intermediates and end–products. Up to now, only Evans et al. have performed such a study to investigate the abatement of TCE from Ar/O₂/H₂O mixtures with dielectric barrier discharges [124]. However, these gas mixtures are not so relevant for industrial applications. Therefore, this study focused on the industrially frequently occurring combination of air waste streams polluted with TCE. For practical applications, the humidity of the air is also an important parameter that significantly affects the removal process [477]. Therefore, the water content of the influent was varied and the outcome on the removal process was investigated.

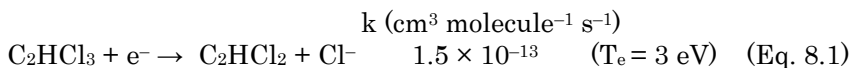
8.2 Description of the model and chemistry

The simulations in this work are performed using the numerical model `Global_kin` developed by Dorai and Kushner [478]. The plasma reactor is considered as a batch reactor with a uniform concentration of species over the entire reactor volume. More details on the model can be found in the papers by Dorai, Kushner and Aerts et al. [478, 479].

In this work, the `Global_kin` model is extended with a reaction analysis module in order to calculate the absolute contributions of all the relevant reactions to the production and loss of all species. These absolute contributions are then used to automatically draw the chemical pathways with `Graphviz` [480].

The chemistry used in the model contains 114 species and 1155 reactions. This large number of reactions is needed for the description of a complex medium like air. The air chemistry is already described in Van Gaens et al. [481] and the TCE chemistry in Evans et al. [124]. We have taken into account electrons, various types of ions and neutrals, as well as nitrogen and oxygen excited states. Below, we summarize the major destruction reactions that can take place. A complete list of all the reactions that lead to the destruction of TCE in air included in the model can be found in the Appendix section (Table A).

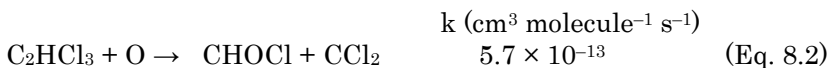
In literature, the destruction of TCE with NTP is described by many possible pathways [477]. The first pathway could be the electron attachment of TCE, leading to its decomposition to C_2HCl_2 and a chlorine anion:



However, the electron density of the corona discharge used for this application (see below) is quite low in comparison with other low temperature plasmas such as dielectric barrier discharges [482]. Together with the low rate coefficient of Eq. 8.1, the contribution of this reaction should be limited.

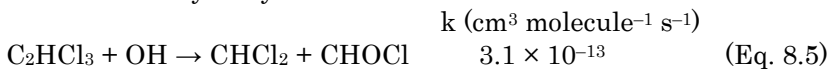
Another possible mechanism is direct dissociation by electrons. Unfortunately, the cross sections for this reaction are not known for TCE. We performed however a study of the direct dissociation by electrons on ethylene and concluded that the contribution was less than one percent [483]. Furthermore, it was stated by Magureanu et al. [145] and Urashima et al. [136] that the direct process would be unlikely, due to the low concentration of TCE in air, and they suggest that TCE oxidation takes place directly by radicals or via oxidation of negative ions.

The dissociation of TCE can also occur by reaction with atomic oxygen leading to numerous end products:

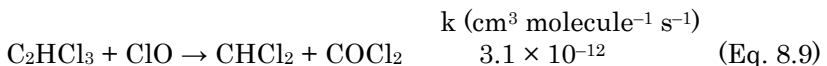


The rate coefficients are in the same order of magnitude as for the electron attachment process. Atomic oxygen has, however, a longer lifetime than the electrons and the reaction with atomic oxygen is therefore more likely to take place.

Especially in humid air, the dissociation of TCE can also be caused by reaction with hydroxyl radicals:



These rate coefficients are also in the same order of magnitude as for the reactions with oxygen atoms, which suggests that the densities of the reactants again have a major influence on the actual rates of the different dissociation reactions. There is also a possibility that TCE is decomposed by radicals originally produced by TCE, e.g. reactions with Cl or ClO radicals:



Eq. 8.9 has a rate coefficient one order of magnitude higher than the previous reactions. However, these reactions can only be a secondary destruction process. Indeed, the densities of Cl and ClO are very low in the beginning but can increase very fast as Cl is a common dissociation product, although the low rate coefficient of Eq. 8.10 will compensate for the higher density.

A final reaction pathway is the dissociation by metastable nitrogen molecules, which are regarded as dominant dissociation species for VOCs [18–21]. As far as we know, no reaction rate coefficients for TCE with metastable nitrogen are published and therefore we have neglected this pathway in our calculations. The metastable nitrogen species $\text{N}_2(\text{A}^3\Sigma_u^+)$ have typically a density of one order of magnitude lower than atomic oxygen in humid air [484]. As a result, the reaction rate coefficient of TCE destruction by $\text{N}_2(\text{A}^3\Sigma_u^+)$ should be at least one order of magnitude higher ($\sim 10^{-12} \text{ cm}^3 \text{ molecule}^{-1} \text{ s}^{-1}$) than the values reported for atomic oxygen. This value can be seen as a critical value for the contribution of nitrogen metastable molecules in the destruction of TCE in air.

As the model used in this work is zero-dimensional, the spatial characteristics of the corona discharge can only be approximated by a variation of power deposition as a function of time, i.e., as one power pulse or by a series of power pulses. Therefore, we distinguish three regions in the corona discharge operating in the glow regime with different values of electron density, based on the calculations made by Callebaut et al. [121]. The first one is the tip of the needle which corresponds to the highest electron density and the shortest pulse duration. The second one corresponds to a zone between the tip and the plate of the corona discharge with an average electron density and pulse duration, while the third region corresponds to the plasma zone at the plate with the lowest electron density and the longest pulse duration. By keeping the total energy deposition fixed for every regime, a comparison can be made between them. Figure 8.1 represents the calculated electron density for the 3 regimes, called

pin, middle and plate, respectively, as a function of the gas residence time used in the model. The “pin regime” has a pulse duration of 0.04 s, whereas the pulse durations of the “middle regime” and the “plate regime” are 0.08 s and 0.26 s, respectively. The electron density is the highest at the tip ($\pm 10^6 \text{ cm}^{-3}$) and the lowest at the plate ($\pm 10^5 \text{ cm}^{-3}$), whereas the electron temperature is more or less constant around 2.5 eV. As illustrated in Figure 8.1, when the gas flows through the reactor, it passes through five power pulses, corresponding to the five pins of the multi-pin-to-plate corona discharge (see below).

We should point out that the main focus of this work is to identify the reaction mechanism in a complex system with humid air and hydrocarbons. Therefore, the description of the plasma itself is narrowed down to five simple power pulses in a zero-dimensional model.

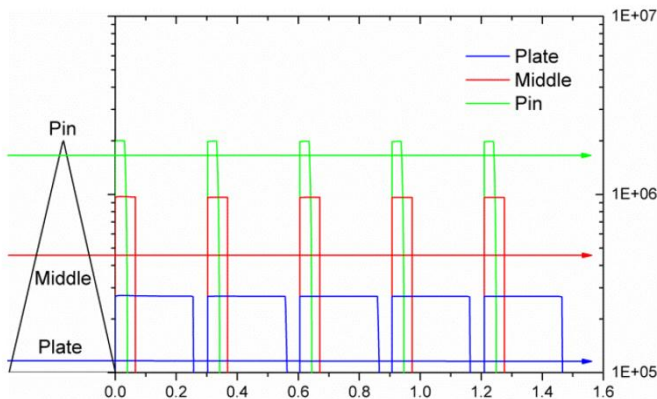


Figure 8.1 Calculated electron density for the 3 regimes (pin, middle and plate) as a function of time, when the gas passes through five pulses corresponding to the five pins of the multi-pin-to-plate corona discharge (see text for more explanation).

8.3 *Experimental conditions*

The experimental conditions used in this study are summarized in Table 8.1.

Table 8.1 Experimental conditions.

Air source	Air Liquide, Alphagaz 1
Flow rate	2 L/min
Relative humidity (20°C)	5–20–50%
Initial TCE concentration	570 ppm
Plasma reactor	A
Optical path length FT-IR	80 cm

8.4 *Results and discussion*

8.4.1 Effect of the energy density on the removal efficiency of TCE

Although we simulate three regimes in the corona discharge, the difference was negligible. Therefore, the following results are shown for the middle regime with a TCE inlet concentration of 570 ppm. To validate the model with experiments, we should compare the simulated results with the experimental data at the same energy density (ED). However, in a corona discharge the plasma volume is much lower compared to the total reactor volume, and this results in an overestimation of the ED and the electron density reported by [121]. To compensate for this observation in our comparison, the actual plasma volume was estimated by assuming a conic volume between pin and plate. The correction factor for the ED, to compensate for this smaller plasma volume is as follows:

$$\text{Correction factor} = \frac{\text{estimated plasma volume}}{\text{total reactor volume}} = 0.1 \quad (\text{Eq. 8.11})$$

This means that an ED of 100 J/L in the experiment is compared with 10 J/L in the model.

Figure 8.2 represents the calculated and measured removal efficiency (RE) as a function of the (experimental) ED for both dry and humid air, corresponding to 5% and 50% relative humidity (RH), respectively.

$$\text{RE (\%)} = \frac{\text{TCE}_{\text{inlet}} - \text{TCE}_{\text{outlet}}}{\text{TCE}_{\text{inlet}}} \times 100 \% \quad (\text{Eq. 8.12})$$

The model and experiment show good agreement for both dry (5% RH) and humid air (50% RH). We observe an increasing trend in the RE upon higher ED, which is related to the higher density of the radicals responsible for destruction of TCE, i.e. ClO, O and OH. Indeed, these radicals are produced by electron impact reactions with the background gas, and the rates of these reactions rise with higher ED, because of the higher electron density. We will explain this in more detail in the next section.

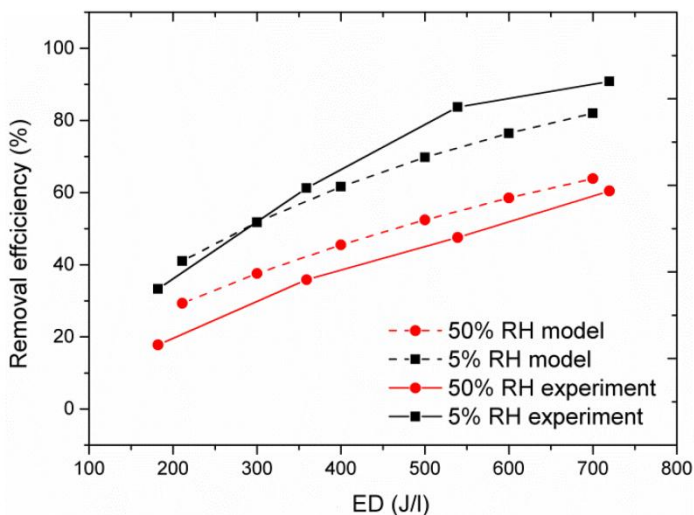


Figure 8.2 Calculated and measured TCE removal efficiency as a function of the ED for dry and humid air.

8.4.2 Effect of the humidity on the removal efficiency of TCE

The effect of humidity is of great interest because water plays an important role in the underlying plasma chemistry. The presence of water affects the removal process since it can quench active plasma species and can limit the electron density due to its electronegative character [477].

Figure 8.3 shows the effect of the humidity on the removal efficiency, at an ED of 220 J/L, for both the experiment and the model. We can see that the removal efficiency drops by $\pm 15\%$ as the humidity increases from 5% to 75%. To explain this effect we first need to

distinguish which reactions mostly contribute to the net loss of TCE, both in dry and humid air.

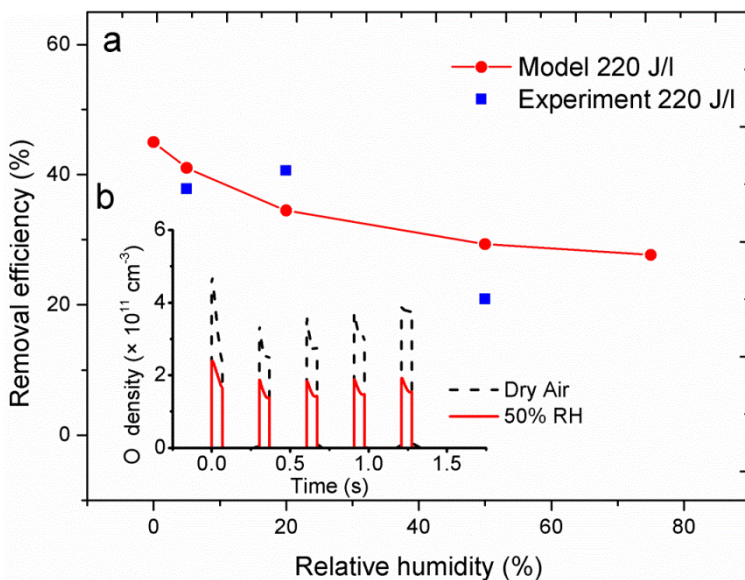


Figure 8.3 Calculated and measured TCE removal efficiency as a function of the relative humidity, for an ED of 220 J/L. The inset shows the calculated O atom density in both dry and humid air (5% and 50% RH, respectively) for the five pulses.

Figure 8.4 illustrates the relative contributions of various reactions to the loss of TCE, at an ED of 220 J/L, for both dry and humid air (i.e. 5% and 50% RH, respectively). We did not observe a difference between different values of ED, but some small differences were found between dry and humid air, as shown in Figure 8.4. It is clear that about 65% and 73% of TCE is destroyed by reaction with either ClO or O radicals, in humid and dry air, respectively. Looking closer into the formation of ClO radicals, the following reaction produces 90% of all ClO:



This means that oxygen atoms actually control the loss of TCE, as they affect the formation of ClO radicals, through the formation of ozone. Indeed the most dominant production of ozone is the third body reaction between atomic and molecular oxygen [16].



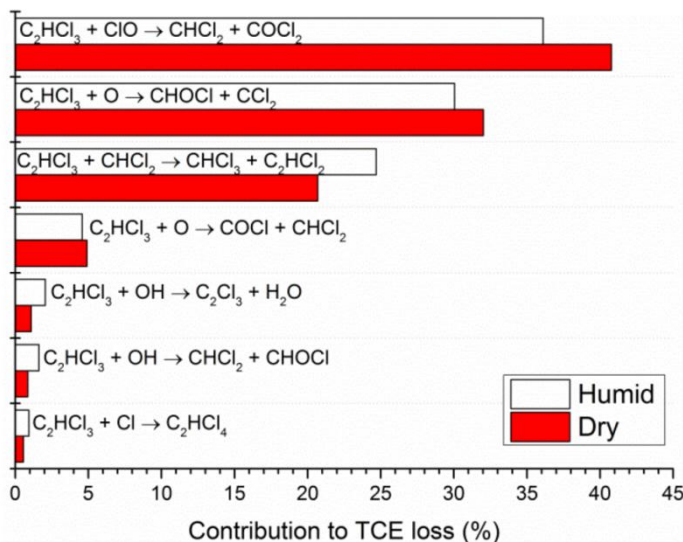


Figure 8.4 Calculated relative contributions of the reactions leading to the loss of TCE for dry and humid air at an ED of 220 J/L.

For the loss and the production of atomic oxygen we can distinguish the following effects of humidity, which will influence the actual density. First, water quenches the production of metastable nitrogen molecules (Eq. 8.15), which will reduce the chemical quenching of oxygen molecules (Eq. 8.16), resulting in a lower atomic oxygen density:



Second, the electron density drops upon increasing humidity, due to the electronegative character of water, giving rise to an increase of the total attachment rate with a factor of 4. Eventually this lower electron density results in a drop in the formation of oxygen atoms by electron impact dissociation of oxygen molecules. These two effects are found to be responsible for the lower atomic oxygen density in humid air, as can be observed from the inset of Figure 8.3. The density almost drops by a factor of 2 between dry and humid air (i.e., 5% and 50% RH, respectively), which explains the negative effect of the humidity on the removal efficiency, also illustrated in Figure 8.3, as well as in Figure 8.2. Furthermore, a higher humidity increases the number of possible destruction reactions between TCE and OH (see Eq. 8.5–8.8).

These reactions are, however, of minor importance than the reaction with O or ClO radicals, as is obvious from Figure 8.4. So in general, the most important effect of the increasing humidity is the lower production of ClO, resulting in a drop in the removal efficiency.

The influence of humidity on the removal of VOCs with NTP has been well summarized in [477]. It seems that addition of water vapor has a negative influence on the properties of the discharge irrespective of the VOC chemical structure. However, depending on the VOC structure, the outcome of increasing air humidity can be designated as an enhancement, a suppression or a neutral effect. Futamura et al. have also experimentally investigated TCE abatement with a BaTiO₃ packed bed [403] and DBD plasma reactor [411] and found that humidity decreases the abatement with about 15–20% and 30–60%, respectively. They suggest that energetic electrons are quenched by ³O₂ to suppress TCE excitation resulting in a decrease of the efficiency. In a recent study by Trushkin et al. [193], the decomposition of toluene was experimentally and numerically studied with a DC atmospheric pressure glow discharge. The authors report that an increase of the humidity leads to an enhancement of the electric field strength and to a higher OH radical density due to electron impact dissociation of H₂O molecules. The increase in OH radical density is responsible for a higher decomposition of toluene and also leads to a catalytic cycle in which OH acts as catalyst which substantially accelerates the recombination of oxygen atoms and suppresses the formation of ozone. In our study, however, the contribution of OH to the TCE abatement is limited to about 5% in total (Figure 8.4) whereas reactions with ClO and O radicals contribute to 63% of the TCE loss in humid air.

8.4.3 Destruction pathway of TCE

In the previous sections we only focus on the species and destruction reactions that contribute to the abatement of TCE. However, in environmental applications the by-products which are formed, are of equal importance due to their possible toxicity. Therefore, we have used a reaction path analyzer which automatically generates the reaction path of the plasma chemistry, illustrating the formation of end- and by-products. Figure 8.5 depicts the loss pathway in the case of humid air, based on the loss rates integrated over the residence time. Note that the reaction pathway looks the same for dry air, although the relative contributions will vary slightly (cf. Figure 8.4), but not in such way that it affects the thickness of the lines in Figure 8.5. The figure only shows species which are produced by destruction of TCE and other intermediate species (Cl, ClO, ...), i.e. the species

produced by the background gas (OH, O, O₂, ...) are not shown, for the sake of clarity.

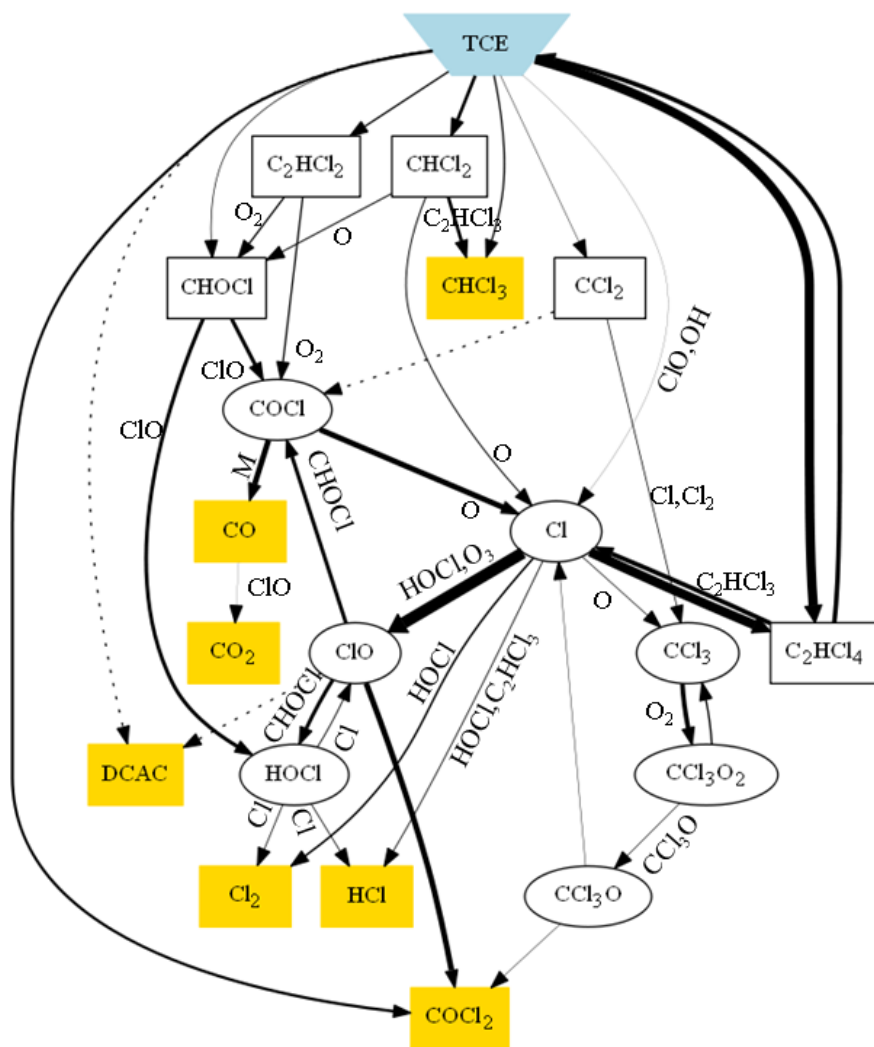
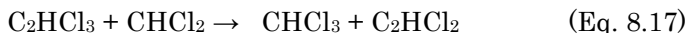


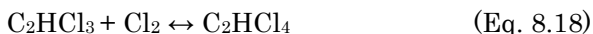
Figure 8.5 Reaction pathway for the loss processes of TCE in humid air. The pathway in dry air looks very similar. The thickness of the arrows is correlated with the rate of this reaction. (rectangles: species predominantly formed from TCE; ovals: intermediate species; yellow rectangles: stable by-products).

Starting from TCE the main loss reactions are with ClO and O (Eq. 8.9 and 8.2, respectively), as well as with CHCl₂:



which is in accordance with the net loss contributions shown in Figure 8.4. Note that these reactions are not important at the very start, because they first need some dissociation of TCE to take place by other (non-Cl related) species as mentioned above, but they soon become dominant.

There is also a significant production of C₂HCl₄, as is clear from Figure 8.5. This species is mainly formed and destroyed by the reaction of TCE with Cl and its reversed decomposition reaction into TCE and Cl.



The rate of production is, however, almost equal to the loss rate, resulting in a net production close to zero. For this reason it does almost not contribute to Figure 8.4.

Looking at the species predominantly formed by these reactions, i.e. COCl₂, CHCl₂, CHOCl, CCl₂, CHCl₃, C₂HCl₂ and C₂HCl₄, (species in rectangles in Figure 8.5) we can already distinguish two toxic by-products (red rectangles), i.e. CHCl₃ (chloroform) and COCl₂ (phosgene). Initially, CHCl₃ will be formed indirectly by Eq. 8.9 producing CHCl₂, which will react again with TCE to produce CHCl₃ in Eq. 8.17. This reaction also produces C₂HCl₂ which is oxidized by molecular oxygen to form CHOCl, as illustrated in Figure 8.5.

CHOCl is produced for ± 50% directly from TCE (Eq. 8.2), for ± 30% out of C₂HCl₂ (cf. above), and for ± 20% by the reaction of atomic oxygen with CHCl₂, as can be deduced from Figure 8.5. Eventually, most of the CHOCl is converted into COCl by reaction with ClO; see Figure 8.5.

Eq. 8.2 also produces CCl₂ directly from TCE, which reacts further on with atomic and molecular chlorine to CCl₃ for almost 85%. The remaining CCl₂ oxidizes with O or OH radicals to COCl. Note that this pathway is drawn in dash in Figure 8.5, because the absolute rate is lower than the threshold, as the line thickness of the paths in Figure 8.5 is proportional to their rates. Eventually, COCl decomposes into Cl and the by-product CO (carbon monoxide). On its turn, CO will be further oxidized by OH radicals to another end-product CO₂ (carbon dioxide).

The Cl atoms, mainly produced by dissociation of COCl, are very important for controlling the TCE destruction chemistry, and largely

contribute to the production of Cl-containing by-products. Firstly, 24% of the Cl atoms will interact with HOCl, producing two end-products, i.e. Cl₂ and HCl. Secondly, around 72% reacts with O₃ to form ClO radicals (see Eq 6.13), which can be used in Eq. 8.9 to destroy TCE (cf. Figure 8.4). The ClO radicals will also react with CHOCl as described above, producing COCl and HOCl.

Finally, the last loss process of the Cl atoms, which contributes for 4%, is the production of CCl₃ upon reaction with CCl₂ as shown in Figure 8.5. Indeed, as already mentioned, the loss rate of Cl atoms by the production of C₂HCl₄ is equal to the production rate of Cl atoms by the reverse process, leading to a negligible contribution to the loss of Cl atoms.

Looking further at CCl₃, it reacts with O₂ to form CCl₃O₂. This species is converted back into O₂ and CCl₃ as well, but the forward reaction rate is twice as high as the backward reaction rate. The remaining CCl₃O₂ will react with NO and itself to form CCl₃O radicals together with O₂ or NO₂. The CCl₃O radicals will on their turn decompose in the by-product COCl₂ (phosgene) and chlorine atoms.

Finally, we also show the production of the by-product CHCl₂COCl (dichloroacetylchloride, DCAC) in Figure 8.5, but only in dashed lines as the rates are below the rate threshold used to produce the graph. DCAC can be produced by oxidation of TCE with OH or ClO, producing DCAC, and H or Cl atoms, respectively (see Eq. 8.8 for the oxidation with OH).

8.4.4 By-products of TCE destruction

In this section, we will discuss the end- and by-products formed during TCE abatement and their effect on the environment and human health. In Table 8.2, a comparison is made for the by-products, as detected in the experiments (with either MS or FT-IR), and calculated with the model for both dry and humid air at an ED of 300 J/L. For the experiments, absolute concentrations could not be obtained with sufficient accuracy, so we only indicate in the table whether these species were detected or not. The calculation results are listed as relative concentrations, with the sum being equal to 100%, to allow an easy comparison between dry and humid air at different removal efficiencies but at the same ED. The experimental diagnostics and the model show a good agreement on a qualitative level, in the sense that the same products are formed in the model and detected in the experiment, except for TCAA (trichloroacetaldehyde), which could not be calculated by the model, simply because of lack of data.

Table 8.2 shows that for both dry and humid air the model predicts that phosgene (COCl_2) and CO account for about 70% of the formed by-products. Phosgene is a highly toxic acylchloride that can cause suffocation by inhalation [485]. It is widely used as an industrial reagent and building block in the synthesis of pharmaceuticals and other organic compounds. Dichloroacetylchloride (DCAC) can cause skin irritation and is used as a reagent for the production of agricultural chemicals and other products. Chloroform (CHCl_3) is a commonly used solvent and reagent in organic synthesis and can cause dizziness, fatigue, and headache [486]. By placing an caustic scrubber downstream of the plasma reactor phosgene and other chlorinated by-products can be hydrolyzed into non-toxic substances [128].

We can see some small differences between the relative concentrations obtained in dry and humid air. Indeed, the relative concentration of COCl_2 slightly drops at increasing humidity as a result of the suppressing effect on ClO, which affects Eq. 8.9 (see also Figure 8.4 and the explanation in section 8.2). Also, the relative concentrations of HCl and Cl_2 drop due to the suppressing effect on ClO. On the other hand, the relative concentrations of CO and CHCl_3 rise. This effect is also related to ClO, as the drop in ClO density gives rise to other TCE destruction reactions, especially by Eq. 8.17. Humid air favors the total production of COCl which is the main source for CO. In dry air most of the COCl is converted into CO by oxidation with O_2 (19%) and ClO (77%); the same is true for humid air, but the oxidation by O_2 becomes more dominant (29%) in relation with ClO (67%). As a result more CHOCl is produced due to oxidation by O_2 which is again a source for CO (as shown in Figure 8.5).

In contrast to CO, the relative concentration of CO_2 decreases with increasing humidity. The reason for this behavior is the combination of the slow oxidation process from CO to CO_2 and the lower absolute CO concentration compared to dry air.

Table 8.2 Comparison of the end- and by-products detected in the experiments and predicted with the model for dry and humid air at 300 J/L.

Product	MS	FT-IR	Relative concentration model dry air (%)	Absolute concentration model dry air (ppm)	Relative concentration model humid air (%)	Absolute concentration model humid air (ppm)
DCAC	✓	✓	1	11	1	5
TCAA	✓		Not included	Not included	Not included	Not included
COCl ₂	✓	✓	30	390	27	211
CHCl ₃			8	98	13	99
CO		✓	40	517	44	341
CO ₂	✓	✓	2	121	1	7
HCl	✓	✓	9	121	7	59
Cl ₂	✓		10	128	7	52

8.4.5 Energy yield

The energy yield of the VOC abatement process is an important parameter that is used to compare the performance of different plasma reactors and operating conditions. The energy yield in g/kWh is calculated as follows:

$$\text{Energy yield} = \frac{C_{in} \times \eta \times M \times 0.15}{\varepsilon} \quad (\text{Eq. 8.19})$$

where C_{in} is the initial concentration (ppm) of the VOC with molecular weight M (g/mol), η is the maximum removal efficiency and ε the corresponding energy density (J/L), i.e. the energy deposited per unit volume of process gas. Each calculation is based on the fact that one mole of a gas occupies 24.04 L volume at standard ambient temperature and pressure (20°C and 101325 Pa).

Table 8.3 compares our result with different studies from literature on TCE abatement with NTP. When we evaluate the energy cost, our plasma reactor can decompose almost 10 g/kWh, which is in the same order as the dielectric barrier discharge (DBD) systems used in [140, 146].

Our numerical and experimental study of TCE abatement with a negative DC corona discharge has shown that formation of unwanted and toxic by-products is an issue that has to be addressed in order to meet current emission legislations to reduce air pollution. Nevertheless, these results help to unravel the underlying plasma chemistry that leads to the destruction of TCE with NTP and are therefore useful because there is still a lack of knowledge about these mechanisms. Furthermore, if a plasma system is combined with a heterogeneous catalyst it is also crucial to know the by-product distribution in order to maximize the efficiency of the process through an optimal choice of catalyst. We have therefore examined Mn-based catalysts which have proven to be effective in terms of activity and selectivity [149, 150].

Table 8.3 Comparison of our study with several other literature results for the abatement of TCE obtained with non-thermal plasma.

Plasma type	Carrier gas	Flow rate (L/min)	Concentration range (ppm)	Energy density (J/L)	Energy yield (g/kWh)	Ref.
DBD	Humid air	0.5	150–200	480	8.1	[140]
Positive corona	Dry air	1.5	100	580	2.2	[147]
DBD	Dry air	0.4	1000	1400	13.7	[146]
Pulsed corona	Dry air	–	100	50	30.9	[157]
Negative corona	Humid air	2	500	180	9.7	own study

8.5 Conclusions

In general, we can conclude that TCE abatement is possible with this corona discharge, with removal efficiencies in the order of 20–80%, increasing with energy deposition. Moreover, the removal efficiency drops by about 15% when the relative humidity increases from 5% to 50%. This is explained by the rates of the loss processes of TCE. A good agreement is reached between the calculation results and the experimental data. Furthermore, the overall pathway for the destruction of TCE is elucidated, pointing out which are the most important end-products, and how they are formed. The humidity has some effect on the pathways, and on the relative contributions of the end-products, but the absolute concentrations are not so much different. Finally, the energy yield of our process compares reasonably well with literature results from other NTP studies.

Chapter 9

TCE abatement with a plasma–catalytic system using a commercial catalyst: Investigation of the synergy effect

This chapter is published as a research article in the following international journal:

A.M. Vandebroucke, M. Mora, C. Jiménez-Sanchidrián, F.J. Romero-Salguero, N. De Geyter, C. Leys, R. Morent,
TCE abatement with a plasma-catalytic combined system using MnO_2 as catalyst
Applied Catalysis B: Environmental 156–157 pp. 94–100, 2014

9.1 Introduction

The aim of this chapter is to study the opportunities of a plasma-catalytic system with a commercial MnO_2 catalyst downstream for the abatement of TCE, in terms of conversion and CO_x selectivity. Also, special attention is given to the effect of catalyst temperature, the role of ozone in the plasma-catalytic TCE abatement and the possible synergy between NTP and catalysis. Finally, a degradation scheme is proposed for the destruction of TCE in the gas-phase and on the catalyst surface.

9.2 Experimental conditions

The experimental conditions used in this study are summarized in Table 9.1.

Table 9.1 Experimental conditions.

Air source	Air Liquide, Alphagaz 1
Flow rate	500 mL/min
Relative humidity (20°C)	0%
Initial TCE concentration	500 ppm
Plasma reactor	B
Catalyst	MnO_2
Catalyst temperature	300–500°C
Optical path length FT-IR	20 cm

9.3 Results and discussion

To investigate the performance of the combined plasma-catalytic system, both parts are initially considered separately, i.e. destruction of TCE through the use of NTP and via catalytic oxidation.

9.3.1 TCE abatement using non-thermal plasma

The abatement of TCE with the plasma system alone was investigated for a gas flow rate of 500 mL/min dry air containing 500 ppm TCE. Figure 9.1 shows the TCE abatement and the selectivity to CO , CO_2 and chlorinated by-products in the plasma as a function of the energy density.

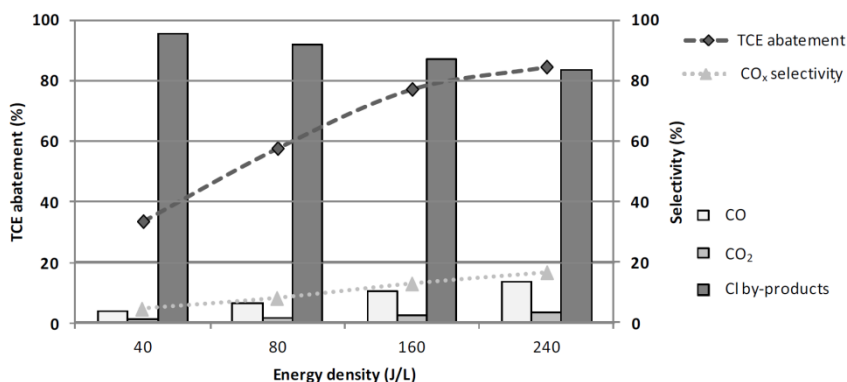


Figure 9.1 TCE abatement with non-thermal plasma.

As expected, an increase of the energy density in the plasma leads to an enhanced TCE abatement. For a maximum energy density of 240 J/L the TCE abatement reaches 85%. This conversion is however related to the formation of undesirable chlorinated by-products such as phosgene (COCl_2) and dichloroacetylchloride (DCAC) [487]. Also, the increase of energy density in the plasma gives an increase of the selectivity to CO and CO_2 . Nevertheless, these selectivities are only 15% at 240 J/L. According to Kirkpatrick et al. [125], DCAC is the major by-product of TCE decomposition with NTP due to reaction of TCE with ClO radicals (generated *in situ* by decomposition of the same VOC in the plasma) according to the following reaction:



The low selectivities to CO and CO_2 can be rationalized if we consider a study by Futamura et al. [135], which refers to the formation of peroxide radicals in the plasma, which would result in oxidative VOC decomposition to CO and CO_2 :



9.3.2 TCE abatement using MnO_2 as catalyst

MnO_2 has been chosen as catalyst due to its excellent results for the oxidation of different VOCs, such as formaldehyde/methanol [488], cyclohexane [114] and benzene/toluene [184]. As the performance of a catalyst depends on the operating temperature, we chose a wide range of temperatures (300–500°C) in order to monitor both the TCE abatement and its selectivity to the various reaction products.

As shown in Figure 9.2, a higher temperature favors the TCE abatement, which exhibits a maximum of 42.6% at 500°C. Also, a large increase is observed for the CO_x-selectivity when comparing both systems, NTP and catalytic reactor, separately, reaching 98% at higher catalyst temperatures, thereby minimizing the formation of chlorinated by-products. This result is quite expected considering that the catalyst can produce the following total oxidation reactions for TCE [489]:



The catalytic activity of the oxide is related to several factors. One of the most important factors is related to the reaction temperature (catalytic furnace temperature) and the oxygen mobility in the crystal lattice of the solid, i.e. the presence of a large number of crystal defects [490].

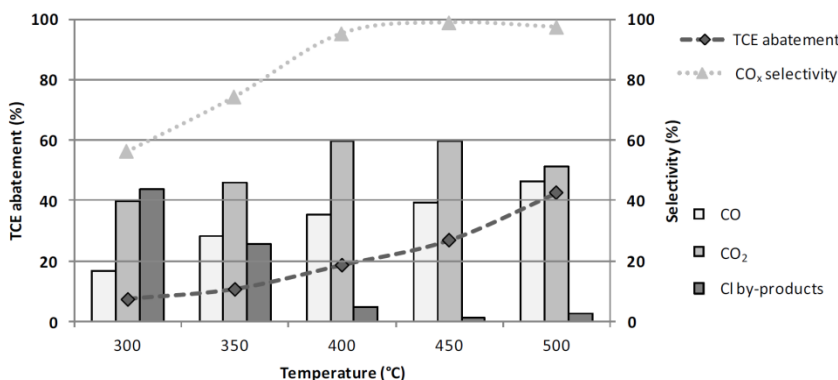


Figure 9.2 TCE abatement with MnO₂.

9.3.3 TCE abatement using the plasma-catalytic combined system

The plasma-catalytic experiments were performed at different values of energy density of the plasma (40–240 J/L) and the catalyst temperature was fixed at 300°C (Figure 9.3). The combined system enhances the TCE abatement compared to the plasma reactor, obtaining a value of 90.5% (plasma-catalysis) versus 84.5% (plasma) at 240 J/L. The abatement of TCE in the catalyst system alone operating at 300°C is only 9.3%. The selectivity of the catalytic and combined system is shown at the bottom of Figure 9.3. At low energy

density the combined system improves the CO_x -selectivity (62.5%) compared to the catalyst alone case (56%), although for higher energy densities there is no real enhancement noticeable. Therefore, experiments should be performed in order to further optimize the combined system and to improve the selectivity of the process. However, at this point we can conclude that the combined system is an effective method for the abatement of TCE.

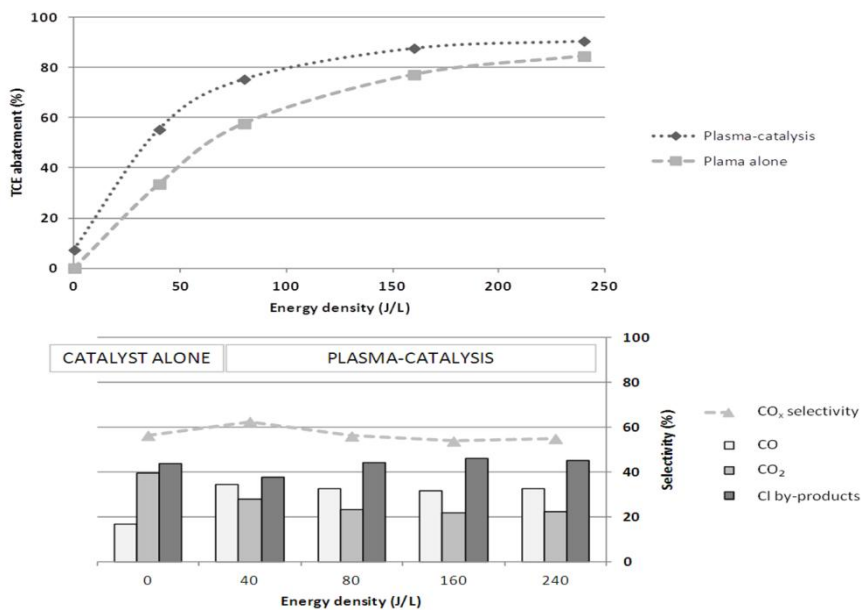


Figure 9.3 TCE abatement with the plasma-catalytic (MnO_2) combined system (oven temperature 300°C).

The formation of various reaction products was evaluated in the plasma-catalytic system at different oven temperatures. The next step was to study the plasma-catalytic abatement of TCE using the same temperature range ($300\text{--}500^\circ\text{C}$) but applying low energy density (40 and 80 J/L) to improve the energy efficiency of the entire system.

Figure 9.4 shows TCE abatement and selectivity to different products for MnO_2 and the plasma-catalytic system. The TCE abatement increases with respect to the temperature in the furnace, obtaining the best value for an energy density of 80 J/L and maximum temperature of 500°C (78%). The CO_x -selectivity depends on the oven temperature but is not much affected by the applied energy density. At 500°C , the combined system slightly improves the CO_x -selectivity while at 300°C there is no distinct effect. If we consider the selectivity to CO and CO_2 , we also find different situations depending on the

presence or the absence of the plasma in the destruction of TCE. Thus, if only the catalyst acts, we find that more CO₂ is produced than CO, while we have the opposite effect when also plasma is involved. Moreover, in the whole temperature range, the combination of plasma and catalysis is the optimal combination to get the best production values of CO and CO₂.

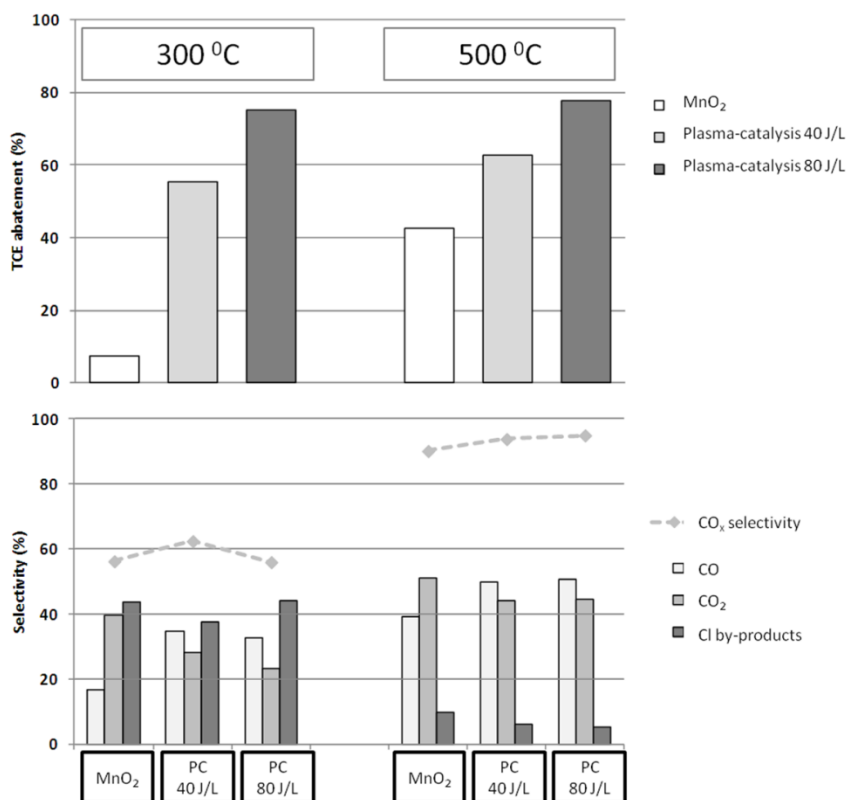


Figure 9.4 Influence of the energy density on TCE abatement and selectivity with the plasma-catalytic combined system.

9.3.4 Calculation of the activation energy for TCE abatement with plasma-catalysis

According to the previous results on the combined system, the use of plasma has a beneficial effect on the performance of the catalyst. In order to examine if the plasma provides an extra activation of the

catalyst, Arrhenius plots were used to calculate the activation energy (E_a) of the three systems (Figure 9.5).

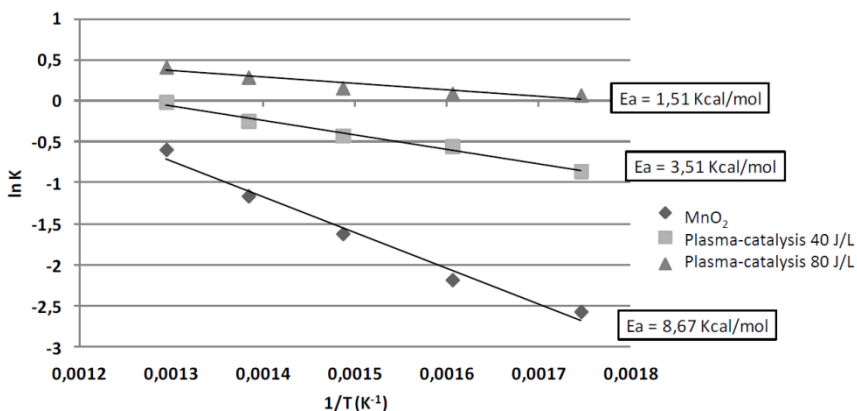


Figure 9.5 Arrhenius plot of the influence of temperature on the activity of MnO₂ for plasma-catalytic TCE abatement.

For the catalytic abatement, a large temperature dependence is observed with respect to the total conversion. The calculated activation energy of 8.67 kcal/mol is in agreement with earlier results obtained for catalytic TCE oxidation [491]. However, in case of plasma-catalysis, the total conversion is much less dependent of the temperature. From these results, it clearly seems that the plasma participates in the transformation of TCE. This also suggests that there is a positive interaction of intermediate oxidation products (phosgene, DCAC) with the catalyst surface. Although this mechanism is not fully elucidated yet, it is reasonable to consider that these intermediates are capable of reaching the catalyst surface. Because these molecules are more susceptible to oxidation by MnO₂, the activation energy is significantly reduced when compared to catalytic oxidation.

9.3.5 Synergy factor in the TCE abatement by plasma-catalysis

Previous studies have shown that the combination of NTP with heterogeneous catalysis often induces a synergetic effect on the removal efficiency of the entire process [234, 269, 277, 345, 492, 493]. To evaluate the synergy in our process, we introduce a synergy factor f for the TCE abatement, as well as for CO and CO₂, which are calculated as followed:

$$f_{TCE} = \frac{(TCE \text{ abatement})_{\text{plasma-catalysis}}}{[(TCE \text{ abatement})_{\text{plasma}} + (TCE \text{ abatement})_{\text{catalysis}}]} \quad (\text{Eq. 9.5})$$

$$f_{CO} = \frac{(Y_{CO})_{\text{plasma-catalysis}}}{[(Y_{CO})_{\text{plasma}} + (Y_{CO})_{\text{catalysis}}]} \quad (\text{Eq. 9.6})$$

$$f_{CO_2} = \frac{(Y_{CO_2})_{\text{plasma-catalysis}}}{[(Y_{CO_2})_{\text{plasma}} + (Y_{CO_2})_{\text{catalysis}}]} \quad (\text{Eq. 9.7})$$

and where Y_{CO} and Y_{CO_2} are the yields to CO and CO₂, respectively, that are defined as:

$$Y_{CO}(\%) = \frac{[CO]_{\text{out}}}{2 \times [TCE]_{\text{in}}} \times 100 \quad (\text{Eq. 9.8})$$

$$Y_{CO_2}(\%) = \frac{[CO_2]_{\text{out}}}{2 \times [TCE]_{\text{in}}} \times 100 \quad (\text{Eq. 9.9})$$

Thus, the synergy factor gives the relation of the studied parameter for plasma–catalysis with respect to the sum of its individual values for plasma and catalyst alone conditions. If this value exceeds 1, a synergetic effect is observed.

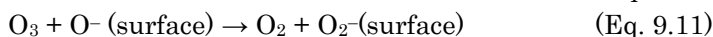
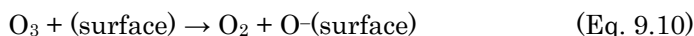
Table 9.2 shows that the synergy factor for TCE abatement is in the range of 0.78–1.35, which indicates that the plasma–catalytic system does not offer a clear synergy with respect to the TCE abatement. Moreover, this factor decreases with the temperature in the oven. This is reasonable because at higher temperatures, the catalyst efficiency for VOC removal increases. In contrast, the synergy factor for the yields to CO and CO₂ ranges from 1.22 to 4.78, indicating that the plasma–catalytic system greatly enhances the selectivity of the process towards total oxidation.

Table 9.2 Synergy factors for plasma–catalytic TCE abatement.

Temp (°C)	f_{TCE}		f_{CO}		f_{CO_2}	
	40 J/L	80 J/L	40 J/L	80 J/L	40 J/L	80 J/L
300	1.35	1.16	4.43	4.78	3.32	3.90
350	0.99	0.97	3.51	3.79	2.64	3.09
400	0.92	0.91	2.48	2.83	1.70	1.97
450	0.89	0.87	1.85	2.23	1.44	1.63
500	0.83	0.78	1.36	1.54	1.22	1.36

9.3.6 The role of the ozone in TCE abatement by plasma–catalysis

The ozone produced in the discharge plays a very important role for the removal of TCE by the combined use of NTP and catalysis. Diverse oxidation reactions using ozone in the feed gas mixture are well known, e.g. catalytic oxidation of benzene [494, 495], toluene [496] and formaldehyde [497]. In all cases, ozone is cleaved at the surface of the catalyst where it can form surface peroxide species over the surface [498] according to the Rideal–Eley mechanism:



To clarify the role of ozone in the plasma–catalytic TCE abatement, the following experiment was carried out. Dry air was fed to the plasma reactor to obtain an ozone concentration of 350 ppm. Next, TCE was introduced in a mixing chamber after the plasma reactor to obtain an ozone/air mixture containing 500 ppm TCE, which was fed to the heated catalyst (indirect process). The ozone concentration was measured at the outlet of the combined system. The TCE abatement and the ozone concentration were compared to the case where the TCE/air mixture was directly fed to the plasma reactor (direct process). In both cases, the temperature in the catalyst bed was maintained at 300°C. The results obtained in both cases are depicted in Figure 9.6.

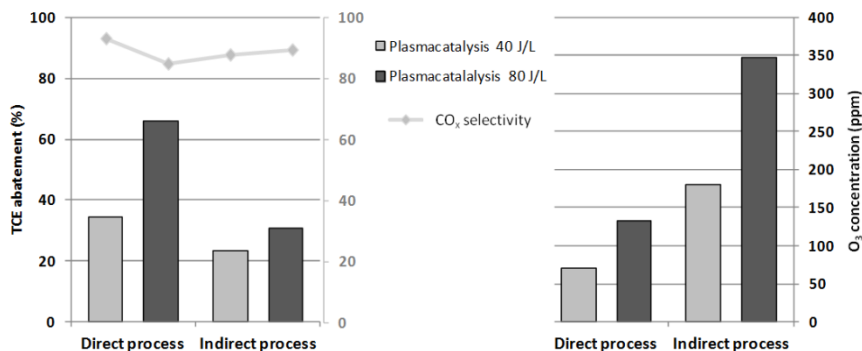


Figure 9.6 Influence of the position of TCE inlet on TCE abatement and ozone concentration for plasma–catalysis.

These experiments provide some useful information about the reaction pathways. The direct process gives a higher TCE abatement than the indirect one, even though the ozone concentration is much higher for the latter one. This is necessarily related to the formation of oxidized compounds in the plasma originated from TCE because a higher concentration of ozone in the reaction mixture should increase the TCE abatement over the catalyst. This is corroborated by two facts. On the one hand, the catalyst gives rise to a higher TCE abatement and CO_x -selectivity for the indirect process than for the catalytic process in absence of plasma discharge (Figure 9.6). On the other hand, the TCE abatement of the indirect process is higher for an energy density of 80 J/L than for 40 J/L. Consequently, the production of oxygenated intermediates, such as phosgene and DCAC, which are more reactive than TCE, improves the performance of the catalyst. These transformations that occur when TCE is introduced in the plasma entail a significant reduction in the concentration of ozone after the catalyst.

As shown in Figure 9.6, the TCE abatement is higher for the direct process. This can be attributed to the fact that for this case energy is transferred to both air and TCE molecules while in the indirect process energy is only transferred to air molecules of the feeding gas. This statement also leads to another conclusion: for the direct process TCE is partially converted to phosgene and DCAC which reach the catalyst surface with a degree of excitation and are therefore more easily decomposed. For the indirect process, however, energy is only transferred to air molecules producing ozone which mainly comes together with TCE at the catalyst surface. To support the latter conclusion, the ozone concentration for the indirect process is twice as high compared to the direct process (Figure 9.6, right).

9.3.7 Transformations in TCE abatement by plasma-catalysis

The TCE abatement and selectivity results obtained in the plasma-catalytic configuration and their comparison to those found in either the catalytic or plasma systems suggest a reaction scheme for the TCE abatement that is represented in Figure 9.7. Firstly, electron-molecule collisions convert N_2 and O_2 molecules to a mixture of ionized, excited, radical and metastable species that are able to decompose TCE to oxygenated intermediates and final oxidation products. Secondly, ozone dissociates on the catalyst surface to form peroxide groups and molecular oxygen in the gas phase. These surface species promote the complete oxidation of TCE to CO , CO_2 , HCl and

Cl₂. This oxidation is more efficient if oxygenated molecules, like phosgene and DCAC, arrive to the surface of the catalyst.

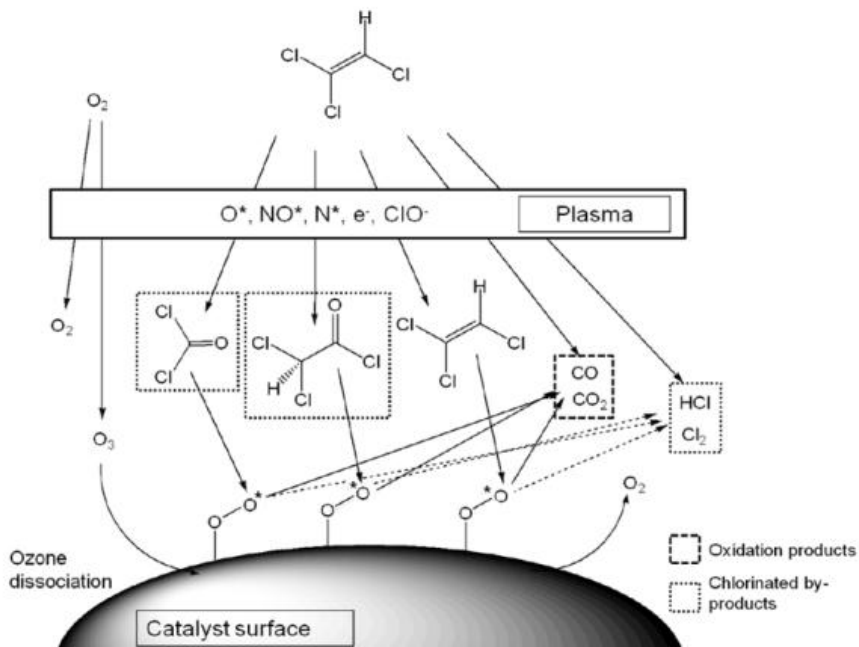


Figure 9.7 Plausible reaction pathway for the plasma–catalytic TCE abatement.

9.4 Conclusions

In this study, we experimentally investigated the abatement of TCE with a plasma–catalytic combined system, formed by a multi–pin–to–plate negative DC corona/glow discharge and MnO₂ catalyst placed downstream of the plasma reactor in a tubular oven.

For the plasma alone system, the main reaction products were oxygenated intermediates (phosgene, DCAC), CO, CO₂, HCl and Cl₂. The CO_x–selectivity did however not exceed 15% even at 240 J/L, indicating that the NTP process is not sufficiently selective.

Under pure catalytic conditions, TCE abatement reached 42.6% at the maximum temperature of 500°C. The CO_x–selectivity significantly improved when compared to the plasma alone system, thereby minimizing the formation of chlorinated by–products.

The combined application of plasma and catalysis led to an enhancement of TCE abatement compared to the separate systems.

Although no clear synergetic effect was found for TCE abatement, the synergy factor for the yield to CO ranged from 1.36 to 4.78 and for CO₂ from 1.22 to 3.90, indicating that the plasma–catalytic system greatly enhances the selectivity of the process towards total oxidation compared to the plasma alone case.

An Arrhenius plot was made in order to calculate the activation energy of the catalytic oxidation and two cases of plasma–catalysis (40–80 J/L). By combining both systems, the activation energy (3.5 – 1.5 kcal/mol) was significantly decreased compared to pure catalytic conditions (8.7 kcal/mol). This suggests that the oxygenated intermediates (phosgene, DCAC) produced by the plasma are more susceptible for catalytic oxidation than TCE.

For the plasma–catalytic process, the role of ozone was studied by introducing TCE after the discharge. These results showed that the role of ozone, generated in the plasma, is not to increase the TCE abatement, but to offer more oxidizing conditions. The ozone is able to dissociate on the catalyst surface by a Rideal–Eley mechanism, thereby creating peroxides surface groups which greatly improve the oxidation of TCE.

Chapter 10

**Plasma-catalysis of low TCE concentration
in air using $\text{LaMnO}_{3+\delta}$ as catalyst:
Influence of the air humidity
and catalyst temperature**

This chapter is published as a research article in the following international journal:

M.T. Nguyen Dinh, J.-M. Giraudon, J.-F. Lamonier, A.M. Vandenbroucke, N. De Geyter, C. Leys, R. Morent,
Plasma-catalysis of low TCE concentration in air using $\text{LaMnO}_{3+\delta}$ as catalyst
Applied Catalysis B: Environmental 147 pp. 904–911, 2014

10.1 Introduction

In this chapter, the performance of $\text{LaMnO}_{3+\delta}$ as post-plasma catalyst was compared to NTP alone for the abatement of TCE in dry air and humid air (RH = 18%). For both processes, the by-product formation was analyzed and discussed. Furthermore, the effect of catalyst temperature was investigated. Finally, the surface of the used catalyst was analyzed by means of XPS.

In the following presentation of the results, $\text{LaMnO}_{3+\delta}$ will be abbreviated by LM. For plasma-catalytic tests, the formulation PPC-LMa-b means that LM is used for post-plasma catalysis performed with relative air humidity “a” and catalyst temperature “b”.

10.2 Experimental conditions

The experimental conditions used in this study are summarized in Table 10.1.

Table 10.1 Experimental conditions.

Air source	Air Liquide, Alphagaz 1
Flow rate	2 L/min
Relative humidity (20°C)	0–18%
Initial TCE concentration	500–600 ppm
Plasma reactor	A
Catalyst	$\text{LaMnO}_{3+\delta}$ (LM)
Catalyst temperature	RT–100–150°C
Optical path length FT-IR	80 cm

10.3 Results and discussion

10.3.1 Destruction of TCE with NTP

Figure 10.1 shows the TCE conversion, the CO_x and O_3 concentrations in function of ED in NTP0 and NTP18 experiments. Compared to NTP0, TCE conversion linearly increases with ED but more rapidly in the presence of water with a slope ratio S_{18}/S_0 of about 1.3. At 500 J/L (16.7 W) the TCE conversion of 73% (NTP0) increases to 85% for NTP18. Therefore, adding small amounts of water appears to be more advantageous from the point of view of TCE decomposition. This might be related to the increase of hydroxyl radicals which may be formed from water. These radicals are well known to be stronger oxidants than others such as oxygen atoms and peroxy radicals.

However, irrespective of the experiments, the carbon mass balance is rather low, about 30% at 500 J/L, with CO as predominant form. The ozone production increases with energy input to achieve a level of 180 and 280 ppm at 460 J/L in wet and dry mixtures, respectively. Hence, O₃ production reduces by one third with water indicating the adverse effect of low humidity on ozone formation.

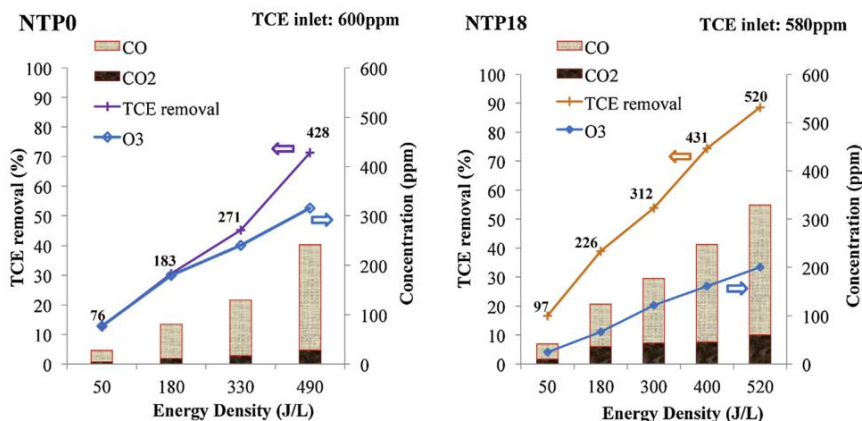


Figure 10.1 TCE removal, CO_x and O₃ concentrations in function of ED in NTP0 and NTP18 experiments (in bolt converted TCE in ppm).

10.3.2 Destruction of TCE with PPC

It must be mentioned that the XRD pattern of the fresh lanthanum manganite sample (not shown here) exhibits only the rhombohedral phase of LaMnO_{3+δ} having a specific surface area of 15 m²/g. Figure 8.2a and b show the TCE conversion, the amount of CO_x produced in function of ED in PPC-LM0-150 and PPC-LM18-150 experiments. When adding water, a significant increase of the TCE conversion for ED less than 460 J/L is observed whereas the discrepancies reduce after that, with removal efficiencies reaching 88 and 93% for dry and humid air, respectively. It is remarkable that the carbon mass balance is significantly improved when adding water vapor, 75% (RH18) compared to 35% (RH0) while the molar CO₂/CO ratio is poorly affected (0.7 and 0.6).

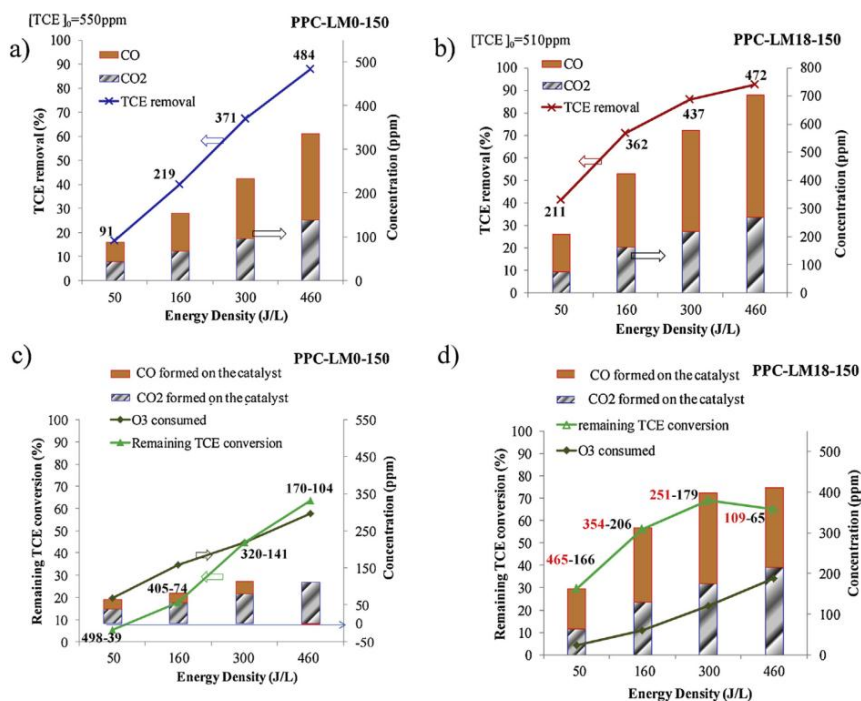
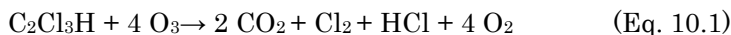


Figure 10.2 TCE removal, CO_x productions in function of ED in a) PPC-LM0-150 and b) PPC-LM18-150 experiments. Remaining TCE removal, CO_x production and O₃ consumption in function of ED in c) PPC-LM0-150 and d) PPC-LM0-150 experiments (in bolt remaining TCE-converted remaining TCE in ppm).

Figures 10.2c and d are related to the performances of the NTP activated catalyst regarding the NTP treated effluent. At 460 J/L, the conversion of the remaining TCE amounts to about 65%. For PPC-LM18-150, a linear evolution is observed between TCE conversion, CO_x production and O₃ consumption for ED ≤ 300 J/L. This shows that O₃ catalytic decomposition produces active oxygen species that are able to convert part of the remaining TCE. Regarding the formal equation below:



The molar ($\text{O}_{3\text{consumed}}/\text{TCE}_{\text{reacted}}$) ratio being less than 4 at low ED implies that other degradation schemes must be considered. At 460 J/L the molar ($\text{CO}_x/\text{TCE}_{\text{reacted}}$) ratio of about 8 clearly shows that the increase of energy enhances the capacity of the catalyst to efficiently destroy the polychlorinated by-products generated in the plasma into CO_x (see below). However, in dry air the plasma-assisted catalyst

appears only as active as in humid air at the highest ED. The catalyst is poorly selective in CO₂ suggesting modifications of the catalyst.

10.3.3 Reaction by-products of TCE decomposition

Figures 10.3 and 10.4 show the FT-IR spectra of both the inlet and outlet stream when the plasma is operated in the same conditions in NTP and PPC experiments, respectively. In NTP, whatever the nature of the carrier gas, along with CO_x formation some polychlorinated by-products have already been partly detected by FT-IR and MS [487]. These include phosgene [499-501], DCAC [502] and TCAD [503, 504]. Another $\nu(\text{C}=\text{O})$ vibration band arising at 1395 cm⁻¹ can also be observed. Its attribution is at the moment questionable. A previous work reported a value of 1794 cm⁻¹ for that band in formylchloride (ClCHO, 1795 cm⁻¹) [505], but in another study the observance of that band is at 1984 cm⁻¹ [506]. Chlorine is also eliminated as HCl (not seen in the figure) and Cl₂ (MS). Formation of ozone and traces of N₂O are also detected in the outlet stream. In plasma alone, collisions of accelerated electrons or radicals with VOC with molecules from the carrier gas (N₂ and O₂) induce reactions of dissociation. In dry air O₂^{*}, N₂^{*} or electrons can react with TCE to give TCE[•] and Cl[•]. Cl[•] can easily react with the reactive double bond of the TCE to give either (CCl₃)CHCl[•] or (CHCl₂)CCl₂[•]. (CCl₃)CHCl[•] and (CHCl₂)CCl₂[•] after reaction with oxygen species (O) and Cl[•] departure give (CCl₃)CHO (trichloroacetaldehyde) and (CHCl₂)COCl (dichloroacetylchloride), respectively. C-C bond cleavage and Cl[•] attack can lead to the formation of phosgene, CO, CO₂, Cl₂, HCl [138].

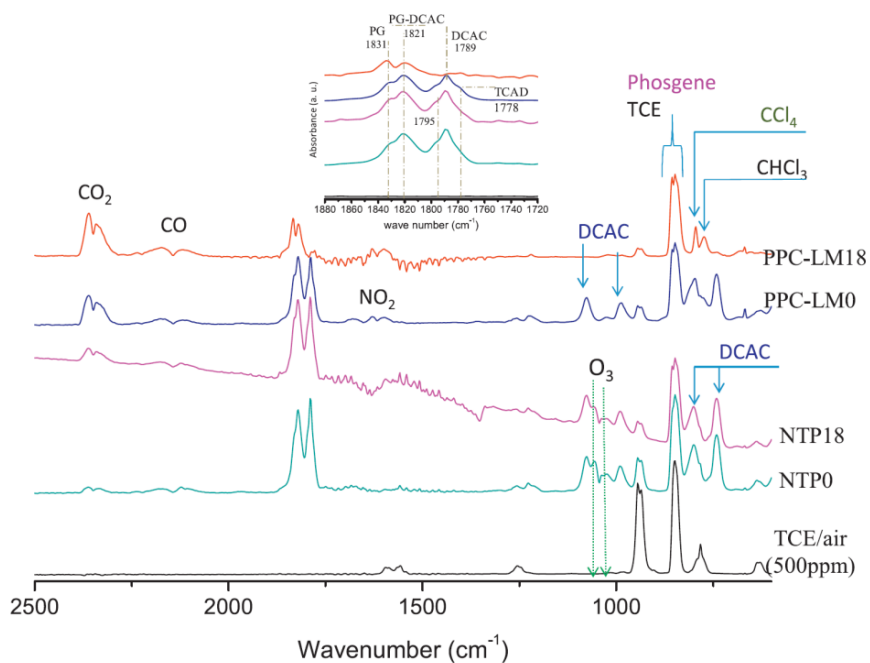


Figure 10.3 FT-IR spectra between 850 and 2500 cm^{-1} of TCE at the inlet and after the plasma and PPC experiments.

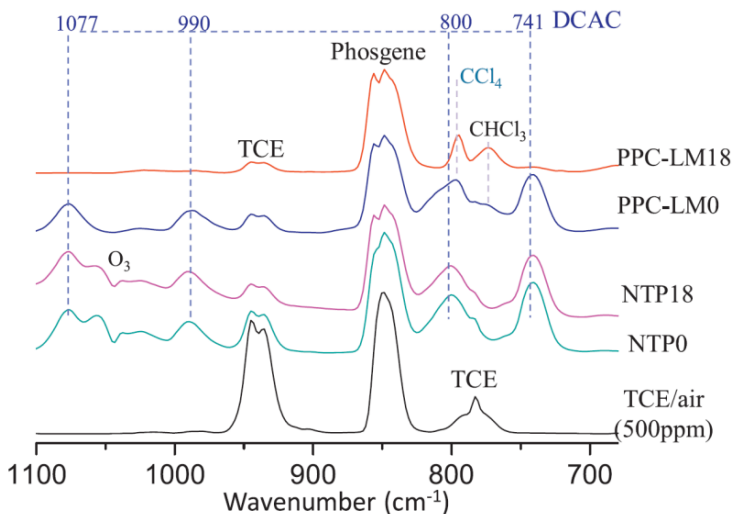


Figure 10.4 FT-IR spectra between 680 and 1100 cm^{-1} of TCE at the inlet and after the plasma and PPC experiments.

In the presence of humidity, direct dissociation of water allows giving the efficient $\text{OH}\cdot$. These species can react with the carbon-carbon double bond of TCE to give $\text{CHCl(OH)-CCl}_2\cdot$. After reaction with O_2 the resulted peroxy radicals transform after radical coupling into chloroethoxyl radicals which can decompose to give phosgene [507]. This pathway can account for the high production of phosgene in NTP0 experiment. When the plasma processed gases, including non-decomposed TCE, ozone and other by-products, were passed through $\text{LaMnO}_{3+\delta}$ catalyst introduced downstream of the plasma reactor, the FT-IR spectra show a decrease in TCE concentration, the disappearance of O_3 as well as the increase of CO_x production (Figures 10.3 and 10.4). Furthermore, DCAC was largely decomposed by passing through the catalyst in humid air. However, DCAC did not decompose in dry air. In addition phosgene and TCAD were decreased, to a lesser extent, when passing through $\text{LaMnO}_{3+\delta}$ catalyst. Although COCl_2 is a toxic industrial chemical, it can be easily removed from the gas stream by simple post-treating with a caustic scrubber. In addition, the appearance of new bands at 794 and 773 cm^{-1} ascribed to C-Cl vibration reveals the presence of two new chlorinated C1 species (Figure 10.4), namely tetrachloromethane (CCl_4) and chloroform (CHCl_3), respectively.

Figure 10.5 shows the relevant $I_x/(I_{95-0}-I_{95})$ ratios in function of the TCE conversion for the different experiments. As expected, these ratios are always lower in PPC experiments compared to NTP ones whatever the TCE conversion under concern, indicating the beneficial role of the catalyst. For NTP, it is remarkable that the relative phosgene production is enhanced compared to those of DCAC and TCAD with humidity. Increasing the TCE conversion in humid air allows to keep the $I_{83}/(I_{95-0}-I_{95})$ ratio stable while decreasing the $I_{82}/(I_{95-0}-I_{95})$ and $I_{63}/(I_{95-0}-I_{95})$ ratios, respectively. Hence, DCAC and TCAD species having a simple carbon-carbon bond were easily broken in the subsequent catalytic reaction into CO_x , HCl , Cl_2 and COCl_2 (for DCAC) as well as to a minor extent to CHCl_3 and CCl_4 with water vapor. In dry air, DCAC is poorly decomposed suggesting catalyst restructuring. Along N_2O , traces of NO_2 have also been detected.

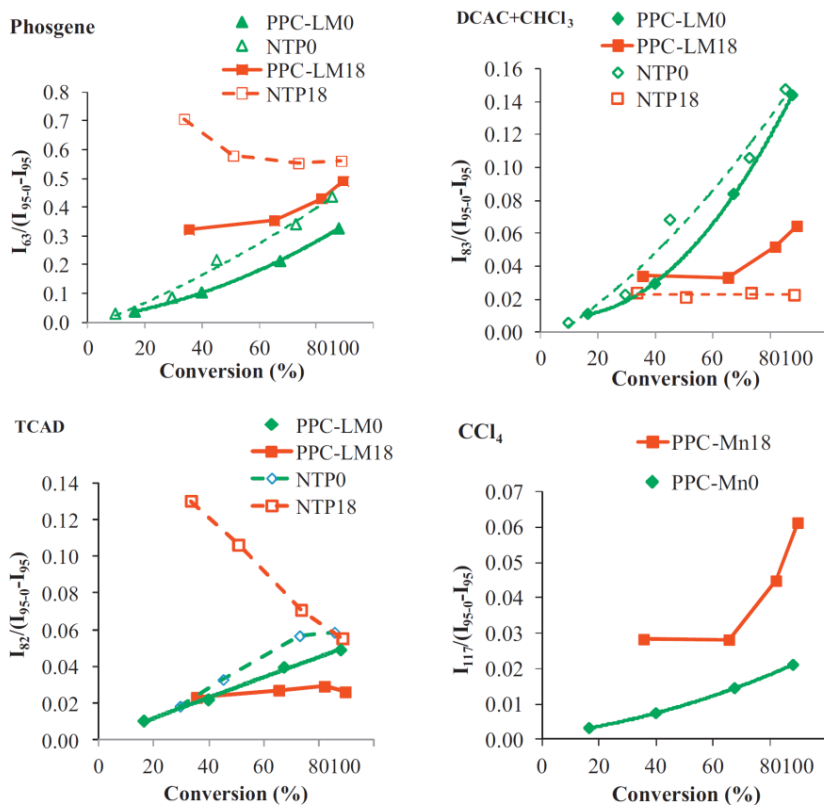


Figure 10.5 Evolution of $I_x/(I_{95-0} - I_{95})$ in function of TCE conversion in NTP and PPC experiments.

The production of Cl_2 and HCl have been monitored by mass-spectroscopy. The $(I_{36}/I_{95-0} - I_{95})$ and $(I_{70}/I_{95-0} - I_{95})$ MS ratios which reflect the selectivity of HCl and Cl_2 , respectively have been plotted in function of ED in the course of the PPC experiments in dry and wet air (Figure 10.6). As shown in the figure, the production of HCl and Cl_2 increase with TCE conversion. In the presence of oxygen without water, the amount of Cl_2 is significantly increased compared to the conditions with humidity. Cl_2 can be a priori formed from the Deacon reaction over possible MnO_xCl_y species which are recognized as possible catalysts of the Deacon reaction but, as already mentioned, the temperatures (150°C) are very low for the reaction to occur at a significant rate. However, chlorine can also be removed from the surface in accordance with the following reaction:



The addition of water can limit the formation of Cl_2 through the Deacon reaction but the effect must be minor due to the low operating temperature. It is believed that water plays a role in the removal of surface chlorine forming thus hydrogen chloride. The decrease of the Cl_2 production can be explained by the change in the mechanism of regeneration of the perovskite as already proposed in the literature [508, 509] in agreement with the following reactions:



Also organic Cl adsorbed species decrease with humidity. It is believed that the chlorine based organic species are destroyed more easily due to the fact that the amount of active sites is higher in wet air due to efficient regeneration of the active sites of the reactions.

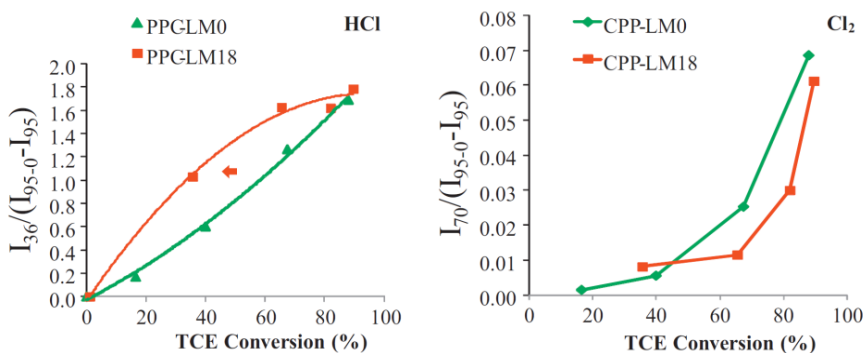


Figure 10.6 Evolution of $I_x/(I_{95-0} - I_{95})$ ($x=36$, HCl; $x=70$, Cl_2) in function of TCE conversion in PPC experiments.

10.3.4 Effect of the temperature

Figure 10.7 shows the conversion of TCE and the carbon mass balance in function of ED for different operating temperatures of the catalyst in dry air. It must be reminded that the experiment at 100°C is carried out just after the one performed at room temperature on contrary to the two other ones which have been performed on fresh catalysts. It is noticeable that, whatever the temperature under concern, adding a catalyst downstream the plasma reactor speeds up the reaction. At 460 J/L , the activity ranks as follows: PPC-LM0-100 (97%) > PPC-LM0-RT (91%) \approx PPC-LM0-150 (88%). Carbon mass

balances as well as CO₂ productions slightly increase with temperature. It is expected that the increase of the temperature of the catalyst reactor may increase the thermal decomposition of ozone in the vicinity of the catalyst leading to a decrease of the disposal of O₃ to be catalytically decomposed on the catalyst. At the same time reactions at the catalyst surface, such as decomposition of ozone and interactions between reactive adsorbed oxygen atoms and TCE and related gaseous polychlorinated by-products, are also accelerated.

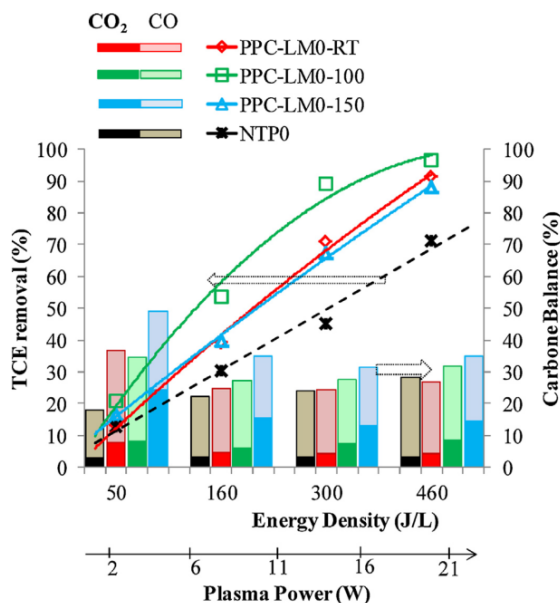


Figure 10.7 Effect of the temperature on the TCE conversion and the carbon mass balance in function of ED.

Figure 10.8 shows the uptake of O₃ at different temperatures compared to the amount of ozone detected at the exit of the NTP in function of ED. Ease of catalytic ozone decomposition increases with temperature even though 10% of O₃ has been estimated to be thermally destroyed at 150°C. Hence the improvement of TCE removal when adding a catalyst is related to its ability to dissociate ozone. Nevertheless, it is surprising that the optimum temperature for TCE removal is at 100°C. A compromise between catalyst deactivation and enhancement of the catalytic reactions may account for such an observation. Regarding the by-products distribution, its nature does not change with temperature. However, it is noticeable that CCl₄ and CHCl₃ relative amounts increase with temperature.

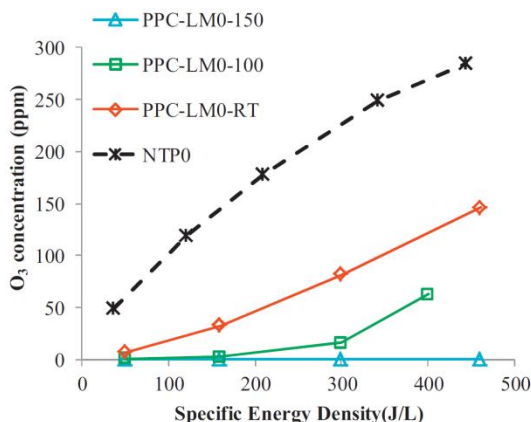


Figure 10.8 O₃ concentration at the exit of the post-plasma catalytic reactor.

10.3.5 XPS characterization of the used catalysts

Table 10.2 presents the atomic composition at the surface of the samples before and after PPC in synthetic air (LM-sa) and ambient air (LM-aa). The XPS atomic La/Mn ratio of the fresh catalyst of 1.61 shows lanthanum enrichment at the surface of the catalyst in accordance with the well known affinity of La³⁺ to react with humidity and CO₂ of ambient air. This ratio remains stable after conducting the test in humid air and significantly increases in dry air. One also notices important carbon enrichment on LM-sa. The high carbon content is explained by the presence of a C1s peak at 282.7 eV ascribed to SiC used as catalyst diluent. High concentrations of chlorine are detected by XPS: 1 Cl atom per 1 M atom (M = La, Mn) to 2 M atoms with humid and dry air, respectively, for an exposure duration to the reactive gaseous effluent of 6 h. Hence, in dry air the extent of chlorine deposit is greatly enhanced compared to humid conditions.

Table 10.2 XPS results of the fresh and tested catalysts.

Samples	Experiments	XPS composition	
		Before test	After test
LM-sa	PPC-LM0-150	LaMn _{0.62} O _{3.46} C _{1.84}	LaMn _{0.49} O _{7.64} C _{5.15} Cl _{1.42}
LM-aa	PPC-LM18-150		LaMn _{0.61} O _{4.21} C _{2.16} Cl _{0.87}

Figure 10.9 shows the decomposition of the Cl 2p and La 4p signals for the tested catalysts. Each envelop can be decomposed into 6 photo-peaks. The two photo-peaks at the lowest binding energies (B.E.) are characteristic of the spin-orbit components La 4p_{3/2} and La 4p_{1/2}. The other four characterize the Cl 2p_{3/2} and Cl 2p_{1/2} components of two distinct chlorine phases (cfr. Table 10.2). The B.E. of the Cl 2p_{3/2} component at 198.3 and 198.7 eV clearly identify mineral chlorine [510]. Formation of (oxi)chlorinated manganese species and oxichlorinated lanthanum could be expected. The value observed at 198.3 eV on LM-aa is lower than the one observed on MnCl₂ (199.2 eV) but matches perfectly to the binding energy of LaOCl Cl 2p_{3/2} at 198.3 eV [508]. This indicates that chlorine atoms are preferentially linked to lanthanum. The second Cl 2p_{3/2} component at 200.3 ± 0.4 eV is ascribed to (oxi)chlorinated organic species such as CH_xCl_y(O_z). A lowering of the (Cl_{org}/Cl_{min}) XPS atomic ratio is shown in humid air (Figure 10.9). These results highlight the role of water which is able to partly cleanup the catalyst surface from chlorine and to delay the perovskite degradation with time on stream.

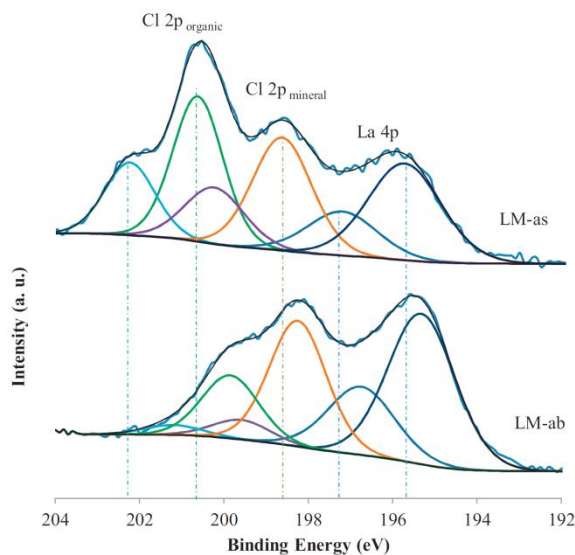


Figure 10.9 XPS of the La 4p and Cl 2p envelop of the tested catalysts

10.4 Conclusion

The decomposition of trichloroethylene was investigated by NTP generated in a DC-excited atmospheric pressure glow discharge using a multi-pin-to-plate electrode configuration and post-plasma catalysis using $\text{LaMnO}_{3+\delta}$ as catalyst. The carrier gas was dry synthetic air and humid air (RH: 18%).

Regarding the NTP process alone:

- The TCE removal efficiency is enhanced in humid air due to the strong oxidation power of OH radicals.
- The carbon mass balances are poor (25–30%) and polychlorinated by-products such as phosgene, DCAC and TCAD are observed along with CO_x , Cl_2 and HCl.
- The O_3 production decreases with humidity.

Regarding the PPC experiments:

- Adding a catalyst downstream the NTP reactor enhances the performances of the process in humid air in terms of TCE removal efficiency and CO_2 selectivity due to the ability of the catalyst to decompose O_3 to generate active oxygen species able to oxidize part of the unreacted TCE and of the polychlorinated by-products.
- The TCE removal efficiency shows an optimal temperature at 100°C in dry air.
- The influence of water is remarkable. Despite the fact that water is able to block the active sites, the performances for TCE degradation are enhanced in humid air due to the role of water to act as a chlorine scavenger at the surface of the catalyst.

Chapter 11

Combination of non-thermal plasma and Pd/LaMnO₃
catalyst for dilute TCE abatement

This chapter is published as a research article in the following international journal:

A.M. Vandenbroucke, M.T. Nguyen Dinh, N. Nuns, J.-M. Giraudon, N. De Geyter, C. Leys, J.-F. Lamonier, R. Morent
Combination of non-thermal plasma and Pd/LaMnO₃ catalyst for dilute trichloroethylene abatement
Chemical Engineering Journal, 283 pp. 668–675, 2016

11.1 Introduction

The aim of the present chapter is to investigate the activity of $\text{LaMnO}_{3+\delta}$ based perovskite catalyst doped with Pd (0.5 wt%) for the oxidation of dilute TCE in humid air (RH = 18%) with a post plasma-catalytic (PPC) system. Particular attention has been paid to the determination of the catalyst surface states with XPS and ToF-SIMS studies before and after the abatement process.

11.2 Experimental conditions

The experimental conditions used in this study are summarized in Table 11.1.

Table 11.1 Experimental conditions.

Air source	Air Liquide, Alphagaz 1
Flow rate	2 L/min
Relative humidity (20°C)	18%
Initial TCE concentration	500–560 ppm
Plasma reactor	A
Catalyst	Pd/LaMnO _{3+δ} (PdLM)
Catalyst temperature	100–150–200°C
Optical path length FT-IR	80 cm

11.3 Results and discussion

11.3.1 TCE abatement with NTP

The abatement of TCE with the plasma alone system has already been reported elsewhere [150], therefore only a brief summary of the results will be given here. The abatement in humid air (RH=18%) increases linearly with energy density and reaches a maximum value of 81% at 460 J/L. However, the CMB which is only based on the formation of CO_x ($x=1, 2$), is rather poor reaching only 32% at 460 J/L. This low value is attributed to the formation of unwanted polychlorinated by-products such as phosgene, dichloroacetylchloride (DCAC) and trichloroacetaldehyde (TCAD). The by-product analysis also reveals the presence of Cl_2 , HCl and small amounts of N_2O while no NO_2 is detected. The ozone concentration increases with energy density reaching 188 ppm at 460 J/L.

11.3.2 TCE abatement with PPC

Figure 11.1 shows the TCE abatement as a function of the energy density for the NTP system and for different temperatures for PPC by adding PdLM downstream of the discharge. We observe that PdLM alone shows nearly no activity for TCE abatement for the temperature range 100–200°C. The TCE abatement curve at 100°C has a similar behavior as the one of NTP treatment but is shifted to higher conversion showing the beneficial effect of the PPC process. After new calcination of the catalyst, it is observed that the TCE abatement at 150°C slightly increases. However, when the temperature of the catalyst was increased to 200°C the TCE abatement decreased. This can be related to a deactivation process of the catalyst. Hence, at 460 J/L the TCE abatement decreases as follows: PPC–150 (96.2%) > PPC–200 (91.7%) > PPC–100 (89.1%) > NTP (82.3%).

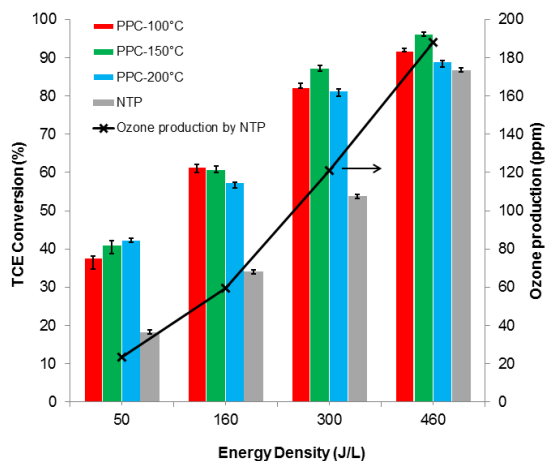


Figure 11.1 TCE abatement as a function of energy density.

Figure 11.2 presents the CMB as a function of the energy density expressed in terms of CO_x selectivity. The CMB as well as the molar CO_2/CO ratio are significantly enhanced for the plasma-catalytic system compared to NTP. At 460 J/L, the CMB for the PPC process at 200°C is about 55% along with a molar CO_2/CO ratio of 0.50 while these values are only 32% and 0.23 for the NTP system, respectively. Hence, the mineralization degree is promoted by adding the PdLM catalyst downstream. It is found that, after re-calcination of the catalyst at 350°C for 4h having operated at 100°C in PPC and further treatment at 150°C, the characteristics in terms of CMB and CO_x selectivities keep unchanged with the margin of uncertainty except for

ED less than 50J/L. By contrast, when the temperature of the catalytic reactor increases from 150 to 200°C we observed a significant enhancement of CMB which amounts now up to 55% mainly due to an increase in CO₂ selectivity.

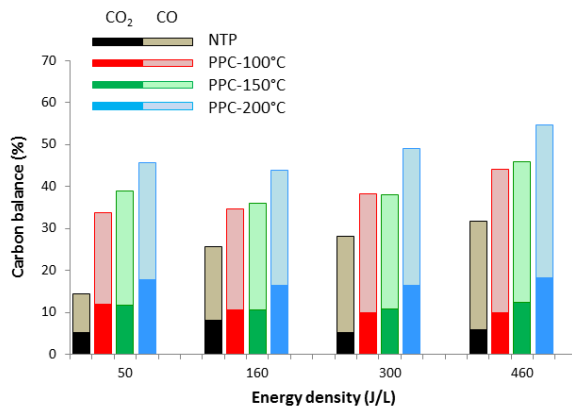
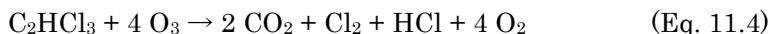


Figure 11.2 Carbon mass balance as a function of energy density.

Figures 11.3 and 11.4 are related to the performances of the NTP activated catalyst regarding the NTP treated effluent. The abatement at 150°C of the remaining TCE increases with ED to reach 70% at 460 J/L while a maximum is observed at 300 J/L for 100°C and 200°C. The molar (O_3 consumed/ $TCE_{reacted}$) ratios in function of ED are rather low, less than 1 for $ED \leq 300$ J/L, and greatly increase for $ED = 460$ J/L with a maximum of ~ 16 at 200°C (Figure 11.4). If we consider that the NTP assisted catalyst quantitatively decomposes O_3 and that the only VOC exposed to the catalyst is non-processed TCE it is expected to obtain molar (O_3 consumed/ $TCE_{reacted}$) ratios between 4 and 2 owing to the following equations:



Hence, the low ratios for $ED \leq 300$ J/L can be explained by the weak NTP produced O_3 amount which limits Eqs. (4) and (5). This means that part of the plasma non-processed TCE is retained on the surface or/and is transformed into C₁ chlorinated compounds as shown below. However, the molar (O_3 consumed/ $TCE_{reacted}$) ratio of about 16 at 200°C for an ED of 460 J/L clearly shows that the active oxygen species issued from the catalytic decomposition of ozone are able to efficiently

destroy part of the polychlorinated by-products generated in the plasma into CO_x as confirmed below by FT-IR spectroscopy.

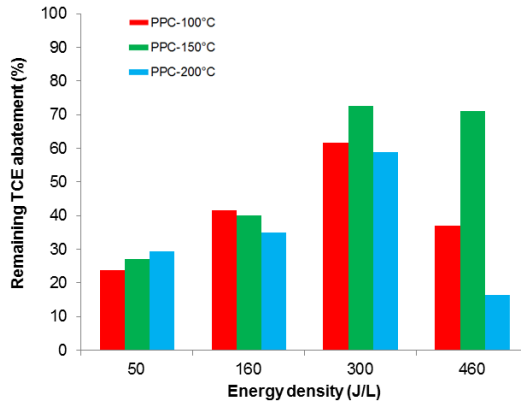


Figure 11.3 Remaining TCE abatement as a function of energy density.

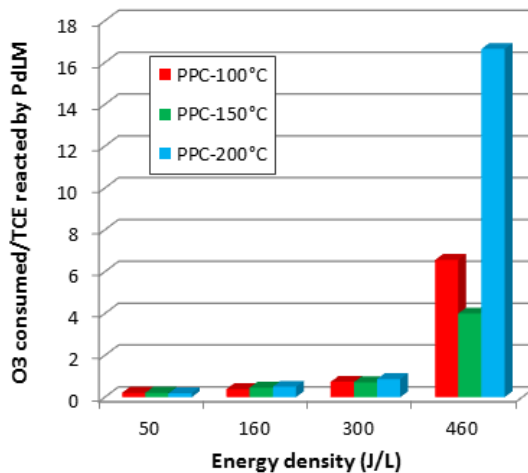


Figure 11.4 Molar ratio O₃ consumed/TCE reacted by PdLM as a function of energy density.

11.3.3 By-product distribution for NTP/PPC

Figures 11.5 and 11.6 compare the IR spectra of the inlet and outlet streams when the plasma is operated at 460 J/L with or without PdLM. The identification of all the products was carried out by

comparing the corresponding absorption bands with the NIST IR spectra standard reference database.

Due to incomplete oxidation of TCE by the plasma, a mixture of unwanted polychlorinated by-products, i.e. phosgene (PG), dichloroacetylchloride (DCAC) and trichloroacetaldehyde (TCAD) is detected in the outlet stream. It is worthwhile to note that these gaseous by-products, especially phosgene, are more toxic than the parent VOC. Nevertheless, final oxidation products such as CO₂, CO and HCl are also formed. Next, ozone and a small amount of N₂O are present due to electron molecule collisions with O₂ and oxidation of N₂, respectively. These results are in accordance with our previous study [487].

For the PPC system, the bands of TCE at 935–945 cm⁻¹ almost completely diminish at 150°C reaching a conversion of 96.2%. The intensity of the bands of DCAC at 740, 990 and 1790 cm⁻¹ decrease with temperature and practically disappear at 200°C. This is related to the high CO_x selectivity at this temperature. Phosgene is also decomposed by PdLM but to a lesser extent compared to DCAC. It is noticeable that the phosgene abatement is enhanced at 150°C when comparing with the perovskite alone [12]. Additionally, by increasing the temperature from 150°C to 200°C the intensity of the resulting band of phosgene at 1832 cm⁻¹ decreases by about 50% in comparison with NTP. Hence, at 200°C incorporation of Pd clearly enhances the phosgene abatement [150]. For all the PPC IR spectra, two new bands at 773 and 794 cm⁻¹ are formed which can be ascribed to the νC–Cl vibration in CHCl₃ and CCl₄ molecules, respectively. The carbon–carbon bond cleavage of adsorbed DCAC and TCAD followed by recombination of the formed species may result in the formation of these Cl chlorinated by-products [150]. The presence of these compounds increases with temperature. At 200°C, the molecular CHCl₃/CCl₄ ratio improves which is beneficial because CHCl₃ is less toxic than CCl₄ [511]. Figure 11.5 also clearly shows that ozone is catalytically decomposed by PdLM irrespective of the temperature. The dissociative decomposition of ozone on the catalyst surface leads to the formation of reactive oxygen radicals that facilitate the abatement of remaining TCE and plasma produced by-products. This observation proves that PdLM is effective for ozone decomposition and substantially enhances the mineralization of TCE compared to the plasma alone system. Finally, a small amount of NO₂ is detected for the PPC process at 150 and 200°C.

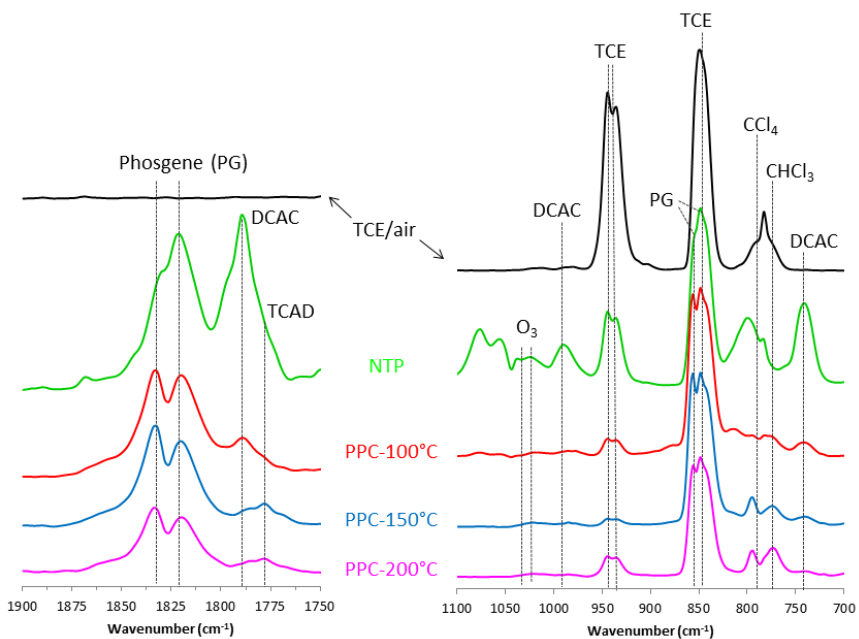


Figure 11.5 FT-IR spectra between 700–1000 cm^{-1} and 1750–1900 cm^{-1} .

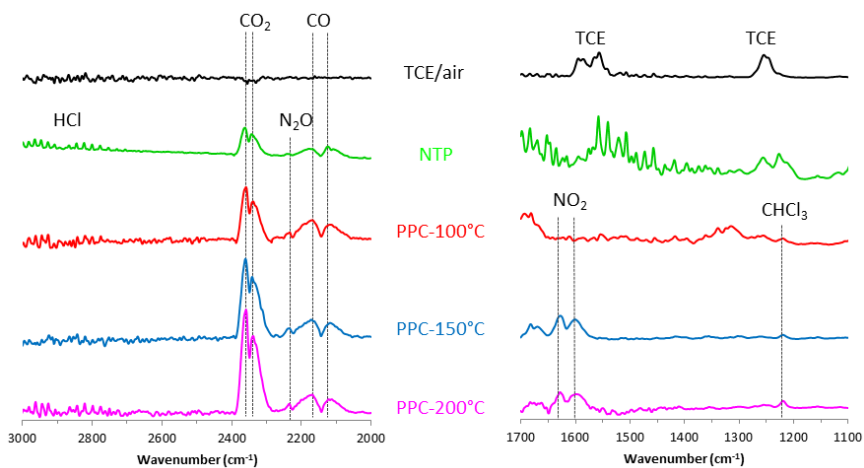


Figure 11.6 FT-IR spectra between 1100–1700 cm^{-1} and 1500–1900 cm^{-1} .

11.3.4 Characterization of the catalyst

11.3.4.1 XPS

The chemical composition and oxidation degrees of the components present at the catalyst surface before and after PPC experiments have been determined by XPS. The duration of each PPC experiment was approximately 4 h. The results are displayed in Tables 11.2 and 11.3 and in Figure 11.7.

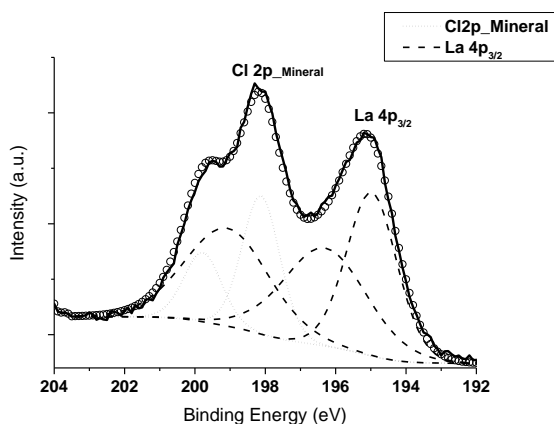


Figure 11.7 Decomposition of the envelope of the Cl 2p and La 4p core levels of the used catalyst.

Table 11.2 XPS results of the catalysts (duration PPC experiment: 4 h).

Samples	La/Mn	C/(La+Mn)	Pd/(La+Mn)	O/(La+Mn)	Cl/(La+Mn)
PdLM fresh	1.23	0.85	0.06	1.94	none
PdLM used	1.30	0.59	0.06	1.80	0.58

Table 11.3 XPS results of the used catalysts (duration PPC experiment: 4 h).

BE (eV)				
Cl 2p _{3/2}	Cl 2p _{1/2}	c4f ⁰	c4f ¹ L bonding	c4f ¹ L anti-bonding
198.1	199.8	195	199.1	196.3

It is found that the La/Mn ratios are in the 1.2–1.3 range as expected for surface lanthanum enrichment [512]. The similarity of the Pd/(La+Mn) ratios indicate that the dispersion of Pd remains unchanged in the course of the reaction. Values of 642.4 and 642.0 eV

were found for the Mn $2p_{3/2}$ peak binding energy maxima for the fresh and used catalysts, respectively. However, as the Mn $2p_{3/2}$ BE of Mn^{3+} and Mn^{4+} are very narrow, this precludes elucidation of the oxidation state of manganese [513]. Hence, the value of the Mn 3s exchange splitting was used to determine the Mn average oxidation state (AOS) in a more quantitative way [514]. It is found that the Mn AOS value is 3.5 which decreases to 3.3 after PPC experiment indicating a slight reduction of the manganese. The Pd 3d core level doublet has well separate spin-orbit components Pd 3 $d_{3/2}$ and Pd 3 $d_{5/2}$ separated by 5.30 eV. The Pd 3 $d_{5/2}$ component at about 337.5 eV has been attributed to Pd in a high oxidation state (+3/+4) existing at the catalyst surface presumably partially incorporated in surface B site of the perovskite [457, 515]. It is found that the BE of Pd 3 $d_{5/2s}$ is at 338.1 eV after PPC experiment. This increase of BE can be explained by the formation of some chloride Pd species. Indeed, this BE is very close to the one reported at 338.2 [516] and 338.4 eV [517] for palladium chloride ($PdCl_2$). The presence of this surface Pd electro-deficient species is supported by the detection of chlorine on the surface of the used sample. Figure 11.7 and Table 11.3 show the decomposition results of the Cl 2p/La 4p envelope.

The La 4p envelope can be decomposed into three peaks. The main peak, denoted $c4f^0$, corresponds to the final state without charge transfer and two satellite peaks correspond to the bonding and anti-bonding components of the final state with charge transfer, denoted cdf^1L bonding and $c4f^1L$ anti-bonding [518]. The resulting Cl 2p core-level spectrum consists of one set of spin-orbit doublet. The Cl 2 $p_{3/2}$ and Cl 2 $p_{1/2}$ peaks were found at 198.1 and 199.8 eV, respectively, giving rise to a spin-orbit splitting of 1.7 eV. The Cl 2 $p_{3/2}$ peak at 198.1 eV may be attributed to Cl forming M-Cl bond (M = Pd, Mn, La) [20].

The Cl/(La+Mn+Pd) XPS ratio of 0.55 shows a high chlorination rate corresponding for a time exposure of about 12 h from the calcination step performed after PPC experiment at 100°C. It should be stressed for sake of comparison that a value of 0.10 was observed on the perovskite alone but for a lower time exposure (6 h), a weight twice as small and for a temperature kept at 150°C. However, these results suggest that the extent of chlorination increases with duration of the reaction.

11.3.4.2 ToF-SIMS of the used catalysts

In order to obtain molecular information of the Cl speciation over the catalyst, a ToF-SIMS study of the fresh and used catalyst has

been performed. ToF-SIMS probes the top layers (1–3 nm) of the catalysts and allows to obtain molecular information about the surface. The ToF-SIMS examination of the Cl^+ and HCl^+ normalized signals given in Figure 11.8 show the presence of chlorine in a significant amount after PPC experiment.

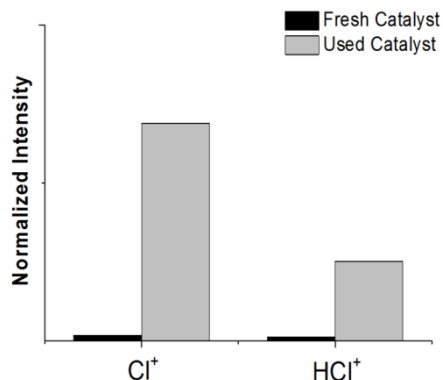


Figure 11.8 Cl^+ and HCl^+ fragment ions contributions on fresh and used PdLM catalysts as a percentage of the total ion counts.

Secondary ions relative to mineral chlorine species excluding those relevant to Pd have been investigated in both polarities. Table 11.4 shows the detected ions relative to the different families: MnCl_x^\pm , LaCl_x^\pm , $\text{Mn}_x\text{O}_y\text{Cl}_z^\pm$, $\text{La}_x\text{O}_y\text{Cl}_z^\pm$ and $\text{La}_x\text{Mn}_x'\text{O}_y\text{Cl}_z^\pm$.

Table 11.4 Selected ions for the different chlorinated mineral (duration PPC experiment: 4 h).

Species	MnCl_x	LaCl_x	$\text{Mn}_x\text{O}_y\text{Cl}_z$	$\text{La}_x\text{O}_y\text{Cl}_z$	$\text{La}_x\text{Mn}_x'\text{O}_y\text{Cl}_z$
Positive mode	MnCl^+	LaCl^+	MnOCl^+	LaOCl^+	$\text{LaMnO}_2\text{Cl}^+$
		LaCl_2^+	Mn_2OCl^+	$\text{La}_2\text{O}_2\text{Cl}^+$	$\text{La}_2\text{MnO}_3\text{Cl}^+$
				$\text{La}_4\text{O}_5\text{Cl}^+$	
Negative mode	MnCl_3^-	LaCl_3^-	MnO_2Cl^-	LaOCl^- ; LaO_2Cl^+ ; LaOCl_2^+	
		LaCl_4^-	MnOCl_2^-	LaOCl_3^+ ; $\text{La}_2\text{O}_2\text{Cl}_2^+$; $\text{La}_2\text{O}_2\text{Cl}_3^+$; $\text{La}_3\text{O}_3\text{Cl}_4^+$	

The fragments ions contributions displayed in Figure 11.9 are in accordance with those found in literature for the perovskite alone [512].

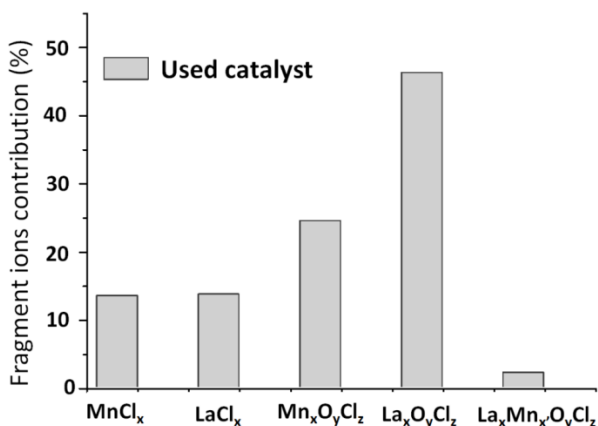


Figure 11.9 Fragment ions contribution on used PdLM.

Hence, chlorination takes place on lanthanum and manganese ions. A semi-quantitative approach, neglecting matrix effects in this case, indicates that La(oxy-hydroxy)chlorination rate is favored compared to the Mn one. The identification of PdOCl⁻ and PdCl₂⁻ ions in negative polarity (Figure 11.10) indicates that species containing both palladium and chlorine existed on the investigated surface.

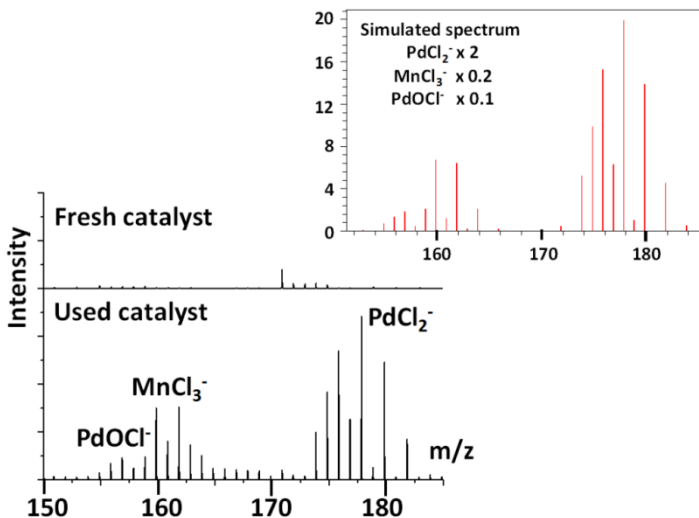


Figure 11.10 ToF-SIMS(-) spectra of PdOCl, MnCl₃⁻ and PdCl₂⁻ for PdLM before and after test.

The most intense palladium ions detected in positive polarity are Pd^+ , PdMn^+ , PdLaO_2^+ and $\text{PdLa}_2\text{O}_3^+$. The research of chlorinated organic ions has also been investigated although no organic Cl species were detected by XPS. The main intensities detected are relative to C_2HCl^+ , CHCl^+ , $\text{C}_3\text{H}_4\text{Cl}^+$ and CH_2Cl^- , CHCl_2^- , $\text{C}_2\text{H}_2\text{O}_2\text{Cl}^-$ ions in positive and negative polarities, respectively (Figure 11.11).

These chlorinated residues bound to the catalytic surface appear in relatively low amounts in line with the previous results. This confirms the beneficial cleaning role of water allowing the surface of the catalyst to get rid of inorganic polychlorinated species [512].

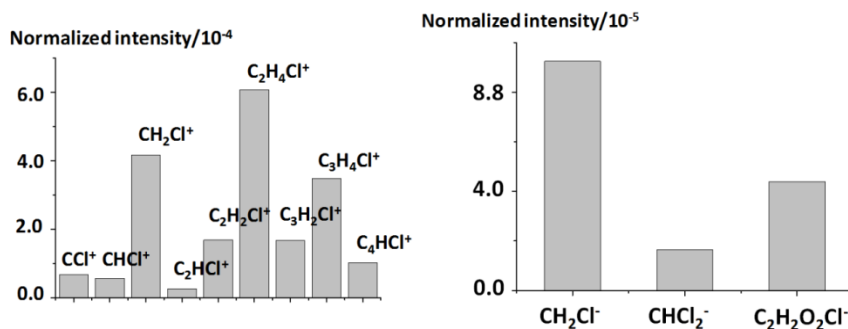


Figure 11.11 Normalized intensity of the organic chlorinated ions in positive and negative mode.

11.4 Conclusions

The CMB as well as the molar CO_2/CO ratio are significantly enhanced for the plasma-catalytic system compared to NTP when using PdLM downstream the NTP. However, study of the performance of the NTP assisted Pd/LaMnO₃ catalyst shows that the O₃ production by the discharge limits the degradation of TCE and chlorinated by-products into CO₂ by active oxygen species originating from the catalytic ozone degradation. Hence, this precludes observing an expected enhancement of the NTP assisted catalyst performances for TCE abatement. Additionally, it is found from the combined XPS and ToF-SIMS results surface Pd electro-deficient species along with La and Mn (oxy)chlorides in line with the (oxy)chlorination of the catalyst in the course of the reaction.

Chapter 12

**Post plasma-catalysis for total oxidation of TCE
over Ce–Mn based oxides synthesized by
a modified “redox-precipitation route”**

This chapter is published as a research article in the following international journal:

M.T. Nguyen Dinh, J.-M. Giraudon, A.M. Vandenbroucke, R. Morent, N. De Geyter, J.-F. Lamonier
Post-plasma catalysis for total oxidation of trichloroethylene over Ce-Mn based oxides synthesized by a modified “redox-precipitation route”
Applied Catalysis B: Environmental 172 pp. 65-72, 2015

12.1 Introduction

In this final chapter, TCE abatement was investigated in moist air (RH=10%) at 150°C with catalyst alone, NTP alone at ambient conditions and with a PPC system. The studied catalysts were two dispersed CeMn_x oxide catalysts (x = 1, 4) prepared by a modified procedure inspired from the “redox–precipitation” route previously described (Section 6.4.4) and one reference MnO_y catalyst. The use of CeMn oxides in the combined system has not been reported so far in PPC experiments despite of their high performances in TCE total oxidation. During this study, particular attention has been paid to investigate the performance of the plasma–assisted catalysts for TCE abatement and to make a correlation with the physico–chemical properties of the tested catalysts.

12.2 Experimental conditions

The experimental conditions used in this study are summarized in Table 12.1.

Table 12.1 Experimental conditions.

Air source	compressor
Flow rate	2 L/min
Relative humidity (20°C)	18%
Initial TCE concentration	360–400 ppm
Plasma reactor	A
Catalyst	MnO _y , CeMn _x O _y (x=1, 4)
Catalyst temperature	150°C
Optical path length FT–IR	20 cm

12.3 Results and discussion

12.3.1 Catalyst properties

The diffractograms of the dried samples consist of a broad 2θ component (20–40°) followed by a large envelop (40–70°) indicative of solid architecture missing substantial “long–range” crystalline order. The diffractogram of the calcined CeMn oxide displayed in Figure 12.1 exhibits the characteristic peaks of the CeO₂ fluorite–like phase (JCPDS 00–004–0593) with no shift in 2θ of the peak position with Mn content. The XRD pattern of the calcined CeMn₄ is rather similar to that of the dried precursor of CeMn sample and compared well with

diffractograms recorded for extremely dispersed ceria systems [519-521].

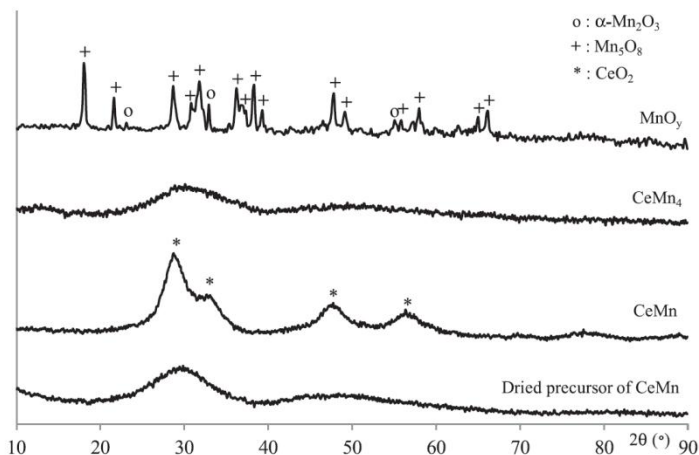


Figure 12.1 XRD patterns of the fresh catalysts.

The XRD pattern of MnO_y shows peaks of higher intensity ascribed to the monoclinic phase of the metastable Mn_5O_8 (Mn_3^{4+} , Mn_2^{2+}) (JCPDS 00–039–1218) phase along with other peaks of lower intensity ascribed to the cubic phase $\alpha\text{-Mn}_2\text{O}_3$ (Mn_2^{3+} , Mn^{2+}) (JCPDS 01–089–2809). From the height ratio of the most intense peaks of each phase ($2\theta = 18^\circ\text{-Mn}_5\text{O}_8$; $2\theta = 32.9^\circ\text{-}\alpha\text{-Mn}_2\text{O}_3$) a rough estimation of the Mn_5O_8 percentage in the powder mixture gives a value of 70%. The S_{BET} values are characterized by a large surface exposure in the calcined CeMn sample ($165\text{ m}^2/\text{g}$) which decreases to $95\text{ m}^2/\text{g}$ when the Mn loading increases (CeMn_4). It is noticeable that the CeMn sample develops an outstanding surface exposure of $165\text{ m}^2/\text{g}$ close to the one of $154\text{ m}^2/\text{g}$ reported by Arena et al. but obtained at a calcination temperature 100°C lower than ours [447]. Contrarily, the specific surface area of the MnO_y sample is only $13\text{ m}^2/\text{g}$. Regarding the XPS results, the $\text{Mn}/(\text{Ce} + \text{Mn})_{\text{XPS}}$ atomic ratio in function of the nominal value $\text{Mn}/(\text{Ce} + \text{Mn})$ affords a straight–line with a slope value of 1.0 indicating a (quasi) molecular dispersion of the active phase in the different samples. The enhanced textural properties developed by the samples along with the absence of substantial “long–range” crystalline order as well as the similarity in terms of surface and bulk composition accounts for the beneficial effect of the synthesis route compared to the co–precipitation synthesis in accordance with the works of Arena et al. [447]. The average oxidation state (AOS) of manganese was determined by XPS from the relation based on a

correlation between the binding energies of the doublet separation of $Mn3s$ (ΔE_s) and the AOS, $AOS = 8.956 - 1.13 \Delta E_s$, given by Galakhov et al. [514]. An AOS value higher than 3.0 is found: 3.3 and 3.5, for the $CeMn$ and $CeMn_4$ samples, respectively. Because of its sensitivity to amorphous components and those with short-range order, Raman spectroscopy is very useful to study the structure of MnO_y materials where crystalline disorder may be expected. The LRS of the $CeMn$ sample (Figure 12.2) shows a mostly amorphous pattern in line with the lack of any long-range crystalline order consistent with the results of Arena et al. [467].

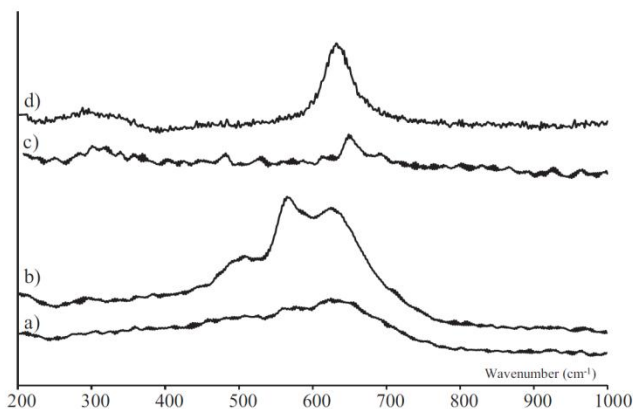


Figure 12.2 LRS of the fresh samples: (a) $CeMn$; (b) $CeMn_4$; (c) and (d) MnO_y .

All the LRS of $CeMn_4$ show similar features of birnessite-type MnO_2 with layered structure having a low Raman activity [522, 523]. Three major peaks can be evidenced at 510, 565 and 625 cm^{-1} with the two high wavenumber peaks dominating all spectra. Indeed, three major features have been previously reported at 500–510, 575–585 and 625–650 cm^{-1} regarding such materials [524]. It is noticeable that the frequency position of these major Raman-active modes can change as a function of the average MnO_6 octahedral polymerization in several manganese oxide structures [525]. This result substantiates the XRD observation of the presence of a possible birnessite phase having a large diffraction peak at $2\theta = 18^\circ$ (Figure 12.1). Regarding the LRS of the MnO_y sample an LRS with high Raman activity having the features characteristic of $\alpha-Mn_2O_3$ (Figure 12.2(c)) [526] with a large peak positioned at 634 cm^{-1} is found. Other spectra show a low Raman activity displaying weak peaks at 480, 535, 620 cm^{-1} as well as a more intense one positioned at 649 cm^{-1} characteristic of the metastable Mn_5O_8 oxide species (Figure 12.2(d)) [527].

12.3.2 TCE decomposition efficiency

Figure 12.3 shows the evolution of η_{TCE} in function of the energy density relative to NTP in NTP (room temperature) and PPC experiments (NTP: room temperature; catalytic reactor: 150°C). Regarding the NTP experiment, the TCE abatement increases with ED due to the formation of more energetic electrons to reach a TCE removal efficiency of 87% at 240 J/L. However, the CO_x selectivity is still low spanning from 20 to 27% whatever ED used. Furthermore, the gas discharge also induces the formation of ozone as hazardous by-product whose production increases with ED to 350 ppm at 240 J/L.

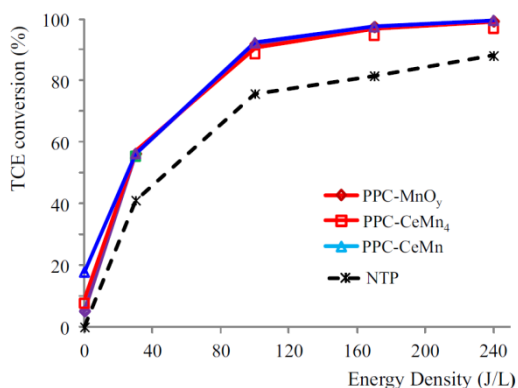


Figure 12.3 TCE conversion in function of the energy density.

The reactivity for TCE degradation has been then investigated over the catalysts without NTP at 150°C after a pre-calcination step at 350°C. The samples can be ranked by increasing TCE conversion ($\eta_{\text{TCE}}_{\text{CAT}}$) as followed: $\text{MnO}_y(5\%) < \text{CeMn}_4(8\%) < \text{CeMn}(18\%)$. Based on the formula of TCE conversion used herein, although CO_2 is the only detected gaseous compound, TCE adsorption on the catalyst may also account for such values. Thus, from carbon-mass balance (CMB) results, it is found that the MnO_y catalyst is highly selective into CO_2 having a CMB close to 100%. However, the low CMBs of 40 and 17% observed for CeMn_4 and CeMn samples, respectively, can mainly be attributed to TCE adsorption in accordance with their porous nature. Also, as expected, the high weight hourly space velocity (WHSV) of 120 L/(h.g) precludes having high TCE conversion on these catalysts without NTP. The evolution of η_{TCE} in function of energy density in PPC experiments (Figures 12.3 and 12.4) displays a similar behavior to the one observed for NTP alone but are translated to higher η

values for a given ED. However it has to be stressed that a direct comparison is not possible in terms of an energetic point of view as the extra input energy to maintain the catalytic reactor to 150°C has not been considered. At 240 J/L, high TCE conversion can be achieved following the increasing sequence: $\text{CeMn}_4(96.9\%) < \text{MnO}_y(99.3\%) \approx \text{CeMn}(99.5\%)$.

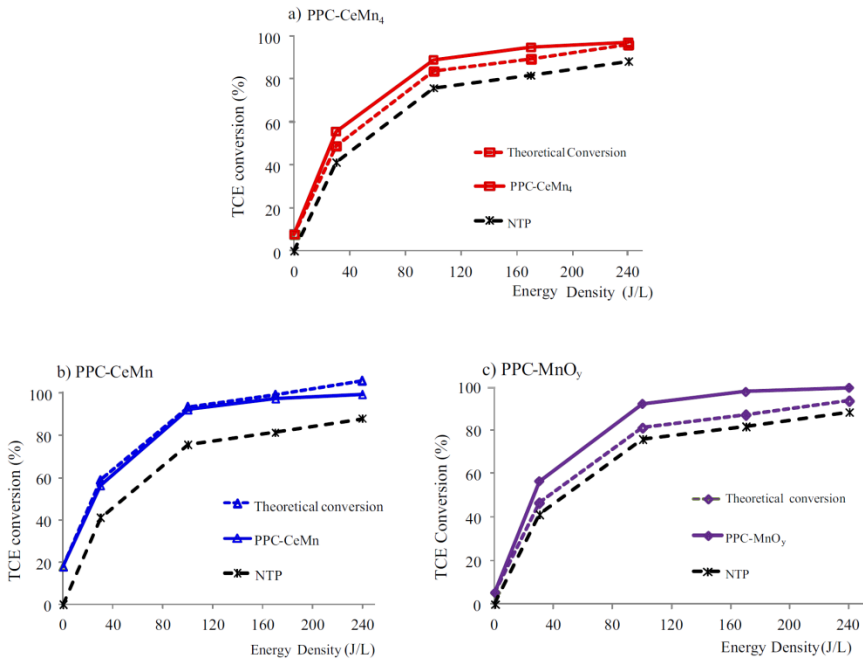


Figure 12.4 Representation of $(\eta_{\text{TCE}})_{\text{NTP}}$, $(\eta_{\text{TCE}})_{\text{CAT}}$ and $(\eta_{\text{TCE}})_{\text{NTP}} + (\eta_{\text{TCE}})_{\text{CAT}}$ in function of the energy density.

Figure 12.4 also shows that, for a given ED, the η_{TCE} achieved with plasma-catalysis is higher than the theoretical TCE conversion $(\eta_{\text{TCE}})_{\text{TH}}$ which is the summation of those of plasma alone $(\eta_{\text{TCE}})_{\text{NTP}}$ and catalyst-alone $(\eta_{\text{TCE}})_{\text{CAT}}$ whatever ED used for MnO_y oxide and up to 170 J/L for the CeMn_4 sample. On the other hand, it is found that the experimental and theoretical curves superimpose up to 170 J/L for CeMn sample. However, as the TCE consumption with the catalyst alone is mostly related to adsorption for CeMn, the theoretical curve is overestimated. As a result, the experimental curve should also have been higher than the true theoretical curve. Hence, it is observed a synergetic effect by combining both NTP and MnO_y catalyst or in interaction with CeO_x . This effect can be related to the efficiency of MnO_y and CeO_2 to dissociatively decompose ozone. This reaction

enables the supply of additional active oxygen species that assist the destruction of remaining TCE exiting the plasma reactor. Indeed, MnO_2 is well recognized to be the best bulk catalyst for this reaction [451].

Figure 12.5 shows the CMB expressed in terms of CO_x selectivities in function of ED. For PPC experiments, a 1.5 to 2-fold increase of the CMB was observed whatever the ED used. For a η_{TCE} of about 95–100%, the CMB values reach 50–65% along with molar CO_2/CO_x ($x = 1, 2$) ratios of 0.45–0.60 compared to 26% and 0.15 with NTP, respectively. Hence, the rate of TCE mineralization increased with the hybrid process, promoting the CO_2 production at the expense of CO.

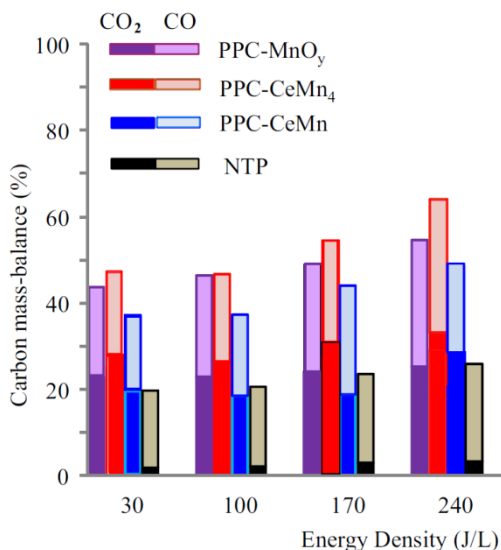
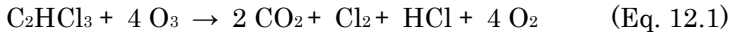


Figure 12.5 Mass carbon balance for the PPC process in function of the energy density.

Figure 12.6 displays the remaining TCE conversion $\eta_{\text{TCE-remaining}}$, which is the rate of destruction of the NTP unreacted TCE over the catalysts under study as well as the molar ratio $R_{(\text{O}_3/\text{TCE})}$ (O_3 consumed/reacted remaining TCE) in function of the ED. Ease of destruction of the NTP unreacted TCE increases over the assisted catalysts irrespective of the ED as follows: $\text{CeMn}_4 < \text{MnO}_y \approx \text{CeMn}$. Regarding the plasma-assisted MnO_y and CeMn samples having the same specific activity, it is found that the intrinsic activity on MnO_y r_{TCE} (MnO_y) is about 13 times higher than the intrinsic activity on CeMn r_{TCE} (CeMn) taking into account the ratio of the specific surface area of the catalysts. Although the Mn content for the CeMn sample is twice as small as that of the MnO_y sample, the value of the relative

ratio of the intrinsic rates shows that the quality (nature) of the active sites has to be considered. The reaction with O_3 is in line with the formal equation:



It is noticeable that the $R_{(O_3/TCE)}$ values become higher than 4 for ED higher than 170 J/L for both catalysts. This can be attributed to the greater ability of all the catalysts to oxidize the NTP gaseous polychlorinated intermediates using O_3 . The higher $R_{(O_3/TCE)}$ for $CeMn_4$ irrespective of ED reflects the better reactivity of this catalyst to transform such gaseous by-products at the expense of the NTP non-processed TCE.

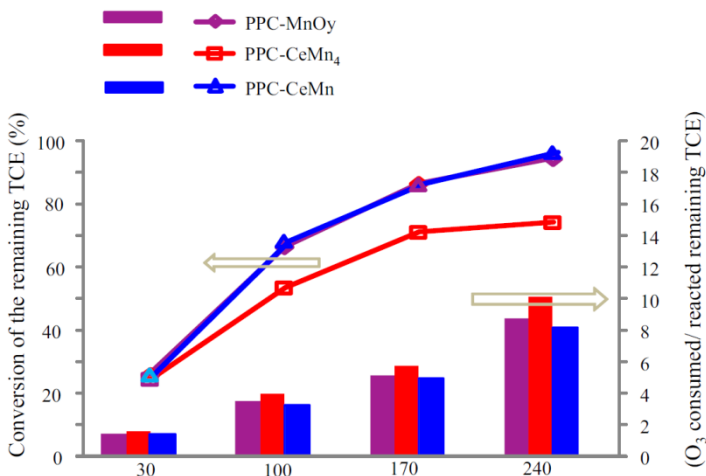


Figure 12.6 TCE conversion and molar ratio $R_{(O_3/TCE)}$ (O_3 consumed/reacted remaining TCE) in function of the energy density.

Figure 12.7 sums up the performance in terms of TCE conversion, CO_2 and CO_x yields of the different processes: total catalytic oxidation, NTP and PPC. Whatever the parameter under concern, PPC was found to be the best alternative to convert TCE into CO_2 while $CeMn_4$ was found to be the best NTP assisted catalyst in terms of CO_2 selectivity.

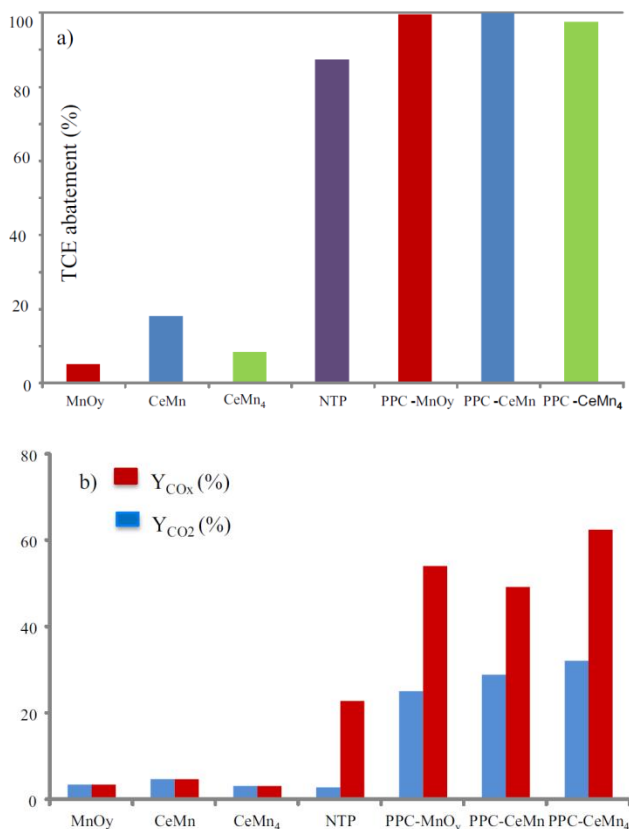


Figure 12.7 (a) η_{TCE} conversion and (b) CO_x and CO₂ yield with catalysts alone (150°C), in NTP alone (RT, 240 J/L) and in PPC experiments (240 J/L).

12.3.3 Detection of the gaseous by-products by FT-IR

Figures 12.8 and 12.9 show the FT-IR spectra of both the inlet and outlet streams when the plasma reactor is operated at 240 J/L with or without catalysts. By carefully comparing these figures with the NIST IR spectra standard reference database, the TCE abatement in NTP is supported by a strong decrease of the absorption bands at 935–945 cm⁻¹. FT-IR reveals formation of phosgene (PG), dichloroacetylchloride (DCAC) and trichloroacetaldehyde (TCAD) as incomplete gaseous oxidation products in accordance with a previous study [487]. TCE is also decomposed to a lesser extent to CO₂, CO and HCl. Formation of O₃ is also detected in the outlet stream which

amounts 350 to ppm at 240 J/L. A small amount of N_2O is also detected due to N_2 oxidation. Regarding the assisted catalysts, total TCE removal is observed in the presence of MnO_y and CeMn catalysts while a very small contribution of TCE still remains in the presence of $CeMn_4$ oxide. The IR absorption bands characteristic of DCAC and TCAD strongly decrease for CeMn and MnO_y and are absent for the $CeMn_4$ sample. The IR bands relative to PG positioned at about 1820 and 1832 cm^{-1} decrease in intensity in accordance with the sequence $CeMn > MnO_y \gg CeMn_4$. These results indicate the better ability of $CeMn_4$ to transform almost all of the toxic gaseous by-products generated by the plasma. However, two new bands at 794 and 773 cm^{-1} have been detected in all PPC experiments. These bands have been ascribed to the $\nu C-Cl$ vibrations of CCl_4 and $CHCl_3$, respectively. These new C1 chlorinated species may be likely formed through recombination of adsorbed species resulting from carbon-carbon bond cleavage of DCAC and TCAD. Furthermore, the absence of O_3 shows that all samples are active ozone-decomposition catalysts. Formation of NO_2 , not detected by the NTP, is also observed.

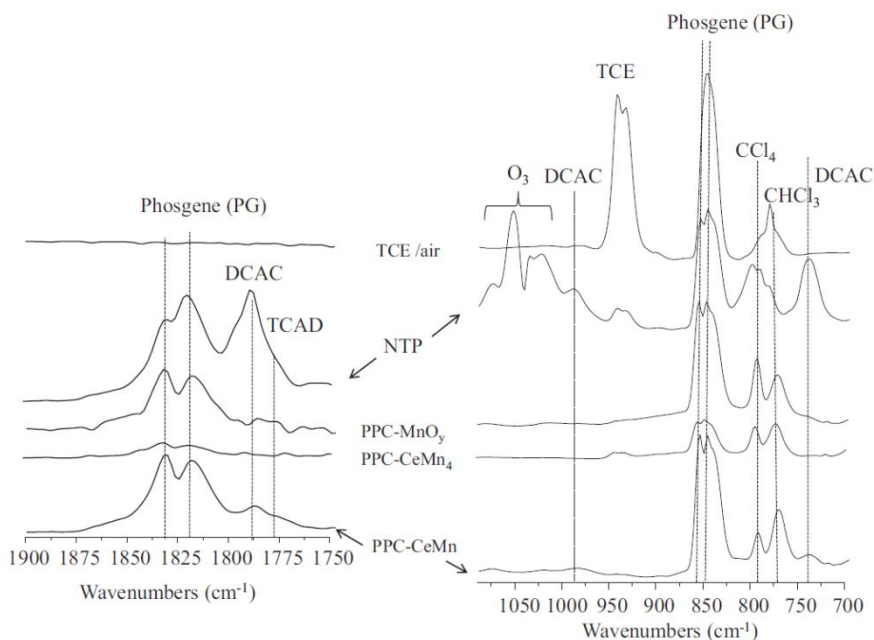


Figure 12.8 FT-IR spectra of the gaseous phase at the exit of the catalytic reactor between 700–1100 cm^{-1} and 1750–1900 cm^{-1} .

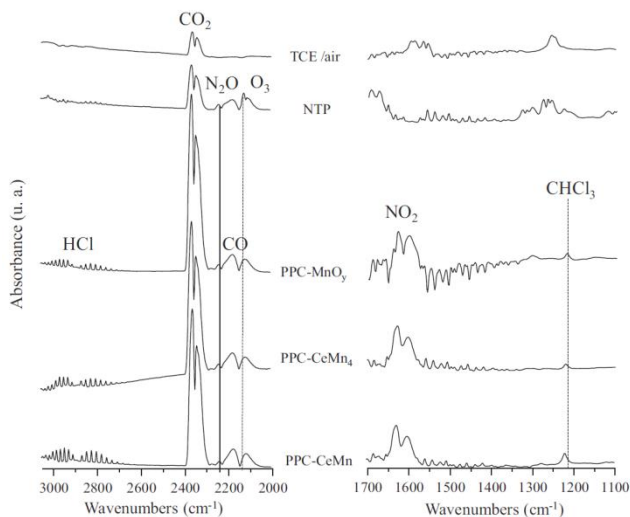


Figure 12.9 FT-IR spectra of the gaseous phase at the exit of the catalytic reactor between 2000–3050 cm^{-1} and 1100–1700 cm^{-1} .

12.3.4 XPS studies of the used catalysts

Table 12.2 shows the atomic XPS composition after PPC. Cl has been detected in all samples. In order to quantify the Cl amount in interaction with the metal, the XPS atomic Cl/(Ce + Mn) ratio is used which allows to rank the catalysts by increasing Cl amount: $\text{MnO}_x(0.09) < \text{CeMn}_4(0.15) < \text{CeMn}(0.23)$. Hence, Cl deposit amount increases with Ce content in the sample. However, it has been noticed that potassium still remains on the CeMn_4 sample despite several washing steps with water.

Table 12.2 XPS characterisation of fresh and used catalysts.

Catalysts	XPS composition		Cl/(Ce+Mn) (%)	Cl _{min} /(Ce+Mn) (%)	Cl _{org} /(Ce+Mn) (%)	Cl _{min} (%)	Cl _{org} (%)	BE (Cl 2p _{3/2}) _{min} (eV)	BE (Cl 2p _{1/2}) _{org} (eV)
	Fresh	Used							
CeMn	CeMn _{1.04} O _{3.4} C _{1.42} Cl _{0.04}	CeMn _{0.92} O _{3.35} C _{1.37} Cl _{0.44}	23	15.4	7.6	67	33	198.8	201.1
CeMn ₄	CeMn _{4.27} O _{8.96} C _{0.33} K _{0.8} Cl _{0.14}	CeMn _{3.74} O _{7.66} C _{0.52} K _{0.5} Cl _{0.71}	15	15	0	100	0	198.6	–
MnO _y	MnO _{1.43} C _{0.66} Cl _{0.015}	MnO _{1.33} C _{0.58} Cl _{0.09}	9	7.4	1.6	82	18	198.7	200.8

The Cl 2p spectra of the tested catalysts are illustrated in Figure 12.10. The decomposition of the Cl 2p XPS signal shows two distinct Cl components for MnO_y and CeMn samples, each one composed of 2 peaks: Cl 2p_{3/2} and Cl 2p_{1/2} due to the spin-orbit interaction, and one component for CeMn₄. The peak observed at 200.9 ± 0.2 eV has been ascribed to organic Cl while the peak at lower B.E. (198.6–198.8 eV) is associated with mineral Cl which is the predominant phase. However, analysis of the data precludes from elucidating the preferential metallic site prone to chlorination to give either metallic oxichlorides or/and chlorides. Regarding the organic Cl component, adsorbed species like C_xCl₂ (200.7 eV [510]) and C_xCl₃ (200.8 eV [510]) may account for the found experimental BE values. These strong organic residues can induce catalyst poisoning thereby decreasing the performance of the NTP assisted catalysts. Furthermore, XPS analysis reveals the presence of a K 2p component constituted of K 2p_{1/2} and K 2p_{3/2} peaks positioned at 292.8 and 295.6 eV for the CeMn₄ sample which shift to approximately 0.4 eV at higher B.E. after test. The presence of K can lead to the formation of a K–birnessite structure at the surface of the catalyst. Failure to observe the Cl organic phase over CeMn₄ could be due to the presence of K⁺ allowing a modification of the nature of the active sites facilitating the destruction of phosgene.

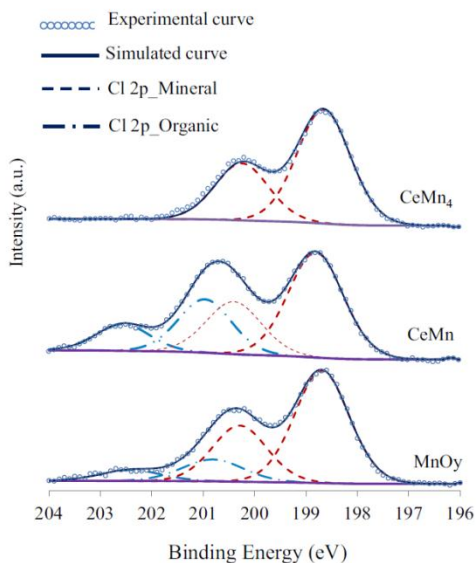


Figure 12.10 XPS decomposition of the Cl 2p envelope.

12.3.5 Scheme of TCE degradation

A simplified degradation scheme of TCE by plasma-catalysis is proposed based on the identified intermediates and by-products. Firstly, electron-molecule collisions convert N_2 and O_2 into a mixture of excited and radical species that are able to decompose TCE. The homogeneous reactions in the discharge zone give rise to mineralization products of TCE, such as CO_x , HCl and Cl_2 . Molecular oxygen is also involved in a three body reaction leading to the formation of O_3 . Furthermore, some unwanted polychlorinated by-products, such as dichloroacetylchloride, phosgene and trichloroacetaldehyde have been detected. The residual TCE, polychlorinated by-products and sub-products of TCE degradation can then diffuse to the catalyst surface. At that stage, the polychlorinated organic by-products can be mainly oxidized into CO_2 over the catalysts by means of active oxygen species owing to path 1 (Figure 12.11). The catalysts take advantage of their high efficiency to decompose plasma generated ozone into active oxygen species. On the other hand, the formation of $CHCl_3$ and CCl_4 may be explained by the decomposition of DCAC and TCAD through C-C bond cleavage accompanied with subsequent Cl transfer owing to path 2 (Figure 12.11). A better tolerance to Cl species, probably linked to the presence of potassium, seems to favor path 1 respective to path 2 for $CeMn_4$.

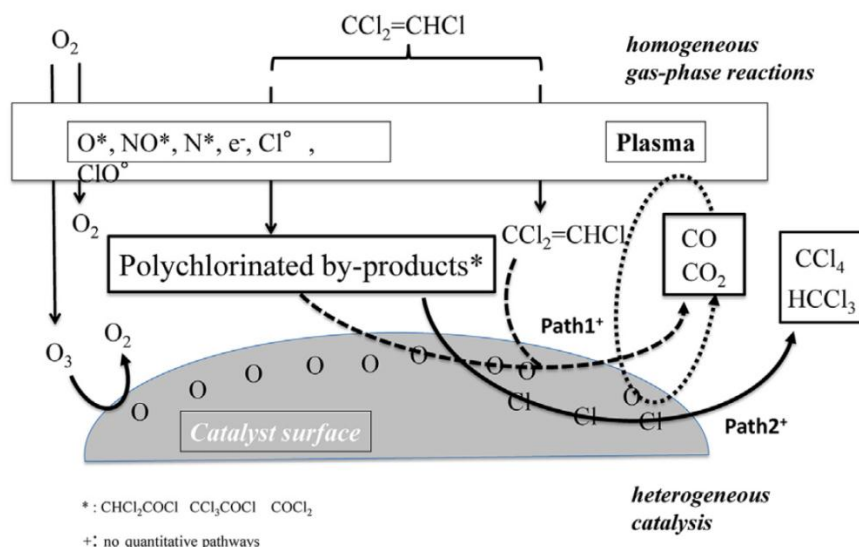


Figure 12.11 Scheme of TCE degradation in PPC experiments.

12.4 Conclusion

In this work, the abatement of TCE was investigated in moist air (RH = 10%; CO₂: 520 ppm; 150°C) with NTP using a 5-pin-to-plate negative DC corona discharge and with PPC using well dispersed nanosized CeMn_xO_y oxides as catalysts which are compared with a MnO_y oxide sample used as a reference. The well dispersed CeMn_x catalysts, synthesized by a modified “redox–precipitation” route, show outstanding physico–chemical properties in terms of textural properties (high surface exposure). PPC was found to be the best process to convert TCE into CO₂ compared to total catalytic oxidation and NTP processes due to the ability of the catalysts to completely decompose NTP generated ozone. In terms of CO₂ yields the best plasma–assisted performance observed for CeMn₄ could be interpreted by a better tolerance to poisoning from Cl organic species.

Chapter 13

General conclusions and future work

13.1 General Conclusions

In this thesis, the use of non-thermal plasma technology for the abatement of volatile organic compounds was investigated. The presented work focused on the abatement of dilute trichloroethylene which is commonly used as an industrial solvent. The essential objectives of this thesis were:

- Identifying the by-products of TCE abatement with NTP
- Developing a numerical model that describes the plasma chemistry involved in the abatement of TCE with NTP
- Improving the performance of NTP by combination with heterogeneous catalysts

It is generally accepted that NTP for VOC abatement is promising. However, formation of undesired by-products is one of the serious drawbacks of this remediation technology. Therefore, the identification of the by-products of TCE abatement was performed by combining the qualitative data from mass spectrometry and Fourier-transform infrared spectroscopy. This analysis confirmed the formation of polychlorinated by-products such as phosgene, dichloroacetylchloride and trichloroacetaldehyde due to incomplete oxidation. Hydrogen chloride, chlorine, carbon monoxide, carbon dioxide and ozone were also detected in the outlet stream.

The development of the numerical model was motivated by the fact that there is still a lack of insight in the underlying mechanisms and reactions that enable the removal of VOCs with NTP. Therefore, a plasma-chemical model was developed and validated with experimental results. It was shown that the Cl atom, mainly produced by dissociation of COCl, is one of the controlling species in the TCE destruction chemistry and contributes to the production of chlorine containing by-products. The main reactions responsible for TCE decomposition were with ClO•, O• and CHCl₂. For practical applications, the humidity of the air is an important parameter that affects the removal process significantly. Therefore, the water content of the influent was varied and the outcome on the removal process was investigated. A good agreement was found between experiments and the model for both dry and humid air. An increase of the relative humidity had a negative effect on the removal efficiency.

Based on the results gathered in these two studies, appropriate catalysts were chosen to combine with the plasma source in order to enhance the performance of the plasma alone system in terms of removal efficiency, selectivity and energy efficiency. Therefore, catalysts were located downstream of the discharge. This thesis proves that manganese based catalysts are efficient candidates for

total oxidation of TCE. This is mainly attributed to the fact that these catalysts are able to effectively decompose ozone produced by NTP. This leads to the production of active oxygen species which are capable of oxidizing remaining TCE and hazardous by-products. It should be stressed that, except for the first catalyst, all others were for the first time investigated in combination with NTP for VOC abatement. Initially, a commercial MnO_2 catalyst was studied. By calculating the activation energy it was shown that the plasma provides an extra activation of the catalyst. By combining both systems, the activation energy was significantly decreased compared to pure catalytic conditions. This suggested that the polychlorinated intermediates produced by the plasma were more susceptible for catalytic oxidation than TCE. Furthermore, a clear synergy was observed for the yields to CO and CO_2 which indicated that the plasma-catalytic system greatly enhanced the selectivity of the process towards total oxidation compared to the plasma alone case.

Further on, perovskite type catalysts were tested because they are known to be among the most active catalysts for the oxidation of chlorinated VOCs. Therefore, lanthanum manganite (LaMnO_3) was chosen as it is an environment-friendly and inexpensive material. For plasma-catalysis in dry air, an optimum catalyst temperature is found to be 100°C resulting from a compromise between catalyst deactivation and enhancement of the catalytic reactions. Although water is known to block active sites and decrease the catalytic activity, the performance for TCE abatement in humid air was enhanced due to the role of water to act as a chlorine scavenger at the surface of the catalyst, therefore retarding the perovskite degradation.

The incorporation of noble metals in low quantity into a perovskite structure is known to increase the catalytic activity as well as enhance its stability. Therefore, LaMnO_3 was doped with palladium (Pd) and studied for TCE abatement in humid air. When the temperature of Pd/LaMnO_3 was increased to 200°C the formation of DCAC was suppressed while the formation of phosgene was decreased in the order of 50% compared to the plasma alone system. No ozone was detected in the outlet stream which proved that Pd/LaMnO_3 was very effective for ozone decomposition and substantially enhanced the mineralization of TCE compared to the plasma alone system.

As a final attempt to enhance the catalytic formulation, Ce-Mn binary oxides were tested. It is known that the surface area of the catalyst plays an important role in the O_3 decomposition. By forming Ce-Mn binary oxides, the dispersion of MnO_x is thought to be greatly improved. Furthermore, their strong ability to eliminate chlorine from the catalyst surface and to provide significant amounts of active oxygen have been recognised as important catalytic properties for

total oxidation of chlorinated VOCs. These Ce–Mn oxides were synthesized by a modified “redox–precipitation” route and tested for total oxidation of TCE in combination with the plasma reactor. The specific surface area of CeMn_xO_y ($x = 1, 4$) was significantly improved compared to MnO_y . Moreover, XPS characterizations showed a homogeneous distribution of the active phase on the catalyst surface. Complete TCE abatement as well as high CO_x selectivity were achieved thanks to the high efficiency of the catalysts to completely decompose O_3 leading to the production of active oxygen species which are able to oxidize remaining TCE and by–products. The best plasma–assisted catalyst performance observed for CeMn_4 was linked to the presence of residual potassium allowing to avoid the poisoning of catalytic sites with chlorinated organic species as well as slowing down the formation of chlorinated mineral phases.

In order to compare the performance of the different catalysts tested in this work, Table 13.1 presents a summary of the optimal results.

13.2 Future work

This work regarding NTP and plasma–catalytic abatement of VOCs demonstrates that there are still scientific challenges that have to be addressed in the future.

For plasma alone systems, incomplete oxidation of VOCs leads to the formation of various intermediate and undesired by–products. Although for certain compounds decomposition mechanisms are proposed as was done in this work for TCE, there is still need to expand the knowledge on plasma–chemical kinetics. The derived information about e.g. the distribution of by–products can be very useful to select an appropriate catalyst or to enhance existing catalytic formulations in order to increase the efficiency of the hybrid system.

In the case of plasma–catalytic systems, synergetic effects on the overall removal efficiency are often observed. The mechanisms that contribute to this synergy are thoroughly investigated and the different elucidations proposed in literature often show discrepancies between them. Therefore, better understanding of which mechanisms have the most important contributions and which chemical species play a dominant role in the decomposition of VOCs together with catalysts is still of great interest. From this point of view, development of well designed instruments specialized in *in-situ* measurements is crucial. In this regard, plasma–chemical models should also be developed which include the catalytic surface reactions.

Table 13.1 Summary of the optimal results obtained in this work.

Process	[TCE] ₀ (ppm)	Flow rate (L/min)	Temp. (°C)	RH (%)	Energy density (J/L)	TCE abatement (%)	CO – CO ₂ selectivity (%)
NTP	580	2	T _{room}	18	520	88	26 – 6
NTP + MnO ₂	500	0.5	300	dry air	240	90.5	32 – 22
NTP + LaMnO ₃	510	2	150	18	460	93	46 – 29
NTP + Pd/LaMnO ₃	500	2	150	18	460	96.2	33 – 12
NTP + CeMnO ₄	360	2	150	10	240	96.9	27 – 30

The research of plasma material interactions for VOC treatment is recently looking at the opportunity to regenerate VOC saturated surfaces with the aid of NTP systems [359, 360, 365, 366, 383, 528-540]. This process of alternate adsorption and desorption can convert flue gases with a large flow rate and low VOC concentration into that with a low flow rate and high concentration. The use of this technique can reduce the reactor size, power supply and total system costs. Further developments could yield an economical VOC removal process for small- and medium-sized facilities that emit diluted VOC waste gases. Therefore, further progress on this subject is suspected in the nearby future. Finally, reactor configurations are being explored where IPC and PPC are combined to further enhance the performance for total VOC oxidation [216].

The work presented in this study explored the use of manganese based catalysts for the plasma-catalytic removal of TCE. Different important process parameters were investigated such as the effect of humidity and catalyst temperature. However, in order to further improve the proposed system different issues and aspects still need to be investigated in more detail. This thesis proved that the combination of low energetic plasma and moderate catalyst temperature is effective for the total oxidation of VOCs. Further improvement of the energy efficiency could be realized by operating catalysts at room temperature which would exclude catalyst heating. This means however that the catalytic formulations need to be further optimized in terms of activity and selectivity. Since industrial emissions usually contain several VOCs, the performance of the hybrid system should be tested with a feed gas containing a relevant VOC mixture. Catalytic stability is a crucial criterion for catalysts in industrial applications. Hence, long term tests need to be carried out to evaluate the catalytic stability and potential deactivation. Furthermore, it should be mentioned that the catalysts in this study were tested in the form of powders. Therefore, it is clear that in order to further explore the opportunities of plasma-catalysis for VOC abatement, appropriate catalyst supports such as honeycomb structures should be studied. This should enable to increase the dimensions of the system to pilot-scale which could pave the way to industrial implementation in the future.

Appendix

Table A

Reactions for the TCE destruction included in the model, as well as the corresponding rate coefficients at 25°C and the references where these data were adopted from. Note “a” means that this value is an estimated value and “b” means the rate coefficient is calculated by an online Boltzmann solver in the model, at initialization conditions. The reactions involving the air chemistry can be found in van Gaens et al. [541, 542]. The rate coefficients are in units of $\text{cm}^3 \text{s}^{-1}$ for the two-body reactions, and in $\text{cm}^6 \text{s}^{-1}$ for the three-body reactions.

#	Reaction	Rate coeff.	Ref.
1	$\text{C}_2\text{HCl}_3 + \text{O}_3 \rightarrow \text{CHOCl} + \text{CCl}_2 + \text{O}_2$	5.00×10^{-20}	[543]
2	$\text{C}_2\text{HCl}_3 + \text{Cl} \rightarrow \text{C}_2\text{HCl}_4$	2.05×10^{-12}	[543]
3	$\text{C}_2\text{HCl}_4 \rightarrow \text{C}_2\text{HCl}_3 + \text{Cl}$	1.74×10^1	[544]
4	$\text{C}_2\text{HCl}_3 + \text{Cl} \rightarrow \text{C}_2\text{Cl}_3 + \text{HCl}$	7.32×10^{-16}	[543]
5	$\text{C}_2\text{HCl}_3 + \text{O} \rightarrow \text{CHOCl} + \text{CCl}_2$	5.73×10^{-13}	[543]
6	$\text{C}_2\text{HCl}_3 + \text{OH} \rightarrow \text{CHCl}_2 + \text{COCl} + \text{H}$	2.39×10^{-14}	[543]
7	$\text{C}_2\text{HCl}_3 + \text{CHCl}_2 \rightarrow \text{CHCl}_3 + \text{C}_2\text{HCl}_2$	9.22×10^{-16}	[543]
8	$\text{C}_2\text{HCl}_3 + \text{ClO} \rightarrow \text{CHCl}_2 + \text{COCl} + \text{Cl}$	5.73×10^{-15}	[543]
9	$\text{C}_2\text{HCl}_3 + \text{ClO} \rightarrow \text{CHCl}_2 + \text{COCl}_2$	3.10×10^{-12}	[543]
10	$\text{C}_2\text{HCl}_3 + \text{ClO} \rightarrow \text{CCl}_3 + \text{CHOCl}$	2.24×10^{-21}	[543]
11	$\text{C}_2\text{HCl}_3 + \text{CCl}_3 \rightarrow \text{CCl}_4 + \text{C}_2\text{HCl}_2$	7.44×10^{-19}	[543]
12	$\text{C}_2\text{HCl}_3 + \text{OH} \rightarrow \text{CHCl}_2 + \text{CHOCl}$	3.08×10^{-13}	[543]
13	$\text{C}_2\text{HCl}_3 + \text{OH} \rightarrow \text{C}_2\text{Cl}_3 + \text{H}_2\text{O}$	5.73×10^{-14}	[543]
14	$\text{C}_2\text{HCl}_3 + \text{OH} \rightarrow \text{C}_2\text{HCl}_2 + \text{OH} + \text{Cl}$	2.43×10^{-13}	[545]
15	$\text{C}_2\text{HCl}_3 + \text{O} \rightarrow \text{COCl} + \text{CHCl}_2$	8.74×10^{-14}	[545]a
16	$\text{C}_2\text{HCl}_3 + \text{O} \rightarrow \text{C}_2\text{Cl}_3 + \text{OH}$	6.30×10^{-15}	[545]
17	$\text{C}_2\text{Cl}_3 + \text{Cl}_2 \rightarrow \text{C}_2\text{Cl}_4 + \text{Cl}$	4.49×10^{-13}	[543]
18	$\text{C}_2\text{Cl}_3 \rightarrow \text{C}_2\text{Cl}_2 + \text{Cl}$	4.50×10^{-30}	[543]
19	$\text{CCl}_4 + \text{O} \rightarrow \text{ClO} + \text{CCl}_3$	3.25×10^{-16}	[124]
20	$\text{ClO} + \text{H}_2 \rightarrow \text{HCl} + \text{OH}$	4.98×10^{-16}	[124]
21	$\text{ClO} + \text{H}_2 \rightarrow \text{HOCl} + \text{H}$	1.10×10^{-20}	[124]
22	$\text{ClO} + \text{O} \rightarrow \text{Cl} + \text{O}_2$	2.93×10^{-11}	[124]
23	$\text{ClO} + \text{ClO} \rightarrow \text{Cl}_2 + \text{O}_2$	4.90×10^{-15}	[124]
24	$\text{CCl}_4 + \text{OH} \rightarrow \text{HOCl} + \text{CCl}_3$	4.38×10^{-16}	[124]
25	$\text{HOCl} + \text{O} \rightarrow \text{OH} + \text{ClO}$	6.53×10^{-15}	[124]

#	Reaction	Rate coeff.	Ref.
26	$\text{HOCl} + \text{OH} \rightarrow \text{H}_2\text{O} + \text{ClO}$	5.66×10^{-13}	[124]
27	$\text{CCl}_3 + \text{H}_2 \rightarrow \text{CHCl}_3 + \text{H}$	3.18×10^{-22}	[546]
28	$\text{CCl}_3 + \text{O} \rightarrow \text{Cl} + \text{COCl}_2$	4.15×10^{-11}	[547]
29	$\text{CCl}_3 + \text{O}_2 + \text{M} \rightarrow \text{CCl}_3\text{O}_2 + \text{M}$	1.20×10^{-30}	[547]
30	$\text{CHCl}_3 + \text{OH} \rightarrow \text{H}_2\text{O} + \text{CCl}_3$	1.08×10^{-13}	[547]
31	$\text{CHCl}_3 + \text{Cl} \rightarrow \text{HCl} + \text{CCl}_3$	7.85×10^{-14}	[547]
32	$\text{COCl}_2 + \text{O} \rightarrow \text{ClO} + \text{COCl}$	9.96×10^{-15}	[547]
33	$\text{COCl}_2 + \text{O}({}^1\text{D}) \rightarrow \text{ClO} + \text{COCl}$	1.00×10^{-10}	[547]
34	$\text{ClO} + \text{ClO} \rightarrow \text{Cl} + \text{ClOO}$	3.40×10^{-15}	[547]
35	$\text{O} + \text{HCl} \rightarrow \text{OH} + \text{Cl}$	1.59×10^{-16}	[547]
36	$\text{OH} + \text{HCl} \rightarrow \text{H}_2\text{O} + \text{Cl}$	7.53×10^{-13}	[547]
37	$\text{H} + \text{HCl} \rightarrow \text{H}_2 + \text{Cl}$	4.42×10^{-14}	[547]
38	$\text{Cl} + \text{H}_2\text{O} \rightarrow \text{OH} + \text{HCl}$	7.84×10^{-24}	[547]
39	$\text{Cl} + \text{H}_2 \rightarrow \text{HCl} + \text{H}$	1.73×10^{-14}	[547]
40	$\text{OH} + \text{Cl} \rightarrow \text{O} + \text{HCl}$	7.10×10^{-16}	[547]
41	$\text{Cl} + \text{O}_3 \rightarrow \text{ClO} + \text{O}_2$	1.20×10^{-11}	[547]
42	$\text{Cl} + \text{CCl}_3 \rightarrow \text{CCl}_4$	5.00×10^{-11}	[547]
43	$\text{Cl} + \text{HOCl} \rightarrow \text{Cl}_2 + \text{OH}$	1.95×10^{-12}	[547]
44	$\text{Cl} + \text{HOCl} \rightarrow \text{HCl} + \text{ClO}$	1.95×10^{-12}	[547]
45	$\text{Cl} + \text{ClO} \rightarrow \text{O} + \text{Cl}_2$	3.94×10^{-19}	[547]
46	$\text{CCl}_3^+ + \text{H}^- \rightarrow \text{CCl}_3 + \text{H}$	5.00×10^{-8}	[548]
47	$\text{CCl}_3^+ + \text{O}^- \rightarrow \text{CCl}_3 + \text{O}$	5.00×10^{-8}	[548]
48	$\text{CCl}_3^+ + \text{O}_2^- \rightarrow \text{CCl}_3 + \text{O}_2$	5.00×10^{-8}	[548]
49	$\text{CCl}_3^+ + \text{Cl}^- \rightarrow \text{CCl}_3 + \text{Cl}$	5.00×10^{-8}	[548]
50	$\text{CCl}_2^+ + \text{H}^- \rightarrow \text{CCl}_2 + \text{H}$	5.00×10^{-8}	[548]
51	$\text{CCl}_2^+ + \text{O}^- \rightarrow \text{CCl}_2 + \text{O}$	5.00×10^{-8}	[548]
52	$\text{CCl}_2^+ + \text{O}_2^- \rightarrow \text{CCl}_2 + \text{O}_2$	5.00×10^{-8}	[548]
53	$\text{CCl}_2^+ + \text{Cl}^- \rightarrow \text{CCl}_2 + \text{Cl}$	5.00×10^{-8}	[548]
54	$\text{CCl}^+ + \text{H}^- \rightarrow \text{CCl} + \text{H}$	5.00×10^{-8}	[548]
55	$\text{CCl}^+ + \text{O}^- \rightarrow \text{CCl} + \text{O}$	5.00×10^{-8}	[548]
56	$\text{CCl}^+ + \text{O}_2^- \rightarrow \text{CCl} + \text{O}_2$	5.00×10^{-8}	[548]
57	$\text{CCl}^+ + \text{Cl}^- \rightarrow \text{CCl} + \text{Cl}$	5.00×10^{-8}	[548]
58	$\text{Cl}_2^+ + \text{H}^- \rightarrow \text{Cl}_2 + \text{H}$	5.00×10^{-8}	[548]
59	$\text{Cl}_2^+ + \text{O}^- \rightarrow \text{Cl}_2 + \text{O}$	5.00×10^{-8}	[548]

#	Reaction	Rate coeff.	Ref.
60	$\text{Cl}_2^+ + \text{Cl}^- \rightarrow \text{Cl}_2 + \text{Cl}$	5.00×10^{-8}	[548]
61	$\text{Cl}^+ + \text{H}^- \rightarrow \text{Cl} + \text{H}$	5.00×10^{-8}	[548]
62	$\text{Cl}^+ + \text{O}^- \rightarrow \text{Cl} + \text{O}$	5.00×10^{-8}	[548]
63	$\text{Cl}^+ + \text{O}_2^- \rightarrow \text{Cl} + \text{O}_2$	5.00×10^{-8}	[548]
64	$\text{Cl}^+ + \text{Cl}^- \rightarrow \text{Cl} + \text{Cl}$	5.00×10^{-8}	[548]
65	$\text{C}^+ + \text{H}^- \rightarrow \text{C} + \text{H}$	5.00×10^{-8}	[548]
66	$\text{C}^+ + \text{O}^- \rightarrow \text{C} + \text{O}$	5.00×10^{-8}	[548]
67	$\text{C}^+ + \text{O}_2^- \rightarrow \text{C} + \text{O}_2$	5.00×10^{-8}	[548]
68	$\text{C}^+ + \text{Cl}^- \rightarrow \text{C} + \text{Cl}$	5.00×10^{-8}	[548]
69	$\text{CCl}_2^{+2} + \text{Cl}^- \rightarrow \text{CCl}_2^+ + \text{Cl}$	5.00×10^{-8}	[548]
70	$\text{O}_2^+ + \text{Cl}^- \rightarrow \text{O}_2 + \text{Cl}$	5.00×10^{-8}	[548]
71	$\text{O}^+ + \text{Cl}^- \rightarrow \text{O} + \text{Cl}$	5.00×10^{-8}	[548]
72	$\text{H} + \text{ClOO} \rightarrow \text{OH} + \text{ClO}$	5.64×10^{-11}	[547]
73	$\text{Cl} + \text{ClOO} \rightarrow \text{Cl}_2 + \text{O}_2$	8.00×10^{-12}	[547]
74	$\text{Cl} + \text{ClOO} \rightarrow \text{ClO} + \text{ClO}$	8.00×10^{-12}	[547]
75	$\text{Cl} + \text{CCl}_2 \rightarrow \text{CCl}_3$	5.00×10^{-11}	[547]
76	$\text{H}_2\text{O}^+ + \text{CCl}_4 \rightarrow \text{CCl}_3^+ + \text{Cl} + \text{H}_2\text{O}$	1.00×10^{-9}	[547]
77	$\text{O}_2^+ + \text{CCl}_4 \rightarrow \text{CCl}_3^+ + \text{Cl} + \text{O}_2$	1.00×10^{-9}	[547]
78	$\text{O}_2^+ + \text{CCl}_4 \rightarrow \text{CCl}_3^+ + \text{Cl} + \text{O}$	1.00×10^{-9}	[547]
79	$\text{CCl}_3\text{O}_2 \rightarrow \text{CCl}_3 + \text{O}_2$	1.42×10^2	[547]
80	$\text{CCl}_3\text{O}_2 + \text{CCl}_3 \rightarrow \text{CCl}_3\text{O} + \text{CCl}_3\text{O}$	1.00×10^{-12}	[547]
81	$\text{CCl}_3\text{O}_2 + \text{CCl}_3\text{O}_2 \rightarrow \text{CCl}_3\text{O} + \text{CCl}_3\text{O} + \text{O}_2$	1.57×10^{-12}	[547]
82	$\text{CCl}_3\text{O} \rightarrow \text{COCl}_2 + \text{Cl}$	1.00×10^5	[547]
83	$\text{Cl} + \text{HO}_2 \rightarrow \text{HCl} + \text{O}_2$	3.00×10^{-11}	[547]
84	$\text{CCl}_4 + \text{O}(^1\text{D}) \rightarrow \text{CCl}_3 + \text{ClO}$	3.54×10^{-10}	[547]
85	$\text{CCl}_3 + \text{OH} \rightarrow \text{HCl} + \text{COCl}_2$	1.00×10^{-11}	[547]
86	$\text{CCl}_2 + \text{O} \rightarrow \text{COCl} + \text{Cl}$	1.00×10^{-11}	[547]
87	$\text{CCl}_2 + \text{OH} \rightarrow \text{HCl} + \text{COCl}$	1.00×10^{-11}	[547]
88	$\text{CCl} + \text{O} \rightarrow \text{COCl}$	1.00×10^{-12}	[547]
89	$\text{CCl} + \text{OH} \rightarrow \text{HCl} + \text{CO}$	4.00×10^{-11}	[547]
90	$\text{CCl} + \text{O} \rightarrow \text{ClO} + \text{C}$	8.09×10^{-35}	[547]
91	$\text{COCl} + \text{Cl} \rightarrow \text{CO} + \text{Cl}_2$	8.26×10^{-12}	[547]
92	$\text{COCl} + \text{O} \rightarrow \text{CO} + \text{ClO}$	1.00×10^{-11}	[547]
93	$\text{Cl}_2 + \text{OH} \rightarrow \text{HOCl} + \text{Cl}$	8.46×10^{-14}	[547]

#	Reaction	Rate coeff.	Ref.
94	$\text{CH}_2\text{O} + \text{O} \rightarrow \text{HCO} + \text{OH}$	1.75×10^{-13}	[547]
95	$\text{CH}_2\text{O} + \text{OH} \rightarrow \text{HCO} + \text{H}_2\text{O}$	1.11×10^{-11}	[547]
96	$\text{CH}_2\text{O} + \text{OH} \rightarrow \text{H} + \text{HCOOH}$	2.00×10^{-13}	[547]
97	$\text{CH}_2\text{O} + \text{H} \rightarrow \text{HCO} + \text{H}_2$	5.75×10^{-14}	[547]
98	$\text{HCOOH} + \text{OH} \rightarrow \text{H}_2\text{O} + \text{CO}_2 + \text{H}$	4.80×10^{-13}	[547]
99	$\text{C}_2\text{Cl}_4 + \text{OH} \rightarrow \text{CHCl}_2 + \text{COCl} + \text{Cl}$	1.64×10^{-13}	[543]
100	$\text{C}_2\text{Cl}_4 + \text{O} \rightarrow \text{COCl}_2 + \text{CCl}_2$	3.67×10^{-17}	[543]
101	$\text{C}_2\text{Cl}_4 + \text{ClO} \rightarrow \text{CCl}_3\text{COCl} + \text{Cl}$	3.67×10^{-17}	[543]
102	$\text{C}_2\text{Cl}_4 + \text{Cl} \rightarrow \text{C}_2\text{Cl}_5$	9.34×10^{-12}	[543]
103	$\text{C}_2\text{HCl}_5 + \text{Cl} \rightarrow \text{C}_2\text{Cl}_5 + \text{HCl}$	1.28×10^{-14}	[543]
104	$\text{C}_2\text{Cl}_5 \rightarrow \text{C}_2\text{Cl}_4 + \text{Cl}$	1.28×10^2	[543]
105	$\text{C}_2\text{HCl}_5 + \text{Cl} \rightarrow \text{C}_2\text{HCl}_4 + \text{Cl}_2$	1.21×10^{-23}	[543]
106	$\text{C}_2\text{Cl}_6 + \text{Cl} \rightarrow \text{Cl}_2 + \text{C}_2\text{Cl}_5$	4.39×10^{-24}	[543]
107	$\text{C}_2\text{HCl}_2 + \text{Cl} \rightarrow \text{HCl} + \text{C}_2\text{Cl}_2$	1.94×10^{-12}	[543]
108	$\text{C}_2\text{HCl}_2 + \text{O}_2 \rightarrow \text{CHOC} + \text{COCl}$	3.67×10^{-17}	[543]
109	$\text{C}_2\text{Cl}_3 + \text{Cl} \rightarrow \text{C}_2\text{Cl}_4$	6.93×10^{-13}	[543]
110	$\text{C}_2\text{Cl}_3 + \text{Cl} \rightarrow \text{C}_2\text{Cl}_2 + \text{Cl}_2$	1.26×10^{-14}	[543]
111	$\text{C}_2\text{Cl}_3 + \text{O}_2 \rightarrow \text{COCl}_2 + \text{COCl}$	3.67×10^{-17}	[543]
112	$\text{C}_2\text{Cl}_3 + \text{O}_2 \rightarrow \text{C}_2\text{Cl}_2 + \text{O} + \text{ClO}$	1.16×10^{-16}	[543]
113	$\text{C}_2\text{Cl}_2 + \text{O} + \text{Cl} \rightarrow \text{CO} + \text{CCl}_3$	1.66×10^{-11}	[543]
114	$\text{C}_2\text{Cl}_3 + \text{O} \rightarrow \text{CO} + \text{CCl}_3$	1.66×10^{-11}	[543]
115	$\text{C}_2\text{Cl}_3 + \text{ClO} \rightarrow \text{CO} + \text{CCl}_4$	1.66×10^{-11}	[543]
116	$\text{CHCl}_2 \text{COCl} + \text{Cl} \rightarrow \text{CCl}_2 \text{COCl} + \text{HCl}$	3.67×10^{-15}	[543]
117	$\text{CHCl}_2 \text{COCl} + \text{Cl} \rightarrow \text{CHCl}_2\text{CO} + \text{Cl}_2$	2.25×10^{-23}	[543]
118	$\text{CCl}_2 \text{COCl} \rightarrow \text{CO} + \text{CCl}_3$	2.21×10^8	[543]
119	$\text{CHCl}_2 \text{CO} \rightarrow \text{CHCl}_2 + \text{CO}$	7.08×10^{-21}	[543]
120	$\text{C}_2\text{HCl}_4 + \text{Cl} \rightarrow \text{CHCl}_2 + \text{CCl}_3$	4.08×10^{-20}	[543]
121	$\text{C}_2\text{Cl}_5 + \text{Cl} \rightarrow \text{CCl}_3 + \text{CCl}_3$	4.68×10^{-16}	[543]
122	$\text{C}_2\text{Cl}_5 + \text{Cl} \rightarrow \text{C}_2\text{Cl}_4 + \text{Cl}_2$	8.86×10^{-10}	[543]
123	$\text{C}_2\text{Cl}_5 + \text{O}_2 \rightarrow \text{CCl}_3 \text{COCl} + \text{ClO}$	2.79×10^{-21}	[543]
124	$\text{CCl}_3\text{COCl} + \text{Cl} \rightarrow \text{CCl}_3 \text{CO} + \text{Cl}_2$	2.25×10^{-23}	[543]
125	$\text{CCl}_3\text{CO} \rightarrow \text{CCl}_3 + \text{CO}$	1.64×10^7	[543]
126	$\text{C}_2\text{Cl}_2 + \text{O}_2 \rightarrow \text{COCl} + \text{COCl}$	3.67×10^{-17}	[543]
127	$\text{C}_2\text{Cl}_2 + \text{ClO} \rightarrow \text{CO} + \text{CCl}_3$	1.66×10^{-12}	[543]

#	Reaction	Rate coeff.	Ref.
128	$C_2Cl_2 + OH \rightarrow CO + CHCl_2$	1.66×10^{-12}	[543]
129	$CHCl_3 + O \rightarrow COCl_2 + HCl$	1.98×10^{-16}	[543]
130	$CHCl_3 + O \rightarrow CCl_3 + OH$	1.20×10^{-15}	[543]
131	$CHCl_3 + Cl \rightarrow CHCl_2 + Cl_2$	7.25×10^{-26}	[543]
132	$CCl_3 + Cl_2 \rightarrow CCl_4 + Cl$	1.71×10^{-16}	[543]
133	$CCl_3 + CCl_3 \rightarrow C_2Cl_6$	8.77×10^{-12}	[543]
134	$CCl_3 + CCl_3 \rightarrow C_2Cl_4 + Cl_2$	1.04×10^{-5}	[543]
135	$CCl_3 + CHCl_2 \rightarrow C_2HCl_5$	1.72×10^{-11}	[543]
136	$CCl_3 + CHCl_2 \rightarrow C_2Cl_4 + HCl$	6.96×10^{-15}	[543]
137	$CHCl_2 + O_2 \rightarrow CHOC + ClO$	5.63×10^{-32}	[543]
138	$CHCl_2 + O \rightarrow CHOC + Cl$	1.66×10^{-10}	[543]
139	$CCl_2 + Cl_2 \rightarrow CCl_3 + Cl$	5.34×10^{-14}	[543]
140	$CHOC + M \rightarrow CO + HCl + M$	9.50×10^{-37}	[543]
141	$CHOC + O \rightarrow OH + COCl$	5.00×10^{-13}	[547]
142	$CHOC + O(^1D) \rightarrow OH + COCl$	1.00×10^{-10}	[547]
143	$CHOC + OH \rightarrow H_2O + COCl$	3.23×10^{-13}	[549]
144	$CHOC + M \rightarrow HCO + Cl + M$	5.96×10^{-53}	[543] _a
145	$CHOC + H \rightarrow HCO + HCl$	3.79×10^{-10}	[543]
146	$CHOC + H \rightarrow CH_2O + Cl$	2.00×10^{-7}	[543]
147	$CHOC + Cl \rightarrow COCl + HCl$	7.93×10^{-13}	[543]
148	$CHOC + ClO \rightarrow COCl + HOCl$	1.23×10^{-8}	[543]
149	$CCl_3 + C_2Cl_2 \rightarrow C_3Cl_5$	7.00×10^{-17}	[543]
150	$C_3Cl_6 + Cl \rightarrow C_3Cl_6 + Cl_2$	1.26×10^{-25}	[543]
151	$C_3Cl_7 \rightarrow C_3Cl_6 + Cl$	2.52×10^{-1}	[543]
152	$CCl_3 + C_2Cl_4 \rightarrow C_3Cl_7$	3.77×10^{-16}	[546]
153	$C_2Cl_3 + C_2Cl_2 \rightarrow C_4Cl_5$	8.93×10^{-16}	[543]
154	$C_2Cl_2 + C_4Cl_5 \rightarrow C_6Cl_7$	3.94×10^{-15}	[543]
155	$C_4Cl_6 + Cl \rightarrow C_4Cl_5 + Cl_2$	1.99×10^{-26}	[543]
156	$C_2Cl_3 + C_2Cl_4 \rightarrow C_4Cl_7$	3.03×10^{-16}	[543]
157	$C_4Cl_7 \rightarrow C_4Cl_6 + Cl$	6.91×10^{-01}	[543]
158	$C_4Cl_6 + C_2Cl_3 \rightarrow C_6Cl_8 + Cl$	1.55×10^{-13}	[543]
159	$C_6Cl_8 \rightarrow C_6Cl_6 + Cl_2$	7.17×10^3	[543]
160	$N + ClO \rightarrow NO + Cl$	4.98×10^{-14}	[550]
161	$ClO + CO \rightarrow CO_2 + Cl$	9.51×10^{-22}	[551]

#	Reaction	Rate coeff.	Ref.
162	$\text{COCl} + \text{M} \rightarrow \text{CO} + \text{Cl} + \text{M}$	2.13×10^{-14}	[543]
163	$\text{COCl} + \text{H} \rightarrow \text{CO} + \text{HCl}$	1.66×10^{-10}	[543]
164	$\text{COCl} + \text{OH} \rightarrow \text{CO} + \text{HOCl}$	1.66×10^{-10}	[543]
165	$\text{COCl} + \text{O} \rightarrow \text{CO}_2 + \text{Cl}$	1.66×10^{-10}	[543]
166	$\text{H} + \text{Cl}_2 \rightarrow \text{HCl} + \text{Cl}$	1.87×10^{-11}	[543]
167	$\text{O} + \text{Cl}_2 \rightarrow \text{ClO} + \text{Cl}$	1.88×10^{-13}	[552]
168	$\text{HO}_2 + \text{Cl} \rightarrow \text{OH} + \text{ClO}$	6.00×10^{-12}	[543]
169	$\text{H} + \text{HOCl} \rightarrow \text{HCl} + \text{OH}$	3.08×10^{-12}	[543]
170	$\text{C}_2\text{Cl}_3 + \text{M} \rightarrow \text{C}_2\text{Cl}_2 + \text{Cl} + \text{M}$	2.82×10^{-29}	[543]
171	$\text{C}_2\text{Cl}_2 + \text{ClO} \rightarrow \text{C}_2\text{Cl} + \text{Cl}_2 + \text{O}$	9.50×10^{-40}	[543]
172	$\text{C}_2\text{Cl}_2 + \text{OH} \rightarrow \text{C}_2\text{Cl} + \text{HOCl}$	8.09×10^{-18}	[543]
173	$\text{C}_2\text{Cl} + \text{O}_2 \rightarrow \text{COCl} + \text{CO}$	3.67×10^{-14}	[543]
174	$\text{CHCl} + \text{Cl}_2 \rightarrow \text{CHCl}_2 + \text{Cl}$	3.08×10^{-11}	[543]
175	$\text{ClO} + \text{OH} \rightarrow \text{HCl} + \text{O}_2$	1.56×10^{-12}	[547]
176	$\text{COCl} + \text{ClO} \rightarrow \text{CO} + \text{Cl}_2 + \text{O}$	1.66×10^{-10}	[543]
177	$\text{COCl} + \text{ClO} \rightarrow \text{CO}_2 + \text{Cl}_2$	1.66×10^{-10}	[543]
178	$\text{H}_2\text{O}_2 + \text{Cl} \rightarrow \text{HO}_2 + \text{HCl}$	1.15×10^{-13}	[547]
179	$\text{Cl}_2\text{O} + \text{O} \rightarrow \text{ClO} + \text{ClO}$	3.02×10^{-12}	[547]
180	$\text{Cl}_2\text{O} + \text{OH} \rightarrow \text{HOCl} + \text{ClO}$	6.50×10^{-12}	[547]
181	$\text{CHCl}_2 + \text{COCl} + \text{O} \rightarrow \text{CCl}_2\text{COCl} + \text{OH}$	5.00×10^{-13}	[547]
182	$\text{CHCl}_2 + \text{COCl} + \text{O} \rightarrow \text{CHCl} + \text{ClO} + \text{COCl}$	5.00×10^{-13}	[547]
183	$\text{ClO} + \text{O}_3 \rightarrow \text{ClOO} + \text{O}_2$	1.62×10^{-18}	[547]
184	$\text{ClO} + \text{O}_3 \rightarrow \text{Cl} + \text{O}_2 + \text{O}_2$	5.25×10^{-15}	[547]
185	$\text{CCl}_3 + \text{O}_3 \rightarrow \text{CCl}_3\text{O} + \text{O}_2$	5.00×10^{-13}	[553]
186	$\text{ClOO} + \text{CO} \rightarrow \text{CO}_2 + \text{ClO}$	3.97×10^{-25}	[543]
187	$\text{ClOO} + \text{O} \rightarrow \text{ClO} + \text{O}_2$	2.27×10^{-11}	[543]
188	$\text{COCl}_2 + \text{Cl} \rightarrow \text{COCl} + \text{Cl}_2$	2.17×10^{-24}	[543]
189	$\text{COCl}_2 + \text{OH} \rightarrow \text{COCl} + \text{HOCl}$	8.09×10^{-20}	[543]
190	$\text{COCl}_2 + \text{H} \rightarrow \text{COCl} + \text{HCl}$	5.73×10^{-13}	[543]
191	$\text{C}_2\text{Cl}_4 + \text{OH} \rightarrow \text{C}_2\text{Cl}_3 + \text{HOCl}$	2.79×10^{-20}	[543]
192	$\text{C}_2\text{Cl}_4 + \text{OH} \rightarrow \text{CHCl}_2 + \text{COCl}_2$	5.73×10^{-13}	[543]
193	$\text{C}_2\text{Cl}_4 + \text{ClO} \rightarrow \text{CCl}_3 + \text{COCl}_2$	5.73×10^{-13}	[543]
194	$\text{C}_2\text{Cl}_4 + \text{Cl} \rightarrow \text{C}_2\text{Cl}_3 + \text{Cl}_2$	1.15×10^{-24}	[543]
195	$\text{C}_2\text{HCl}_3 + \text{e}^- \rightarrow \text{C}_2\text{HCl}_3^+ + \text{e}^- + \text{e}^-$	6.33×10^{-14}	[554]b

#	Reaction	Rate coeff.	Ref.
196	$\text{C}_2\text{HCl}_3 + \text{e}^- \rightarrow \text{C}_2\text{HCl}_2 + \text{Cl}^-$	1.43×10^{-13}	[555]b
197	$\text{C}_2\text{HCl}_3^+ + \text{H}^- \rightarrow \text{C}_2\text{HCl}_3 + \text{H}$	5.00×10^{-8}	[548]a
198	$\text{C}_2\text{HCl}_3^+ + \text{O}^- \rightarrow \text{C}_2\text{HCl}_3 + \text{O}$	5.00×10^{-8}	[548]a
199	$\text{C}_2\text{HCl}_3^+ + \text{O}_2^- \rightarrow \text{C}_2\text{HCl}_3 + \text{O}_2$	5.00×10^{-8}	[548]a
200	$\text{C}_2\text{HCl}_3^+ + \text{Cl}^- \rightarrow \text{C}_2\text{HCl}_3 + \text{Cl}$	5.00×10^{-8}	[548]a
201	$\text{ClOO} + \text{OH} \rightarrow \text{ClO} + \text{HO}_2$	2.85×10^{-18}	[556]
202	$\text{OH} + \text{CO} \rightarrow \text{CO}_2 + \text{H}$	1.56×10^{-13}	[557]

References

- [1] http://europa.eu/rapid/press-release_IP-14-976_en.htm
- [2] R. Atkinson, Atmospheric chemistry of VOCs and NO_x, *Atmospheric Environment*, 34 (2000) 2063–2101.
- [3] <http://eurlex.europa.eu/legalcontent/EN/TXT/PDF/?uri=CELEX:31999L0013&from=EN>
- [4] A. Van Amstel, Methane: A review, *Journal of Integrative Environmental Sciences*, 9 (2012) 5–30.
- [5] I. Karakurt, G. Aydin, K. Aydiner, Sources and mitigation of methane emissions by sectors: A critical review, *Renewable Energy*, 39 (2012) 40–48.
- [6] <http://www.eea.europa.eu/media/infographics>
- [7] R.E. Hester, R.M. Harrison, *Volatile organic compounds in the atmosphere*, Royal Society of Chemistry, 1995.
- [8] J.G. Watson, J.C. Chow, E.M. Fujita, Review of volatile organic compound source apportionment by chemical mass balance, *Atmospheric Environment*, 35 (2001) 1567–1584.
- [9] R. Koppmann, *Volatile organic compounds in the atmosphere*, Wiley-Blackwell, 2007.
- [10] B.D. Costello, A. Amann, H. Al-Kateb, C. Flynn, W. Filipiak, T. Khalid, D. Osborne, N.M. Ratcliffe, A review of the volatiles from the healthy human body, *Journal of Breath Research*, 8 (2014) 014001.
- [11] <http://www.eea.europa.eu/data-and-maps/indicators/eea-32-non-methane-volatile-1/assessment-4#toc-2>
- [12] <http://www.vmm.be/pub/lozingen-in-de-lucht-2000-2012/rapport-lozingen-in-de-lucht-2000-2012>
- [13] <http://cfpub.epa.gov/eroe/index.cfm?fuseaction=detail.viewPDF&ch=46&IShowInd=0&subtop=341&lv=list.listByChapter&r=209842>
- [14] F. Loreto, M. Dicke, J.-P. Schnitzler, T.C.J. Turlings, Plant volatiles and the environment, *Plant, Cell & Environment*, 37 (2014) 1905–1908.
- [15] J. Laothawornkitkul, J.E. Taylor, N.D. Paul, C.N. Hewitt, Biogenic volatile organic compounds in the Earth system, *New Phytologist*, 183 (2009) 27–51.

- [16] F. Loreto, J.-P. Schnitzler, Abiotic stresses and induced BVOCs, *Trends in Plant Science*, 15 (2010) 154–166.
- [17] J. Kesselmeier, M. Staudt, Biogenic Volatile organic compounds (VOC): An overview on emission, physiology and ecology, *Journal of Atmospheric Chemistry*, 33 (1999) 23–88.
- [18] J. Penuelas, M. Staudt, BVOCs and global change, *Trends in Plant Science*, 15 (2010) 133–144.
- [19] J. Penuelas, D. Asensio, D. Tholl, K. Wenke, M. Rosenkranz, B. Piechulla, J.P. Schnitzler, Biogenic volatile emissions from the soil, *Plant Cell and Environment*, 37 (2014) 1866–1891.
- [20] U. Effmert, J. Kalderás, R. Warnke, B. Piechulla, Volatile mediated interactions between bacteria and fungi in the soil, *Journal of Chemical Ecology*, 38 (2012) 665–703.
- [21] P. Ciccioli, M. Centritto, F. Loreto, Biogenic volatile organic compound emissions from vegetation fires, *Plant Cell and Environment*, 37 (2014) 1810–1825.
- [22] G.P. Brasseur, J.J. Orlando, G.S. Tyndal, *Atmospheric chemistry and global change*, Oxford University Press, 1999.
- [23] K.B. Schnelle, C.A. Brown, *Air pollution control technology handbook*, CRC Press, 2001.
- [24] P.S. Monks, C. Granier, S. Fuzzi, A. Stohl, M.L. Williams, H. Akimoto, M. Amann, A. Baklanov, U. Baltensperger, I. Bey, N. Blake, R.S. Blake, K. Carslaw, C.O. R., F. Dentener, D. Fowler, E. Fragkou, G.J. Frost, S. Generoso, P. Ginoux, V. Grewet, A. Guenther, H.C. Hansson, S. Hennew, J. Hjorth, A. Hofzumahaus, H. Huntrieser, I.S.A. Isaksen, M.E. Jenkin, J. Kaiser, M. Kanakidou, Z. Klimont, M. Kulmala, P. Laj, M.G. Lawrence, J.D. Lee, C. Liousse, M. Maione, G. McFiggans, A. Metzger, A. Mieville, N. Moussiopoulos, J.J. Orlando, C.D. O’Dowd, P.I. Palmer, D.D. Parrish, A. Petzold, U. Platt, U. Pöschl, A.S.H. Prevot, C.E. Reeves, S. Reimann, Y. Rudich, K. Sellegri, R. Steinbrecher, D. Simpson, H. ten Brink, J. Theloke, G.R. van der Werf, R. Vautard, V. Vestreng, C. Vlachokostas, R. von Glasow, *Atmospheric composition change – global and regional air quality*, *Atmospheric Environment* 43 (2009) 5268–5350.
- [25] R. Atkinson, Gas-phase tropospheric chemistry of volatile organic compounds .1. Alkanes and alkenes, *Journal of Physical and Chemical Reference Data*, 26 (1997) 215–290.

- [26] X. Shen, Y. Zhao, Z. Chen, D. Huang, Heterogeneous reactions of volatile organic compounds in the atmosphere, *Atmospheric Environment*, 68 (2013) 297–314.
- [27] B. Huang, C. Lei, C. Wei, G. Zeng, Chlorinated volatile organic compounds (Cl-VOCs) in environment – sources, potential human health impacts, and current remediation technologies, *Environment International*, 71 (2014) 118–138.
- [28] C. Wu, J. Shaum, Exposure assessment of trichloroethylene, *Environmental Health Perspectives*, 108 (2000) 359–363.
- [29] R.E. Doherty, A history of the production and use of carbon tetrachloride, tetrachloroethylene, trichloroethylene and 1,1,1-trichloroethane in the United States: Part 2 – Trichloroethylene and 1,1,1-trichloroethane, *Environmental Forensics*, 1 (2000) 83–93.
- [30] C.S. Scott, V.J. Cogliano, Trichloroethylene health risks – State of science, *Environmental Health Perspectives*, 108 (2000) 159–160.
- [31] W.H.A. Chiu, J. Jinot, C.S. Scott, S.L. Makris, G.S. Cooper, R.C. Dzubow, A.S. Bale, M.V. Evans, K.Z. Guyton, N. Keshava, J.C. Lipscomb, S. Barone, J.F. Fox, M.R. Gwinn, J. Schaum, J.C. Caldwell, Human health effects of trichloroethylene: Key findings and scientific issues, *Environmental Health Perspectives*, 121 (2013) 303–311.
- [32] I. Rusyn, W.H.A. Chiu, L.H. Lash, H. Kromhout, J. Hansen, K.Z. Guyton, Trichloroethylene: Mechanistic, epidemiologic and other supporting evidence of carcinogenic hazard, *Pharmacology & Therapeutics*, 141 (2014) 55–68.
- [33] <http://monographs.iarc.fr/ENG/Monographs/vol106/mono106-001.pdf>
- [34] J.T. Houghton, *Global warming – The complete briefing*, 4th edition ed., Cambridge University Press, 2009.
- [35] Y. Jing, J. Shi, T. Wang, R. Sussmann, Mapping global atmospheric CO₂ concentration at high spatiotemporal resolution, *Atmosphere*, 5 (2014) 870–888.
- [36] <http://www.edfenergy.com/energyfuture/energy-gap-climatechange/greenhouse-effect>
- [37] W.R. Simpson, R. von Glasow, K. Riedel, P. Anderson, P. Ariya, J. Bottenheim, J. Burrows, L.J. Carpenter, U. Friess, M.E. Goodsite, D. Heard, M. Hutterli, H.W. Jacobi, L. Kaleschke, B. Neff, J. Plane, U. Platt, A. Richter, H. Roscoe, R. Sander, P. Shepson, J. Sodeau, A. Steffen, T. Wagner, E. Wolff, Halogens and their role in polar boundary–

- layer ozone depletion, *Atmospheric Chemistry and Physics*, 7 (2007) 4375–4418.
- [38] S. Solomon, Stratospheric ozone depletion: A review of concepts and history, *Reviews of Geophysics*, 37 (1999) 275–316.
- [39] A.R. Douglass, P.A. Newman, S. Solomon, The Antarctic ozone hole: An update, *Physics Today*, 67 (2014) 42–48.
- [40] <http://www.epa.gov/ozone/defns.html>
- [41] M. Norval, R.M. Lucas, A.P. Cullen, F.R. de Gruijl, J. Longstreth, Y. Takizawa, J.C. van der Leun, The human health effects of ozone depletion and interactions with climate change, *Photochemical & Photobiological Sciences*, 10 (2011) 199–225.
- [42] <https://collidecolumn.wordpress.com/2012/09/15/when-worlds-collide-33-montreal-protocol-25-saluting-defenders-of-the-sky/>
- [43] <http://ozone.unep.org/pdfs/Montreal-Protocol2000.pdf>
- [44] S.E. Manahan, *Environmental chemistry*, 9th edition ed., CRC Press, 2009.
- [45] <http://pixshark.com/ozone-definition.htm>
- [46] S.T. Oyama, Chemical and catalytic properties of ozone, *Catalysis Reviews–Science and Engineering*, 42 (2000) 279–322.
- [47] M. Lippmann, Health effect of ozone – A critical review, *The Journal of the Air & Waste Management Association*, 39 (1989) 672–695.
- [48] A.W. Davison, J.D. Barnes, Effects of ozone on wild plants, *New Phytologist*, 139 (1998) 135–151.
- [49] P. Carrer, M. Maroni, D. Alcini, D. Cavallo, Allergens in indoor air: environmental assessment and health effects, *Science of the Total Environment*, 270 (2001) 33–42.
- [50] A.P. Jones, Indoor air quality and health, *Atmospheric Environment*, 33 (1999) 4535–4564.
- [51] M. Maroni, R. Axelrad, A. Bacaloni, NATO efforts to set indoor air quality guidelines and standards, *American Industrial Hygiene Association Journal*, 56 (1995) 499–508.
- [52] C.A. Redlich, J. Sparer, M.R. Cullen, Sick-building syndrome, *Lancet*, 349 (1997) 1013–1016.

- [53] A.M. Evuti, A synopsis on biogenic and anthropogenic volatile organic compounds emission: Hazards and control, *International Journal of Engineering Sciences*, 2 (2013) 145–153.
- [54] <http://www.unece.org/fileadmin/DAM/env/lrtap/full%20text/1979.CLR.TAP.e.pdf>
- [55] <http://www.unece.org/fileadmin/DAM/env/lrtap/full%20text/1999%20Multi.E.Amended.2005.pdf>
- [56] <http://eur-lex.europa.eu/legal-content/EN/TXT/PDF/?uri=CELEX:32001L0081&from=NL>
- [57] F.I. Khan, A.K. Ghoshal, Removal of volatile organic compounds from polluted air, *Journal of Loss Prevention in the Process Industries*, 13 (2000) 527–545.
- [58] G.R. Parmar, N.N. Rao, Emerging control technologies for volatile organic compounds, *Critical Reviews in Environmental Science & Technology*, 39 (2009) 41–78.
- [59] M.C. Delhomenie, M. Heitz, Biofiltration of air: A review, *Critical Reviews in Biotechnology*, 25 (2005) 53–72.
- [60] P.L. Bishop, *Pollution prevention: Fundamentals and practice*, McGraw-Hill, 2004.
- [61] W.M. Vatavuk, *Estimating costs of air pollution control*, Lewis Publishers, 1990.
- [62] D. Bathen, Gas phase adsorption in environmental technology – Achievements and prospects, *Chemie Ingenieur Technik*, 74 (2002) 209–216.
- [63] H. Huang, F. Haghghat, P. Blondeau, Volatile organic compound (VOC) adsorption on material: influence of gas phase concentration, relative humidity and VOC type, *Indoor Air*, 16 (2006) 236–247.
- [64] U. Arachchige, M.C. Melaaen, Selection of packing material for gas absorption, *European Journal of Scientific Research*, 87 (2012) 117–126.
- [65] P. Hunter, S.T. Oyama, *Control of volatile organic compound emissions: Conventional and emerging technologies*, John Wiley and Sons, 2000.
- [66] S. Navaladian, C.M. Janet, B. Viswanathan, R.P. Viswanath, On the possible treatment procedures for organic contaminants, in: S. Kaneco, B. Viswanathan, H. Katsumata (Eds.) *Photo/Electrochemistry and Photobiology in the Environment, Energy and Fuel*, 2007, pp. 1–51.

- [67] <http://www.globalspec.com/reference/81443/203279/chapter-22-shell-and-tube-heat-exchangers-heat-transfer-fouling-resistance>
- [68] J. Degreve, K. Everaert, J. Baeyens, The use of gas membranes for VOC-air separations, *Filtration & Separation*, 38 (2001) 49–54.
- [69] L. Zhang, H.X. Weng, H.L. Chen, C.J. Gao, Remove volatile organic compounds(VOCs) with membrane separation techniques, *Journal of Environmental Sciences–China*, 14 (2002) 181–187.
- [70] J. Yao, H. Wang, Zeolitic imidazolate framework composite membranes and thin films: synthesis and applications, *Chemical Society Reviews*, 43 (2014) 4470–4493.
- [71] A. Kumar, J. Dewulf, H. Van Langenhove, Membrane-based biological waste gas treatment, *Chemical Engineering Journal*, 136 (2008) 82–91.
- [72] S. Mudliar, B. Giri, K. Padoley, D. Satpute, R. Dixit, P. Bhatt, R. Pandey, A. Juwarkar, A. Vaidya, Bioreactors for treatment of VOCs and odours – A review, *Journal of Environmental Management*, 91 (2010) 1039–1054.
- [73] Z. Shareefdeen, A. Singh, *Biotechnology for odor and air pollution control*, Springer, 2005.
- [74] M.A. Fulazzaky, A. Talaiekhosani, M. Ponraj, M.Z. Abd Majid, T. Hadibarata, A. Goli, Biofiltration process as an ideal approach to remove pollutants from polluted air, *Desalination and Water Treatment*, 52 (2014) 3600–3615.
- [75] A.H. Wani, R.M.R. Branion, A.K. Lau, Biofiltration: A promising and cost-effective control technology for odors, VOCs and air toxics, *Journal of Environmental Science and Health Part A–Toxic/Hazardous Substances & Environmental Engineering*, 32 (1997) 2027–2055.
- [76] C. Kennes, E.R. Rene, M.C. Veiga, Bioprocesses for air pollution control, *Journal of Chemical Technology and Biotechnology*, 84 (2009) 1419–1436.
- [77] K. Everaert, J. Baeyens, Catalytic combustion of volatile organic compounds, *Journal of Hazardous Materials*, 109 (2004) 113–139.
- [78] M. Misono, *Heterogeneous catalysis of mixed oxides – Perovskite and heteropoly catalysts*, Elsevier, 2013.
- [79] L.F. Liotta, Catalytic oxidation of volatile organic compounds on supported noble metals, *Applied Catalysis B–Environmental*, 100 (2010) 403–412.

- [80] S. Ojala, S. Pitkaaho, T. Laitinen, N.N. Koivikko, R. Brahmi, J. Gaalova, L. Matejova, A. Kucherov, S. Paivarinta, C. Hirschmann, T. Nevanpera, M. Riihimaki, M. Pirila, R.L. Keiski, *Catalysis in VOC abatement, Topics in Catalysis*, 54 (2011) 1224–1256.
- [81] J. Zhao, X.D. Yang, Photocatalytic oxidation for indoor air purification: a literature review, *Building and Environment*, 38 (2003) 645–654.
- [82] K. Demeestere, J. Dewulf, H. Van Langenhove, Heterogeneous photocatalysis as an advanced oxidation process for the abatement of chlorinated, monocyclic aromatic and sulfurous volatile organic compounds in air: State of the art, *Critical Reviews in Environmental Science & Technology*, 37 (2007) 489–538.
- [83] M.N. Rashed, *Organic pollutants – Monitoring, risk and treatment*, InTech, 2013.
- [84] A. Mizuno, J.S. Clements, R.H. Davis, A device for the removal of SO₂ from exhaust gas by pulsed energization of free electrons, *Conference Records of IEEE/IAS Annual Meeting*, (1984) 1015–1020.
- [85] A. Mizuno, J.S. Clements, R.H. Davis, A method for the removal of sulfur dioxide from exhaust gas utilizing pulsed streamer corona for electron energization, *IEEE Transactions on Industry Applications*, 22 (1986) 516–522.
- [86] J.S. Clements, A. Mizuno, W.C. Finney, R.H. Davis, Combined removal of SO₂, NO_x and fly ash from simulated flue gas using pulsed streamer corona, *IEEE Transactions on Industry Applications*, 25 (1989) 62–69.
- [87] M. Higashi, S. Uchida, N. Suzuki, K. Fujii, Soot elimination and NO_x and SO_x reduction in diesel exhaust by a combination of discharge plasma and oil dynamics, *IEEE Transactions on Plasma Science*, 20 (1992) 1–12.
- [88] M. Venugopalan, S. Veprek, Kinetics and catalysis in plasma chemistry, *Topics in Current Chemistry*, 107 (1983) 1–58.
- [89] A. Gicquel, S. Cavadias, J. Amouroux, Heterogeneous catalysis in low-pressure plasma, *Journal of Physics. D: Applied Physics*, 19 (1986) 2013–2041.
- [90] D.E. Rapakoulias, S. Cavadias, D. Mataras, Heterogeneous catalysis in interaction of plasma excited species with surfaces, *High Temperature Chemical Processes*, 2 (1993) 231–246.
- [91] J.P.S. Badyal, Catalysis and plasma chemistry at solid surfaces, *Topics in catalysis*, 3 (1996) 255–264.

- [92] J.C. Devins, M. Burton, Formation of hydrazine in electrical discharge decomposition of ammonia *Journal of the American Chemical Society*, 76 (1954) 2618–2626.
- [93] H.H. Kim, Nonthermal plasma processing for air–pollution control: A historical review, current issues, and future prospects, *Plasma Processes and Polymers*, 1 (2004) 91–110.
- [94] A. Mizuno, Industrial applications of atmospheric non–thermal plasma in environmental remediation, *Plasma Physics and Controlled Fusion*, 49 (2007) A1–A15.
- [95] J.S. Chang, P.A. Lawless, T. Yamamoto, Corona discharge processes, *IEEE Transactions on Plasma Science*, 19 (1991) 1152–1166.
- [96] A. Fridman, A. Chirokov, A. Gutsol, Non–thermal atmospheric pressure discharges, *Journal of Physics D–Applied Physics*, 38 (2005) R1–R24.
- [97] U. Kogelschatz, Dielectric–barrier discharges: Their history, discharge physics, and industrial applications, *Plasma Chemistry and Plasma Processing*, 23 (2003) 1–46.
- [98] V. Nehra, A. Kumar, H.K. Dwivedi, Atmospheric non–thermal plasma sources, *International Journal of Engineering*, 2 (2008) 53–68.
- [99] R. Hackam, H. Akiyama, Air pollution control by electrical discharges, *IEEE Transactions on Dielectrics and Electrical Insulation*, 7 (2000) 654–683.
- [100] T. Yamamoto, S. Futamura, Nonthermal plasma processing for controlling volatile organic compounds, *Combustion Science and Technology*, 133 (1998) 117–133.
- [101] B. Eliasson, M. Hirth, U. Kogelschatz, Ozone synthesis from oxygen in dielectric barrier discharges, *Journal of Physics D–Applied Physics*, 20 (1987) 1421–1437.
- [102] G.J. Pietsch, Peculiarities of dielectric barrier discharges, *Contributions to Plasma Physics*, 41 (2001) 620–628.
- [103] S. Masuda, S. Hosokawa, X.L. Tu, K. Sakakibara, S. Kitoh, S. Sakai, Destruction of gaseous–pollutants by surface–induced plasma chemical process (SPCS), *IEEE Transactions on Industry Applications*, 29 (1993) 781–786.
- [104] S. Masuda, S. Hosokawa, X. Tu, Z. Wang, Novel plasma chemical technologies – PPCP and SPCP for control of gaseous pollutants and air toxics, *Journal of Electrostatics*, 34 (1995) 415–438.

- [105] K. Urashima, J.S. Chang, T. Ito, Reduction of NO_x from combustion flue gases by superimposed barrier discharge plasma reactors, *IEEE Transactions on Industry Applications*, 33 (1997) 879–886.
- [106] R. McAdams, Prospects for non-thermal atmospheric plasmas for pollution abatement, *Journal of Physics D–Applied Physics*, 34 (2001) 2810–2821.
- [107] J. Jarrige, P. Vervisch, Decomposition of three volatile organic compounds by nanosecond pulsed corona discharge: Study of by-product formation and influence of high voltage pulse parameters, *Journal of Applied Physics*, 99 (2006) 113303.
- [108] M. Nifuku, M. Horvath, J. Bodnar, G.Y. Zhang, T. Tanaka, E. Kiss, G. Woynarovich, H. Katoh, A study on the decomposition of volatile organic compounds by pulse corona, *Journal of Electrostatics*, 40–1 (1997) 687–692.
- [109] E.H.W.M. Smulders, B.E.J.M. van Heesch, S.S.V.B. van Paasen, Pulsed power corona discharges for air pollution control, *IEEE Transactions on Plasma Science*, 26 (1998) 1476–1484.
- [110] K.F. Shang, Y. Wu, J. Li, G.F. Li, D. Li, N.H. Wang, Reduction of NO_x/SO₂ by wire-plate type pulsed discharge reactor with pulsed corona radical shower, *Plasma Chemistry and Plasma Processing*, 26 (2006) 443–454.
- [111] Y. Shi, J. Ruan, X. Wang, W. Ll, T. Tan, Decomposition of mixed malodorants in a wire-plate pulse corona reactor, *Environmental Science & Technology*, 39 (2005) 6786–6791.
- [112] W.J. Liang, J. Li, Y.Q. Jin, Abatement of toluene from gas streams via ferro-electric packed bed dielectric barrier discharge plasma, *Journal of Hazardous Materials*, 170 (2009) 633–638.
- [113] A. Ogata, N. Shintani, K. Mizuno, S. Kushiya, T. Yamamoto, Decomposition of benzene using a nonthermal plasma reactor packed with ferroelectric pellets, *IEEE Transactions on Industry Applications*, 35 (1999) 753–759.
- [114] U. Roland, F. Holzer, F.D. Kopinke, Improved oxidation of air pollutants in a non-thermal plasma, *Catalysis Today*, 73 (2002) 315–323.
- [115] S. Okazaki, M. Kogoma, M. Uehara, Y. Kimura, Appearance of stable glow-discharge in air, argon, oxygen and nitrogen at atmospheric-pressure using a 50-Hz source, *Journal of Physics D–Applied Physics*, 26 (1993) 889–892.

- [116] Y. Akishev, A. Deryugin, V. Karal'nik, I. Kochetov, A. Napartovich, N. Trushkin, Numerical simulation and experimental study of an atmospheric pressure direct-current glow discharge, *Plasma Physics Reports*, 20 (1994) 511–524.
- [117] D. Trunec, A. Brablec, F. Stastny, Experimental study of atmospheric pressure glow discharge, *Contributions to Plasma Physics*, 38 (1998) 435–445.
- [118] E.E. Kunhardt, Generation of large-volume, atmospheric-pressure, nonequilibrium plasmas, *IEEE Transactions on Plasma Science*, 28 (2000) 189–200.
- [119] Y.S. Akishev, M.E. Grushin, I.V. Kochetov, A.P. Napartovich, M.V. Pankin, N.I. Trushkin, Transition of a multipin negative corona in atmospheric air to a glow discharge, *Plasma Physics Reports*, 26 (2000) 157–163.
- [120] Y. Akishev, O. Goossens, T. Callebaut, C. Leys, A. Napartovich, N. Trushkin, The influence of electrode geometry and gas flow on corona-to-glow and glow-to-spark threshold currents in air, *Journal of Physics D—Applied Physics*, 34 (2001) 2875–2882.
- [121] T. Callebaut, I. Kochetov, Y. Akishev, A. Napartovich, C. Leys, Numerical simulation and experimental study of the corona and glow regime of a negative pin-to-plate discharge in flowing ambient air, *Plasma Sources Science & Technology*, 13 (2004) 245–250.
- [122] R. Vertriest, R. Morent, J. Dewulf, C. Leys, H. Van Langenhove, Multi-pin-to-plate atmospheric glow discharge for the removal of volatile organic compounds in waste air, *Plasma Sources Science & Technology*, 12 (2003) 412–416.
- [123] D.S. Antao, D.A. Staack, A. Fridman, B. Farouk, Atmospheric pressure DC corona discharges: operating regimes and potential applications, *Plasma Sources Science & Technology*, 18 (2009) 035016.
- [124] D. Evans, L.A. Rosocha, G.K. Anderson, J.J. Coogan, M.J. Kushner, Plasma Remediation of Trichloroethylene in Silent Discharge Plasmas, *Journal of Applied Physics*, 74 (1993) 5378–5386.
- [125] M.J. Kirkpatrick, W.C. Finney, B.R. Locke, Chlorinated organic compound removal by gas phase pulsed streamer corona electrical discharge with reticulated vitreous carbon electrodes, *Plasmas and Polymers*, 8 (2003) 165–177.

- [126] M.C. Hsiao, B.T. Merritt, B.M. Penetrante, G.E. Vogtlin, P.H. Wallman, Plasma-assisted decomposition of methanol and trichloroethylene in atmospheric-pressure air streams by electrical-discharge processing, *Journal of Applied Physics*, 78 (1995) 3451–3456.
- [127] L. Prager, H. Langguth, S. Rummel, R. Mehnert, Electron-beam degradation of chlorinated hydrocarbons in air, *Radiation Physics and Chemistry*, 46 (1995) 1137–1142.
- [128] T. Hakoda, S. Hashimoto, Y. Fujiyama, A. Mizuno, Decomposition mechanism for electron beam irradiation of vaporized trichloroethylene-air mixtures, *Journal of Physical Chemistry A*, 104 (2000) 59–66.
- [129] T. Hakoda, G. Zhang, S. Hashimoto, Decomposition of chloroethenes in electron beam irradiation, *Radiation Physics and Chemistry*, 54 (1999) 541–546.
- [130] S.A. Vitale, K. Hadidi, D.R. Cohn, P. Falkos, The effect of a carbon-carbon double bond on electron beam-generated plasma decomposition of trichloroethylene and 1,1,1-trichloroethane, *Plasma Chemistry and Plasma Processing*, 17 (1997) 59–78.
- [131] E. Sanhueza, I.C. Hisatsune, J. Heicklen, Oxidation of haloethylenes, *Chemical Reviews*, 76 (1976) 801–826.
- [132] G. Huybrech, L. Meyers, Gas-phase chlorine-photosensitized oxidation of trichloroethylene, *Transactions of the Faraday Society*, 62 (1966) 2191–2199.
- [133] L. Bertrand, J.A. Franklin, P. Goldfing, G. Huybrech, Point of attack of a chlorine atom on trichloroethylene, *Journal of Physical Chemistry*, 72 (1968) 3926–3928.
- [134] B.M. Penetrante, M.C. Hsiao, J.N. Bardsley, B.T. Merritt, G.E. Vogtlin, A. Kuthi, C.P. Burkhart, J.R. Bayless, Identification of mechanisms for decomposition of air pollutants by non-thermal plasma processing, *Plasma Sources Science & Technology*, 6 (1997) 251–259.
- [135] S. Futamura, T. Yamamoto, Byproduct identification and mechanism determination in plasma chemical decomposition of trichloroethylene, *IEEE Transactions on Industry Applications*, 33 (1997) 447–453.
- [136] K. Urashima, J.S. Chang, Removal of volatile organic compounds from air streams and industrial flue gases by non-thermal plasma technology, *IEEE Transactions on Dielectrics and Electrical Insulation*, 7 (2000) 602–614.

- [137] J.S. Chang, K. Urashima, T. Ito, Mechanism of non-thermal plasma treatment of volatile organic compounds in dry air, in: D.W. Tedder, F.G. Pohland (Eds.) *Emerging Technologies in hazardous waste management*, ACS Press, Atlanta, 1994, pp. 203–206.
- [138] S.B. Han, T. Oda, Decomposition mechanism of trichloroethylene based on by-product distribution in the hybrid barrier discharge plasma process, *Plasma Sources Science & Technology*, 16 (2007) 413–421.
- [139] C. Subrahmanyam, M. Magureanu, D. Laub, A. Renken, L. Kiwi-Minsker, Nonthermal plasma abatement of trichloroethylene enhanced by photocatalysis, *Journal of Physical Chemistry C*, 111 (2007) 4315–4318.
- [140] M. Magureanu, N.B. Mandache, V.I. Parvulescu, C. Subrahmanyam, A. Renken, L. Kiwi-Minsker, Improved performance of non-thermal plasma reactor during decomposition of trichloroethylene: Optimization of the reactor geometry and introduction of catalytic electrode, *Applied Catalysis B-Environmental*, 74 (2007) 270–277.
- [141] T. Oda, K. Yamaji, Dilute trichloroethylene decomposition in air by using non-thermal plasma – Catalyst effect, *Journal of Advanced Oxidation Technologies*, 6 (2003) 93–99.
- [142] T. Oda, K. Yamaji, T. Takahashi, Decomposition of dilute trichloroethylene by nonthermal plasma processing – Gas flow rate, catalyst, and ozone effect, *IEEE Transactions on Industry Applications*, 40 (2004) 430–436.
- [143] S.B. Han, T. Oda, R. Ono, Improvement of the energy efficiency in the decomposition of dilute trichloroethylene by the barrier discharge plasma process, *IEEE Transactions on Industry Applications*, 41 (2005) 1343–1349.
- [144] M. Magureanu, N.B. Mandache, J.C. Hu, R. Richards, M. Florea, V.I. Parvulescu, Plasma-assisted catalysis total oxidation of trichloroethylene over gold nano-particles embedded in SBA-15 catalysts, *Applied Catalysis B-Environmental*, 76 (2007) 275–281.
- [145] M. Magureanu, N.B. Mandache, V.I. Parvulescu, Chlorinated organic compounds decomposition in a dielectric barrier discharge, *Plasma Chemistry and Plasma Processing*, 27 (2007) 679–690.
- [146] T. Oda, T. Takahashi, S. Kohzuma, Decomposition of dilute trichloroethylene by using nonthermal plasma processing–frequency and catalyst effects, *IEEE Transactions on Industry Applications*, 37 (2001) 965–970.

- [147] R. Morent, J. Dewulf, N. Steenhaut, C. Leys, H. Van Langenhove, Hybrid plasma–catalyst system for the removal of trichloroethylene in air, *Journal of Advanced Oxidation Technologies*, 9 (2006) 53–58.
- [148] H. Kohno, A.A. Berezin, J.S. Chang, M. Tamura, T. Yamamoto, A. Shibuya, S. Hondo, Destruction of volatile organic compounds used in a semiconductor industry by a capillary tube discharge reactor, *IEEE Transactions on Industry Applications*, 34 (1998) 953–966.
- [149] A.M. Vandenbroucke, M. Mora, C. Jimenez–Sanchidrian, F.J. Romero–Salguero, N. De Geyter, C. Leys, R. Morent, TCE abatement with a plasma–catalytic combined system using MnO_2 as catalyst, *Applied Catalysis B–Environmental*, 156 (2014) 94–100.
- [150] M.T. Nguyen Dinh, J.M. Giraudon, J.F. Lamonier, A. Vandenbroucke, N. De Geyter, C. Leys, R. Morent, Plasma–catalysis of low TCE concentration in air using $\text{LaMnO}_{3+\delta}$ as catalyst, *Applied Catalysis B–Environmental*, 147 (2014) 904–911.
- [151] A. Ogata, N. Shintani, K. Yamanouchi, K. Mizuno, S. Kushiyama, T. Yamamoto, Effect of water vapor on benzene decomposition using a nonthermal–discharge plasma reactor, *Plasma Chemistry and Plasma Processing*, 20 (2000) 453–467.
- [152] H.H. Kim, H. Kobara, A. Ogata, S. Futamura, Comparative assessment of different nonthermal plasma reactors on energy efficiency and aerosol formation from the decomposition of gas–phase benzene, *IEEE Transactions on Industry Applications*, 41 (2005) 206–214.
- [153] Z. Falkenstein, J.J. Coogan, Microdischarge behaviour in the silent discharge of nitrogen–oxygen and water–air mixtures, *Journal of Physics D–Applied Physics*, 30 (1997) 817–825.
- [154] M.P. Cal, M. Schluep, Destruction of benzene with non–thermal plasma in dielectric barrier discharge reactors, *Environmental Progress*, 20 (2001) 151–156.
- [155] B.Y. Lee, S.H. Park, S.C. Lee, M. Kang, S.J. Choung, Decomposition of benzene by using a discharge plasma – photocatalyst hybrid system, *Catalysis Today*, 93–5 (2004) 769–776.
- [156] Z.L. Ye, Y.N. Zhang, P. Li, L.Y. Yang, R.X. Zhang, H.Q. Hou, Feasibility of destruction of gaseous benzene with dielectric barrier discharge, *Journal of Hazardous Materials*, 156 (2008) 356–364.
- [157] C.Q. Jiang, A.A.H. Mohamed, R.H. Stark, J.H. Yuan, K.H. Schoenbach, Removal of volatile organic compounds in atmospheric pressure air by means of direct current glow discharges, *IEEE Transactions on Plasma Science*, 33 (2005) 1416–1425.

- [158] K. Satoh, T. Matsuzawa, H. Itoh, Decomposition of benzene in a corona discharge at atmospheric pressure, *Thin Solid Films*, 516 (2008) 4423–4429.
- [159] N. Goto, H. Kurimoto, S. Kudo, Y. Wanatabe, Decomposition of benzene by barrier discharge in N_2 at low concentrations of O_2 , *IEEEJ Transactions on Fundamentals and Materials*, 123 (2003) 900–906.
- [160] H.H. Kim, A. Ogata, S. Futamura, Oxygen partial pressure–dependent behavior of various catalysts for the total oxidation of VOCs using cycled system of adsorption and oxygen plasma, *Applied Catalysis B–Environmental*, 79 (2008) 356–367.
- [161] M.F. Golde, Reactions of $N_2(A^3-\Sigma_u^+)$, *International Journal of Chemical Kinetics*, 20 (1988) 75–92.
- [162] G.R. Dey, A. Sharma, K.K. Pushpa, T.N. Das, Variable products in dielectric–barrier discharge assisted benzene oxidation, *Journal of Hazardous Materials*, 178 (2010) 693–698.
- [163] B. Lu, X. Zhang, X. Yu, T. Feng, S. Yao, Catalytic oxidation of benzene using DBD corona discharges, *Journal of Hazardous Materials*, 137 (2006) 633–637.
- [164] S. Futamura, H. Einaga, H. Kabashima, L.Y. Hwan, Synergistic effect of silent discharge plasma and catalysts on benzene decomposition, *Catalysis Today*, 89 (2004) 89–95.
- [165] D.W. Park, S.H. Yoon, G.J. Kim, H. Sekiguchi, The effect of catalyst on the decomposition of dilute benzene using dielectric barrier discharge, *Journal of Industrial and Engineering Chemistry*, 8 (2002) 393–398.
- [166] H.H. Kim, A. Ogata, S. Futamura, Y.H. Lee, Decomposition of gas–phase benzene using hybrid systems of a non–thermal plasma and catalysts, *Journal of the Korean Physical Society*, 44 (2004) 1163–1167.
- [167] T. Zhu, J. Li, Y. Jin, Y. Liang, G. Ma, Decomposition of benzene by non–thermal plasma processing: photocatalyst and ozone effect, *International Journal of Environmental Science and Technology*, 5 (2008) 375–384.
- [168] Z.L. Ye, Y. Shen, R.X. Zhang, H.Q. Hou, Destruction of benzene in an air stream by the outer combined plasma photolysis method, *Journal of Physics D–Applied Physics*, 41 (2008) 025201.

- [169] M.A. Malik, Y. Minamitani, K.H. Schoenbach, Comparison of catalytic activity of aluminum oxide and silica gel for decomposition of volatile organic compounds (VOCs) in a plasmacatalytic reactor, *IEEE Transactions on Plasma Science*, 33 (2005) 50–56.
- [170] H.H. Kim, Y.H. Lee, A. Ogata, S. Futamura, Plasma-driven catalyst processing packed with photocatalyst for gas-phase benzene decomposition, *Catalysis Communications*, 4 (2003) 347–351.
- [171] H.H. Kim, A. Ogata, S. Futamura, Atmospheric plasma-driven catalysis for the low temperature decomposition of dilute aromatic compounds, *Journal of Physics D–Applied Physics*, 38 (2005) 1292–1300.
- [172] A. Ogata, D. Ito, K. Mizuno, S. Kushiyama, A. Gal, T. Yamamoto, Effect of coexisting components on aromatic decomposition in a packed-bed plasma reactor, *Applied Catalysis A–General*, 236 (2002) 9–15.
- [173] A. Ogata, K. Miyamae, K. Mizuno, S. Kushiyama, M. Tezuka, Decomposition of benzene in air in a plasma reactor: Effect of reactor type and operating conditions, *Plasma Chemistry and Plasma Processing*, 22 (2002) 537–552.
- [174] N. Xu, W. Fu, C. He, L. Cao, X. Liu, J. Zhao, H. Pan, Benzene removal using non-thermal plasma with CuO/AC catalyst: Reaction condition optimization and decomposition mechanism, *Plasma Chemistry and Plasma Processing*, 34 (2014) 1387–1402.
- [175] Y. Li, Z. Fan, J. Shi, Z. Liu, J. Zhou, W. Shanguan, Removal of volatile organic compounds (VOCs) at room temperature using dielectric barrier discharge and plasma-catalysis, *Plasma Chemistry and Plasma Processing*, 34 (2014) 801–810.
- [176] N. Jiang, N. Lu, K. Shang, J. Li, Y. Wu, Innovative approach for benzene degradation using hybrid surface/packed-bed discharge plasmas, *Environmental Science & Technology*, 47 (2013) 9898–9903.
- [177] N. Jiang, N. Lu, K. Shang, J. Li, Y. Wu, Effects of electrode geometry on the performance of dielectric barrier/packed-bed discharge plasmas in benzene degradation, *Journal of Hazardous Materials*, 262 (2013) 387–393.
- [178] J. Karuppiyah, E.L. Reddy, P.M.K. Reddy, B. Ramaraju, R. Karvembu, C. Subrahmanyam, Abatement of mixture of volatile organic compounds (VOCs) in a catalytic non-thermal plasma reactor, *Journal of Hazardous Materials*, 237 (2012) 283–289.

- [179] N. Jiang, N. Lu, J. Li, Y. Wu, Degradation of benzene by using a Ss silent-packed bed hybrid discharge plasma reactor, *Plasma Science & Technology*, 14 (2012) 140–146.
- [180] W. Mista, R. Kacprzyk, Decomposition of toluene using non-thermal plasma reactor at room temperature, *Catalysis Today*, 137 (2008) 345–349.
- [181] Z. Machala, E. Marode, M. Morvová, P. Lukáč, DC glow discharge in atmospheric air as a source for volatile organic compounds abatement, *Plasma Processes and Polymers*, 2 (2005) 152–161.
- [182] S. Ognier, S. Cavadias, J. Amouroux, Aromatic VOC removal by formation of microparticles in pure nitrogen discharge, *Plasma Processes and Polymers*, 4 (2007) 528–536.
- [183] Y.F. Guo, D.Q. Ye, K.F. Chen, Y.F. Tian, Humidity effect on toluene decomposition in a wire-plate dielectric barrier discharge reactor, *Plasma Chemistry and Plasma Processing*, 26 (2006) 237–249.
- [184] J. Van Durme, J. Dewulf, W. Sysmans, C. Leys, H. Van Langenhove, Abatement and degradation pathways of toluene in indoor air by positive corona discharge, *Chemosphere*, 68 (2007) 1821–1829.
- [185] M. Schiorlin, E. Marotta, M. Rea, C. Paradisi, Comparison of toluene Removal in air at atmospheric conditions by different corona discharges, *Environmental Science & Technology*, 43 (2009) 9386–9392.
- [186] J.H. Byeon, J.H. Park, Y.S. Jo, K.Y. Yoon, J. Hwang, Removal of gaseous toluene and submicron aerosol particles using a dielectric barrier discharge reactor, *Journal of Hazardous Materials*, 175 (2010) 417–422.
- [187] C.L. Chang, T.S. Lin, Decomposition of toluene and acetone in packed dielectric barrier discharge reactors, *Plasma Chemistry and Plasma Processing*, 25 (2005) 227–243.
- [188] C.H. Lin, H. Bai, Energy effectiveness of nonthermal plasma reactors for toluene vapor destruction, *Journal of Environmental Engineering*, 127 (2001) 648–654.
- [189] S. Delagrangé, L. Pinard, J.M. Tatibouet, Combination of a non-thermal plasma and a catalyst for toluene removal from air: Manganese based oxide catalysts, *Applied Catalysis B–Environmental*, 68 (2006) 92–98.

- [190] A.M. Harling, D.J. Glover, J.C. Whitehead, K. Zhang, Novel method for enhancing the destruction of environmental pollutants by the combination of multiple plasma discharges, *Environmental Science & Technology*, 42 (2008) 4546–4550.
- [191] A.D. Koutsospyros, S.M. Yin, C. Christodoulatos, K. Becker, Plasmochemical degradation of volatile organic compounds (VOC) in a capillary discharge plasma reactor, *IEEE Transactions on Plasma Science*, 33 (2005) 42–49.
- [192] J. Wu, Y. Huang, Q. Xia, Z. Li, Decomposition of toluene in a plasma catalysis system with NiO, MnO₂, CeO₂, Fe₂O₃, and CuO catalysts, *Plasma Chemistry and Plasma Processing*, 33 (2013) 1073–1082.
- [193] A.N. Trushkin, M.E. Grushin, I.V. Kochetov, N.I. Trushkin, Y.S. Akishev, Decomposition of toluene in a steady–state atmospheric–pressure glow discharge, *Plasma Physics Reports*, 39 (2013) 167–182.
- [194] W.–J. Liang, L. Ma, H. Liu, J. Li, Toluene degradation by non–thermal plasma combined with a ferroelectric catalyst, *Chemosphere*, 92 (2013) 1390–1395.
- [195] B. Dou, F. Bin, C. Wang, Q. Jia, J. Li, Discharge characteristics and abatement of volatile organic compounds using plasma reactor packed with ceramic Raschig rings, *Journal of Electrostatics*, 71 (2013) 939–944.
- [196] X. Tang, F. Feng, L. Ye, X. Zhang, Y. Huang, Z. Liu, K. Yan, Removal of dilute VOCs in air by post–plasma catalysis over Ag–based composite oxide catalysts, *Catalysis Today*, 211 (2013) 39–43.
- [197] M. Lu, R. Huang, P. Wang, L. Chen, J. Wu, M. Fu, W. Wen, B. Huang, D. Ye, Plasma–catalytic oxidation of toluene on Mn_xO_y at atmospheric pressure and room temperature, *Plasma Chemistry and Plasma Processing*, 34 (2014) 1141–1156.
- [198] W.F.L.M. Hoeben, F.J.C.M. Beckers, A.J.M. Pemen, E.J.M. van Heesch, W.L. Kling, Oxidative degradation of toluene and limonene in air by pulsed corona technology, *Journal of Physics D–Applied Physics*, 45 (2012) 055202.
- [199] T. Zhu, Y. Wan, H. Li, S. Chen, Y. Fang, VOCs decomposition via modified ferroelectric packed bed dielectric barrier discharge plasma, *IEEE Transactions on Plasma Science*, 39 (2011) 1695–1700.
- [200] H. Huang, D. Ye, D.Y.C. Leung, Abatement of toluene in the plasma–driven catalysis: Mechanism and reaction kinetics, *IEEE Transactions on Plasma Science*, 39 (2011) 877–882.

- [201] M. Magureanu, D. Piroi, N.B. Mandache, V.I. Parvulescu, V. Parvulescu, B. Cojocaru, C. Cadigan, R. Richards, H. Daly, C. Hardacre, In situ study of ozone and hybrid plasma Ag–Al catalysts for the oxidation of toluene: Evidence of the nature of the active sites, *Applied Catalysis B–Environmental*, 104 (2011) 84–90.
- [202] H.M. Lee, M.B. Chang, Gas–phase removal of acetaldehyde via packed–bed dielectric barrier discharge reactor, *Plasma Chemistry and Plasma Processing*, 21 (2001) 329–343.
- [203] K. Faungnawakij, N. Sano, D. Yamamoto, T. Kanki, T. Charinpanitkul, W. Tanthapanichakoon, Removal of acetaldehyde in air using a wetted–wall corona discharge reactor, *Chemical Engineering Journal*, 103 (2004) 115–122.
- [204] C. Klett, S. Touchard, A. Vega–Gonzalez, M. Redolfi, X. Bonnin, K. Hassouni, X. Duten, Experimental and modeling study of the oxidation of acetaldehyde in an atmospheric–pressure pulsed corona discharge, *Plasma Sources Science & Technology*, 21 (2012) 045001.
- [205] O. Koeta, N. Blin–Simiand, W. Faider, S. Pasquiers, A. Bary, F. Jorand, Decomposition of acetaldehyde in atmospheric pressure filamentary nitrogen plasma, *Plasma Chemistry and Plasma Processing*, 32 (2012) 991–1023.
- [206] W. Faider, S. Pasquiers, N. Blin–Simiand, L. Magne, Role of quenching of metastable states in acetaldehyde decomposition by a non–equilibrium nitrogen plasma at sub–atmospheric pressure, *Journal of Physics D–Applied Physics*, 46 (2013) 105202.
- [207] S. Pasquiers, N. Blin–Simiand, L. Magne, Kinetics of organic molecules in pulsed plasmas of nitrogen or N_2/O_2 mixtures at near atmospheric pressure, *Plasma Physics and Controlled Fusion*, 55 (2013) 124023.
- [208] W. Faider, S. Pasquiers, N. Blin–Simiand, L. Magne, Effect of oxygen on the conversion of acetaldehyde in homogeneous plasmas of $N_2/O_2/CH_3CHO$ mixtures, *Plasma Sources Science & Technology*, 22 (2013) 065010.
- [209] Z. Jia, A. Vega–Gonzalez, M. Ben Amar, K. Hassouni, S. Tieng, S. Touchard, A. Kanaev, X. Duten, Acetaldehyde removal using a diphasic process coupling a silver–based nano–structured catalyst and a plasma at atmospheric pressure, *Catalysis Today*, 208 (2013) 82–89.
- [210] T. Oda, A. Kumada, K. Tanaka, T. Takahashi, S. Masuda, Low–temperature atmospheric–pressure discharge plasma processing for volatile organic compounds, *Journal of Electrostatics*, 35 (1995) 93–101.

- [211] T. Oda, R. Yamashita, I. Haga, T. Takahashi, S. Masuda, Decomposition of gaseous organic contaminants by surface discharge induced plasma chemical processing SPCP, *IEEE Transactions on Industry Applications*, 32 (1996) 118–124.
- [212] R. Rudolph, K.P. Francke, H. Miessner, Concentration dependence of VOC decomposition by dielectric barrier discharges, *Plasma Chemistry and Plasma Processing*, 22 (2002) 401–412.
- [213] H.C. Wang, D. Li, Y. Wu, J. Li, G.F. Li, Removal of four kinds of volatile organic compounds mixture in air using silent discharge reactor driven by bipolar pulsed power, *Journal of Electrostatics*, 67 (2009) 547–553.
- [214] M.N. Lyulyukin, A.S. Besov, A.V. Vorontsov, The influence of corona electrodes thickness on the efficiency of plasmachemical oxidation of acetone, *Plasma Chemistry and Plasma Processing*, 31 (2011) 23–39.
- [215] M.G. Sobacchi, A.V. Saveliev, A.A. Fridman, A.F. Gutsol, L.A. Kennedy, Experimental assessment of pulsed corona discharge for treatment of VOC emissions, *Plasma Chemistry and Plasma Processing*, 23 (2003) 347–370.
- [216] T. Hung Quang, Y.S. Mok, Plasma–catalytic oxidation of acetone in annular porous monolithic ceramic–supported catalysts, *Chemical Engineering Journal*, 251 (2014) 199–206.
- [217] X. Zhu, X. Gao, C. Zheng, Z. Wang, M. Ni, X. Tu, Plasma–catalytic removal of a low concentration of acetone in humid conditions, *RSC Advances*, 4 (2014) 37796–37805.
- [218] J. Hoard, T.J. Wallington, R.L. Bretz, A. Malkin, R. Dorai, M.J. Kushner, Importance of $O(P^3)$ atoms and OH radicals in hydrocarbon oxidation during the nonthermal plasma treatment of diesel exhaust inferred using relative–rate methods, *International Journal of Chemical Kinetics*, 35 (2003) 231–238.
- [219] A. Rousseau, O. Guaitella, L. Gatilova, M. Hannemann, J. Ropcke, Measurement of the C_2H_2 destruction kinetics by infrared laser absorption spectroscopy in a pulsed low pressure dc discharge, *Journal of Physics D–Applied Physics*, 40 (2007) 2018–2025.
- [220] C. Fitzsimons, F. Ismail, J.C. Whitehead, J.J. Wilman, The chemistry of dichloromethane destruction in atmospheric–pressure gas streams by a dielectric packed–bed plasma reactor, *Journal of Physical Chemistry A*, 104 (2000) 6032–6038.

- [221] R.A. Korzekwa, M.G. Grothaus, R.K. Hutcherson, R.A. Roush, R. Brown, Destruction of hazardous air pollutants using a fast rise time pulsed corona reactor, *Review of Scientific Instruments*, 69 (1998) 1886–1892.
- [222] E. Marotta, G. Scorrano, C. Paradisi, Ionic reactions of chlorinated volatile organic compounds in air plasma at atmospheric pressure, *Plasma Processes and Polymers*, 2 (2005) 209–217.
- [223] M. Sugasawa, G. Annadurai, S. Futamura, Reaction behavior of toluene–dichloromethane mixture in nonthermal plasma, *IEEE Transactions on Industry Applications*, 45 (2009) 1499–1505.
- [224] M. Sugasawa, T. Terasawa, S. Futamura, Additive Effect of water on the decomposition of VOCs in nonthermal plasma, *IEEE Transactions on Industry Applications*, 46 (2010) 1692–1698.
- [225] D.G. Storch, M.J. Kushner, Destruction Mechanisms for formaldehyde in atmospheric–pressure low–temperature plasmas, *Journal of Applied Physics*, 73 (1993) 51–55.
- [226] N. Blin–Simiand, S. Pasquiers, F. Jorand, C. Postel, J.R. Vacher, Removal of formaldehyde in nitrogen and in dry air by a DBD: importance of temperature and role of nitrogen metastable states, *Journal of Physics D–Applied Physics*, 42 (2009) 122003.
- [227] W.–J. Liang, J. Li, J.–X. Li, T. Zhu, Y.–Q. Jin, Formaldehyde removal from gas streams by means of NaNO₂ dielectric barrier discharge plasma, *Journal of Hazardous Materials*, 175 (2010) 1090–1095.
- [228] Y. Wan, X. Fan, T. Zhu, Removal of low–concentration formaldehyde in air by DC corona discharge plasma, *Chemical Engineering Journal*, 171 (2011) 314–319.
- [229] H.X. Ding, A.M. Zhu, X.F. Yang, C.H. Li, Y. Xu, Removal of formaldehyde from gas streams via packed–bed dielectric barrier discharge plasmas, *Journal of Physics D–Applied Physics*, 38 (2005) 4160–4167.
- [230] A. Ogata, K. Mizuno, S. Kushiya, T. Yamamoto, Methane decomposition in a barium titanate packed–bed nonthermal plasma reactor, *Plasma Chemistry and Plasma Processing*, 18 (1998) 363–373.
- [231] K.J. Pringle, J.C. Whitehead, J.J. Wilman, J.H. Wu, The chemistry of methane remediation by a non–thermal atmospheric pressure plasma, *Plasma Chemistry and Plasma Processing*, 24 (2004) 421–434.

- [232] A. Mfopara, M.J. Kirkpatrick, E. Odic, Dilute methane treatment by atmospheric pressure dielectric barrier discharge: Effects of water vapor, *Plasma Chemistry and Plasma Processing*, 29 (2009) 91–102.
- [233] H. Lee, D.H. Lee, Y.H. Song, W.C. Choi, Y.K. Park, D.H. Kim, Synergistic effect of non-thermal plasma-catalysis hybrid system on methane complete oxidation over Pd-based catalysts, *Chemical Engineering Journal*, 259 (2015) 761–770.
- [234] A. Baylet, P. Marecot, D. Duprez, X. Jeandel, K. Lombaert, J.M. Tatibouet, Synergetic effect of plasma/catalysis hybrid system for CH₄ removal, *Applied Catalysis B-Environmental*, 113 (2012) 31–36.
- [235] K. Krawczyk, M. Młotek, B. Ulejczyk, K. Pryciak, K. Schmidt-Szałowski, Oxidative methane conversion in dielectric barrier discharge, *European Physical Journal: Applied Physics*, 61 (2013) 24307.
- [236] G. Horvath, M. Zahoran, N.J. Mason, S. Matejcik, Methane decomposition leading to deposit formation in a DC positive CH₄-N₂ corona discharge, *Plasma Chemistry and Plasma Processing*, 31 (2011) 327–335.
- [237] M. Derakhshesh, J. Abedi, H. Hassanzadeh, Mechanism of methanol decomposition by non-thermal plasma, *Journal of Electrostatics*, 68 (2010) 424–428.
- [238] R. Taranto, D. Frochot, P. Pichat, Combining cold plasma and TiO₂ photocatalysis to purify gaseous effluents: A preliminary study using methanol-contaminated air, *Industrial & Engineering Chemistry Research*, 46 (2007) 7611–7614.
- [239] T. Sato, M. Kambe, H. Nishiyama, Analysis of a methanol decomposition process by a nonthermal plasma flow, *International Journal Series B-Fluids and Thermal Engineering*, 48 (2005) 432–439.
- [240] S.L. Hill, J.C. Whitehead, K. Zhang, Plasma processing of propane at hyper-atmospheric pressure: Experiment and modelling, *Plasma Processes and Polymers*, 4 (2007) 710–718.
- [241] V. Demidyuk, S.L. Hill, J.C. Whitehead, Enhancement of the destruction of propane in a low-temperature plasma by the addition of unsaturated hydrocarbons: Experiment and modeling, *Journal of Physical Chemistry A*, 112 (2008) 7862–7867.
- [242] S.L. Hill, H.H. Kim, S. Futamura, J.C. Whitehead, The destruction of atmospheric pressure propane and propene using a surface discharge plasma reactor, *Journal of Physical Chemistry A*, 112 (2008) 3953–3958.

- [243] O. Aubry, J.M. Cormier, Improvement of the diluted propane efficiency treatment using a non-thermal plasma, *Plasma Chemistry and Plasma Processing*, 29 (2009) 13–25.
- [244] N. Moreau, S. Pasquiers, N. Blin-Simiand, L. Magne, F. Jorand, C. Postel, J.R. Vacher, Propane dissociation in a non-thermal high-pressure nitrogen plasma, *Journal of Physics D–Applied Physics*, 43 (2010) 285201.
- [245] Y.S. Mok, C.M. Nam, M.H. Cho, I.S. Nam, Decomposition of volatile organic compounds and nitric oxide by nonthermal plasma discharge processes, *IEEE Transactions on Plasma Science*, 30 (2002) 408–416.
- [246] I. Orlandini, U. Riedel, Oxidation of propene and the formation of methyl nitrate in non-thermal plasma discharges, *Catalysis Today*, 89 (2004) 83–88.
- [247] G.K. Anderson, H. Snyder, J. Coogan, Oxidation of styrene in a silent discharge plasma, *Plasma Chemistry and Plasma Processing*, 19 (1999) 131–151.
- [248] A. Ostapczuk, A.G. Chmielewski, V. Honkonen, J. Ruuskanen, J. Tarhanen, B. Svarfvar, Preliminary test in decomposition of styrene by electron beam treatment, *Radiation Physics and Chemistry*, 56 (1999) 369–371.
- [249] H. Zhang, K. Li, T. Sun, J. Jia, Z. Lou, L. Feng, Removal of styrene using dielectric barrier discharge plasmas combined with sol-gel prepared TiO₂ coated gamma-Al₂O₃, *Chemical Engineering Journal*, 241 (2014) 92–102.
- [250] W. Tanthapanichakoon, T. Charinpanitkul, S. Chaiyo, N. Dhattavorn, J. Chaichanawong, N. Sano, H. Tamon, Effect of oxygen and water vapor on the removal of styrene and ammonia from nitrogen by non-pulse corona-discharge at elevated temperatures, *Chemical Engineering Journal*, 97 (2004) 213–223.
- [251] X. Zhang, J. Zhu, X. Li, Z. Liu, X. Ren, K. Yan, Characteristics of styrene removal with an AC/DC streamer corona plasma system, *IEEE Transactions on Plasma Science*, 39 (2011) 1482–1488.
- [252] H. Zhang, K. Li, C. Shu, Z. Lou, T. Sun, J. Jia, Enhancement of styrene removal using a novel double-tube dielectric barrier discharge (DDBD) reactor, *Chemical Engineering Journal*, 256 (2014) 107–118.
- [253] X. Zhang, F. Feng, S. Li, X. Tang, Y. Huang, Z. Liu, K. Yan, Aerosol formation from styrene removal with an AC/DC streamer corona plasma system in air, *Chemical Engineering Journal*, 232 (2013) 527–533.

- [254] X. Zhang, W. Feng, Z. Yu, S. Li, J. Zhu, K. Yan, Comparison of styrene removal in air by positive and negative DC corona discharges, *International Journal of Environmental Science and Technology*, 10 (2013) 1377–1382.
- [255] B.M. Penetrante, M.C. Hsiao, J.N. Bardsley, B.T. Merritt, G.E. Vogtlin, P.H. Wallman, A. Kuthi, C.P. Burkhart, J.R. Bayless, Electron–beam and pulsed corona processing of carbon–tetrachloride in atmospheric–pressure gas streams, *Physics Letters A*, 209 (1995) 69–77.
- [256] R.G. Tonkyn, S.E. Barlow, T.M. Orlando, Destruction of carbon tetrachloride in a dielectric barrier/packed–bed corona reactor, *Journal of Applied Physics*, 80 (1996) 4877–4886.
- [257] A. Lamenta, S. Jodzis, K. Krawczyk, K. Schmidt–Szalowski, Carbon tetrachloride decomposition in spark discharge plasma, *Polish Journal of Chemistry*, 83 (2009) 169–174.
- [258] S.J. Rubio, M.C. Quintero, A. Rodero, Application of microwave air plasma in the destruction of trichloroethylene and carbon tetrachloride at atmospheric pressure, *Journal of Hazardous Materials*, 186 (2011) 820–826.
- [259] H. Kohno, M. Tamura, S. Honda, A. Shibuya, T. Yamamoto, A.A. Berezin, J.S. Chang, Generation of aerosol particles in the process of xylene and TCE decomposition from air streams by a ferroelectric packed–bed barrier discharge reactor, *Journal of Aerosol Science*, 28 (1997) S413–S414.
- [260] H.M. Lee, M.B. Chang, Abatement of gas–phase p–xylene via dielectric barrier discharges, *Plasma Chemistry and Plasma Processing*, 23 (2003) 541–558.
- [261] Z. Ye, C. Wang, Z. Shao, Q. Ye, Y. He, Y. Shi, A novel dielectric barrier discharge reactor with photocatalytic electrode based on sintered metal fibers for abatement of xylene, *Journal of Hazardous Materials*, 241 (2012) 216–223.
- [262] F. Holzer, U. Roland, F.D. Kopinke, Combination of non–thermal plasma and heterogeneous catalysis for oxidation of volatile organic compounds Part 1. Accessibility of the intra–particle volume, *Applied Catalysis B–Environmental*, 38 (2002) 163–181.
- [263] H.L. Chen, H.M. Lee, S.H. Chen, M.B. Chang, S.J. Yu, S.N. Li, Removal of volatile organic compounds by single–stage and two–stage plasma catalysis systems: A review of the performance enhancement mechanisms, current status, and suitable applications, *Environmental Science & Technology*, 43 (2009) 2216–2227.

- [264] X. Chen, J. Rozak, J.C. Lin, S.L. Suib, J. Hayashi, H. Matsumoto, Oxidative decomposition of chlorinated hydrocarbons by glow discharge in PACT (plasma and catalyst integrated technologies) reactors, *Applied Catalysis A-General*, 219 (2001) 25–31.
- [265] M.B. Chang, H.M. Lee, Abatement of perfluorocarbons with combined plasma catalysis in atmospheric-pressure environment, *Catalysis Today*, 89 (2004) 109–115.
- [266] S.J. Yu, M.B. Chang, Oxidative conversion of PFC via plasma processing with dielectric barrier discharges, *Plasma Chemistry and Plasma Processing*, 21 (2001) 311–327.
- [267] F. Holzer, F.D. Kopinke, U. Roland, Influence of ferroelectric materials and catalysts on the performance of non-thermal plasma (NTP) for the removal of air pollutants, *Plasma Chemistry and Plasma Processing*, 25 (2005) 595–611.
- [268] H.L. Chen, H.M. Lee, S.H. Chen, M.B. Chang, Review of packed-bed plasma reactor for ozone generation and air pollution control, *Industrial & Engineering Chemistry Research*, 47 (2008) 2122–2130.
- [269] U. Roland, F. Holzer, E.D. Kopinke, Combination of non-thermal plasma and heterogeneous catalysis for oxidation of volatile organic compounds Part 2. Ozone decomposition and deactivation of gamma-Al₂O₃, *Applied Catalysis B-Environmental*, 58 (2005) 217–226.
- [270] J.O. Chae, V. Demidiouk, M. Yeulash, I.C. Choi, T.G. Jung, Experimental study for indoor air control by plasma-catalyst hybrid system, *IEEE Transactions on Plasma Science*, 32 (2004) 493–497.
- [271] J.G. Wang, C.J. Liu, Y.P. Zhang, K.L. Yu, X.L. Zhu, F. He, Partial oxidation of methane to syngas over glow discharge plasma treated Ni-Fe/Al₂O₃ catalyst, *Catalysis Today*, 89 (2004) 183–191.
- [272] Z.H. Li, S.X. Tian, H.T. Wang, H.B. Tian, Plasma treatment of Ni catalyst via a corona discharge, *Journal of Molecular Catalysis a-Chemical*, 211 (2004) 149–153.
- [273] X.L. Zhu, P.P. Huo, Y.P. Zhang, C.J. Liu, Characterization of argon glow discharge plasma reduced Pt/Al₂O₃ catalyst, *Industrial & Engineering Chemistry Research*, 45 (2006) 8604–8609.
- [274] C.J. Liu, J.J. Zou, K.L. Yu, D.G. Cheng, Y. Han, J. Zhan, C. Ratanatawanate, B.W.L. Jang, Plasma application for more environmentally friendly catalyst preparation, *Pure and Applied Chemistry*, 78 (2006) 1227–1238.

- [275] C. Ratanatawanate, M. Macias, B.W.L. Jang, Promotion effect of the nonthermal RF plasma treatment on Ni/Al₂O₃ for benzene hydrogenation, *Industrial & Engineering Chemistry Research*, 44 (2005) 9868–9874.
- [276] Y.R. Zhu, Z.H. Li, Y.B. Zhou, J. Lv, H.T. Wang, Plasma treatment of Ni and Pt catalysts for partial oxidation of methane, *Reaction Kinetics and Catalysis Letters*, 87 (2005) 33–41.
- [277] Y.F. Guo, D.Q. Ye, K.F. Chen, J.C. He, W.L. Chen, Toluene decomposition using a wire–plate dielectric barrier discharge reactor with manganese oxide catalyst in situ, *Journal of Molecular Catalysis A–Chemical*, 245 (2006) 93–100.
- [278] Y.P. Zhang, P.S. Ma, X.L. Zhu, C.J. Liu, Y.T. Shen, A novel plasma–treated Pt/NaZSM–5 catalyst for NO reduction by methane, *Catalysis Communications*, 5 (2004) 35–39.
- [279] Y.F. Guo, D.Q. Ye, K.F. Chen, J.C. He, Toluene removal by a DBD–type plasma combined with metal oxides catalysts supported by nickel foam, *Catalysis Today*, 126 (2007) 328–337.
- [280] A.E. Wallis, J.C. Whitehead, K. Zhang, Plasma–assisted catalysis for the destruction of CFC–12 in atmospheric pressure gas streams using TiO₂, *Catalysis Letters*, 113 (2007) 29–33.
- [281] A.S. Pribytkov, G.N. Baeva, N.S. Telegina, A.L. Tarasov, A.Y. Stakheev, A.V. Tel'nov, V.N. Golubeva, Effect of electron irradiation on the catalytic properties of supported Pd catalysts, *Kinetics and Catalysis*, 47 (2006) 765–769.
- [282] A.E. Wallis, J.C. Whitehead, K. Zhang, The removal of dichloromethane from atmospheric pressure nitrogen gas streams using plasma–assisted catalysis, *Applied Catalysis B–Environmental*, 74 (2007) 111–116.
- [283] A. Rousseau, O. Guaitella, J. Ropcke, L.V. Gatilova, Y.A. Tolmachev, Combination of a pulsed microwave plasma with a catalyst for acetylene oxidation, *Applied Physics Letters*, 85 (2004) 2199–2201.
- [284] J. Van Durme, J. Dewulf, K. Demeestere, C. Leys, H. Van Langenhove, Post–plasma catalytic technology for the removal of toluene from indoor air: Effect of humidity, *Applied Catalysis B–Environmental*, 87 (2009) 78–83.
- [285] Y.F. Guo, D.Q. Ye, K.F. Chen, Y.F. Tian, Humidity effect on toluene decomposition in a wire–plate dielectric barrier discharge reactor, *Plasma Chemistry and Plasma Processing*, 26 (2006) 237–249.

- [286] H.H. Kim, A. Ogata, S. Futamura, Effect of different catalysts on the decomposition of VOCS using flow-type plasma-driven catalysis, *IEEE Transactions on Plasma Science*, 34 (2006) 984–995.
- [287] T. Sano, N. Negishi, E. Sakai, S. Matsuzawa, Contributions of photocatalytic/catalytic activities of TiO₂ and gamma-Al₂O₃ in nonthermal plasma on oxidation of acetaldehyde and CO, *Journal of Molecular Catalysis A-Chemical*, 245 (2006) 235–241.
- [288] H.B. Huang, D.Q. Ye, M.L. Fu, F. Da Feng, Contribution of UV light to the decomposition of toluene in dielectric barrier discharge plasma/photocatalysis system, *Plasma Chemistry and Plasma Processing*, 27 (2007) 577–588.
- [289] H.H. Kim, S.M. Oh, A. Ogata, S. Futamura, Decomposition of gas-phase benzene using plasma-driven catalyst (PDC) reactor packed with Ag/TiO₂ catalyst, *Applied Catalysis B-Environmental*, 56 (2005) 213–220.
- [290] M. Kang, B.J. Kim, S.M. Cho, C.H. Chung, B.W. Kim, G.Y. Han, K.J. Yoon, Decomposition of toluene using an atmospheric pressure plasma/TiO₂ catalytic system, *Journal of Molecular Catalysis A-Chemical*, 180 (2002) 125–132.
- [291] M. Kang, Y.R. Ko, J.M. K., L.S. C., C.S. J., P.J. Y., K. S., C.S. H., Characterization of Bi/TiO₂ nanometer sized particle synthesized by solvothermal method and CH₃CHO decomposition in a plasma-photocatalytic system, *Journal of Photochemistry and Photobiology A: Chemistry*, 173 (2005) 128–136.
- [292] S. Chavadej, K. Saktrakool, P. Rangsunvigit, L.L. Lobban, T. Sreethawong, Oxidation of ethylene by a multistage corona discharge system in the absence and presence of Pt/TiO₂, *Chemical Engineering Journal*, 132 (2007) 345–353.
- [293] A. Ogata, H.H. Kim, S.M. Oh, S. Futamura, Evidence for direct activation of solid surface by plasma discharge on CFC decomposition, *Thin Solid Films*, 506 (2006) 373–377.
- [294] K. Takaki, K. Urashima, J.S. Chang, Ferro-electric pellet shape effect on C₂F₆ removal by a packed-bed-type nonthermal plasma reactor, *IEEE Transactions on Plasma Science*, 32 (2004) 2175–2183.
- [295] K. Urashima, K.G. Kostov, J.S. Chang, Y. Okayasu, T. Iwaizumi, K. Yoshimura, T. Kato, Removal of C₂F₆ from a semiconductor process flue gas by a ferroelectric packed-bed barrier discharge reactor with an adsorber, *IEEE Transactions on Industry Applications*, 37 (2001) 1456–1463.

- [296] C. Leys, D. Neiryneck, R. Morent, E. Temmerman, DC-excited cold atmospheric pressure plasmas, *Czechoslovak Journal of Physics*, 56 (2006) B896–B902.
- [297] H.B. Huang, D.Q. Ye, Combination of photocatalysis downstream the non-thermal plasma reactor for oxidation of gas-phase toluene, *Journal of Hazardous Materials*, 171 (2009) 535–541.
- [298] H.B. Huang, D.Q. Ye, X.J. Guan, The simultaneous catalytic removal of VOCs and O₃ in a post-plasma, *Catalysis Today*, 139 (2008) 43–48.
- [299] Y.F. Guo, D.Q. Ye, K.F. Chen, J.C. He, Toluene removal by a DBD-type plasma combined with metal oxides catalysts supported by nickel foam, *Catalysis Today*, 126 (2007) 328–337.
- [300] N. Blin-Simiand, P. Tardiveau, A. Risacher, F. Jorand, S. Pasquiers, Removal of 2-heptanone by dielectric barrier discharges – The effect of a catalyst support, *Plasma Processes and Polymers*, 2 (2005) 256–262.
- [301] K. Krawczyk, B. Ulejczyk, H.K. Song, A. Lamenta, B. Paluch, K. Schmidt-Szalowski, Plasma-catalytic reactor for decomposition of chlorinated hydrocarbons, *Plasma Chemistry and Plasma Processing*, 29 (2009) 27–41.
- [302] V. Demidiouk, J.O. Chae, Decomposition of volatile organic compounds in plasma-catalytic system, *IEEE Transactions on Plasma Science*, 33 (2005) 157–161.
- [303] K. Hayashi, H. Yasui, M. Tanaka, S. Futamura, S. Kurita, K. Aoyagi, Temperature dependence of toluene decomposition behavior in the discharge-catalyst hybrid reactor, *IEEE Transactions on Industry Applications*, 45 (2009) 1553–1558.
- [304] K. Hensel, S. Katsura, A. Mizuno, DC microdischarges inside porous ceramics, *IEEE Transactions on Plasma Science*, 33 (2005) 574–575.
- [305] M.J. Kirkpatrick, W.C. Finney, B.R. Locke, Plasma-catalyst interactions in the treatment of volatile organic compounds and NO_x with pulsed corona discharge and reticulated vitreous carbon Pt/Rh-coated electrodes, *Catalysis Today*, 89 (2004) 117–126.
- [306] C. Subrahmanyam, A. Renken, L. Kiwi-Minsker, Novel catalytic non-thermal plasma reactor for the abatement of VOCs, *Chemical Engineering Journal*, 134 (2007) 78–83.
- [307] C. Subrahmanyam, A. Renken, L. Kiwi-Minsker, Novel catalytic dielectric barrier discharge reactor for gas-phase abatement of isopropanol, *Plasma Chemistry and Plasma Processing*, 27 (2007) 13–22.

- [308] C. Subrahmanyam, A. Renken, L. Kiwi-Minsker, Catalytic non-thermal plasma reactor for abatement of toluene, *Chemical Engineering Journal*, 160 (2010) 677–682.
- [309] X. Chen, J. Rozak, J.C. Lin, S.L. Suib, Y. Hayashi, H. Matsumoto, Oxidative decomposition of chlorinated hydrocarbons by glow discharge in PACT (plasma and catalyst integrated technologies) reactors, *Applied Catalysis A: General* 219 (2001) 25–31.
- [310] A. Ogata, K. Yamanouchi, K. Mizuno, S. Kushiyama, T. Yamamoto, Oxidation of dilute benzene in an alumina hybrid plasma reactor at atmospheric pressure, *Plasma Chemistry and Plasma Processing*, 19 (1999) 383–394.
- [311] A. Ogata, K. Yamanouchi, K. Mizuno, S. Kushiyama, T. Yamamoto, Decomposition of benzene using alumina-hybrid and catalyst-hybrid plasma reactors, *IEEE Transactions on Industry Applications*, 35 (1999) 1289–1295.
- [312] Y.H. Song, S.J. Kim, K.I. Choi, T. Yamamoto, Effects of adsorption and temperature on a nonthermal plasma process for removing VOCs, *Journal of Electrostatics*, 55 (2002) 189–201.
- [313] A. Ogata, D. Ito, K. Mizuno, S. Kushiyama, T. Yamamoto, Removal of dilute benzene using a zeolite-hybrid plasma reactor, *IEEE Transactions on Industry Applications*, 37 (2001) 959–964.
- [314] S.M. Oh, H.H. Kim, A. Ogata, H. Einaga, S. Futamura, D.W. Park, Effect of zeolite in surface discharge plasma on the decomposition of toluene, *Catalysis Letters*, 99 (2005) 101–104.
- [315] S.M. Oh, H.H. Kim, H. Einaga, A. Ogata, S. Futamura, D.W. Park, Zeolite-combined plasma reactor for decomposition of toluene, *Thin Solid Films*, 506 (2006) 418–422.
- [316] M. Magureanu, N.B. Mandache, P. Eloy, E.M. Gaigneaux, V.I. Parvulescu, Plasma-assisted catalysis for volatile organic compounds abatement, *Applied Catalysis B-Environmental*, 61 (2005) 12–20.
- [317] A.E. Wallis, J.C. Whitehead, K. Zhang, The removal of dichloromethane from atmospheric pressure air streams using plasma-assisted catalysis, *Applied Catalysis B-Environmental*, 72 (2007) 282–288.
- [318] A. Ogata, H. Einaga, H. Kabashima, S. Futamura, S. Kushiyama, H.H. Kim, Effective combination of nonthermal plasma and catalysts for decomposition of benzene in air, *Applied Catalysis B-Environmental*, 46 (2003) 87–95.

- [319] H. Grossmannova, D. Neiryneck, C. Leys, Atmospheric discharge combined with Cu–Mn/Al₂O₃ catalyst unit for the removal of toluene, *Czechoslovak Journal of Physics*, 56 (2006) B1156–B1161.
- [320] A. Vandenbroucke, R. Morent, N. De Geyter, M.T. Nguyen Dinh, J.M. Giraudon, J.F. Lamonier, C. Leys, Plasma–catalytic decomposition of TCE, *International Journal of Plasma Environmental Science and Technology*, 4 (2010) 135–138.
- [321] P. Da Costa, R. Marques, S. Da Costa, Plasma catalytic oxidation of methane on alumina–supported noble metal catalysts, *Applied Catalysis B–Environmental*, 84 (2008) 214–222.
- [322] T. Blackbeard, V. Demidyuk, S.L. Hill, J.C. Whitehead, The effect of temperature on the plasma–catalytic destruction of propane and propene: A comparison with thermal catalysis, *Plasma Chemistry and Plasma Processing*, 29 (2009) 411–419.
- [323] T. Yamamoto, K. Mizuno, I. Tamori, A. Ogata, M. Nifuku, M. Michalska, G. Prieto, Catalysis–assisted plasma technology for carbon tetrachloride destruction, *IEEE Transactions on Industry Applications*, 32 (1996) 100–105.
- [324] C.L. Chang, H.L. Bai, S.J. Lu, Destruction of styrene in an air stream by packed dielectric barrier discharge reactors, *Plasma Chemistry and Plasma Processing*, 25 (2005) 641–657.
- [325] M.B. Chang, H.M. Lee, Abatement of perfluorocarbons with combined plasma–catalysis in atmospheric pressure environment, *Catalysis Today*, 89 (2004) 109–115.
- [326] V. Demidyuk, J.C. Whitehead, Influence of temperature on gas–phase toluene decomposition in plasma–catalytic system, *Plasma Chemistry and Plasma Processing*, 27 (2007) 85–94.
- [327] V. Demidiouk, S.I. Moon, J.O. Chae, D.Y. Lee, Application of a plasma–catalytic system for decomposition of volatile organic compounds, *Journal of the Korean Physical Society*, 42 (2003) S966–S970.
- [328] C.L. Chang, T.S. Lin, Elimination of carbon monoxide in the gas streams by dielectric barrier discharge systems with Mn catalyst, *Plasma Chemistry and Plasma Processing*, 25 (2005) 387–401.
- [329] H.L. Chen, H.M. Lee, L.C. Cheng, M.B. Chang, S.J. Yu, S.N. Li, Influence of nonthermal plasma reactor type on CF₄ and SF₆ abatements, *IEEE Transactions on Plasma Science*, 36 (2008) 509–515.

- [330] J. Jarrige, P. Vervisch, Plasma-enhanced catalysis of propane and isopropyl alcohol at ambient temperature on a MnO₂-based catalyst, *Applied Catalysis B-Environmental*, 90 (2009) 74–82.
- [331] X. Fan, T.L. Zhu, M.Y. Wang, X.M. Li, Removal of low concentration BTX in air using a combined plasma catalysis system, *Chemosphere*, 75 (2009) 1301–1306.
- [332] T. Zhu, J. Li, W.J. Liang, Y.Q. Jin, Synergistic effect of catalyst for oxidation removal of toluene, *Journal of Hazardous Materials*, 165 (2009) 1258–1260.
- [333] T. Hakoda, K. Matsumoto, A. Mizuno, K. Hirota, Role of metals loaded on a TiO₂ surface in the oxidation of xylene in air using an electron beam irradiation/catalytic process, *Applied Catalysis A-General*, 357 (2009) 244–249.
- [334] A.S. Besov, A.V. Vorontsov, Acceleration of acetone destruction process under synergistic action of photocatalytic oxidation and barrier discharge, *Plasma Chemistry and Plasma Processing*, 27 (2007) 624–634.
- [335] T. Oda, T. Takahashi, K. Yamaji, Nonthermal plasma processing for dilute VOCs decomposition, *IEEE Transactions on Industry Applications*, 38 (2002) 873–878.
- [336] R.B. Sun, Z.G. Xi, F.H. Chao, W. Zhang, H.S. Zhang, D.F. Yang, Decomposition of low-concentration gas-phase toluene using plasma-driven photocatalyst reactor, *Atmospheric Environment* 41 (2007) 6853–6859.
- [337] O. Guaitella, F. Thevenet, E. Puzenat, C. Guillard, A. Rousseau, C₂H₂ oxidation by plasma/TiO₂ combination: Influence of the porosity, and photocatalytic mechanisms under plasma exposure, *Applied Catalysis B-Environmental*, 80 (2008) 296–305.
- [338] F. Thevenet, O. Guaitella, E. Puzenat, C. Guillard, A. Rousseau, Influence of water vapour on plasma/photocatalytic oxidation efficiency of acetylene, *Applied Catalysis B-Environmental*, 84 (2008) 813–820.
- [339] H.B. Huang, D.Q. Ye, D.Y.C. Leung, Removal of toluene using UV-irradiated and nonthermal plasma-driven photocatalyst system, *Journal of Environmental Engineering-Asce*, 136 (2010) 1231–1236.
- [340] M. Kogoma, Y. Miki, K. Tanaka, K. Takahashi, Highly efficient VOC decomposition using a complex system (OH Radical, Ozone-UV, and TiO₂), *Plasma Processes and Polymers*, 3 (2006) 727–733.

- [341] T. Oda, T. Takahashi, K. Yamaji, TCE decomposition by the non-thermal plasma process concerning ozone effect, *IEEE Transactions on Industry Applications*, 40 (2002) 1249–1256.
- [342] A.M. Vandenbroucke, R. Morent, N. De Geyter, C. Leys, Decomposition of trichloroethylene with plasma-catalysis: A review, *Journal of Advanced Oxidation Technologies*, 14 (2011) 165–173.
- [343] H.H. Kim, S.M. Oh, A. Ogata, S. Futamura, Decomposition of benzene using Ag/TiO₂ packed plasma-driven catalyst reactor: influence of electrode configuration and Ag-loading amount, *Catalysis Letters*, 96 (2004) 189–194.
- [344] H.Y. Fan, C. Shi, X.S. Li, D.Z. Zhao, Y. Xu, High-efficiency plasma catalytic removal of dilute benzene from air, *Journal of Physics D–Applied Physics*, 42 (2009) 225105.
- [345] A.M. Harling, V. Demidyuk, S.J. Fischer, J.C. Whitehead, Plasma-catalysis destruction of aromatics for environmental clean-up: Effect of temperature and configuration, *Applied Catalysis B–Environmental*, 82 (2008) 180–189.
- [346] T. Zhu, J. Li, Y.Q. Jin, Y.H. Liang, G.D. Ma, Gaseous phase benzene decomposition by non-thermal plasma coupled with nano titania catalyst, *International Journal of Environmental Science and Technology*, 6 (2009) 141–148.
- [347] S. Chavadej, W. Kiatubolpaiboon, P. Rangsunvigit, T. Sreethawong, A combined multistage corona discharge and catalytic system for gaseous benzene removal, *Journal of Molecular Catalysis A–Chemical*, 263 (2007) 128–136.
- [348] J. Li, S.T. Han, S.P. Bai, X.C. Shi, S.L. Han, H. Song, X.M. Zhu, Y.K. Pu, X. Zhu, W.C. Chen, Effect of Pt/ γ -Al₂O₃ catalyst on nonthermal plasma decomposition of benzene and byproducts, *Environmental Engineering Science*, 28 (2011) 395–404.
- [349] M.A. Malik, X.Z. Jiang, Catalyst assisted destruction of trichloroethylene and toluene in corona discharges, *Journal of Environmental Sciences*, 12 (2000) 7–11.
- [350] D.A. Li, D. Yakushiji, S. Kanazawa, T. Ohkubo, Y. Nomoto, Decomposition of toluene by streamer corona discharge with catalyst, *Journal of Electrostatics*, 55 (2002) 311–319.
- [351] Y.F. Guo, X. Liao, J.H. He, W. Ou, D.Q. Ye, Effect of manganese oxide catalyst on the dielectric barrier discharge decomposition of toluene, *Catalysis Today*, 153 (2010) 176–183.

- [352] Y.F. Guo, X.B. Liao, D.Q. Ye, *Journal of Environmental Science – China*, 20 (2008) 1429.
- [353] X.B. Liao, Y.F. Guo, J.H. He, W.J. Ou, D.Q. Ye, Hydroxyl radicals formation in dielectric barrier discharge during decomposition of toluene, *Plasma Chemistry and Plasma Processing*, 30 (2010) 841–853.
- [354] J. Van Durme, J. Dewulf, W. Sysmans, C. Leys, H. Van Langenhove, Efficient toluene abatement in indoor air by a plasma catalytic hybrid system, *Applied Catalysis B–Environmental*, 74 (2007) 161–169.
- [355] H.B. Huang, D.Q. Ye, D.Y.C. Leung, Plasma–driven catalysis process for toluene abatement: Effect of water vapor, *IEEE Transactions on Plasma Science*, 39 (2011) 576–580.
- [356] H. Huang, D.Q. Ye, D.Y.C. Leung, F. Feng, X.J. Guan, Byproducts and pathways of toluene destruction via plasma–catalysis, *Journal of Molecular Catalysis A–Chemical*, 336 (2011) 87–93.
- [357] A. Mizuno, Y. Kisanuki, M. Noguchi, S. Katsura, S.H. Lee, U.K. Hong, S.Y. Shin, J.H. Kang, Indoor air cleaning using a pulsed discharge plasma, *IEEE Transactions on Industry Applications*, 35 (1999) 1284–1288.
- [358] T. Ohshima, T. Kondo, N. Kitajima, M. Sato, Adsorption and plasma decomposition of gaseous acetaldehyde on fibrous activated carbon, *IEEE Transactions on Industry Applications*, 46 (2010) 23–28.
- [359] C. Klett, X. Duten, S. Tieng, S. Touchard, P. Jestin, K. Hassouni, A. Vega–González, Acetaldehyde removal using an atmospheric non–thermal plasma combined with a packed bed: Role of the adsorption process, *Journal of Hazardous Materials*, 279 (2014) 356–364.
- [360] C. Barakat, P. Gravejat, O. Guaitella, F. Thevenet, A. Rousseau, Oxidation of isopropanol and acetone adsorbed on TiO₂ under plasma generated ozone flow: Gas phase and adsorbed species monitoring, *Applied Catalysis B: Environmental*, 147 (2014) 302–313.
- [361] A. Rousseau, O. Guaitella, L. Gatilova, F. Thevenet, C. Guillard, J. Ropcke, G.D. Stancu, Photocatalyst activation in a pulsed low pressure discharge, *Applied Physics Letters*, 87 (2005) 221501.
- [362] A.M. Harling, A.E. Wallis, J.C. Whitehead, The effect of temperature on the removal of DCM using non–thermal, atmospheric–pressure plasma–assisted catalysis, *Plasma Processes and Polymers*, 4 (2007) 463–470.

- [363] A. Ogata, K. Saito, H.H. Kim, M. Sugawara, H. Aritani, H. Einaga, Performance of an ozone decomposition catalyst in hybrid plasma reactors for volatile organic compound removal, *Plasma Chemistry and Plasma Processing*, 30 (2010) 33–42.
- [364] H.X. Ding, A.M. Zhu, F.G. Lu, Y. Xu, J. Zhang, X.F. Yang, Low-temperature plasma-catalytic oxidation of formaldehyde in atmospheric pressure gas streams, *Journal of Physics D–Applied Physics*, 39 (2006) 3603–3608.
- [365] K. Saulich, S. Mueller, Removal of formaldehyde by adsorption and plasma treatment of mineral adsorbent, *Journal of Physics D–Applied Physics*, 46 (2013) 045201.
- [366] D.Z. Zhao, X.S. Li, C. Shi, H.Y. Fan, A.M. Zhu, Low-concentration formaldehyde removal from air using a cycled storage–discharge (CSD) plasma catalytic process, *Chemical Engineering Science*, 66 (2011) 3922–3929.
- [367] R. Marques, S. Da Costa, P. Da Costa, Plasma-assisted catalytic oxidation of methane – On the influence of plasma energy deposition and feed composition, *Applied Catalysis B–Environmental*, 82 (2008) 50–57.
- [368] J. Kim, B. Han, Y. Kim, J.H. Lee, C.R. Park, J.C. Kim, J.C. Kim, K.J. Kim, Removal of VOCs by hybrid electron beam reactor with catalyst bed, *Radiation Physics and Chemistry*, 71 (2004) 429–432.
- [369] K.J. Kim, J.C. Kim, J.Y. Kim, Y. Sunwoo, Development of hybrid technology using E-beam and catalyst for aromatic VOCs control, *Radiation Physics and Chemistry*, 73 (2005) 85–90.
- [370] L.W. Huang, K. Nakajyo, T. Hari, S. Ozawa, H. Matsuda, Decomposition of carbon tetrachloride by a pulsed corona reactor incorporated with in situ absorption, *Industrial & Engineering Chemistry Research*, 40 (2001) 5481–5486.
- [371] T. Hakoda, A. Shimada, A. Kimura, M. Taguchi, Y. Sugo, K. Arak, E.B. Dally, K. Hirota, An electron-beam irradiation/catalytic oxidation system for purification of aromatic hydrocarbons/air mixture under practical gas-flow condition, *Industrial & Engineering Chemistry Research*, 49 (2010) 5517–5522.
- [372] T. Hakoda, K. Matsumoto, A. Shimada, T. Narita, T. Kojima, K. Hirota, Application of ozone decomposition catalysts to electron-beam irradiated xylene/air mixtures for enhancing carbon dioxide production, *Radiation Physics and Chemistry*, 77 (2008) 585–590.

- [373] T. Hakoda, K. Matsumoto, A. Mizuno, T. Kojima, K. Hirota, Catalytic oxidation of xylene in air using TiO₂ under electron beam irradiation, *Plasma Chemistry and Plasma Processing*, 28 (2008) 25–37.
- [374] T. Hakoda, K. Matsumoto, A. Mizuno, T. Narita, T. Kojima, K. Hirota, Oxidation process of xylene in air using Ag/TiO₂ under electron beam irradiation, *IEEE Transactions on Industry Applications*, 44 (2008) 1950–1956.
- [375] T. Hakoda, K. Matsumoto, A. Mizuno, K. Hirota, Oxidation of xylene and its irradiation byproducts using an electron-beam irradiating gamma-Al₂O₃ bed, *Journal of Physics D–Applied Physics*, 41 (2008) 155202.
- [376] K.P. Francke, H. Miessner, R. Rudolph, Cleaning of air streams from organic pollutants by plasma-catalytic oxidation, *Plasma Chemistry and Plasma Processing*, 20 (2000) 393–403.
- [377] T. Kuroki, K. Hirai, R. Kawabata, M. Okubo, T. Yamamoto, Decomposition of adsorbed xylene on adsorbents using nonthermal plasma with gas circulation, *IEEE Transactions on Industry Applications*, 46 (2010) 672–679.
- [378] B. Wei, C. Y., Y. M., S. Z., H. Y., S. Y., Enhanced degradation of gaseous xylene using surface acidized TiO₂ catalyst with non-thermal plasmas, *Plasma Chemistry and Plasma Processing*, 35 (2014) 173–186.
- [379] J.Y. Ban, Y.H. Son, M. Kang, S.J. Choung, Highly concentrated toluene decomposition on the dielectric barrier discharge (DBD) plasma-photocatalytic hybrid system with Mn-Ti-incorporated mesoporous silicate photocatalyst (Mn-Ti-MPS), *Appl. Surf. Sci.*, 253 (2006) 535–542.
- [380] M. Magureanu, N.B. Mandache, E. Gaigneaux, C. Paun, V.I. Parvulescu, Toluene oxidation in a plasma-catalytic system, *Journal of Applied Physics*, 99 (2006) 123301.
- [381] A.M. Harling, D.J. Glover, J.C. Whitehead, K. Zhang, The role of ozone in the plasma-catalytic destruction of environmental pollutants, *Applied Catalysis B–Environmental*, 90 (2009) 157–161.
- [382] V. Demidiouk, S.I. Moon, J.O. Chae, Toluene and butyl acetate removal from air by plasma-catalytic system, *Catalysis Communications*, 4 (2003) 51–56.
- [383] F. Feng, L. Ye, J. Liu, K. Yan, Non-thermal plasma generation by using back corona discharge on catalyst, *Journal of Electrostatics*, 71 (2013) 179–184.

- [384] B.M. Penetrante, M.C. Hsiao, J.N. Bardsley, B.T. Merritt, G.E. Vogtlin, A. Kuthi, C.P. Burkhart, J.R. Bayless, Decomposition of methylene chloride by electron beam and pulsed corona processing, *Physics letters A*, 235 (1997) 76–82.
- [385] J. Li, S.P. Bai, X.C. Shi, S.L. Han, X.M. Zhu, W.C. Chen, Y.K. Pu, Effects of temperature on benzene oxidation in dielectric barrier discharges, *Plasma Chemistry and Plasma Processing*, 28 (2008) 39–48.
- [386] D.H. Kim, Y.S. Mok, S.B. Lee, Effect of temperature on the decomposition of trifluoromethane in a dielectric barrier discharge reactor, *Thin Solid Films*, 519 (2011) 6960–6963.
- [387] B.M. Penetrante, M.C. Hsiao, J.N. Bardsley, B.T. Merritt, G.E. Vogtlin, P.H. Wallman, Electron beam and pulsed corona processing of volatile organic compounds in gas streams, *Pure and Applied Chemistry*, 68 (1996) 1083–1087.
- [388] A.M. Harling, H.H. Kim, S. Futamura, J.C. Whitehead, Temperature dependence of plasma–catalysis using a nonthermal, atmospheric pressure packed bed; the destruction of benzene and toluene, *Journal of Physical Chemistry C*, 111 (2007) 5090–5095.
- [389] C.M. Du, J.H. Yan, B. Cheron, Decomposition of toluene in a gliding arc discharge plasma reactor, *Plasma Sources Science & Technology*, 16 (2007) 791–797.
- [390] A.S. Chiper, N. Blin–Simiand, M. Heninger, H. Mestdagh, P. Boissel, F. Jorand, J. Lemaire, J. Leprovost, S. Pasquiers, G. Popa, C. Postel, Detailed characterization of 2–heptanone conversion by dielectric barrier discharge in N_2 and N_2/O_2 mixtures, *Journal of Physical Chemistry A*, 114 (2010) 397–407.
- [391] N. Blin–Simiand, F. Jorand, L. Magne, S. Pasquiers, C. Postel, J.R. Vacher, Plasma reactivity and plasma–surface interactions during treatment of toluene by a dielectric barrier discharge, *Plasma Chemistry and Plasma Processing*, 28 (2008) 429–466.
- [392] L.A. Rosocha, R.A. Korzekwa, Advanced oxidation and reduction processes in the gas phase using non–thermal plasmas, *Journal of Advanced Oxidation Technologies*, 4 (1999) 247–264.
- [393] S. Futamura, M. Sugawara, Additive effect on energy efficiency and byproduct distribution in VOC decomposition with nonthermal plasma, *IEEE Transactions on Industry Applications*, 44 (2008) 40–45.

- [394] Y.S. Mok, V. Demidyuk, J.C. Whitehead, Decomposition of hydrofluorocarbons in a dielectric-packed plasma reactor, *Journal of Physical Chemistry A*, 112 (2008) 6586–6591.
- [395] H.C. Kang, Decomposition of chlorofluorocarbon by non-thermal plasma, *Journal of Industrial and Engineering Chemistry*, 8 (2002) 488–492.
- [396] J.H. Oh, Y.S. Mok, S.B. Lee, Destruction of HCFC-22 and distribution of byproducts in a nonthermal plasma reactor packed with dielectric pellets, *Journal of Korean Physical Society*, 54 (2009) 1539–1546.
- [397] T. Kuroki, T. Oishi, T. Yamamoto, M. Okubo, Bromomethane decomposition using a pulsed dielectric barrier discharge, *IEEE Transactions on Industry Applications*, 49 (2013) 293–297.
- [398] M.S. Gandhi, Y.S. Mok, Decomposition of trifluoromethane in a dielectric barrier discharge non-thermal plasma reactor, *Journal of Environmental Sciences-China*, 24 (2012) 1234–1239.
- [399] A.M. Vandenbroucke, R. Aerts, W. Van Gaens, N. De Geyter, C. Leys, R. Morent, A. Bogaerts, Modeling and experimental study of trichloroethylene abatement with a negative direct current corona discharge, *Plasma Chemistry and Plasma Processing*, 35 (2015) 217–230.
- [400] L. Fouad, S. Elhazek, Effect of humidity on positive corona discharge in a 3 electrode system, *Journal of Electrostatics*, 35 (1995) 21–30.
- [401] H. Ge, L. Zhang, L. Yan, D. Mi, Y. Zhu, Parameter optimization of excited OH radical in multi-needle to plate negative DC corona discharge, *Journal of Electrostatics*, 69 (2011) 529–532.
- [402] Y. Nakagawa, H. Fujisawa, R. Ono, T. Oda, Dilute trichloroethylene decomposition by using high pressure non-thermal plasma-Humidity effects, 2010 IEEE Industry Applications Society Annual Meeting, (2010).
- [403] S. Futamura, A.H. Zhang, T. Yamamoto, The dependence of nonthermal plasma behavior of VOCs on their chemical structures, *Journal of Electrostatics*, 42 (1997) 51–62.
- [404] A.A. Assadi, A. Bouzaza, C. Vallet, D. Wolbert, Use of DBD plasma, photocatalysis, and combined DBD plasma/photocatalysis in a continuous annular reactor for isovaleraldehyde elimination – Synergetic effect and byproducts identification, *Chemical Engineering Journal*, 254 (2014) 124–132.

- [405] H. Einaga, T. Ibusuki, S. Futamura, Performance evaluation of a hybrid system comprising silent discharge plasma and manganese oxide catalysts for benzene decomposition, *IEEE Transactions on Industry Applications*, 37 (2001) 1476–1482.
- [406] S. Futamura, A.H. Zhang, H. Einaga, H. Kabashima, Involvement of catalyst materials in nonthermal plasma chemical processing of hazardous air pollutants, *Catalysis Today*, 72 (2002) 259–265.
- [407] X. Fan, T. Zhu, Y. Wan, X. Yan, Effects of humidity on the plasma–catalytic removal of low–concentration BTX in air, *Journal of Hazardous Materials*, 180 (2010) 616–621.
- [408] K. Krawczyk, B. Ulejczyk, Influence of water vapor on CCl_4 and CHCl_3 conversion in gliding discharge, *Plasma Chemistry and Plasma Processing*, 24 (2004) 155–167.
- [409] A.A. Abdelaziz, T. Seto, M. Abdel–Salam, Y. Otani, Influence of nitrogen excited species on the destruction of naphthalene in nitrogen and air using surface dielectric barrier discharge, *Journal of Hazardous Materials*, 246 (2013) 26–33.
- [410] J. Karupiah, R. Karvembu, C. Subrahmanyam, The catalytic effect of MnO_x and CoO_x on the decomposition of nitrobenzene in a non–thermal plasma reactor, *Chemical Engineering Journal*, 180 (2012) 39–45.
- [411] S. Futamura, H. Einaga, A.H. Zhang, Comparison of reactor performance in the nonthermal plasma chemical processing of hazardous air pollutants, *IEEE Transactions on Industry Applications*, 37 (2001) 978–985.
- [412] R. Yamashita, T. Takahashi, T. Oda, Humidity effect on non–thermal plasma processing for VOCs decomposition, *Ias '96 – Conference Record of the 1996 IEEE Industry Applications Conference, Thirty–First Ias Annual Meeting, Vols 1–4*, (1996) 1826–1829.
- [413] S.Y. Lu, X.M. Sun, X.D. Li, J.H. Yan, C.M. Du, Decomposition of toluene in a rotating glidarc discharge reactor, *IEEE Transactions on Plasma Science*, 40 (2012) 2151–2156.
- [414] S. Agnihotri, M.P. Cal, J. Prien, Destruction of 1,1,1–trichloroethane using dielectric barrier discharge nonthermal plasma *Jorunal of Enironmental Engineering* 130 (2004) 349–355.
- [415] Y.S. Mok, S.B. Lee, J.H. Oh, K.S. Ra, B.H. Sung, Abatement of trichloromethane by using nonthermal plasma reactors, *Plasma Chemistry and Plasma Processing*, 28 (2008) 663–676.

- [416] M.S. Gandhi, Y.S. Mok, S.B. Lee, H. Park, Effect of various parameters for butane decomposition under ambient temperature in a dielectric barrier discharge non-thermal plasma reactor, *Journal of the Taiwan Institute of Chemical Engineers*, 44 (2013) 786–794.
- [417] Y. Kim, K.T. Kim, M.S. Cha, Y.H. Song, S.J. Kim, CF_4 decompositions using streamer- and glow-mode in dielectric barrier discharges, *IEEE Transactions on Plasma Science*, 33 (2005) 1041–1046.
- [418] S. Futamura, A.H. Zhang, T. Yamamoto, Mechanisms for formation of inorganic byproducts in plasma chemical processing of hazardous air pollutants, *IEEE Transactions on Industry Applications*, 35 (1999) 760–766.
- [419] A.A. Abdelaziz, T. Seto, M. Abdel-Salam, Y. Otan, Influence of N_2/O_2 mixtures on decomposition of naphthalene in surface dielectric barrier discharge based reactor, *Plasma Chemistry and Plasma Processing*, 34 (2014) 1371–1385.
- [420] L. Yu, X.D. Li, X. Tu, Y. Wang, S.Y. Lu, J.H. Yan, Decomposition of naphthalene by DC gliding arc gas discharge, *Journal of Physical Chemistry A*, 114 (2010) 360–368.
- [421] Z. Falkenstein, Effects of the O_2 concentration on the removal efficiency of volatile organic compounds with dielectric barrier discharges in Ar and N_2 , *Journal of Applied Physics*, 85 (1999) 525–529.
- [422] A.N. Trushkin, I.V. Kochetov, Simulation of toluene decomposition in a pulse-periodic discharge operating in a mixture of molecular nitrogen and oxygen, *Plasma Physics Reports*, 38 (2012) 407–431.
- [423] A.M. Harling, D.J. Glover, J.C. Whitehead, K. Zhang, Industrial scale destruction of environmental pollutants using a novel plasma reactor, *Industrial & Engineering Chemistry Research*, 47 (2008) 5856–5860.
- [424] Y. Shi, J.J. Ruan, X. Wang, W. Li, T.E. Tan, Evaluation of multiple corona reactor modes and the application in odor removal, *Plasma Chemistry and Plasma Processing*, 26 (2006) 187–196.
- [425] M. Huebner, O. Guaitella, A. Rousseau, J. Roepcke, A spectroscopic study of ethylene destruction and by-product generation using a three-stage atmospheric packed-bed plasma reactor, *Journal of Applied Physics*, 114 (2013) 033301.
- [426] T. Callebaut, Experimentele studie en numerieke simulatie van het corona- en het glimregime in een negatieve pin-plaat-ontlading bij atmosferedruk, in: *Applied Physics*, Ghent University, 2004, pp. 77.

- [427] J.S. Townsend, The potentials required to maintain current between coaxial cylinders, *Philosophical Magazine*, 28 (1914) 83–87.
- [428] O. Goossens, T. Callebaut, Y. Akishev, A. Napartovich, N. Trushkin, C. Leys, The DC glow discharge at atmospheric pressure, *IEEE Transactions on Plasma Science*, 30 (2002) 176–177.
- [429] J.M. Brown, *Molecular spectroscopy*, Oxford Press, 1998.
- [430] B.H. Stuart, *Biological Applications of Infrared Spectroscopy*, Wiley, 1997.
- [431] H. Gunzler, H.–U. Gremlich, *IR Spectroscopy: An introduction*, Wiley–VCH, 2002.
- [432] W. Herschel, Experiments on the refrangibility of the invisible rays of the Sun, *Philosophical Transactions of the Royal Society of London*, 90 (1800) 284–292.
- [433] B.R. Smith, *Fundamentals of Fourier Transform Infrared Spectroscopy*, CRC Press, 2011.
- [434] J. Kauppinen, J. Partanen, *Fourier transforms in spectroscopy*, Wiley–VCH, 2001.
- [435] NIST, 2011, Chemical kinetics database, <http://www.kinetics.nist.gov>.
- [436] J. Benedikt, A. Hecimovic, D. Ellerweg, A. von Keudell, Quadrupole mass spectrometry of reactive plasmas, *Journal of Physics D–Applied Physics*, 45 (2012) 403001.
- [437] <http://www.istcgroup.com/pdf/Mass%20Spectrometer%20Catalog%202005%20-%202007.pdf>
- [438] H. Hertz, Ueber einen Einfluss des ultravioletten Lichtes auf die elektrische Entladung, *Annalen der Physik*, 267 (1887) 983–1000.
- [439] M. Stamm, *Polymer surface and interface; characterization, modification and applications.*, Springer, 2008.
- [440] A.M. Belu, D.J. Graham, D.G. Castner, Time-of-flight secondary ion mass spectrometry: techniques and applications for the characterization of biomaterial surfaces, *Biomaterials*, 24 (2003) 3635–3653.
- [441] http://tmi.utexas.edu/wp-content/uploads/2014/01/TOF_SIMS_Supplementary_Information.pdf
- [442] <http://www.webexhibits.org/pigments/intro/spectroscopy.html>

- [443] <http://hyperphysics.phy-astr.gsu.edu/hbase/quantum/bragg.html>
- [444] <https://www.bruker.com/products/infrared-near-infrared-and-raman-spectroscopy/ft-ir-research-spectrometers/vertex-series/vertex-7070v/overview.html>
- [445] <http://lnls.cnpem.br/beamlines/xafs/equipments/mass-spectrometer/>
- [446] http://www.ozone-engineering.com/api_model450.html
- [447] F. Arena, G. Trunfio, J. Negro, B. Fazio, L. Spadaro, Basic evidence of the molecular dispersion of MnCeO_x catalysts synthesized via a novel "Redox-Precipitation" route, *Chemistry of Materials*, 19 (2007) 2269–2276.
- [448] <http://www.kratos.com/products/axis-ultra-ddd>
- [449] <http://www.iontofusa.com/news.htm>
- [450] J.P. Borra, A. Goldman, M. Goldman, D. Boulaud, Electrical discharge regimes and aerosol production in point-to-plane dc high-pressure cold plasmas: Aerosol production by electrical discharges, *Journal of Aerosol Science*, 29 (1998) 661–674.
- [451] B. Dhandapani, S.T. Oyama, Gas phase ozone decomposition catalysts, *Applied Catalysis B-Environmental*, 11 (1997) 129–166.
- [452] H. Einaga, S. Futamura, Catalytic oxidation of benzene with ozone over alumina-supported manganese oxides, *Journal of Catalysis*, 227 (2004) 304–312.
- [453] M.A. Peluso, L.A. Gambaro, E. Pronsato, D. Gazzoli, H.J. Thomas, J.E. Sambeth, Synthesis and catalytic activity of manganese dioxide (type OMS-2) for the abatement of oxygenated VOCs, *Catalysis Today*, 133 (2008) 487–492.
- [454] P. Ruetschi, Cation-vacancy model for MnO₂, *Journal of the Electrochemical Society*, 131 (1984) 2737–2744.
- [455] C. Lahousse, A. Bernier, P. Grange, B. Delmon, P. Papaefthimiou, T. Ioannides, X. Verykios, Evaluation of gamma-MnO₂ as a VOC removal catalyst: Comparison with a noble metal catalyst, *Journal of Catalysis*, 178 (1998) 214–225.
- [456] S. Futamura, A. Gurusamy, Synergy of nonthermal plasma and catalysts in the decomposition of fluorinated hydrocarbons, *Journal of Electrostatics*, 63 (2005) 949–954.

- [457] J.M. Giraudon, A. Elhachimi, G. Leclercq, Catalytic oxidation of chlorobenzene over Pd/perovskites, *Applied Catalysis B–Environmental*, 84 (2008) 251–261.
- [458] S. Maghsoodi, J. Towfighi, A. Khodadadi, Y. Mortazavi, The effects of excess manganese in nano–size lanthanum manganite perovskite on enhancement of trichloroethylene oxidation activity, *Chemical Engineering Journal*, 215 (2013) 827–837.
- [459] C. Zhang, C. Wang, W. Zhan, Y. Guo, Y. Guo, G. Lu, A. Baylet, A. Giroir–Fendler, Catalytic oxidation of vinyl chloride emission over LaMnO_3 and $\text{LaB}_{0.2}\text{Mn}_{0.8}\text{O}_3$ (B = Co, Ni, Fe) catalysts, *Applied Catalysis B–Environmental*, 129 (2013) 509–516.
- [460] S.X. Chen, Y. Wang, A.P. Jia, H.H. Liu, M.F. Luo, J.Q. Lu, Enhanced activity for catalytic oxidation of 1,2–dichloroethane over Al–substituted LaMnO_3 perovskite catalysts, *Appl. Surf. Sci.*, 307 (2014) 178–188.
- [461] R. Spinicci, M. Faticanti, P. Marini, S. De Rossi, P. Porta, Catalytic activity of LaMnO_3 and LaCoO_3 perovskites towards VOCs combustion, *Journal of Molecular Catalysis a–Chemical*, 197 (2003) 147–155.
- [462] J.J. Zhu, H.L. Li, L.Y. Zhong, P. Xiao, X.L. Xu, X.G. Yang, Z. Zhao, J.L. Li, Perovskite oxides: Preparation, characterizations, and applications in heterogeneous catalysis, *ACS Catalysis*, 4 (2014) 2917–2940.
- [463] K. Poplawski, J. Lichtenberger, F.J. Keil, K. Schnitzlein, M.D. Amiridis, Catalytic oxidation of 1,2–dichlorobenzene over ABO(3)–type perovskites, *Catalysis Today*, 62 (2000) 329–336.
- [464] H. Najjar, J.F. Lamonier, O. Mentre, J.M. Giraudon, H. Batis, Optimization of the combustion synthesis towards efficient LaMnO_{3+y} catalysts in methane oxidation, *Applied Catalysis B–Environmental*, 106 (2011) 149–159.
- [465] A. Musialik–Piotrowska, H. Landmesser, Noble metal–doped perovskites for the oxidation of organic air pollutants, *Catalysis Today*, 137 (2008) 357–361.
- [466] F. Arena, J. Negro, A. Parmaliana, L. Spadaro, G. Trunfio, Improved MnCeO_x systems for the catalytic wet oxidation (CWO) of phenol in wastewater streams, *Industrial & Engineering Chemistry Research*, 46 (2007) 6724–6731.
- [467] F. Arena, G. Trunfio, B. Fazio, J. Negro, L. Spadaro, Nanosize effects, physicochemical properties and catalytic oxidation pattern of the redox–precipitated MnCeO_x system, *Journal of Physical Chemistry C*, 113 (2009) 2822–2829.

- [468] X.Y. Wang, Q. Kang, D. Li, Low-temperature catalytic combustion of chlorobenzene over $\text{MnO}_x\text{-CeO}_2$ mixed oxide catalysts, *Catalysis Communications*, 9 (2008) 2158–2162.
- [469] Q.G. Dai, X.Y. Wang, G.Z. Lu, Low-temperature catalytic combustion of trichloroethylene over cerium oxide and catalyst deactivation, *Applied Catalysis B-Environmental*, 81 (2008) 192–202.
- [470] H.F. Li, G.Z. Lu, Q.G. Dai, Y.Q. Wang, Y. Guo, Y.L. Guo, Efficient low-temperature catalytic combustion of trichloroethylene over flower-like mesoporous Mn-doped CeO_2 microspheres, *Applied Catalysis B-Environmental*, 102 (2011) 475–483.
- [471] NIST, Chemistry Webbook, Standard Reference Database Number 69, in, 2011.
- [472] G. Socrates, *Infrared and Raman characteristic group frequencies: Tables and charts*, third ed., John Wiley & sons, LTD, 2004.
- [473] H.A. Szymanski, *Interpreted infrared spectra*, in, Plenum Press, 1964.
- [474] H.A. Szymanski, *IR theory and practice of infrared spectroscopy*, Plenum Press, 1964.
- [475] R. Morent, C. Leys, Ozone generation in air by a DC-excited multi-pin-to-plane plasma source, *Ozone-Science & Engineering*, 27 (2005) 239–245.
- [476] NIST, Chemical kinetics database, in, 2011.
- [477] A.M. Vandenbroucke, R. Morent, N. De Geyter, C. Leys, Non-thermal plasmas for non-catalytic and catalytic VOC abatement, *Journal of Hazardous Materials*, 195 (2011) 30–54.
- [478] R. Dorai, M.J. Kushner, Effect of propene on the remediation of NO_x from engine exhausts, *SAE/SP*, No. 1999-01-3683 (1999) 81–88.
- [479] R. Aerts, T. Martens, A. Bogaerts, Influence of vibrational states on CO_2 splitting by dielectric barrier discharges, *Journal of Physical Chemistry C*, 116 (2012) 23257–23273.
- [480] www.graphviz.org
- [481] W. Van Gaens, A. Bogaerts, Kinetic modelling for an atmospheric pressure argon plasma jet in humid air, *Journal of Physics D-Applied Physics*, 46 (2013) 275201.
- [482] A. Fridman, *Plasma chemistry*, in, Cambridge University Press, New York, 2008.

- [483] R. Aerts, X. Tu, C. De Bie, J.C. Whitehead, A. Bogaerts, An Investigation into the dominant reactions for ethylene destruction in non-thermal atmospheric plasmas, *Plasma Processes and Polymers*, 9 (2012) 994–1000.
- [484] I.A. Kossyi, A.Y. Kostinsky, A.A. Matveyev, V.P. Silakov, Kinetic scheme of the non-equilibrium discharge in nitrogen-oxygen mixtures, *Plasma Sources Science & Technology*, 1 (1992) 207–220.
- [485] J.S. Gift, R. McGaughy, D.V. Singh, B. Sonawane, Health assessment of phosgene: Approaches for derivation of reference concentration, *Regulatory Toxicology and Pharmacology*, 51 (2008) 98–107.
- [486] A. McCulloch, Chloroform in the environment: occurrence, sources, sinks and effects, *Chemosphere*, 50 (2003) 1291–1308.
- [487] A.M. Vandenbroucke, D. Minh Tuan Nguyen, J.-M. Giraudon, R. Morent, N. De Geyter, J.-F. Lamonier, C. Leys, Qualitative by-product identification of plasma-assisted TCE abatement by mass spectrometry and Fourier-transform infrared spectroscopy, *Plasma Chemistry and Plasma Processing*, 31 (2011) 707–718.
- [488] M.C. Alvarez-Galvan, B. Pawelec, V.A.D. O'Shea, J.L.G. Fierro, P.L. Arias, Formaldehyde/methanol combustion on alumina-supported manganese-palladium oxide catalyst, *Applied Catalysis B-Environmental*, 51 (2004) 83–91.
- [489] E. Finocchio, G. Sapienza, M. Baldi, G. Busca, Trichloroethylene catalytic conversion over acidic solid catalysts, *Applied Catalysis B-Environmental*, 51 (2004) 143–148.
- [490] V.P. Santos, M.F.R. Pereira, J.J.M. Orfao, J.L. Figueiredo, The role of lattice oxygen on the activity of manganese oxides towards the oxidation of volatile organic compounds, *Applied Catalysis B-Environmental*, 99 (2010) 353–363.
- [491] C.M. Su, R.W. Puls, Kinetics of trichloroethene reduction by zerovalent iron and tin: Pretreatment effect, apparent activation energy, and intermediate products, *Environmental Science & Technology*, 33 (1999) 163–168.
- [492] C. Ayrault, J. Barrault, N. Blin-Simiand, F. Jorand, S. Pasquiers, A. Rousseau, J.M. Tatibouet, Oxidation of 2-heptanone in air by a DBD-type plasma generated within a honeycomb monolith supported Pt-based catalyst, *Catalysis Today*, 89 (2004) 75–81.

- [493] A. Maciucă, C. Batiot-Dupeyrat, J.-M. Tatibouet, Synergetic effect by coupling photocatalysis with plasma for low VOCs concentration removal from air, *Applied Catalysis B-Environmental*, 125 (2012) 432-438.
- [494] A. Naydenov, D. Mehandjiev, Complete oxidation of benzene on manganese-dioxide by ozone, *Applied Catalysis a-General*, 97 (1993) 17-22.
- [495] H. Einaga, A. Ogata, Benzene oxidation with ozone over supported manganese oxide catalysts: Effect of catalyst support and reaction conditions, *Journal of Hazardous Materials*, 164 (2009) 1236-1241.
- [496] E. Rezaei, J. Soltan, Low temperature oxidation of toluene by ozone over MnO_x/gamma-alumina and MnO_x/MCM-41 catalysts, *Chemical Engineering Journal*, 198 (2012) 482-490.
- [497] D.-Z. Zhao, C. Shi, X.-S. Li, A.-M. Zhu, B.W.L. Jang, Enhanced effect of water vapor on complete oxidation of formaldehyde in air with ozone over MnO_x catalysts at room temperature, *Journal of Hazardous Materials*, 239 (2012) 362-369.
- [498] W. Li, G.V. Gibbs, S.T. Oyama, Mechanism of ozone decomposition on a manganese oxide catalyst. I. In situ Raman spectroscopy and ab initio molecular orbital calculations, *Journal of the American Chemical Society*, 120 (1998) 9041-9046.
- [499] I. Hannus, I. Kiricsi, G. Tasi, P. Fejes, Infrared spectroscopic study of adsorption of phosgene and carbon tetrachloride on zeolites - Fermi resonance, *Applied Catalysis*, 66 (1990) L7-L10.
- [500] J.F. Fan, J.T. Yates, Mechanism of photooxidation of trichloroethylene on TiO₂: Detection of intermediates by infrared spectroscopy, *Journal of the American Chemical Society*, 118 (1996) 4686-4692.
- [501] S.K. Joung, T. Amemiya, M. Murabayashi, R. Cai, K. Itoh, Chemical adsorption of phosgene on TiO₂ and its effect on the photocatalytic oxidation of trichloroethylene, *Surface Science*, 598 (2005) 174-184.
- [502] A. Miyake, I. Nakagawa, T. Miyazawa, I. Ichishima, T. Shimanouchi, S. Mizushima, Infrared and raman spectra of dichloroacetyl chloride in relation to rotational isomerism, *Spectrochimica Acta*, 13 (1958) 161-167.
- [503] L.J. Bellamy, R.L. Williams, Infrared spectra and polar effects in alpha-halogenated aldehydes and acid chlorides, *Journal of the Chemical Society*, (1958) 3465-3468.

- [504] G. Lucazeau, A. Novak, Spectres de vibration des aldéhydes CCl_3CHO , CCl_3CDO et CBr_3CHO , *Spectrochimica Acta*, 25 (1969) 1615–1629.
- [505] J. Borisch, S. Pilkenton, M.L. Miller, D. Raftery, J.S. Francisco, TiO_2 photocatalytic degradation of dichloromethane: An FTIR and solid-state NMR study, *Journal of Physical Chemistry B*, 108 (2004) 5640–5646.
- [506] H. Niki, P.D. Maker, L.P. Breitenbach, C.M. Savage, FT–IR studies of kinetics and mechanism for reaction of Cl atom with formaldehyde, *Chemical Physics Letters*, 57 (1978) 596–599.
- [507] R. Atkinson, Kinetics and mechanisms of the gas–phase reactions of the hydroxyl radical with organic compounds under atmospheric conditions, *Chemical Reviews*, 86 (1986) 69–201.
- [508] G. Sinquin, C. Petit, S. Libs, J.P. Hindermann, A. Kiennemann, Catalytic destruction of chlorinated C–2 compounds on a $\text{LaMnO}_{3+\delta}$ perovskite catalyst, *Applied Catalysis B–Environmental*, 32 (2001) 37–47.
- [509] D. Kiessling, R. Schneider, P. Kraak, M. Haftendorn, G. Wendt, Perovskite–type oxides – catalysts for the total oxidation of chlorinated hydrocarbons, *Applied Catalysis B–Environmental*, 19 (1998) 143–151.
- [510] C.D. Wagner, W.M. Riggs, L.E. Davis, J.F. Mulder, *Handbook of X–ray photoelectron spectroscopy*, PerkinElmer Corporation, Eden Prairie, 1978.
- [511] D. Henschler, Toxicity of Chlorinated Organic Compounds: Effects of the introduction of chlorine in organic molecules, *Angewandte Chemie International Edition in English*, 33 (1994) 1920–1935.
- [512] C. Nuns, A. Beaurain, M.T. Nguyen Dinh, A.M. Vandenbroucke, N. De Geyter, R. Morent, C. Leys, J.M. Giraudon, J.F. Lamonier, A combined ToF–SIMS and XPS study for the elucidation of the role of water in the performances of a Post–Plasma Process using $\text{LaMnO}_{3+\delta}$ as catalyst in the total oxidation of trichloroethylene, *Applied Surface Science*, 320 (2014) 154–160.
- [513] H.W. Nesbitt, D. Banerjee, Interpretation of XPS Mn(2p) spectra of Mn oxyhydroxides and constraints on the mechanism of MnO_2 precipitation, *American Mineralogist*, 83 (1998) 305–315.
- [514] V.R. Galakhov, M. Demeter, S. Bartkowski, M. Neumann, N.A. Ovechkina, E.Z. Kurmaev, N.I. Logachevskaya, Y.M. Mukovskii, J. Mitchell, D.L. Ederer, Mn 3s exchange splitting in mixed–valence manganites, *Physical Review B*, 65 (2002) 113102.

- [515] M. Uenishi, M. Taniguchi, H. Tanaka, M. Kimura, Y. Nishihata, J. Mizuki, T. Kobayashi, Redox behavior of palladium at start-up in the Perovskite-type LaFePdO_x automotive catalysts showing a self-regenerative function, *Applied Catalysis B-Environmental*, 57 (2005) 267–273.
- [516] J.A. Diaz-Aunon, M.C. Roman-Martinez, C.S.M. de Lecea, P.C. L'Argentiere, E.A. Cagnola, D.A. Liprandi, M.E. Quiroga, $\text{PdCl}_2\{\text{NH}_2(\text{CH}_2)_{12}\text{CH}_3\}_2$ supported on an active carbon: effect of the carbon properties on the catalytic activity of cyclohexene hydrogenation, *Journal of Molecular Catalysis a-Chemical*, 153 (2000) 243–256.
- [517] M.C. Militello, S.J. Simko, Elemental palladium by XPS, *Surface Science Spectra*, 3 (1994) 387–394.
- [518] M.F. Sunding, K. Hadidi, S. Diplas, O.M. Lovvik, T.E. Norby, A.E. Gunnaes, XPS characterisation of in situ treated lanthanum oxide and hydroxide using tailored charge referencing and peak fitting procedures, *Journal of Electron Spectroscopy and Related Phenomena*, 184 (2011) 399–409.
- [519] R. Craciun, Structure/activity correlation for unpromoted and CeO_2 -promoted $\text{MnO}_2/\text{SiO}_2$ catalysts, *Catalysis Letters*, 55 (1998) 25–31.
- [520] X.C. Zheng, S.P. Wang, X.Y. Wang, S.R. Wang, X.Y. Wang, S.H. Wu, Synthesis, characterization and catalytic property of ceria spherical nanocrystals, *Materials Letters*, 59 (2005) 2769–2773.
- [521] S. Tsunekawa, R. Sivamohan, S. Ito, A. Kasuya, T. Fukuda, Structural study on monosize CeO_{2-x} nano-particles, *Nanostructured Materials*, 11 (1999) 141–147.
- [522] S. Franger, S. Bach, J. Farcy, J.P. Pereira-Ramos, N. Baffier, Synthesis, structural and electrochemical characterizations of the sol-gel birnessite $\text{MnO}_{1.84}$ center dot $0.6\text{H}_2\text{O}$, *Journal of Power Sources*, 109 (2002) 262–275.
- [523] J.L. Zhou, L. Yu, M. Sun, S.Y. Yang, F. Ye, J. He, Z.F. Hao, Novel Synthesis of birnessite-type MnO_2 nanostructure for water treatment and electrochemical capacitor, *Industrial & Engineering Chemistry Research*, 52 (2013) 9586–9593.
- [524] C. Julien, M. Massot, R. Baddour-Hadjean, S. Franger, S. Bach, J.P. Pereira-Ramos, Raman spectra of birnessite manganese dioxides, *Solid State Ionics*, 159 (2003) 345–356.

- [525] C. Julien, M. Massot, Spectroscopic studies of the local structure in positive electrodes for lithium batteries, *Physical Chemistry Chemical Physics*, 4 (2002) 4226–4235.
- [526] Y. Luo, Y.Q. Deng, W. Mao, X.J. Yang, K.K. Zhu, J. Xu, Y.F. Han, Probing the surface structure of $\alpha\text{-Mn}_2\text{O}_3$ nanocrystals during CO oxidation by operando raman spectroscopy, *Journal of Physical Chemistry C*, 116 (2012) 20975–20981.
- [527] C.B. Azzoni, M.C. Mozzati, P. Galinetto, A. Paleari, V. Massarotti, D. Capsoni, M. Bini, Thermal stability and structural transition of metastable Mn_5O_8 : in situ micro-Raman study, *Solid State Communications*, 112 (1999) 375–378.
- [528] T. Kuroki, T. Fujioka, R. Kawabata, M. Okubo, T. Yamamoto, Regeneration of honeycomb zeolite by nonthermal plasma desorption of toluene, *IEEE Transactions on Industry Applications*, 45 (2009) 10–15.
- [529] H.H. Kim, S. Tsubota, M. Date, A. Ogata, S. Futamura, Catalyst regeneration and activity enhancement of Au/TiO_2 by atmospheric pressure nonthermal plasma, *Applied Catalysis A-General*, 329 (2007) 93–98.
- [530] T. Kuroki, T. Fujioka, M. Okubo, T. Yamamoto, Toluene concentration using honeycomb nonthermal plasma desorption, *Thin Solid Films*, 515 (2007) 4272–4277.
- [531] L. Sivachandiran, F. Thevenet, A. Rousseau, Regeneration of isopropyl alcohol saturated Mn_xO_y surface: Comparison of thermal, ozonolysis and non-thermal plasma treatments, *Chemical Engineering Journal*, 246 (2014) 184–195.
- [532] G. Qu, D. Liang, D. Qu, Y. Huang, J. Li, Comparison between Dielectric barrier discharge plasma and ozone regenerations of activated carbon exhausted with pentachlorophenol, *Plasma Science & Technology*, 16 (2014) 608–613.
- [533] M.S. Gandhi, A. Ananth, Y.S. Mok, J.-I. Song, K.-H. Park, Time dependence of ethylene decomposition and byproducts formation in a continuous flow dielectric-packed plasma reactor, *Chemosphere*, 91 (2013) 685–691.
- [534] R. Basner, A. Akimalieva, R. Brandenburg, Effect of atmospheric surface plasma on the adsorption of ethanol at activated carbon filter element, *Surface & Coatings Technology*, 234 (2013) 126–131.

- [535] L. Sivachandiran, F. Thevenet, P. Gravejat, A. Rousseau, Isopropanol saturated TiO₂ surface regeneration by non-thermal plasma: Influence of air relative humidity, *Chemical Engineering Journal*, 214 (2013) 17–26.
- [536] X. Dang, J. Huang, L. Cao, Y. Zhou, Plasma-catalytic oxidation of adsorbed toluene with gas circulation, *Catalysis Communications*, 40 (2013) 116–119.
- [537] T. Yamamoto, S. Asada, T. Iida, Y. Ehara, Novel NO_x and VOC treatment using concentration and plasma decomposition, *IEEE Transactions on Industry Applications*, 47 (2011) 2235–2240.
- [538] Y.S. Mok, D.H. Kim, Treatment of toluene by using adsorption and nonthermal plasma oxidation process, *Current Applied Physics*, 11 (2011) S58–S62.
- [539] T. Kuroki, K. Hirai, S. Matsuoka, J.Y. Kim, M. Okubo, Oxidation system of adsorbed VOCs on adsorbent using nonthermal plasma flow, *IEEE Transactions on Industry Applications*, 47 (2011) 1916–1921.
- [540] K. Inoue, H. Okano, Y. Yamagata, K. Muraoka, Y. Teraoka, Performance tests of newly developed adsorption/plasma combined system for decomposition of volatile organic compounds under continuous flow condition, *Journal of Environmental Sciences–China*, 23 (2011) 139–144.
- [541] W. Van Gaens, A. Bogaerts, Reaction pathways of biomedically active species in an Ar plasma jet, *Plasma Sources Science & Technology*, 23 (2014) 035015.
- [542] W. Van Gaens, A. Bogaerts, Kinetic modelling for an atmospheric pressure argon plasma jet in humid air, *Journal of Physics D–Applied Physics*, 46 (2013) 275201.
- [543] W.D. Chang, S.M. Senkan, Detailed chemical kinetic modeling of fuel-rich C₂HCl₃/O₂/Ar flames, *Environmental Science & Technology*, 23 (1989) 442–450.
- [544] S.W. Benson, M. Weissman, Mechanism of the pyrolysis of C₂HCl₅, molecular and radical steps, *International Journal of Chemical Kinetics*, 14 (1982) 1287–1304.
- [545] L. Zhu, PhD Thesis, in, New Jersey Institute of Technology, 2003.
- [546] W.G. Mallard, F. Westley, J.T. Herron, R.F. Hampson, NIST chemical kinetics database – Version 6.0, NIST Standard Reference Database 17, Gaithersburg, 1994.

- [547] A.C. Gentile, Kinetic processes and plasma remediation of toxic gases PhD Thesis, University of Illinois, 1995.
- [548] R.E. Olson, J.R. Peterson, J. Moseley, Ion-ion recombination total cross sections – Atomic species, *Journal of Chemical Physics*, 53 (1970) 3391–3397.
- [549] R. Atkinson, D.L. Baulch, R.A. Cox, R.F. Hampson, J.A. Kerr, M.J. Rossi, J. Troe, Evaluated kinetic and photochemical data for atmospheric chemistry: Supplement VI – IUPAC subcommittee on gas kinetic data evaluation for atmospheric chemistry, *Journal of Physical and Chemical Reference Data*, 26 (1997) 1329–1499.
- [550] C.G. Freeman, L.F. Phillips, Kinetics of chlorine oxide reactions 2. Reactions of nitrogen atoms with Cl₂O, *Journal of Physical Chemistry*, 72 (1968) 3028–3030.
- [551] F. Louis, C.A. Gonzalez, J.P. Sawerysyn, Ab initio study of the oxidation reaction of CO by ClO radicals, *Journal of Physical Chemistry A*, 107 (2003) 9931–9936.
- [552] W.D. Chang, S.B. Karra, S.M. Senkan, A detailed mechanism for the high temperature oxidation of C₂HCl₃, *Combustion Science and Technology*, 49 (1986) 107–121.
- [553] M.A.A. Clyne, J.A. Coxon, Kinetic studies of oxy-halogen radical systems, *Proceedings of the Royal Society of London Series A–Mathematical and Physical Sciences*, 303 (1968) 207–231.
- [554] J.E. Hudson, C. Vallance, M. Bart, P.W. Harland, Absolute electron-impact ionization cross sections for a range of C-1 to C-5 chlorocarbons, *Journal of Physics B–Atomic Molecular and Optical Physics*, 34 (2001) 3025–3039.
- [555] Y.V. Vasilev, V.G. Voinov, D.F. Barofsky, M.L. Deinzer, Absolute dissociative electron attachment cross-sections of chloro- and bromo-ethylenes, *International Journal of Mass Spectrometry*, 277 (2008) 142–150.
- [556] Z.F. Xu, R.S. Zhu, M.C. Lin, Ab initio studies of ClO_x reactions. 3. Kinetics and mechanism for the OH plus OClO reaction, *Journal of Physical Chemistry A*, 107 (2003) 1040–1049.
- [557] D.L. Baulch, C.J. Cobos, R.A. Cox, C. Esser, P. Frank, T. Just, J.A. Kerr, M.J. Pilling, J. Troe, R.W. Walker, J. Warnatz, Evaluated kinetic data for combustion modeling, *Journal of Physical and Chemical Reference Data*, 21 (1992) 411–734.

